



# Development of a hybrid coating associating biomimetic hydroxyapatite and natural antibiotics with antibacterial properties

Estelle Palierse

## ► To cite this version:

Estelle Palierse. Development of a hybrid coating associating biomimetic hydroxyapatite and natural antibiotics with antibacterial properties. Material chemistry. Sorbonne Université, 2019. English. NNT : 2019SORUS316 . tel-03141223

**HAL Id: tel-03141223**

**<https://theses.hal.science/tel-03141223>**

Submitted on 15 Feb 2021

**HAL** is a multi-disciplinary open access archive for the deposit and dissemination of scientific research documents, whether they are published or not. The documents may come from teaching and research institutions in France or abroad, or from public or private research centers.

L'archive ouverte pluridisciplinaire **HAL**, est destinée au dépôt et à la diffusion de documents scientifiques de niveau recherche, publiés ou non, émanant des établissements d'enseignement et de recherche français ou étrangers, des laboratoires publics ou privés.

# Sorbonne Université

Ecole doctorale 397 Physique et Chimie des Matériaux

*Laboratoire de Chimie de la Matière Condensée de Paris*

*Laboratoire de Réactivité de Surface*

## Development of a hybrid coating associating biomimetic hydroxyapatite and natural antibiotics with antibacterial properties

*Développement d'un revêtement hybride aux propriétés antibactériennes  
associant hydroxyapatite biomimétique et antibiotiques naturels*

Par Estelle Palierse

Thèse de doctorat de Physique et Chimie des matériaux

Dirigée par Thibaud Coradin et Claude Jolival

Présentée et soutenue publiquement le 10 octobre 2019

Devant un jury composé de :

Christèle Combes	Professeur	Rapporteur
Jean-Marie Nédélec	Professeur	Rapporteur
Catherine Debiemme-Chouvy	Directrice de recherche	Examinatrice
Franck Bouchart	Maître de conférences	Examineur
Claude Jolival	Professeur	Directrice de thèse
Thibaud Coradin	Directeur de recherche	Directeur de thèse

# Remerciements

J'aimerais tout d'abord remercier les membres du jury pour avoir accepté d'évaluer mon travail, Christèle Combes et Jean-Marie Nédélec en tant que rapporteurs et Catherine Debiemme-Chouvy et Franck Bouchart en tant qu'examinateurs.

Je remercie Florence Babonneau et Hélène Pernot de m'avoir accueillie au Laboratoire de Chimie de la Matière Condensée de Paris, et au Laboratoire de Réactivité de Surface pendant ces trois ans et demi de travail, d'abord en master puis en doctorat. Mes remerciements vont également à Christian Bonhomme et François Ribot, qui ont pris la suite de Florence à la tête du LCMCP.

Je tiens à remercier chaleureusement ma directrice et mon directeur de thèse, Claude Jolival et Thibaud Coradin. Merci de m'avoir fait confiance pour travailler sur ce sujet. Merci d'avoir toujours répondu présents pour m'aider et m'encourager, malgré vos emplois du temps très chargés. J'aurai beaucoup appris à vos côtés pendant ces 3 ans et demi et j'ai été ravie d'avoir pu travailler avec vous deux.

J'aimerais remercier tout particulièrement Laetitia Valentin pour son aide de tous les jours, que ce soit en salle de microbio ou pour tout le reste. Merci d'avoir rendu ma vie de doctorante plus facile, même quand il fallait étaler 180 boîtes en deux heures. Merci à Vincent Humblot pour m'avoir fait partager son expertise tout au long de ma thèse, et à Christophe Hélyary pour son aide en culture cellulaire et en bactériologie, domaines dans lesquels j'étais plus que novice.

Cette thèse est enrichie de nombreuses techniques d'analyse que je n'aurai pas pu réaliser sans l'aide de nombreuses personnes. Je remercie Antoine Miche et Christophe Métivier pour les manips d'XPS et Jessem Landoulsi pour son aide dans l'analyse, Isabelle Génois, Sandra Casale et David Montero pour les clichés MEB, ainsi que Patrick Le Griel et Gervaise Mosser pour les images TEM. Merci à Sylvie Masse et Guillaume Laurent pour la RMN du solide.

Je remercie Jean-Marc Krafft pour son aide avec les spectroscopies vibrationnelles, mais aussi pour m'avoir proposé de faire partie de la commission ACTS du LRS. Je remercie les différents membres de cette commission avec lesquelles nous avons travaillé. Cette expérience sur la sécurité au laboratoire était très enrichissante.

Mes remerciements vont également à Cédric Pryzbylski, pour m'avoir fait découvrir la spectrométrie de masse. Merci pour la disponibilité et la gentillesse dont tu as toujours fait preuve lors de nos échanges.

Je remercie Claude et Thibaud de m'avoir permis de découvrir Hong-Kong et Buenos Aires dans le cadre d'échanges pendant ma thèse. Je remercie Margareth Ip, Sandra Lau, et Ben Chan de m'avoir accueillie à Hong-Kong. Merci également à Martin Desimone et toute son équipe, en particulier Ines, Christian et Juan pour leur accueil et leur aide lors de mon séjour à Buenos Aires.

Je remercie enfin l'ensemble des membres permanents et non permanents des laboratoires LRS et LCMCP, pour la bonne ambiance qui y règne et qui permet de travailler sereinement. Merci en particulier aux membres de l'équipe Matbio. Je pense également à Nadia et Mathias, ainsi qu'à Ilhem, avec qui j'ai partagé un bureau. Merci à Ambre d'avoir travaillé avec moi pendant 4 mois, ce qui a enrichi ce manuscrit. Merci à Yacine, à Antoine, à Isabelle et à tous ceux avec qui j'ai partagé des pauses goûter. Parce que pendant ces trois ans nous sommes devenus amis, je remercie les membres de ma promo, et particulièrement Karol.

Je remercie finalement ma famille et mes amis de m'avoir encouragé pendant cette aventure







## Outline

List of abbreviations .....	iv
General introduction .....	3
References .....	6
1. Literature Review .....	11
1.1 Total hip arthroplasty: generalities, loosening and infections .....	13
1.2 Osseointegration improvement strategies .....	14
1.3 Hydroxyapatite coatings process .....	23
1.4 Antibacterial strategies .....	37
1.4 Conclusion: our strategy .....	51
References .....	53
2. Molecular study: interactions between calcium and biologically-active molecules .....	67
2.2 Introduction .....	69
2.3 Antibacterial and antioxidant activities of BAMs. ....	69
2.4 Interactions of calcium with natural polyphenols exhibiting antioxidant properties .....	72
2.5 Stability of baicalin and baicalein at different pH and effect on calcium complexation .....	88
2.6 General conclusions .....	107
References .....	108
3. Formation of hybrid hydroxyapatite – biologically active molecule nanoparticles .....	115
3.1 Introduction .....	117
3.2 Hydroxyapatite synthesis .....	117
3.3 Incorporation of BAMs .....	118
3.4 Biological activity of hydroxyapatite – baicalein hybrid particles obtained by adsorption .....	134
3.5 Conclusions .....	141
References .....	143
4. Elaboration of hybrid hydroxyapatite – biologically active molecules coatings on Ti6Al4V titanium alloys .....	149

4.1 Introduction.....	151
4.2 Deposition of biomimetic hydroxyapatite in SBF.....	151
4.3 Incorporation of biologically active molecules.....	166
4.4 Biological activity of hydroxyapatite-baicalin coatings .....	180
4.5 Conclusions.....	190
4.6 Summary.....	191
References.....	195
General conclusions and perspectives .....	201
Experimental section.....	I
Materials.....	I
Characterization techniques .....	I
Résumé de la thèse en français.....	V

## List of abbreviations

### Organics

AMP	Antimicrobial peptide
BAM	Biologically active molecule
BA	Baicalin
BE	Baicalein
BMP	Bone-morphogenetic protein
CA	Chlorogenic acid
PEG	Poly(ethylene glycol)
RA	Rosmarinic acid
RGD	Arginylglycylaspartic acid (Arg-Gly-Asp)

### Inorganics

ACP	Amorphous calcium phosphate
CDHA	Calcium deficient hydroxyapatite
DCPA	Dicalcium phosphate anhydrous
DCPD	Dicalcium phosphate dehydrate
FAp	Fluoroapatite
HAp	Hydroxyapatite
IEP	Isoelectric point
NP	Nanoparticle
OCP	Octacalcium phosphate
TCP	Tricalcium phosphate
Ti	Titanium
TiAlV or Ti6Al4V	Alloy Titanium-Aluminium-Vanadium (90/6/4)
TNT	Titania nanotube
TTCP	Tetracalcium phosphate

## Synthesis methods

IHT	Induction heating treatment
MAO	Micro-arc oxidation
SBF	Simulated Body Fluid
TSBF	Tas- Simulated Body Fluid

## Biology

BHI	Brain Heart Infusion
DMEM	Dulbecco's modified Eagles medium
DPBD	Dulbecco's Phosphate Buffered Saline
ECM	Extracellular matrix
EPS	Extrapolymeric substance
LB	Lysogeny broth
MIC	Minimum Inhibitory Concentration
MDR	Multidrug resistant
MH	Mueller-Hilton
MRSA	Methicillin resistant <i>Staphylococcus aureus</i>
PJI	Prosthetic joint infection

## Characterization techniques

ESI-MS	Electrospray ionization mass spectrometry
FE-SEM	Field emission scanning electron microscopy
FTIR-ATR	Fourier transformed infrared spectroscopy – attenuated total reflectance
HPLC	High performance liquid chromatography
NMR	Nuclear magnetic resonance
QCM	Quartz crystal microbalance
XRD	X-ray diffraction
XPS	X-ray photoemission spectroscopy









# General introduction

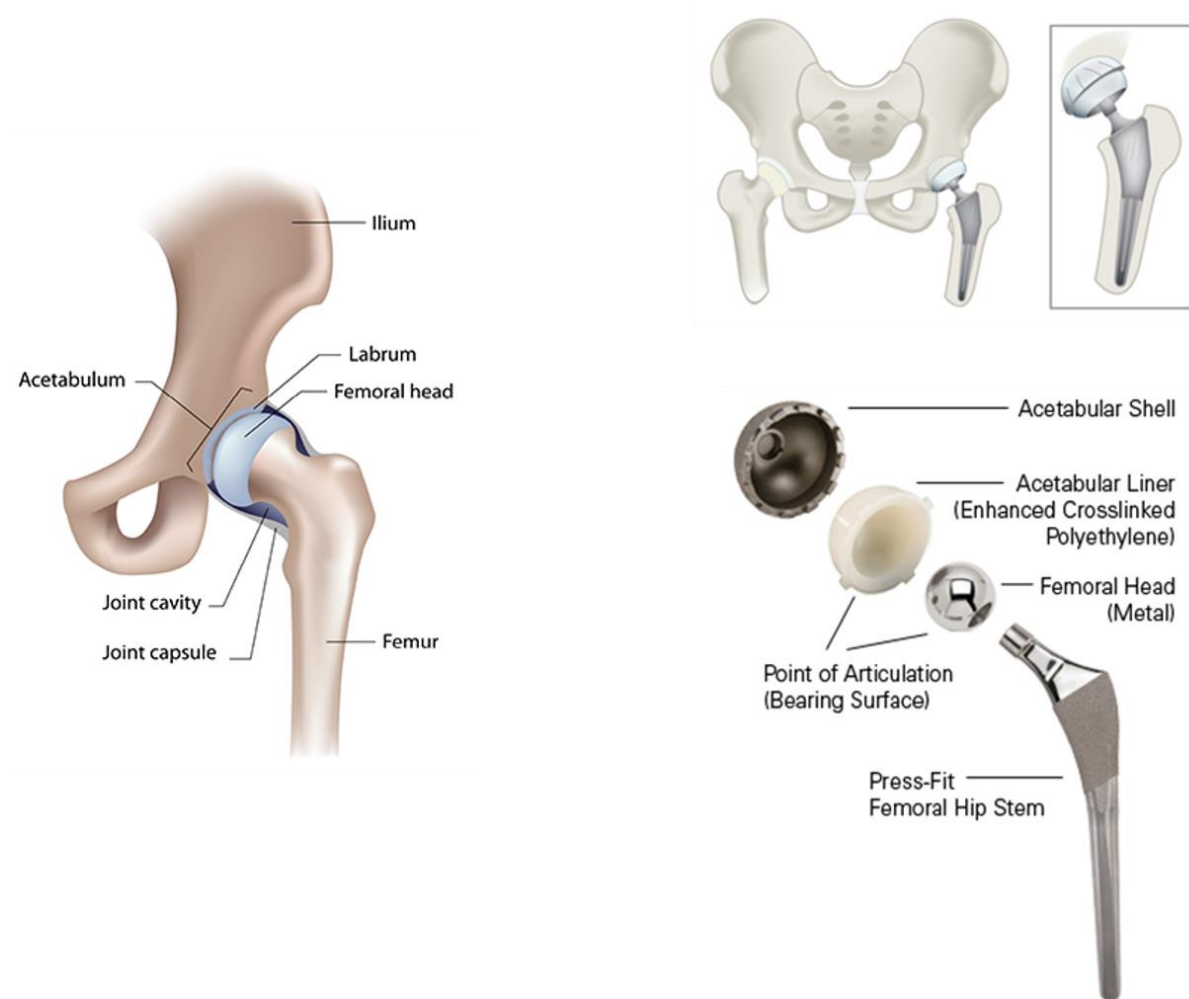


## General introduction

A human body is constituted by 206 bones connected by more than 290 joints. An example of joint is the hip that connects the limb and the pelvis. It involves the femoral head and the cuplike acetabulum formed at the union of three pelvic bones (the ilium, pubis and ischium), as seen on **Figure 0.1**. Its role is mainly to support the weight of the body, during standing and walking. The joint is freely movable. However, hip pain is common with ageing, caused by osteoarthritis, a disease characterized by the disappearance of the cartilage favoring the sliding of the head of the femur in the acetabulum. To reduce pain and recover the function of the joint with the goal to improve the quality of life of the patients, the defective joint is replaced by an implant during a total hip arthroplasty. It is one of the most common orthopedic surgery, with more than 100 000 people operated each year in France<sup>1</sup>.

For ages, people have tried to replace defective part of the body by implants made by natural or synthetic materials. For hip replacements, the earliest recorded attempts date back from 1891, in Germany, with the use of ivory (a natural material, component of teeth and elephant tusks) to replace the femoral head<sup>2</sup>. Implants used today are very close to the one developed in the 1960's by Sir John Charnley. These implants are constituted in three parts, a metallic femoral stem, a polyethylene acetabular component and acrylic bone cement. The cement improves the prosthetic fixation, acting like a glue. Nowadays, three types of prosthesis are available, metal-on-polyethylene, metal-on-metal and ceramic-on-ceramic, each with advantages and disadvantages. Cementless techniques are also developed to avoid the use of cement that is degraded during locomotion, causing inflammatory response and failure of the implant. A scheme of a classical hip prosthesis is presented in **Figure 0.1**.

Concerning cementless prostheses, two main issues remain, aseptic loosening and infections, causing an incidence of revision surgeries of about 10 %<sup>3,4</sup>. Firstly, aseptic loosening is due to a poor interaction between the implant and the bone. Metallic implants are biocompatible, meaning that they do not induce an inflammatory response, but they cannot enhance bone growth as such. Modifications of surface state of the metallic substrate by physical or chemical methods are possible to improve the osseointegration. For instance, the use of hydroxyapatite, the mineral constituting of mammals bones and teeth, as a coating allows a better interaction between bones and implants. The second issue about prostheses is a significant development of infection, despite the preventive treatment by prophylactic antibiotics and aseptic surgeries techniques. A promising strategy is to use the implant as the support of the antimicrobial strategy, with the possibility to achieve higher dosages near the affected site thereby improving efficiency and reducing the treatment duration and side effect<sup>5</sup>.



**Figure 0.1** Hip joint anatomy, position of the implant at the place of the joint and description of a classical implant

In this context, this thesis aims to develop an antimicrobial coating on metallic implant, by associating hydroxyapatite and antibacterial molecules, as presented in **Figure 0.2**. We decided to synthesize biomimetic hydroxyapatite to achieve the best interaction between bone and implant. As antimicrobial resistance is one of the main challenges for public health in the 21<sup>st</sup> century, our choice of antibiotics inclined towards natural molecules, extracted from plants, known to be antibacterial, but never used in the field. Four molecules were chosen, baicalin, baicalein, rosmarinic acid and chlorogenic acid. The main objective of this work was thus the incorporation of these natural molecules on or in hydroxyapatite. With this goal, we investigated the interaction between molecules and hydroxyapatite at different levels, in solution, with nanoparticles and finally with the coating.

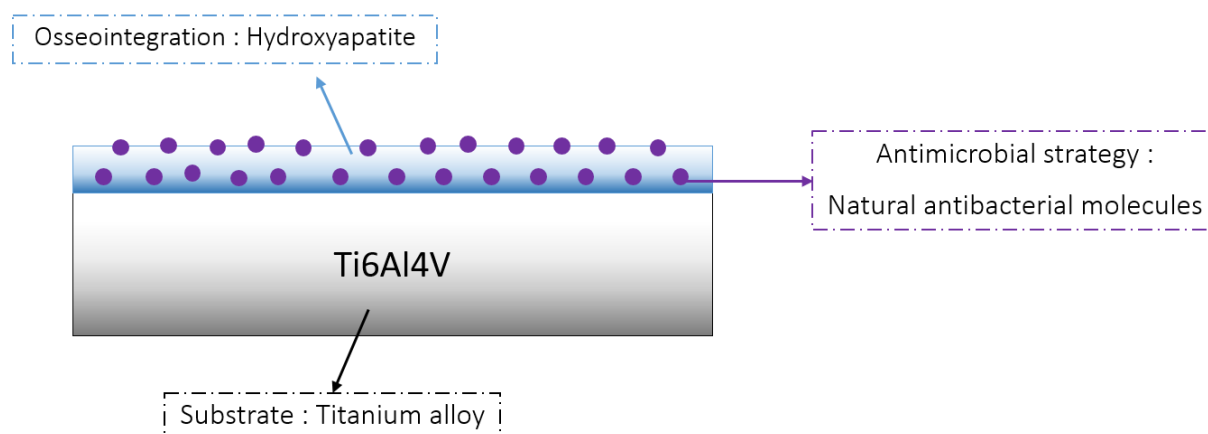
The first chapter of this manuscript is a literature review on the design of coatings on metallic implants with osseointegration and/or antibacterial properties. Techniques to improve osseointegration will be presented, before an important part devoted to hydroxyapatite synthesis and deposition. Finally, a study of the antibacterial strategies available will lead us to present our strategy to develop an antibacterial hydroxyapatite coating.

The second chapter will be devoted to a study of the four selected molecules in solution, their biological activities and their interaction with calcium. On one side, the complexation of rosmarinic acid and chlorogenic acid with calcium was studied by spectroscopic and spectrometric methods. On the other side, we deeply investigated the stability of baicalin and baicalein in aqueous solution at different pHs, before examining their interaction with calcium. The effect of complexation with calcium on the biological activity of the four molecules was studied.

The third chapter focuses on the incorporation of the antibacterial molecules on/within hydroxyapatite nanoparticles by two methods, during synthesis of hydroxyapatite or by adsorption on pre-synthesized hydroxyapatite. The effect of the presence of organic molecules on hydroxyapatite synthesis was investigated. Baicalein being the molecule incorporated with the highest rate by adsorption, biological activities of nanoparticles with adsorbed baicalein were studied.

The last chapter is dedicated to the development of the biomimetic hydroxyapatite coating on a metallic substrate, the Ti6Al4V titanium alloy. After selection of suitable deposition conditions, biologically-active molecules were incorporated in the coating during synthesis of hydroxyapatite or by adsorption on pre-synthesized hydroxyapatite, and the two methods were compared. Finally, biological activities of coatings with baicalein, incorporated by the two methods, were investigated.

A conclusion with our main findings and perspectives will end this manuscript.



**Figure 0.2** Strategy developed in this thesis

## References

- 1 Haute Autorité de Santé. Prothèses de hanche. Phase contradictoire suite à la révision d'une catégorie de dispositifs médicaux. Saint-Denis La Plaine : HAS ; 2014
- 2 S. R. Knight, R. Aujla and S. P. Biswas, *Orthop Rev*, 2011, **3**, 72–74.
- 3 S. Kurtz, F. Mowat, K. Ong, N. Chan, E. Lau and M. Halpern, *The Journal of Bone and Joint Surgery*, 2011, **87-A**, 1487–1497.
- 4 B. Zhang, D. Myers, G. Wallace, M. Brandt and P. Choong, *International Journal of Molecular Sciences*, 2014, **15**, 11878–11921.
- 5 R. Dorati, A. DeTrizio, T. Modena, B. Conti, F. Benazzo, G. Gastaldi and I. Genta, *Pharmaceuticals*, 2017, **10**, 96.







# Literature review



# 1. Literature Review

## Outline

1. Literature Review .....	11
1.1 Total hip arthroplasty: generalities, loosening and infections.....	13
1.2 Osseointegration improvement strategies .....	14
1.2.1 Parameters improving osseointegration.....	14
1.2.2 Topological modifications .....	15
1.2.3 Incorporation of extracellular matrix components .....	17
1.2.4 Calcium phosphate based coatings .....	20
1.3 Hydroxyapatite coatings process .....	23
1.3.1 Synthesis of hydroxyapatite particles .....	24
1.3.2 Coatings process.....	28
1.4 Antibacterial strategies .....	37
1.4.1 Surface topology tuning .....	38
1.4.2 Surface functionalization.....	40
1.4 Conclusion: our strategy.....	51
References.....	53



## 1.1 Total hip arthroplasty: generalities, loosening and infections

“Biomaterials are defined as substances, other than drugs, that can be used to treat, augment, replace, or repair any tissue or organ of the body in vivo for any period of time”<sup>1</sup>. It can be either metals, ceramics or polymers. With ageing of population, the demand for biomaterials is constantly increasing, especially in the field of joint replacements (hip, knee). In the field of joint replacements, the requirements for physical properties do not leave many options in the choice of the material, only metals have acceptable stress and fatigue resistance. Due to the necessity of biocompatibility, titanium and its alloys are widely used. Biocompatibility is defined as the “ability of a biomaterial to perform its desired function with respect to a medical therapy, without eliciting any undesirable local or systemic effects in the recipient or beneficiary of that therapy, but generating the most appropriate beneficial cellular or tissue response to that specific situation, and optimizing the clinically relevant performance of that therapy” by the William dictionary of biomaterials<sup>2</sup>. Other metals and alloys are good candidates, such as chromium, magnesium and nickel alloy. However, toxicity of chromium and nickel ions limits their use in hip and knee prostheses, and magnesium has an in vitro corrosion rate too important to be used. In this thesis, we will focus on the study of the Ti-6Al-4V alloy, composed of titanium, aluminum and vanadium, because there is a consensus nowadays about its use, as its resistance to the corrosion in body fluids at physiological temperature and pH is better than commercially pure Titanium, with comparable physical properties<sup>3</sup>.

Total hip arthroplasty, which is the surgical procedure where the patient’s joint is replaced by an implant, affects more than 100 000 people each year in France<sup>4</sup>. Several studies underline the increasing rate of revisions arthroplasties<sup>5</sup> these last 20 years, reaching around 10 % of the total amount of joint arthroplasties each year in Australia<sup>6</sup>, due to the implant failure, from the first days after implantation to two years post-surgery. Two main reasons explain this failure, the aseptic loosening and the development of infections. Aseptic loosening can be separated in two major cases, depending on the type of implant with or without cement. The cement is used to fix the prosthesis in the implantation site, but the repetition of mechanical stress during locomotion degrades the bone-cement and cement-implant interfaces, leading to the disintegration of the cement and the production of debris particles which can trigger an inflammatory response<sup>6</sup>. In cementless arthroplasty, the loosening is related to the ability of osseointegration of the implant material into the bone<sup>6</sup>. The term osseointegration refers to the direct contact between living bone and implant<sup>7</sup>, meaning the absence of an interfacial fibrous tissue. The bone grows directly into or onto the implant surface<sup>8</sup>, which implies that the biomaterial surface is osteoconductive. When the material cannot promote bone growth, osseointegration is poor and the risk of loosening increases. This is the case for all untreated metallic surfaces of bone implant. The second reason for failure is the development of infections near the

implantation site, with a rate of 0.3-0.4 % depending of the study<sup>9,10</sup>, 15 infections over 5060 studied cases in the first study, and 154 infections over 36340 cases in the second. The main bacterial strains encountered in such infections are gram-positive bacteria such as *Staphylococcus aureus* and *S. epidermidis*. The rate of infection remains low thanks to the use of prophylactic antibiotics and aseptic surgical procedures as preventive measures, but is not negligible. In the next sections, we will explore different strategies to improve the osseointegration, and then we will see how to develop an antibacterial surface useable for bone implantation.

## 1.2 Osseointegration improvement strategies

### 1.2.1 Parameters improving osseointegration

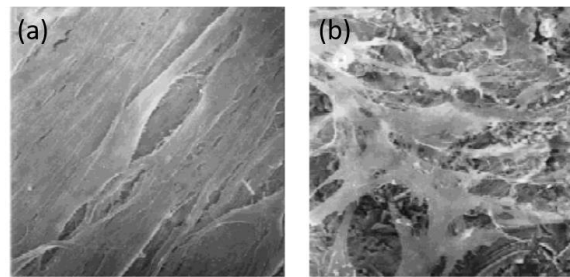
Before exploring the critical points to improve the integration of implants in the bone site, it is necessary to understand how the implant interacts with its environment, and how bone is forming on the implant surface. In a healthy body, bone is constantly remodeled through a process involving osteogenic cells: osteoclasts that degrade the old bone, and osteoblasts, which are able to synthesize the newly formed bone. On an implant surface, the formation of a new bone is conditioned by the osteoblasts' activity. Davies<sup>11,12</sup> assumed that the formation of a new bone at the implant surface occurs in a three-stage process, first osteoconduction, secondly "de novo" bone formation and finally bone remodeling. Osteoconduction is the phenomenon where osteogenic cells, i.e. non-fully differentiated bone cells, migrate to the implant surface. The second step consists of their differentiation into osteoblasts that will synthesize new bone. The differentiation is possible at the contact of the implant surface, or the osteogenic cell can differentiate near the implant surface, leading to a distance bone formation. The contact/ distance osteogenesis depends on the surface characteristics, in terms of chemistry, roughness, topology and wettability.

Before colonization of the surface by osteogenic cells, the first interaction between the biomaterial and its environment is through the blood circulation, reservoir of proteins that will adhere to the surface. The interaction between those proteins and the migratory cells through different signal pathways will end by the cell adhesion to the implant surface. It is then necessary to understand the key surface parameters leading to a good protein adsorption. Proteins interact with the surface through hydrophobic interactions, electrostatic interactions, hydrogen bonding and/or Van der Waals forces. The chemistry of the surface, as well as its surface energy and wettability, are then important parameters that affect the protein adsorption. Because proteins are mainly within the nanometer range, the dimension scale of the surface is a relevant parameter, especially through the topography design (roughness, porosity)<sup>13</sup>. Two main strategies can therefore be used to improve the surface osseointegration, one involving only a physical or chemical surface treatment, and the second using

the deposition of a coating<sup>6</sup>, modifying both physical and chemical properties of the implant. The next two paragraphs will give some examples of these two strategies.

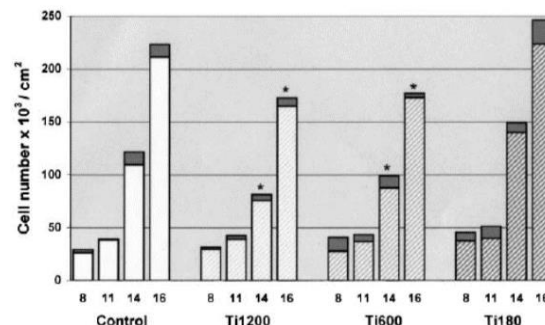
### 1.2.2 Topological modifications

It has been commonly accepted that a rough hydrophilic surface is better for protein adsorption and cells adhesion than a smooth hydrophobic surface and that the roughness organization is also a critical parameter. To develop surfaces with suitable roughness and wettability, several technics can be used, such as sandblasting, polishing, acid etching as well as laser and thermal treatments. Anselme *et al.* showed that adhesion and proliferation of osteoblasts after 14 days of culture is better on mechanically-polished Ti6Al4V surface than on sandblasted one<sup>14</sup> (**Figure 1.1**). In the case of polishing, grooves are all oriented in the same direction, which cannot be obtain through sandblasting. Moreover, sandblasted surface is enriched with aluminum oxide, explaining the poor adhesion<sup>15</sup>. Al species can be released during the *in vivo* dissolution of the oxide layer, which can be toxic for the cells.



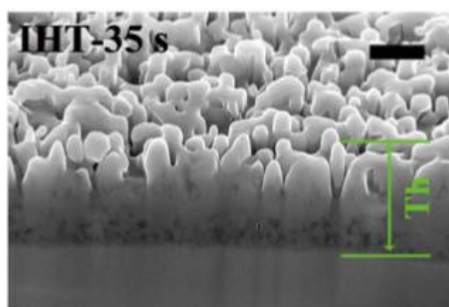
**Figure 1.1** SEM images of human osteoblasts on TiAlV samples after 14 days of cell cultures (a) on mechanically polished surface with P4000 SiC paper and (b) on sandblasted surface with 500 µm alumina particles<sup>14</sup>

Deligianni *et al.* further studied the influence of the polishing grain, showing that protein adhesion, as well as cell adhesion and proliferation, is better on the rougher substrates. (**Figure 1.2**)<sup>16</sup>.



**Figure 1.2** Human bone marrow cell proliferation after 8, 11, 14 and 16 days of culture on TiAlV mechanically polished with 1200-, 600- and 180-grit SiC paper, and on tissue culture plate (control)<sup>16</sup>

The roughness orientation can be achieved through other technics such as laser interference lithography, which permits the formation of surface with arrays, dots or dimple with controlled roughness and hydrophilicity depending on the irradiation time<sup>17</sup>. Liu et al<sup>17</sup> showed that cell adhesion is not dependent of the surface nanostructuration, while it is critical for proliferation, with the best proliferation rate visible for doted rough surface. It was also suggested that nanopillars obtained with induction heating treatment (IHT) could serve as anchor points for cell adhesion and also promote osteoblast differentiation (**Figure 1.3**)<sup>18</sup>.

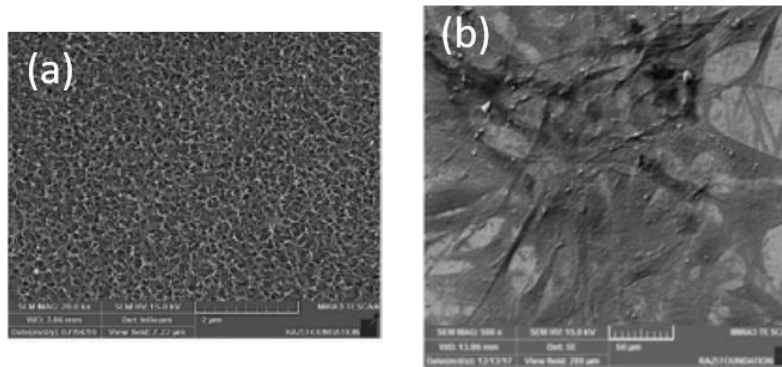


**Figure 1.3** A cross sectionnall view of the FE-SEM images of oriented TiO<sub>2</sub> nanopillar layer growth on the TiAlV surfaces after IHT oxidation for 35 s; scale bar = 500 nm <sup>18</sup>

When increasing surface roughness from 0.56 to 2.73  $\mu\text{m}$  of average roughness value through laser surface melting method<sup>19</sup>, only effect on proliferation was visible. Besides elimination of cracks, this method allows a homogeneous distribution of Ti and Al at the surface. A similar situation was met after oxidation in air at 750 °C of smooth or acid-etched rough TiAlV substrates<sup>20</sup>. A polycrystalline titanium oxide was obtained at the surface together with an increase in the aluminium content from 2 to 10 %. Despite these phase changes, the wettability of the surface remained the same, which could explain why authors did not see any difference in cell adhesion on both oxidized surfaces. However, a higher production of differentiation markers for etched oxidized surfaces confirmed that osteoblast were maturing and forming new bones. From these data, the microroughness (due to acid etching) appears more critical than nanoscale modifications (oxidation). A thermal treatment under argon atmosphere at 1000 °C can also be used to modify the surface TiO<sub>2</sub> oxide phase, increasing its wettability and roughness and, consequently cell adhesion and bone formation *in vivo*<sup>21</sup>. The thermal treatment may also be performed after hydroxylation in alkali solution, this “alkali heat treatment” being widely used in the field. Shahriyari *et al.* used this process combined to friction hardening to obtain nanostructured surfaces of titanate, enhancing cell adhesion and proliferation (**Figure 1.4**)<sup>22</sup>. However, it is important to note that they studied the effect on adipose-derived stem cells. A two-step plasma treatment was also recently reported for the nanostructuration of the titanium surface<sup>23</sup>. The surface roughness was increased thanks to ultrasonic surface rolling processing, and then the surface



wettability was improved with plasma nitriding. The nanocrystallisation of a TiN and Ti<sub>2</sub>N layer at the surface was shown to enhance the viability of cells.



**Figure 1.4** FE-SEM image of (a) the friction-hardened sample heated at 600 °C for 1 h after immersion in NaOH 10 M at 30 °C for 12 h and (b) adipose-derived stem cells cultured on this surface <sup>22</sup>

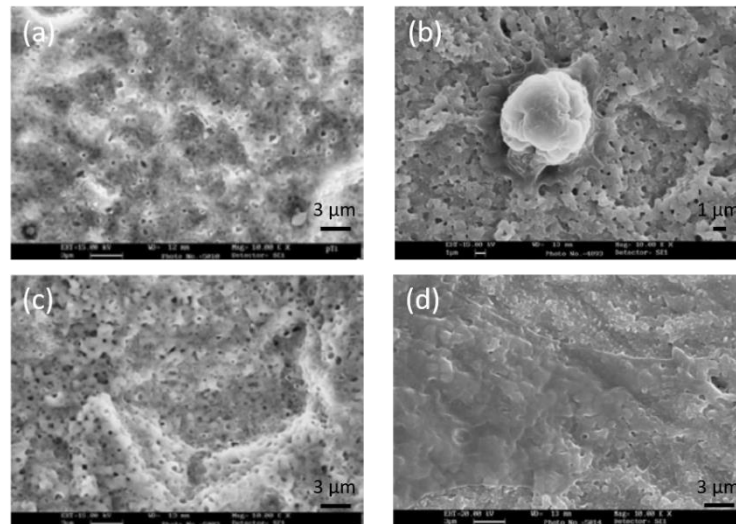
To sum up this part, roughness and wettability are key points to increase the cell adhesion and proliferation on the implant surface, and different strategies are available in the scientist's toolbox to achieve the desired surface properties without any coating.

### 1.2.3 Incorporation of extracellular matrix components

Extracellular matrix (ECM) is the network of macromolecules organized around the cells to give tissue a stability. It is mainly composed of collagens and proteoglycans, and it is a reservoir for bioactive molecules such as growth factors<sup>24</sup>. One way to promote cell adhesion and proliferation on titanium implant is therefore to functionalize its surface with ECM components.

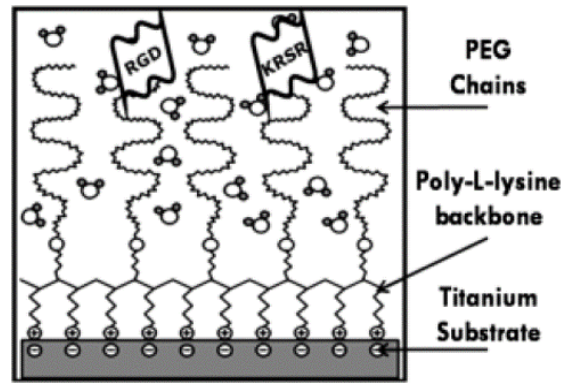
Collagen immobilization has been used for years in the field of orthopedic and dental implant to improve osseointegration. Collagen is the main structural protein in the extracellular matrix, and the main organic component of bones. It is also found in fibrous tissues. The easiest way to immobilize collagen is by adsorption in physiological conditions. Collagen can be adsorbed either in a fibrillar or non-fibrillar structure. Nevertheless, results obtained after functionalization with collagen at a density of 3-6 µg/cm<sup>2</sup> of collagen are contrasting. Becker *et al.*<sup>25</sup> did not observe any significant difference between coated and non-coated Ti6Al4V implants on rat calvarial osteoblasts, while Geßler *et al.*<sup>26</sup> found a better cell spreading on coated surfaces, whereas the number of adhered cells was similar to uncoated surfaces. During an *in vivo* study, a higher fibroblasts activity was observed 7 days after implantation on coated implants, together with the presence of osteoblasts, while on uncoated implant osteoblasts are visible only 14 days post-implantation<sup>27</sup>. However, no significant difference in osteoblast activity was found after 28 days between the two surfaces, suggesting that the collagen I (one of the most common collagen form in the body) coating improved the integration in its early

stages. As an example of covalently-grafted collagen coating, Morra *et al.* described the nanostructuration of a Ti implant by anodization followed by grafting of acid acrylic and collagen I coupling (**Figure 1.5 (a) and (b)**)<sup>28</sup>. The implant was first nano structured by anodization, before *in vitro*, They observed a better cell spreading on collagen coated nanostructured titanium *in vitro* (**Figure 1.5 (c) and (d)**) and an improved bone-implant interaction *in vivo*.



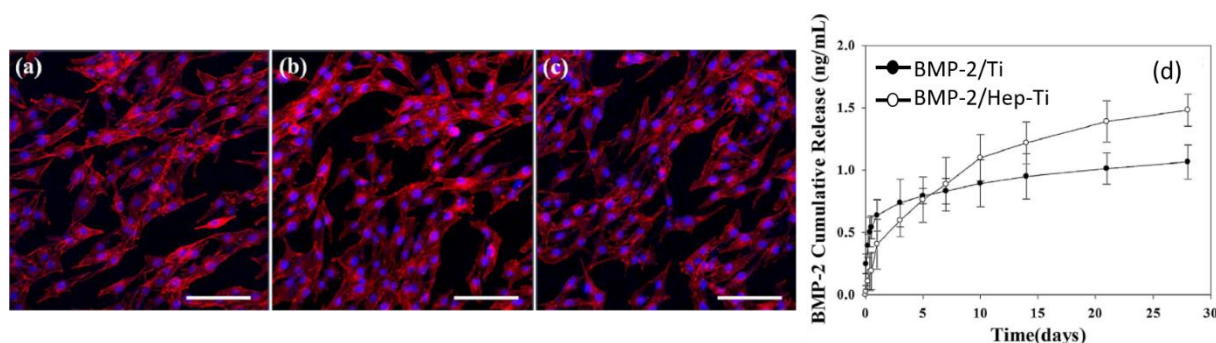
**Figure 1.5** SEM images of (a) anodized titanium; (b) anodized titanium coated with collagen; Human mesenchymal cells after 2 h of culture on (c) anodized titanium and (d) anodized titanium coated with collagen<sup>28</sup>

Overall, collagen I coating may have a slight effect in osseointegration improvement, but not significant when used alone. That is why research focused on the immobilization of other ECM components, like the Arg-Gly-Asp (RGD) peptide or growth factors. The RGD peptide is an amino acid sequence recognized by integrins, *i.e.* cell adhesion proteins. Its immobilization through covalent grafting or physical adsorption<sup>29</sup> could promote osteoblasts adhesion. The covalent grafting of RGD can be obtained through silanization of the titanium surface<sup>30</sup>, or thio-anchorage on a deposited gold layer<sup>31</sup>. In both cases RGD-coated surfaces enhance osteoblast activity *in vitro* and bone formation and thickness *in vivo*. Schueler *et al.* used a different strategy where the peptide was grafted on a poly(L-lysine)-*graft*-poly(ethylene glycol) co-polymer adsorbed on the titanium surface<sup>32</sup> (see **Figure 1.6**). The presence of this anti-fouling coating that does not promote cell adhesion allowed to evidence the effect of RGD on cell adhesion and spreading. However, the same authors later showed that in this configuration RGD could not promote osteoblast differentiation, possibly due to an unsuitable orientation of the peptide on the coating<sup>33</sup>.



**Figure 1.6** Schematic of peptide-functionalized poly-L-Lysine grafted polyethylene glycol (PLL-g-PEG) following self-assembly on the titanium SLA surface<sup>33</sup>

As previously mentioned, the ECM also contains proteins, termed growth factors, which promote the differentiation of osteoblasts from the mesenchymal stem cells (multipotent stromal cells that can differentiate in various types of cells) and control factors during osteoinduction<sup>34,35</sup>. Among these proteins, the bone morphogenetic protein (BMP) family is widely studied and used in the field of orthopedic implants, especially the BMP-2. Immobilization of the protein on the implant surface can be achieved by physical adsorption, covalent grafting or incorporation into a polymeric or a ceramic coating. One can take advantage of the known ionic interactions between BMP-2 and anionic molecules, heparin for example, to immobilize the protein. After heparin covalent grafting on functionalized Ti surface, adsorption of BMP-2 is performed. This allows a controlled release over 28 days, with cell proliferation and osteogenic differentiation enhanced compare to Ti surfaces alone or with nonspecific adsorption of BMP-2<sup>36,37</sup> (see **Figure 1.7**). Bae *et al.*<sup>38</sup> synthesized a nano cluster of BMP-2 and chondroitin sulfate that was then adsorbed on a calcium phosphate layer deposited at the titanium surface. With a similar approach, BMP-2 and heparin were adsorbed at the surface of a hydroxyapatite layer formed by electrochemical deposition<sup>39</sup>. In each case, cell proliferation and osteogenic differentiation were improved when the growth factor is present. It is also possible to load polymeric films with BMP-2, for example using polyelectrolyte membranes<sup>40</sup>. Direct covalent grafting of BMP-2 on a titanium surface can also be achieved by modifying it with amine groups via a plasma treatment with allyl amine<sup>41</sup>. A spacer can be used to keep the protein far from the surface, preserving its conformation and therefore its osteogenic activity.



**Figure 1.7** F-actin staining images of human osteosarcoma MG-63 cells grown on (a) Ti, (b) Ti after BMP-2 adsorption (BMP-2/Ti), and (c) heparin-conjugated Ti surface after BMP-2 adsorption (BMP-2/Hep-Ti) after 24 h incubation; (d) release kinetics of BMP-2 from BMP-2/Ti and BMP-2/Hep-Ti<sup>36</sup>

#### 1.2.4 Calcium phosphate based coatings

Due to their similarity with bone, composed by hydroxyapatite as the mineral phase, calcium phosphates have been widely studied in the field of bone regeneration and osseointegration<sup>42,43</sup>. This mineral family is composed of twelve main compounds presented in **Table 1.1**, which differ from their Ca/P ratio that strongly influences their chemical and physical properties<sup>42–44</sup>.

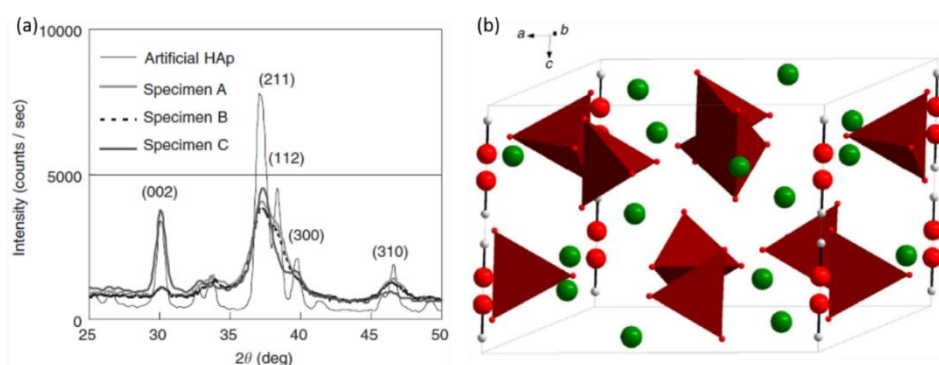
Dicalcium phosphate dihydrate (DCPD, brushite mineral), and dicalcium phosphate anhydrous (DCPA, monetite mineral) possess a Ca/P ratio of 1.0. DCPA is rarely found *in vivo*, but DCPD has been proposed as an intermediate in bone mineralization. None of them were studied as coatings for improved osseointegration, in contrast to octacalcium phosphate (OCP, Ca/P = 1.33) and tricalcium phosphate (TCP, Ca/P = 1.5). OCP is a possible precursor of carbonated apatite in bone, with a structure similar to the one of hydroxyapatite. Due to its high solubility in biological fluids, OCP is used in bone cement for filling bone defects, as it induces hydroxyapatite formation. TCP exists under two crystal forms,  $\alpha$ -TCP and  $\beta$ -TCP. TCP is a high-temperature phase of calcium phosphate that cannot be precipitated from aqueous solution, and the  $\alpha$ -TCP is produced at even higher temperature than  $\beta$ -TCP. Their solubility is rather high but  $\beta$ -TCP being more stable than  $\alpha$ -TCP, it is used in the field of bone regeneration and osseointegration. It has been shown that this phase is osteoconductive, as well as osteoinductive.

Hydroxyapatite is the main base component of bone and teeth. This mineral has a Ca/P ratio of 1.67, with a formula of  $\text{Ca}_{10}(\text{PO}_4)_6(\text{OH})_2$ , but it is never found in this stoichiometric form *in vivo*. The *in vivo* HAp is calcium deficient, and mainly nanocrystalline (see **Figure 1.8 (a)**). Because of a crystal lattice allowing substitutions (see **Figure 1.8 (b)**), the calcium ions can be substituted by several ions found in the biological fluids like  $\text{Mg}^{2+}$ ,  $\text{Na}^+$ ,  $\text{K}^+$ ... whose charge is compensated by oxygen lacunas. Moreover,  $\text{OH}^-$  and  $\text{PO}_4^{3-}$  can easily be substituted by carbonate ions.

Ca/P	Name	Formula
0.5	Monocalcium phosphate monohydrate (MCPM)	$\text{Ca}(\text{H}_2\text{PO}_4)_2 \cdot \text{H}_2\text{O}$
0.5	Monocalcium phosphate anhydrous (MCPA)	$\text{Ca}(\text{H}_2\text{PO}_4)_2$
1.0	Dicalcium phosphate dihydrate (DCPD)	$\text{Ca}(\text{HPO}_4) \cdot 2 \text{H}_2\text{O}$
1.0	Dicalcium phosphate anhydrous (DCPA)	$\text{CaHPO}_4$
1.33	Octacalcium phosphate (OCP)	$\text{Ca}_8(\text{HPO}_4)_2(\text{PO}_4)_4 \cdot 5 \text{H}_2\text{O}$
1.5	$\alpha$ -Tricalcium phosphate ( $\alpha$ -TCP)	$\alpha -\text{Ca}_3(\text{PO}_4)_2$
1.5	$\beta$ -Tricalcium phosphate ( $\beta$ -TCP)	$\beta -\text{Ca}_3(\text{PO}_4)_2$
1.2 – 2.2	Amorphous calcium phosphate (ACP)	$\text{Ca}_x\text{H}_y(\text{PO}_4)_z \cdot n\text{H}_2\text{O}$ $n = 3-4, 5; 15-20\% \text{H}_2\text{O}$
1.5 – 1.67	Calcium-deficient hydroxyapatite (CDHA)	$\text{Ca}_{10-x}(\text{HPO}_4)_x(\text{PO}_4)_{6-x}(\text{OH})_{2-x}$ ( $0 < x < 1$ )
1.67	Hydroxyapatite (HAp)	$\text{Ca}_{10}(\text{PO}_4)_6(\text{OH})_2$
1.67	Fluoroapatite (FAP)	$\text{Ca}_{10}(\text{PO}_4)_6\text{F}_2$
2.0	Tetracalcium phosphate (TTCP)	$\text{Ca}_4(\text{PO}_4)_2\text{O}$

**Table 1.1** (Ortho)calcium phosphate family. Minerals with their names and formula are sorted by their Ca/P ratio.

Hydroxyapatite is the more stable calcium phosphate phase, to the exception of fluoroapatite, in which hydroxyl is substituted by fluoride that increases mechanical and physical properties of the compound. Due to its very low solubility, and toxicity of fluorides at high doses, fluoroapatite is rarely used for bone regeneration. On the opposite of fluoroapatite, amorphous calcium phosphate (ACP, Ca/P = 1.15-1.67) is poorly if even crystallized, and very unstable in biological fluids. In aqueous solution, it forms hydroxyapatite by a dissolution/precipitation process.



**Figure 1.8** (a) XRD pattern of a synthetic ("artificial") HAp and three bone specimens<sup>45</sup> and (b) representation of the unit cell of hexagonal HAp. (Ca in green, O in red,  $\text{PO}_4$  tetrahedra in brown)<sup>46</sup>

Hydroxyapatite possesses osteoconductivity property, and osteoinductivity in the presence of osteogenic supplements. It is used as cement for bone tissue engineering, or as coating for metallic implants. A mixture of TCP and HAp, called biphasic calcium phosphate, with ratio between HAp and TCP commonly around 60/40 combines osteoinductivity and solubility of TCP with the stability of hydroxyapatite, as well as its similarity with bone. The osteoconductivity and osteoinductivity of HAp and TCP coatings is due to their partial dissolution in biological fluids and reprecipitation on their surfaces of biological apatite that favors bone growth. Syntheses and deposition processes of calcium phosphate ceramics coatings will be further investigated in part 2.3.1.

For the use of calcium phosphate coatings in the field of osseointegration of implants, several parameters have to be taken into account<sup>42,47</sup>. As said before, surface roughness is a key parameter for protein adsorption, and then cell adhesion. However, data on effect of calcium phosphate surface topography on cell adhesion are contradictory<sup>47</sup>. Porosity is also a factor influencing protein adsorption, where pore size ranging from 20 nm to 500  $\mu\text{m}$  have been shown to favor the adsorption. Moreover, porous ceramics will allow a rapid invasion of fluids, cells and bone tissue growth. The surface charge and ionic environment are also important. Proteins are charged macromolecules; hydrophilic surfaces will induce a higher protein adsorption than hydrophobic surfaces. Protein adsorption is mediated by pH and ionic strength. Dissolution of calcium phosphate coating will induce a change in calcium and phosphate concentration near the surface, modifying the pH, and consequently protein adsorption. Concerning protein adsorption, TCP or BCP would be the preferred calcium phosphates, thanks to their higher dissolution rate compared to hydroxyapatite. Ion release and recrystallization from TCP to HAp plays important roles in cell adhesion and proliferation. The low crystallinity is more favorable for initial cell attachment and proliferation. Upon dissolution of the coating,  $\text{Ca}^{2+}$  in the culture medium induces an increase in alkaline phosphatase (ALP) activity and osteocalcin mRNA expression in mouse primary osteoblasts. However, the presence of amorphous calcium phosphate with high dissolution rate may have an adverse effect on the long-term. In particular, poorly attached coatings will be delaminated from the substrate.

Hydroxyapatite coatings can be a support to integrate bioactive compounds such as growth factors and peptide-mediated adhesion. For example, Xie et al. co-deposited chitosan and Ag nanoparticles with hydroxyapatite by electrochemical deposition on commercially pure titanium<sup>39</sup>. BMP-2 and heparin were then loaded on the 20  $\mu\text{m}$  thick coating, by adsorption and evaporation at room temperature. Coatings of hydroxyapatite with chitosan favored osteoblasts attachment and spreading, probably due to the biomimetic structure of hydroxyapatite. Incorporated chitosan allowed a long-term release of BMP *in vitro*. Proliferation of bone mesenchymal stem cells was nearly equal for the HAp-only coating and with chitosan and BMP-2. However, the later coating induced a higher



differentiation in osteoblasts and was positively tested *in vivo*, with bone maturation 12 weeks after implantation. BMP-2 can also be adsorbed on hydroxyapatite synthesized by a biomimetic method (see 2.3.2.2.2), with sustained release over 28 days, and improvement of osteoblast proliferation and activity<sup>38</sup>. An attempt to take advantage of both osteoconductivity of hydroxyapatite and RGD peptide adhesion properties has been explored by Bitschnau et al.<sup>48</sup> Stainless steel wires were coated with hydroxyapatite by electrochemical-assisted deposition and then loaded with a cyclic RGD and bisphosphonates. No difference in bone growth was found between the hydroxyapatite-only coating and in presence of RGD, possibly due to the fact that the osteoconductive effect of hydroxyapatite “overwhelmed” the effect of RGD.

### 1.3 Hydroxyapatite coatings processes

Two main strategies are available to form hydroxyapatite coatings. On one hand, several deposition techniques exist to coat a substrate with presynthesized hydroxyapatite particles; on the other hand, it is possible to get the mineral to crystallize directly at the substrate surface. Current requirements for hydroxyapatite coating in bone regeneration are listed in **Table 1.2**, as expected by the American Food and Drug Administration (FDA) for commercialization of the implant, following ISO standards. Coatings should be pure hydroxyapatite with good crystallinity. It is interesting to note that the Ca/P ratio corresponds to stoichiometric or even sur-stoichiometric hydroxyapatite, meaning that FDA requirements are distant from the characteristics of biomimetic hydroxyapatite coatings.

This chapter will focus first on different methods to synthesize hydroxyapatite powders, followed by the presentation on the available coating techniques.

Essential	Requirement
Thickness	Not specific
Ca/P ratio	1.67 – 1.76
Phase purity	95 % minimum
Crystallinity	62 % minimum
Tensile strength	> 50.8 MPa
Shear strength	> 22 MPa
Density	2.98 g/cm <sup>3</sup>
Heavy metals	< 50 ppm
Abrasion	Not specific

**Table 1.2** HAp coating requirements by FDA, following ISO standards<sup>49</sup>

### 1.3.1 Synthesis of hydroxyapatite particles

Hydroxyapatite can be synthesized by wet or solid-state methods.

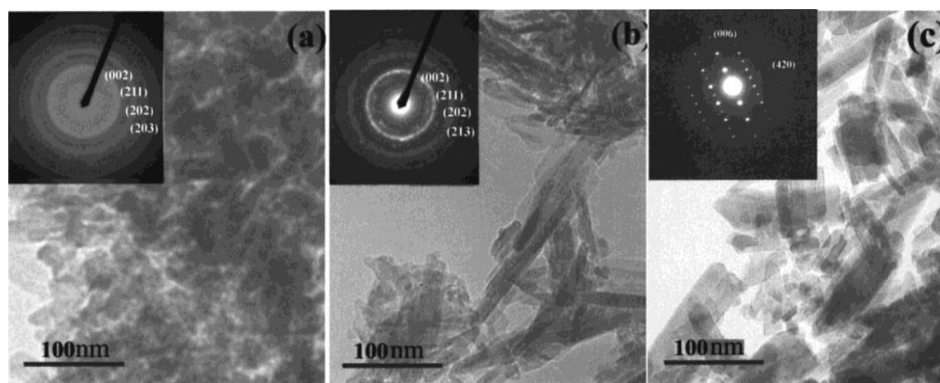
#### 1.3.1.1 Co-precipitation synthesis

Co-precipitation is the more used synthesis method, because it is simple to perform and several precursors can be used. It consists in adding at once or dropwise one of the precursor in an aqueous solution to a solution of the other one. Solutions are heated at temperature comprised between 25 and 100 °C, with a precise control of pH. It has to be basic, around 8 to 10, to induce hydroxyapatite precipitation. After a mixing phase, an aging phase is performed with duration between several hours to days, with or without heating and stirring. Long aging times under air atmosphere yield to carbonated hydroxyapatite, which can be interesting in bone integration. After drying, the obtained precipitate undergoes a thermal treatment to improve the crystallinity of hydroxyapatite. Temperature of thermal treatment has to be chosen cautiously as hydroxyapatite decomposes at high temperature (700 °C)<sup>50</sup>. Synthesized nanoparticles are most of the time needle-shaped, but may also have a plate-like morphology (**Figure 1.9**).

Calcium nitrate  $\text{Ca}(\text{NO}_3)_2 \cdot 4\text{H}_2\text{O}$  is the more commonly used calcium precursor<sup>46,50–53</sup>, while ammonium phosphate  $(\text{NH}_4)_2\text{HPO}_4$  or  $(\text{NH}_4)\text{H}_2\text{PO}_4$  are mainly used as phosphate precursors. Potassium or sodium salts are less used because  $\text{Na}^+$  and  $\text{K}^+$  ions can integrate the hydroxyapatite crystal lattice. Depending of the precursor choice, the synthesis is referred to a double decomposition, for calcium and phosphate salts, or neutralization if precursors are calcium hydroxide and phosphoric acid<sup>54</sup>. Residual ammonium and nitrate are removed by heating. Advantage of neutralization method is the absence of residual ions.

L. M. Rodríguez-Lorenzo et al.<sup>51</sup> systematically studied the influence of temperature, reaction time and aging time on the stoichiometry and crystallinity of hydroxyapatite. Temperature during synthesis influences the crystal size at same reaction and aging times: at 25 °C obtained small crystals are similar to bone, while at 90 °C larger crystals are more similar to enamel. For a reaction at 90 °C, two hours are necessary to synthesize stoichiometric HAp, while shorter times or lower temperature yield to calcium-deficient hydroxyapatite. Generally, crystal size was higher when the time of reaction increased, but this parameter also affected stoichiometry and morphology of particles. The aging time allowed an increase of Ca/P ratio and carbonate uptake.



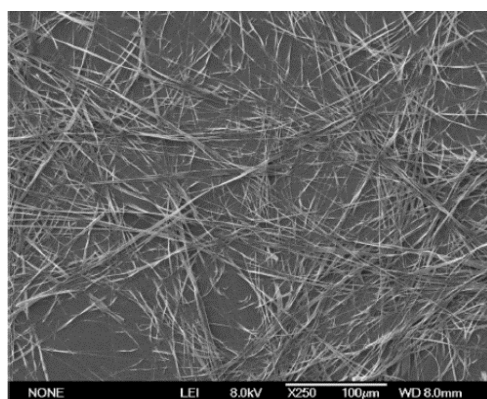


**Figure 1.9** TEM micrographs and electrodiffraction patterns (inset) of HAp samples obtained at (a) 25 °C, (b) 90 °C and (c) 90 °C with 24 h of reaction <sup>51</sup>

### 1.3.1.2 Hydrothermal synthesis

Hydrothermal synthesis can be defined as a method of synthesis of single crystals that depends on the solubility of minerals in hot water under a high pressure<sup>55</sup>. Solutions of calcium and phosphate precursors in aqueous solutions are transferred in a sealed autoclave and heated at temperature between 100 and 200 °C. When organic solvents are used, the method is called solvothermal<sup>56,57</sup>. Precursors used are mainly the same as for the co-precipitation method (calcium nitrate and ammonium phosphate). pH is adjusted before the hydrothermal treatment by sodium, potassium or ammonium hydroxide<sup>56–60</sup>, or gradually increased during process by urea decomposition<sup>57</sup> (see **Figure 1.10**).

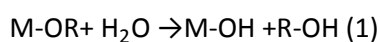
By hydrothermal and solvothermal synthesis, nanorods and nanoribbons can be formed. With addition of surfactants and additives, like CTAB, oleic acid or glutamic acid, ultralong nanowires (up to hundreds of micrometers) are obtained<sup>58,60</sup>. The hydrothermal or solvothermal phase is relatively long, from several hours to days, so it is now combined with microwave heating<sup>58</sup>. Reaction time is reduced to 15 minutes, allowing to obtain hydroxyapatite with carbonate substitutions.



**Figure 1.10** SEM image of the ultralong HAp micro/nanoribbons synthesized by hydrothermal method with pH controlled by urea decomposition<sup>57</sup>

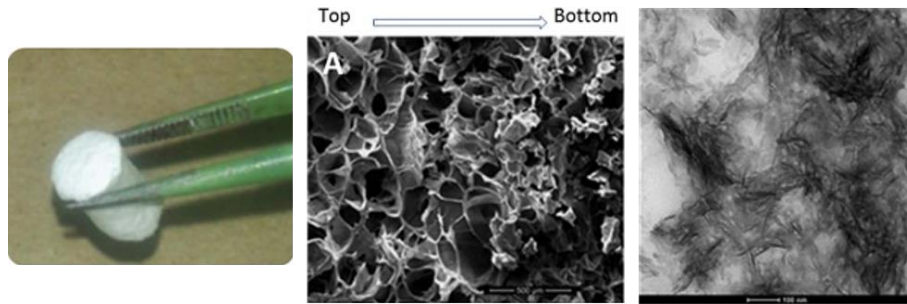
### 1.3.1.3 Sol-gel synthesis

Sol-gel synthesis corresponds to the mixing at molecular level of calcium and phosphorous precursors, which improves the chemical homogeneity of the resulting hydroxyapatite. The chemistry is based on hydrolysis and polycondensation reactions of precursors (see **Equation 1.1**). Reactions may be in aqueous phase<sup>61</sup> or in organic solvent<sup>62–65</sup>, mainly ethanol. In ethanol, phosphate precursors are phosphorous alkoxides, hydrolyzed by a little amount of water (ratio P:H<sub>2</sub>O 3:1). Liu et al. suggested that triethyl phosphite has higher activity for hydrolysis than triethyl phosphate<sup>61</sup>, reducing the time needed for reaction. Calcium nitrate, or Ca(OEt)<sub>2</sub><sup>65</sup>, used as precursors, are added in stoichiometric proportions to the phosphorous alcoxide solution. Solutions are aged for several hours depending on the chosen temperature to obtain a gel. 120 minutes at 45 °C are enough<sup>66</sup>, while 16 hours are necessary at room temperature<sup>61</sup>. However, alkoxides are expensive reagents and research has focused on finding other precursors, such as P<sub>2</sub>O<sub>5</sub><sup>62,63</sup>, that can be reacted with alcohol to form the alkoxide P(O)(OR)<sub>3</sub>.



**Equation 1.2** (1) Hydrolysis and (2) condensation of metal alcoxide by sol-gel route

Before thermal treatment, the gel is composed of amorphous calcium phosphate. Calcination is necessary to obtain hydroxyapatite, which is one of the disadvantage of sol-gel method. Calcination temperature depends on the previous reaction parameters. Temperature used are comprised between 350 °C and 1200 °C<sup>64,65</sup>. Very high crystalline hydroxyapatite is obtained after high sintering temperature, but thermal decomposition may occur at temperature higher than 700 °C. HAp synthesized in ethanol was found more stable than synthesized in water towards thermal decomposition<sup>61</sup>. Advantage of this method is the formation of homogeneous materials, with an easy processing by dip or spin coating to obtain films. It is also very convenient to form composite<sup>67</sup> and hybrid material<sup>68</sup> for bone regeneration. Raucci et al. synthesized a scaffold composed of gelatin and hydroxyapatite by sol-gel method and freeze drying. Needle-like nanoparticles were homogeneously distributed in the porous polymeric matrix, with intimate interaction between both components (**Figure 1.11**).

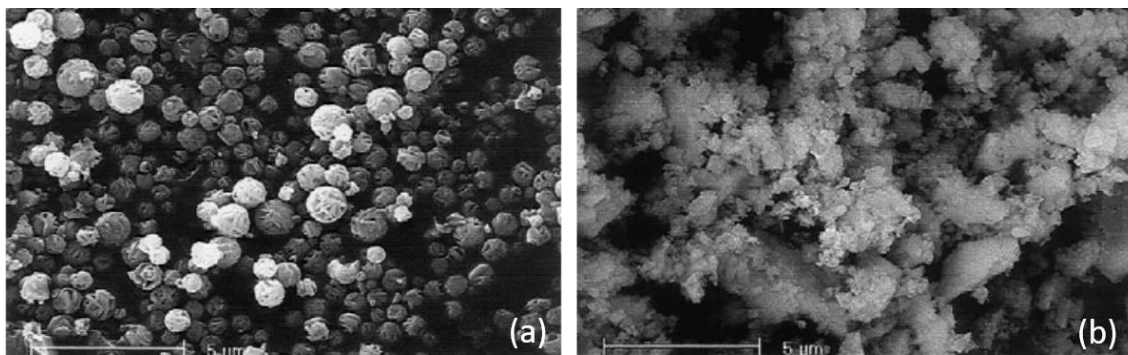


**Figure 1.11** Gelatin hydroxyapatite scaffold obtained by freeze drying process and crosslinked (a), SEM image (b) and TEM image (c) of the scaffold <sup>68</sup>

#### 1.3.1.4 Solid state synthesis

In solid-state synthesis, solid precursors are mixed in stoichiometric quantities and heated at high temperature (1000 °C). Precursors may be tribasic calcium phosphate (TCP)<sup>69</sup>, dicalcium phosphate dihydrate (DCPD)<sup>70,71</sup>, calcium pyrophosphate<sup>72</sup>, calcium hydroxide<sup>69</sup>, and calcium carbonate<sup>71,72</sup>. Precursors are first sieved and ball milled in water<sup>69,70,72</sup> or organic solvent<sup>71,72</sup> for homogeneous mixing. The solvent chosen for milling is important, as the morphology obtained after milling in acetone or water is different<sup>72</sup> (see

**Figure 1.12**). Temperature of calcination is also to consider, as at temperature under 1000 °C, mixtures of HAp, DCP, DCPD, TCP and CaO are formed<sup>69</sup>. This method necessitates a lot of energy to obtain pure hydroxyapatite, but may be interesting to obtain biphasic compositions like biphasic calcium phosphate (BCP, mixture of HAp and  $\beta$ -TCP), used in bone regeneration. In order to reduce consumption of time and energy, microwave heating may be an interesting process for solid-state synthesis<sup>73</sup>. An original approach of Wu et al. allows the formation of carbonated hydroxyapatite from DCPD and eggshell powders, in order to reuse waste. Eggshells are mainly composed by calcium carbonate. 10 hours of reaction at 1000 °C are necessary to form pure hydroxyapatite<sup>70</sup>.

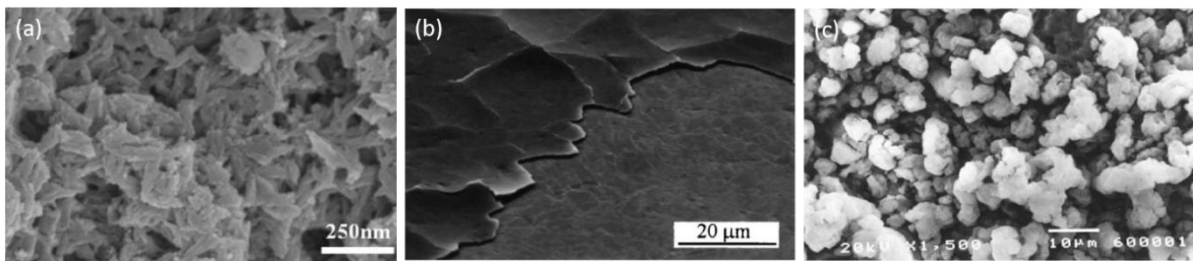


**Figure 1.12** SEM image of HAp obtained after 8 h milling in acetone (a) and water (b) and heat treatment at 1100 °C for 1 h<sup>72</sup>

### 1.3.2 Coatings process

#### 1.3.2.1 From preformed particles

A large number of deposition methods are available to coat a surface, metallic or polymeric with hydroxyapatite, and in a larger extent calcium phosphate mineral. A number of books or reviews deals with methods to deposit calcium phosphates and more precisely hydroxyapatite on metallic substrates<sup>74–76</sup>. **Table 1.3** gathers some of coating process used to deposit hydroxyapatite on metallic substrates. Plasma-spray technique is the only one that is approved by the American Food and Drug Administration (FDA) for biomedical applications. It is the most widely studied. Control of coating composition, morphology and porosity are possible depending on the technique. With the majority of the process described, a thermal post treatment is necessary to obtain crystalline and adherent coatings. To improve the adherence to the substrate, the modification of the surface may be envisaged, by deposit an interfacial layer ( $\text{TiO}_2$  or  $\text{TiN}$ ) at the titanium surface, through acid etching or plasma treatment. SEM images of coatings obtained through different techniques are presented on **Figure 1.13**.



**Figure 1.13** SEM image of hydroxyapatite deposited by (a) plasma-spray technique<sup>77</sup>, (b) ion-beam assisted deposition<sup>78</sup> and (c) dip coating<sup>79</sup>

Technique	Principe	Advantages	Inconvenients	References
<b>Thermal spray</b> (plasma, flame, electrical arc, high-velocity oxy-fuel)	Acceleration and propulsion of melted particles toward the surface by gases, atomization jets or plasma gun	Dense and thick coating High deposition rate Inexpensive process Plasma spray: FDA approved	Poor coating adherence Non-uniform composition and crystallinity Loss of stoichiometry Large loss of material powder	Xu et al. <sup>77</sup>
<b>Pulsed laser deposition</b>	Melting and vaporization of HAp powder by a laser source to form a plasma plume in a vacuum or gas environment. Condensation of vaporized particles on the surface	Uniform coating Conservation of the stoichiometry Control over thickness and crystallinity Possibility to deposit multilayers coatings Better adherence	Expensive process	Rau et al. <sup>80</sup>
<b>Sputter coating</b> (Radio-frequency, Ion beam, Direct current, Reactive direct current)	Generation of high energy gaseous ions by a plasma that are accelerated by high voltage and bombard the HAp powder toward the substrate	Defect-free coating Strong adherence High reproducibility Control of the microstructure and chemical composition	Poor crystallinity Loss of stoichiometry Thermal treatment needed	Hamdi et al. <sup>81</sup>
<b>Ion beam deposition</b>	Combinaison of ion beam bombardment and physical vapor deposition. Deposition on a cold plasma atmosphere in a vacuum chamber	Strong adherence High reproducibility Control of microstructure and chemical composition	Loss of stoichiometry Amorphous coating Thermal treatment needed	Choi et al. <sup>78</sup>
<b>Electrophoretic deposition</b>	Migration under electrical current of charged colloidal particles suspended in a liquid medium	Inexpensive and easy to set up process High degree of control over thickness and morphology	Poor initial adherence Thermal treatment needed Specific to metallic substrate	Asri et al. <sup>82</sup>
<b>Electrospray</b>	Generation and spraying of an aerosol through a nozzle under high voltage influence. Coating from solutions of precursors or dispersions of pre-formed nanoparticles	Inexpensive process Production of porous coating Formation of thin coating Control over morphology	T>300 °C Amorphous coating (if coating from precursors solutions) Thermal treatment needed	Bosco et al. <sup>83</sup>
<b>Dip coating</b>	Deposition of a wet liquid film by withdrawal of a substrate from a liquid medium	Easy to set up Control over thickness Formation of thin coating Possibility to form multilayers coating High adherence	Thermal treatment needed Formation of cracks	Asri et al. <sup>82</sup> Hsieh et al. <sup>79</sup>

Table 1.3 Deposition of HAp via different coating techniques

### 1.3.2.2 Wet process

#### 1.3.2.2.1 Electrochemical deposition and micro-arc oxidation coatings

In electrochemical cathodic deposition, an electric current goes through two electrodes in an electrolyte solution, containing calcium and phosphates ions. Reduction of water near the electrode produces hydroxyl ions, leading a local increase in pH. The solubility of calcium phosphates decreases with pH increasing, so it precipitates at the electrode surface<sup>74,75,84,85</sup>. Heterogeneous precipitation being more favorable than homogeneous precipitation in solution, the electrode is coated. Advantages of this technique are numerous, such as possibility to deposit a thin layer with crystallite size close to bone mineral, control of thickness and chemical composition, homogeneity of the coating, duration of process, and its low need for energy, reducing the cost. However, two major problems are faced: hydroxyl formation affects the composition of the deposited mineral and hydrogen produced during water reduction may interact with the surface, resulting in poor coating adhesion. The deposited mineral is often brushite or monetite, or amorphous calcium phosphate, because pH is not high enough to produce hydroxyapatite. However a subsequent alkaline treatment in sodium hydroxide allows the crystallization of HAp. Deposition temperature affects the deposited amount, crystallinity and crystal size: the higher the temperature, the thicker and crystalline the coating. The composition of the electrolyte is also critical to control the deposited coating. Importantly, the mild conditions used in this technique are compatible with the incorporation of organic components like collagen, growth factors, peptides or small molecules with antibacterial properties<sup>39</sup>.

Another electrochemical method to deposit calcium phosphate mineral from aqueous solution directly on the substrate is micro-arc oxidation coating (MAO). It is a combination of electrochemical oxidation, plasma chemical oxidation and thermal diffusion in an electrolyte containing calcium and phosphates salts<sup>86</sup>. The substrate acts like the anode and is immersed in the aqueous electrolyte. Process is fast, only 5 to 180 minutes are needed to achieve thickness around 1-100  $\mu\text{m}$ . Concentration and composition of the electrolytes influence the morphological characteristics, porosity, thickness, corrosion resistance and biocompatibility of the coating. The process can also be used to deposit a titanium oxide layer at the surface of Ti to improve the hydroxyapatite forming ability of the surface.

#### 1.3.2.2.2 Biomimetic deposition

All techniques presented before lead to crystalline and stoichiometric hydroxyapatite, either during process or after a post treatment. One way to obtain bioactive hydroxyapatite, i.e. non-stoichiometric poorly crystalline hydroxyapatite with calcium deficiency and substitutions is biomimetic deposition. The methods consists in soaking the substrate in a solution slightly supersaturated in calcium and

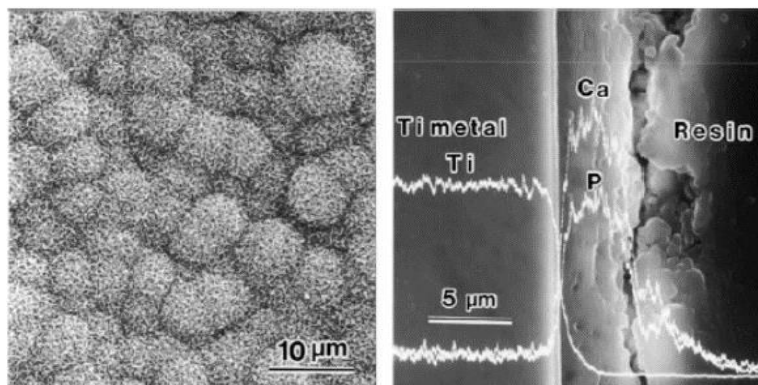


phosphate whose composition mimicks blood plasma. Deposition occurs at physiological pH and temperature (pH 7.4, 37 °C).

Kokubo was the first to report a solution allowing the deposition of hydroxyapatite on bioactive surface. He called this solution the Simulated Body Fluid (SBF). The initial uses of SBF were the conversion of bioglasses, which are materials composed of a  $\text{SiO}_2$  matrix with different oxides like  $\text{MgO}$ ,  $\text{CaO}$  or  $\text{P}_2\text{O}_5$ , into hydroxyapatite, and the understanding of their mechanism of bioactivity in the body<sup>87</sup>. The solution mimicked the ionic composition and concentration of the blood plasma, except for  $\text{Cl}^-$  and carbonated whose concentrations are lowered to maintain the stability of the solution (see **Table 1.4**). Subsequently, the ability of SBF to form hydroxyapatite on ceramics, metals and polymers was tested, as criterion for bioactivity evaluation: if hydroxyapatite was formed, then a good *in vivo* activity to enhance bone formation could be expected. The success of this approach led other researchers to use it directly as a coating process, especially on titanium and titanium alloy implants. The original SBF missed the sulfate ions in its composition, which was corrected in 1991 by Kokubo. Mechanism of the hydroxyapatite deposition was further elucidated in 1998<sup>88</sup>. For titanium, a pretreatment was shown to be necessary to make the surface bioactive. As it is well-known that the rutile phase of  $\text{TiO}_2$  is bioactive, an acidic treatment followed by crystallization at 600 °C was used to favor its formation. An alkaline treatment in  $\text{NaOH}$  can also be used to form  $\text{Ti-OH}$  groups at the surface that are useful to deposit hydroxyapatite. After alkali treatment, the substrate is covered by a sodium titanate layer that interacts with calcium ions of SBF, producing a layer of amorphous calcium titanate. Then, phosphate ions from the solution react with the surface to produce an amorphous calcium phosphate layer, with a  $\text{Ca/P}$  ratio close to 1.40. This layer is converted into hydroxyapatite during the maturation step to reach an atomic ratio of 1.65, close to the one of bone hydroxyapatite. The coating was shown to also contain magnesium ions<sup>89</sup>. Morphology of the produced coating is quite typical of the biomimetic process (see **Figure 1.14**): apatite crystals are plate-like, while, in co-precipitation synthesis, needle-shaped crystals are often produced. The dense and homogeneous layer of hydroxyapatite is usually formed of spherical aggregates that increase in size with time of deposition to cover the whole surface. Coating is well-adherent to the substrate surface thanks to the calcium titanate-sticking layer.

Various surface treatments have been investigated to find the best way to rapidly produce hydroxyapatite. Acidic treatment with  $\text{HCl}$ , piranha solution ( $\text{H}_2\text{SO}_4$ ,  $\text{H}_2\text{O}_2$ ), or mixture of  $\text{HCl}$  and  $\text{H}_2\text{SO}_4$  were tested. Different alkali and alkali heat treatments were used to form a sodium titanate layer at the substrate surface under the form of a gel or crystalline phase. Pattanayak et al.<sup>92</sup> found that there is no difference in hydroxyapatite deposition after acidic or basic treatment, with or without heating

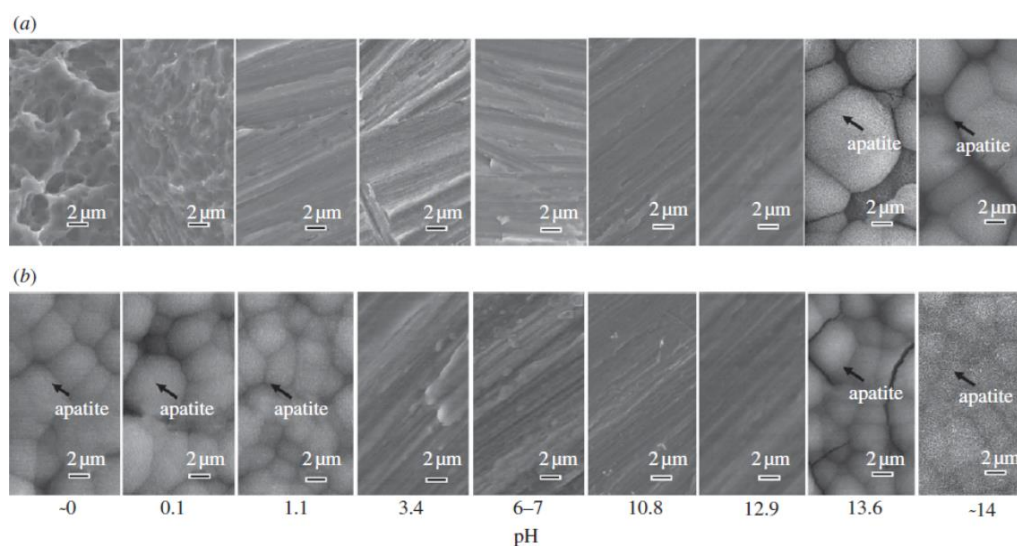
at 600 °C, but even after heat treatment, surface soaked in solution with neutral pH did not show any hydroxyapatite deposition (see **Figure 1.15**).



**Figure 1.14** SEM image of surface (left) and cross section (right) of apatite layer formed in SBF on an alkali heat-treated titanium surface<sup>90</sup>

	Na <sup>+</sup>	K <sup>+</sup>	Ca <sup>2+</sup>	Mg <sup>2+</sup>	Cl <sup>-</sup>	HCO <sub>3</sub> <sup>2-</sup>	HPO <sub>4</sub> <sup>2-</sup>	SO <sub>4</sub> <sup>2-</sup>
Blood plasma	142.0	5.0	2.5	1.5	103.0	27.0	1.0	0.5
Conventional SBF <sup>87</sup>	142.0	5.0	2.5	1.5	147.8	4.2	1.0	0.5
Revised SBF <sup>93</sup>	142.0	5.0	2.5	1.5	103.0	27.0	1.0	0.5
Tas-SBF <sup>91</sup>	142.0	5.0	2.5	1.5	125.0	27.0	1.0	0.5

**Table 1.4** Ionic compositions of blood plasma and different SBF formula

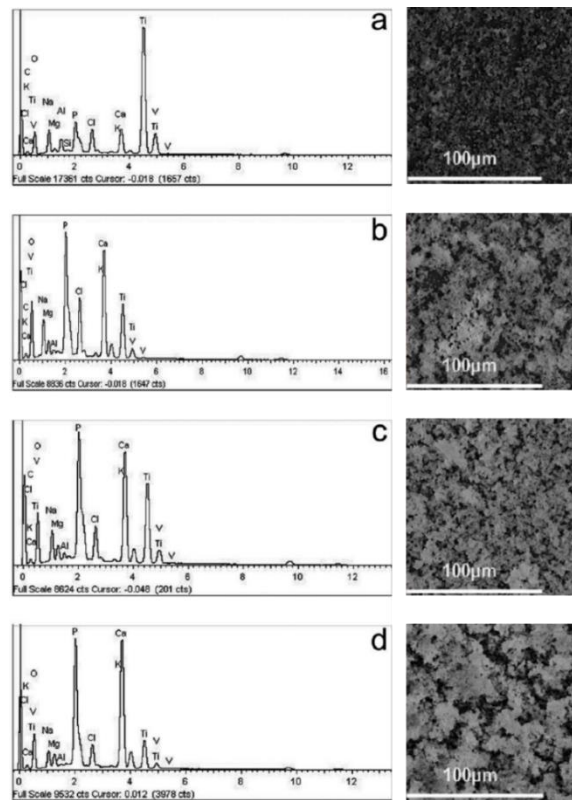


**Figure 1.15** Before (a) and after (b) heat treatment at 600 °C. FE-SEM images of surfaces of Ti soaked in SBF for 3 days after exposure to solutions with different pHs<sup>92</sup>



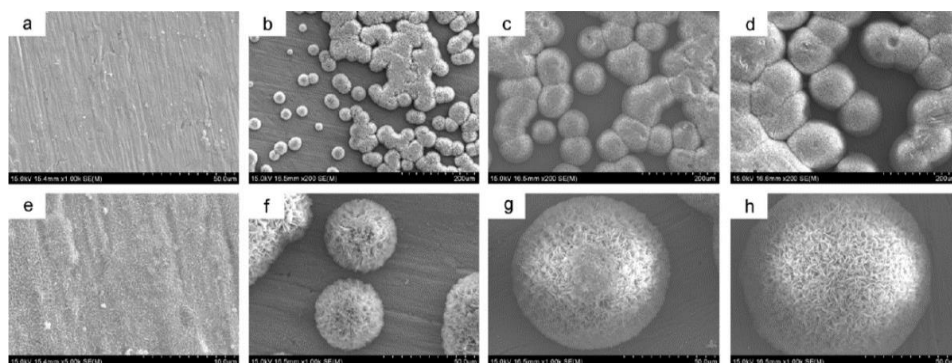
As mentioned before, the chloride and carbonate contents of the original SBF are not exactly equal to the one in blood plasma. Oyane et al.<sup>93</sup> tried to synthesize hydroxyapatite from a solution with the correct concentration in chloride and carbonate but observed the precipitation of calcium carbonate in solution. Takadama et al.<sup>89,90</sup> revised the concentration of chloride while keeping the carbonate concentration similar to SBF. This solution, labelled n-SBF (newly-improved SBF) had the same stability as SBF, with the same ability to form hydroxyapatite. The influence of carbonate concentration on the structure and crystallinity of the deposited hydroxyapatite was studied using SBF buffered with HEPES or by addition of CO<sub>2</sub> in the solution<sup>94</sup>. Solutions with HEPES were unstable while CO<sub>2</sub> bubbling was convenient, except that the exact concentration of carbonate ions in solution is unknown. It was found that increasing the carbonate concentration make the deposited layer thicker. Substitution of HEPES by TRIS<sup>91,95,96</sup> to buffer the carbonated solution allowed to decrease the extent of homogeneous precipitation. Overall, higher carbonate contents seem to be favorable to hydroxyapatite deposition on titanium or titanium alloy, but a correct stability of the solution requires the addition of a buffer and the chloride concentration has to remain similar to the one in conventional SBF.

Even if the standard SBF solution is already highly metastable, several attempts to modify the concentration of the solution have been made to enhance the hydroxyapatite deposition. Indeed, in order to deposit a relatively thick layer from SBF, a minimum of 14 days of deposition are needed with regular replenishments of the solution. The most popular way to speed up the deposition is to concentrate the SBF solution, and increase the processing temperature. Jalota et al<sup>96</sup>. used 1.5 x concentrated SBF. Deposition lasted 7, 14 or 21 days with replenishments of the solution every 48 hours. They reported homogeneous precipitation of hydroxyapatite in the solution due to too high supersaturation, but without any effect on the coating if substrates are placed vertically in the deposition solution. Deposition of hydroxyapatite from a 2x concentrated SBF was also studied<sup>97</sup>. Evolution of composition and morphology of coatings after 12 hours and 4, 8 and 14 days of deposition on TiAlV is visible on **Figure 1.16**. Along time, thickening of the coating is visible on the EDX spectrum, as the Ti contribution decreases while Ca and P increase. The substitutions are visible by the presence of Na and Mg contributions.



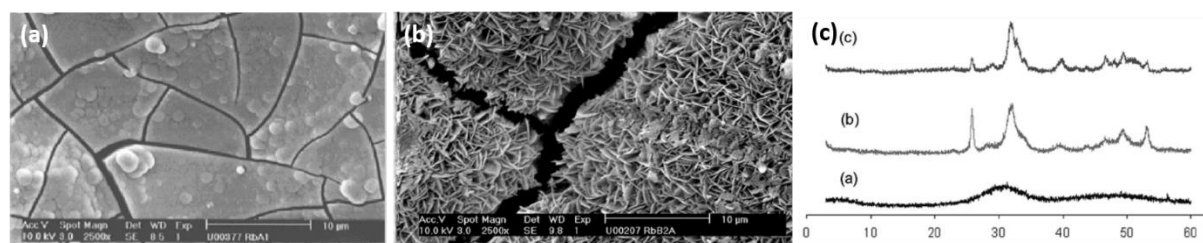
**Figure 1.16** SEM images and EDX spectra of HAp coatings on titanium alloy after different times of immersion in SBF: 12 h (a), 4 days (b), 8 days (c) and 14 days (d) <sup>97</sup>

Li et al.<sup>98</sup> studied the deposition of hydroxyapatite from a 3x concentrated SBF, at 57 °C. As they did not increase the TRIS concentration, pH was lower than expected (pH 6.8). Deposition time varied from 1 to 4 days, with refreshment every day. As seen in **Figure 1.17** coatings consisted in spherical aggregates increasing in size with time of deposition, but the coating was not homogeneous and the whole surface was not covered. They found that brushite was formed in the earlier time of deposition and transformed afterwards into hydroxyapatite.



**Figure 1.17** SEM images of (a) Ti samples treated by alkali heat treatment and subsequently soaked at 57 °C in 3 x SBF for (b) 1 days, (c) 2 days and (d) 4 days. (e) – (h) are high magnification images<sup>98</sup>

In another approach, Habibovic et al.<sup>99</sup> separated the coating procedure in two steps. First they deposited a thin and amorphous calcium phosphate layer on the TiAlV surface in a solution (SBF-A) consisting of SBF concentrated 5 times, without TRIS buffer and sulfate ions. The second step was the transformation of this layer in a thick and crystallized apatite film using a solution (SBF-B) similar to the previous one but with lower concentrations of  $Mg^{2+}$  and  $HCO_3^-$ , known as inhibitors of apatite crystallization. The pH of both solutions was adjusted by a  $CO_2$  gas flow during the preparation of the solutions. The coating steps lasted 24 h at 37 °C for the first, and 48 h at 50 °C for the second. After soaking the substrate in SBF-A, a carbonated amorphous calcium phosphate was deposited on the surface (**Figure 1.18 (a)**). In SBF-B, the dissolution of ACP occurred followed by the crystallization of HAp (**Figure 1.18 (b)**). In these conditions of high supersaturation, nucleation occurred both in the solution and on the substrate surface but it was suggested that formed nuclei are more stable on the preexisting ACP layer.

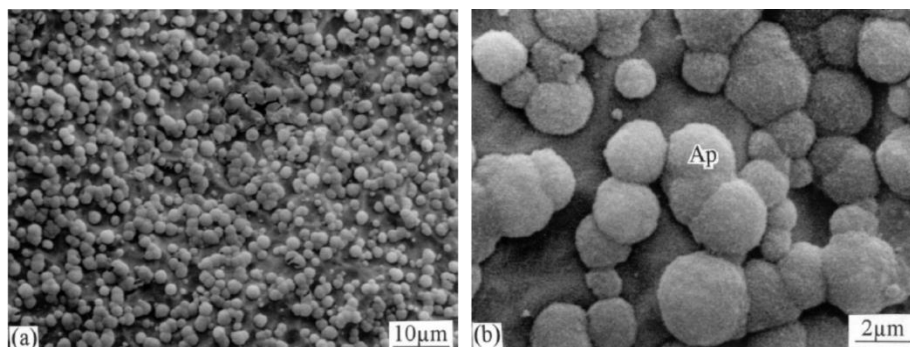


**Figure 1.18** SEM images of (a) SBF-A coating and (b) SBF-B coating after 24 hours; (c) XRD diffractogram of (a) bone, (b) SBF-A coating, and (c) SBF-B coating after 24 hours<sup>99</sup>

A study on the formulation of revised simulated body fluid showed that the concentration of the solution affects the morphology and the stoichiometry of the deposited calcium phosphate<sup>100</sup>. When the concentration of the SBF increases, the Ca/P ratio and the amount of incorporated carbonates also increased. The composition of the films was less close to the bone than when deposited in conventional or revised SBF at the usual concentrations. To conclude, it is better to keep the ionic concentrations in SBF close to the ones of blood plasma, in order to prevent precipitation in solution and to obtain a coating composition as close as possible to bone hydroxyapatite. An exception can be made for carbonate content, which can be lowered like in conventional SBF, or the same than in blood plasma like in the revised SBF, if the chloride content remains high.

Other media can be used as solution for biomimetic deposition. The Dulbecco's phosphate buffered saline (DPBS) (see composition in **Table 1.4**) allowed to deposit hydroxyapatite with 7 days at 60°C on commercially pure titanium, pretreated by physical vapor deposition to obtain a  $TiO_2$  anatase surface<sup>101</sup>. Hypercalcified solution like Fast calcification solution (FCS) and Hank's balanced salt solution (HBSS) are also available to deposit hydroxyapatite on titanium surface after surface pretreatment<sup>102</sup>.

HBBS contains more diverse ions than FCS (see **Table 1.4**), but both are at physiological pH. In this study, the titanium surface underwent an acidic treatment in  $\text{H}_3\text{PO}_4$  and an alkali heat treatment in NaOH solutions for 5 hours at  $140^\circ\text{C}$  under 3 bars of pressure. Deposition from FCS and HBSS solutions lasted 14 days at  $37^\circ\text{C}$  with replenishments of the solution every day. By SEM, they showed a homogeneous deposition of HAp but the surface was not fully covered (**Figure 1.19**).



**Figure 1.19** SEM image of titanium surface after 2 weeks immersion in HBSS (a) and enlargement (b)

Cell culture medium containing the appropriate concentrations of calcium and phosphate ions is also a potential choice to deposit hydroxyapatite on titanium substrates. With this idea, Faure et al.<sup>103</sup> used Dulbecco's modified Eagles medium (DMEM), which is a non-buffered acellular culture medium containing inorganic ions but also amino acids, vitamins and glucose (see composition in **Table 1.5**). Titanium was pretreated in NaOH and soaked in DMEM at  $37^\circ\text{C}$  for 4 or 15 days. After 15 days, the surface was fully covered with hydroxyapatite, with 10-15  $\mu\text{m}$  coating thickness. It was suggested that the deposition mechanism is similar to SBF, with first the nucleation of amorphous calcium phosphate on the surface, followed by phase transformation in hydroxyapatite and crystal growth. A major advantage of this method is the commercial availability of DMEM that avoid the fastidious preparation of SBF solutions.

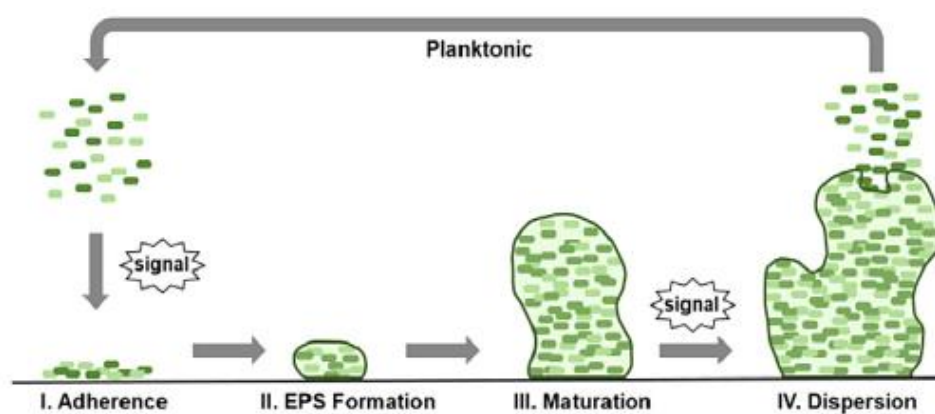
	$\text{Na}^+$	$\text{K}^+$	$\text{Mg}^{2+}$	$\text{Ca}^{2+}$	$\text{Cl}^-$	$\text{HPO}_4^{2-}$	$\text{SO}_4^{2-}$	$\text{HCO}_3^{2-}$
DPBS	448	10	4.1	2.5	242	14	-	-
FCS	137	3.71	-	3.10	145	1.86	-	-
HBSS	142	5.81	0.898	1.26	146	0.779	0.406	4.17
DMEM	154.56	5.37	0.8	1.82	120.5	1.0	0.8	44
SBF	141.8	5.0	1.5	2.5	148.0	1.0	0.5	4.2

**Table 1.5** Ionic compositions of solution to deposit HAp on titanium and comparison with SBF

As a summary, biomimetic deposition is a convenient method to coat metal substrates, but also ceramics and polymers, with a hydroxyapatite phase close to bone in composition, morphology and crystallinity. Compared to conventional methods like plasma spray, it is possible to achieve calcium substitutions and obtain carbonated hydroxyapatite. The morphology is also clearly distinct, as plate-like shaped particles are obtained compared to needle-shaped crystals usually obtained by co-precipitation methods. Coatings can be homogeneous in composition and crystallinity, in contrast to thermal methods often leading to the deposition of several calcium phosphate phases. Adherence of the coating to the substrate is important, thanks to the sticking layer of calcium titanate obtained after alkali pretreatment. Another advantage is also the possibility to coat non-planar substrates, as it is a wet method consisting in soaking the substrate in the solution. However, deposition lasts several days or weeks, which is the major disadvantage of this method. To accelerate the deposition, it is possible to concentrate the solution, while keeping in mind that it is very likely to induce precipitation in solution and make the deposited hydroxyapatite less “biomimetic”.

## 1.4 Antibacterial strategies

Prosthetic joint infections (PJI) are a major concern nowadays as their number is constantly increasing. Indeed, even if their prevalence is lower than before, as the number of patients expands every year, the number of infections goes the same way. The most frequent bacterial strain encountered in PJIs is the gender *Staphylococcus*, especially *S. aureus* and *S. epidermidis*, besides *S. haemolyticus*, *S. capitis*, and *S. hominis*. The principal mechanism in the development of infections is the biofilm formation<sup>104</sup> on a surface. Bacteria live in two states, the planktonic state when they are in solution, and an adhered biofilm state on a surface. The stages of biofilm development are 1- Initial attachment and adherence of planktonic cells to an abiotic or biotic surface; 2- recruitment of adhered cells and production of extracellular polymeric substance (EPS); 3- maturation and development of full biofilm architecture; and 4- dispersion of the biofilm to yield back planktonic cells<sup>105</sup> (**Figure 1.20**). Being in a biofilm state increases the resistance of bacteria to biocides. Dispersion is the deleterious stage, as bacteria are released in biological fluids in the case of biofilm formed on implant surface, spreading the infection in the entire body<sup>105</sup>. Combating biofilm formation is very important to avoid the development of PJIs. Two main strategies are currently implemented, alone or in combination: avoid bacterial adhesion to the surface of the implant, and/or kill the bacteria under contact or in solution by the release of a biocide agent.



**Figure 1.20** Bacterial life cycle<sup>105</sup>

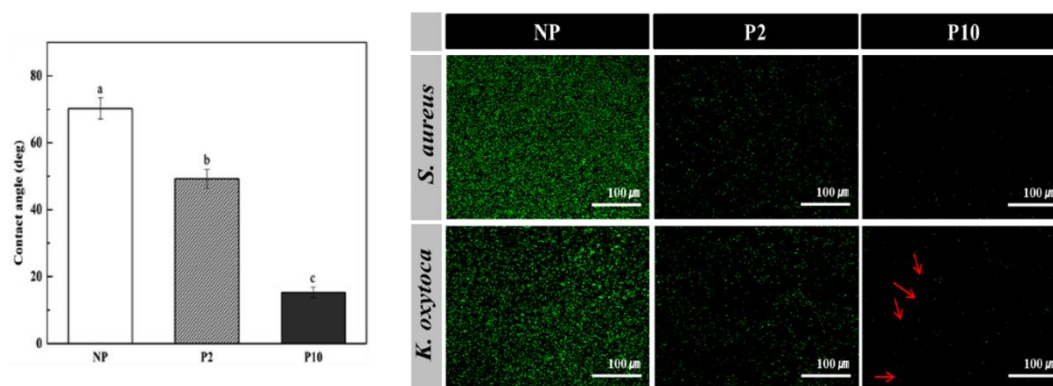
The majority of bacteria have a hydrophobic surface, because their membranes are composed by peptidoglycans for Gram + bacteria and phospholipids for Gram – bacteria. To prevent bacterial adhesion, one can play with surface hydrophilicity, with chemical treatments, nanopatterning, or different coatings like polymers or titania. Such surfaces are named antiadherent, in contrast with bactericide surfaces that kill planktonic or adhered bacteria thanks to bactericidal agents like metal ions or nanoparticles or antibiotics (encapsulated or tethered). This part will present these different methods used to achieve antibacterial surfaces. First, we will focused on surface modifications, then we will discuss the use of bactericidal metals such as silver, and finally we will explore the use of antibiotics, with an insight on antibioresistance and the necessity of using new antibacterial agents.

#### 1.4.1 Surface topology tuning

Titanium surface before any treatment is slightly hydrophilic (water contact angle  $\approx 70^\circ$ <sup>106,107</sup>). To increase the hydrophilicity of the surface, plasma<sup>107</sup>, laser<sup>106</sup>, UV<sup>108</sup> and chemical<sup>109</sup> treatments are used.

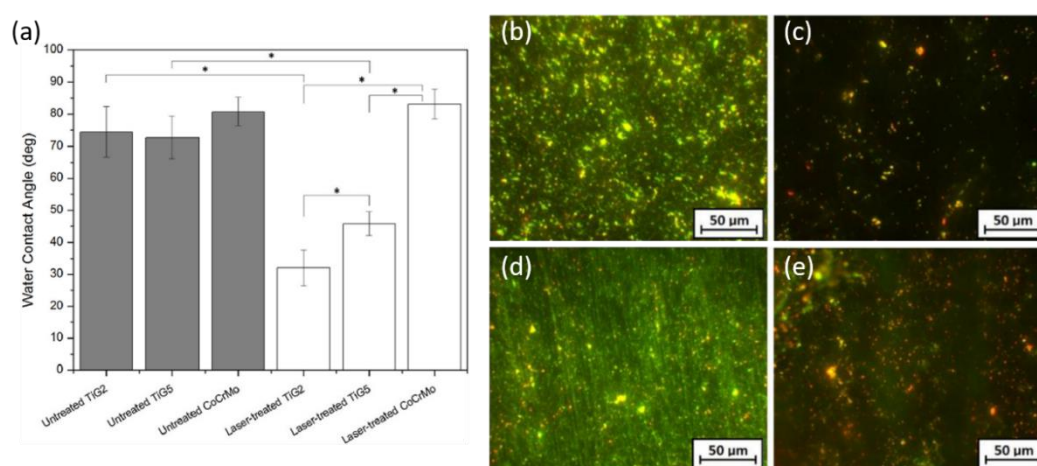
A non-thermal ambient atmosphere plasma treatment used on pure titanium surfaces allowed the formation of a TiO<sub>2</sub> anatase upper layer, together with the formation of imine and imides functional groups<sup>107</sup>. Treatment duration affected the surface energy and water contact angle of the surface. A 10 minutes treatment lead to more hydrophilic surface than the 2 minutes one, see **Figure 1.21 (a)**. These surfaces were tested against Gram + and Gram – bacteria. Bacterial adhesion and biofilm formation were reduced after treatment, with an enhanced effect for the longest treatment. Gram-negative bacteria were more impacted than gram-positive (**Figure 1.21 (b)**), probably because of the difference between their outer membranes.





**Figure 1.21** (a) Contact angle of water on non-treated Ti surface (NP), after 2 min (P2) and 10 (P10) minutes of plasma treatment; (b) Fluorescent images showing the live (green) and dead (red, arrow) stained bacteria *Staphylococcus aureus* and *Klebsiella oxytoca* adherent to titanium disc<sup>107</sup>

Exposition to UV irradiation at 257.7 nm for 15 hours enhanced the hydrophilicity of a TiAlV surface with a positive effect on different strains of *S. aureus* and *S. epidermidis*. Lower adhesion rates and ability to retain bacterial cells under flow conditions were observed compared with non-irradiated surfaces<sup>108</sup>. Fiber laser surface engineering is another route to enhance the hydrophilicity of titanium and titanium alloy surfaces. A laser treatment at 1064 nm in nitrogen environment led to the formation of TiN and TiO species and increased surface roughness<sup>106</sup>. Compared to non-treated surfaces that were covered with living bacteria (**Figure 1.22 (b) and (d)**), the number of *S. aureus* was reduced on treated Ti and TiAlV surfaces, especially on Ti (**Figure 1.22 (c)**), and dead bacteria were a majority on TiAlV (**Figure 1.22 (e)**).



**Figure 1.22** (a) Water contact angle on different substrates before and after laser treatment; Fluorescence images for the untreated (b, d) and laser-treated (c, e) samples after 24 h of *S. aureus* ATCC 65.38 culture: Ti (b, c) and TiAlV (d, e)<sup>106</sup>

Recently, research has focused on the nanopatterning of titanium surfaces<sup>110,111</sup>. Producing nanoscale structures, sometimes inspired by Nature, with specific dimensions on the surface could mechanically kill the bacteria, in addition to the anti-adhesion effect. Numerous fabrication processes are available, among them anodizing<sup>112–114</sup>, chemical etching<sup>109</sup> and hydrothermal are the most popular. Dimension of nanopatterns is the key parameter for the bactericidal property. Most studies report the bactericidal behavior for dimensions ranging between 100 and 1000 nm in height, 10 to 300 nm in diameter/width and spacing lower than 500 nm<sup>110</sup>. Rupture of the cell wall by penetration of high aspect ratio nanopatterns is commonly assumed as the underlying bactericidal mechanism. The control of anodization time of TiAlV substrates at a constant voltage of 20 V in an electrolyte containing H<sub>2</sub>SO<sub>4</sub> and HF can control the nanopattern obtained at the end of the process. 5 min leads to nanoporous TiO<sub>2</sub> while after 60 minutes nanotubular oxide is formed<sup>112</sup>. However, *S. aureus* and *S. epidermidis* adhesion is the same on nanoporous and nanotubular surfaces. Chemical etching in acidic oxidant solution (H<sub>2</sub>SO<sub>4</sub> and H<sub>2</sub>O<sub>2</sub> mixture) can form TiO<sub>2</sub> nanopores on TiAlV substrates<sup>109</sup>. After 30 minutes of etching, surfaces exhibit a trend to hydrophobic behavior, while after 60 minutes the hydrophilicity is enhanced. Adhesion of fungi (*Candida albicans*) depends on the time of contact with the surface. After 2 hours of contact, adhesion is reduced on treated surface, while after 6 hours the cell viability is higher on surfaces treated for 60 minutes, because the dimension of created pores is different depending on the treatment duration and pore dimension seems to have an effect on cell viability.

Overall, modification in surface hydrophilicity and nanopatterning are promising ways to reduce bacterial adhesion and activity on implant surface, with easy to handle techniques without an additional coating. In case of nanopatterning, surfaces may also be mechanically bactericidal.

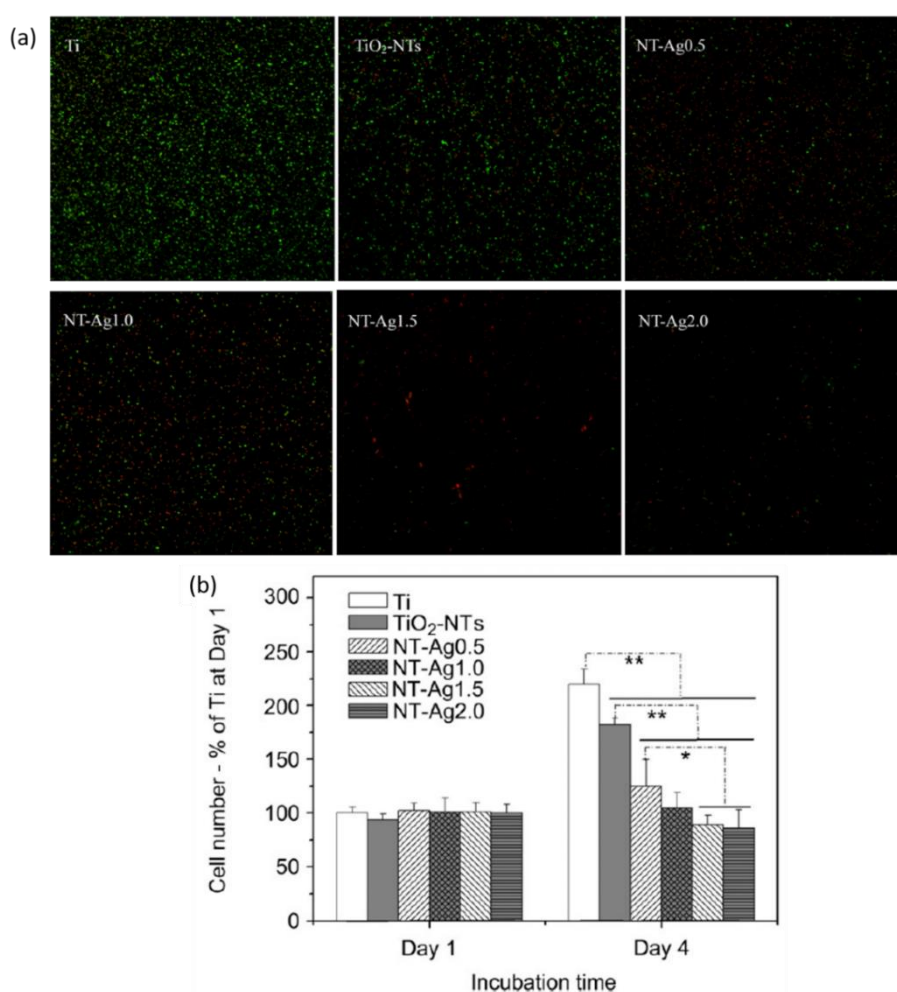
## 1.4.2 Surface functionalization

### 1.4.2.1 With inorganics compounds

Some metals have intrinsic antibacterial activity, like copper, zinc, and silver, which is the most studied. Metals may be added on the implant by incorporation within a coating of titania<sup>115</sup>, titania nanotubes<sup>114,116</sup> or calcium phosphate coatings<sup>117,118</sup>. Metals are interesting bactericide agents because they are active against both Gram-positive and Gram-negative bacteria. Because it is a very potent bactericide, silver is widely used, especially under the form of nanoparticles (NPs). It is commonly accepted that the antibacterial activity of Ag NPs comes from Ag<sup>+</sup> ions released upon NPs dissolution. Silver ion is capable to bind to bacterial DNA and RNA to prevent bacterial proliferation<sup>116,118</sup>. Silver NPs were incorporated in hydroxyapatite coating deposited on TiAlV substrates by a Ag mirror reaction (formation of metallic silver as a result of an oxidation-reduction reaction)<sup>118</sup>. Morphology of the

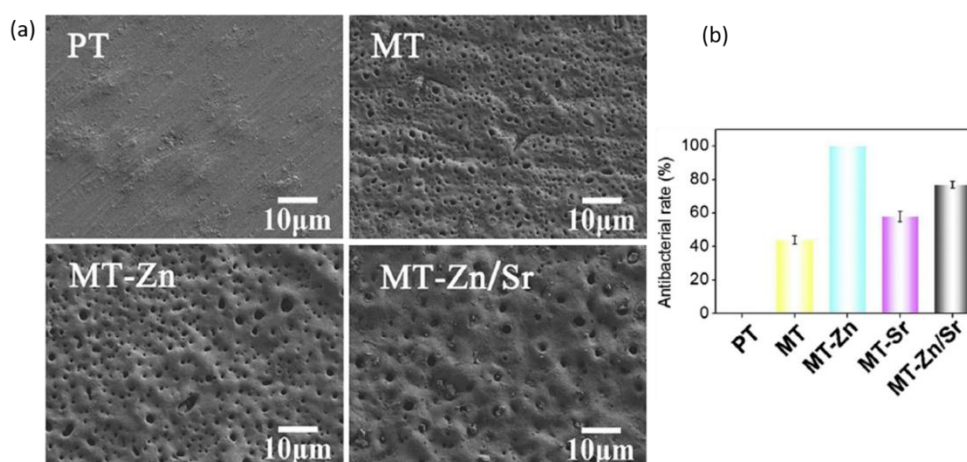


hydroxyapatite coating affected the Ag release, as nanorods and nanoplates arrays retained more Ag than smooth surfaces over 70 hours. However, it did not affect antibacterial activity and the Ag-incorporating coating reduced the number of viable bacteria by 100 %. Toxicity of coatings were evaluated on human bone mesenchymal stem cells. Cells adhered and proliferated on every surfaces, meaning that the presence of silver at these concentrations was not cytotoxic. However cytotoxicity of silver is usually a major concern, requiring the control of silver ion release. For instance, Ag NPs loaded in titania nanotubes (TNT) were release in two steps, a first rapid initial burst release and then a sustained one over 14 days<sup>114</sup>. These coatings were very efficient against *S. aureus* (**Figure 1.23 (a)**), but exhibited cytotoxicity, as shown in **Figure 1.23 (b)** with a reduced of number of primary rats osteoblasts compared to controls. The toxic burst release of silver ions may be delayed by coating loaded TNT by a polyelectrolyte films<sup>116</sup>. This protective coating did not affect the antibacterial activity of Ag loaded TNT, but prevented the toxicity towards osteoblasts and played a key role in adhesion and spreading.



**Figure 1.23** Fluorescence images of bacteria on samples after 7 days of incubation (a), and primary rat osteoblasts cell numbers on samples after 1 and 4 days of incubation (b) <sup>114</sup>

Zinc ions are interesting because they are less toxic than silver. They were introduced on  $\text{TiO}_2$  grown on titanium surface by micro-arc oxidation<sup>115</sup>. Coatings synthesized by this method were uniform and porous (see **Figure 1.24 (a)**). After 24 hours of incubation with *S. aureus*, the antibacterial activity of zinc-incorporated coating reached 100 %, while titania coating itself exhibited only 40 % of antibacterial activity. Strontium ions were added for osseointegration property, but antibacterial activity of mixed Zn-Sr/ $\text{TiO}_2$  coating was lowered to 80 % (**Figure 1.24 (b)**). Alternatively, polymeric coatings such as polydopamine, known to enhance cell adhesion and spreading, may encapsulate and release Zn ions for 6 days<sup>119</sup>. When deposited on titanium, they exhibited 100 % of antibacterial activity against *S. aureus* and *E. coli* compared to undoped polydopamine coatings.



**Figure 1.24** SEM images of pure Ti (PT), titania coating (MT), Zn-incorporated titania coating (MT-Zn) and Zn/Sr-incorporated titania coating (a); antibacterial rate of surfaces against *S. aureus* (b)<sup>115</sup>

One can take advantage to the flexibility of the structure of hydroxyapatite, which is favorable for ionic substitutions and insertions. Numerous studies have been done to dope HAp with various metal ions, such as silver<sup>120</sup>, zinc<sup>121–123</sup>, copper<sup>122,124–126</sup>, iron<sup>127–129</sup>, strontium<sup>130,131</sup>, lanthanides<sup>132</sup>, in order to enhance its biological activity. In particular, substitutions – or insertions – of copper and zinc are very promising for their antibacterial properties. Depending on the ionic content and synthesis method, doping ions may substituted calcium, or inserted into the hydroxyl channel, which does not modify crystals lattice parameters<sup>121,128</sup>. Employed as nanopowders, Cu- and Zn-doped HAp showed bacteria reduction against *E. coli* and in a lesser extent *S. aureus*<sup>122</sup>. Copper substituted hydroxyapatite reached more than 98 % of activity against *S. aureus*<sup>125</sup>. Combined doping of bismuth and silver  $\text{Bi}_{0.5}\text{Ag}_{0.5}\text{Ca}_4(\text{PO}_4)_3\text{OH}$  was also very efficient against *E. coli* and *S. aureus*<sup>120</sup>. However, doped-hydroxyapatite are mainly used as nanoparticles or cement. To the best of our knowledge, only few very recent promising studies have been conducted on doped-hydroxyapatite coatings. Solution

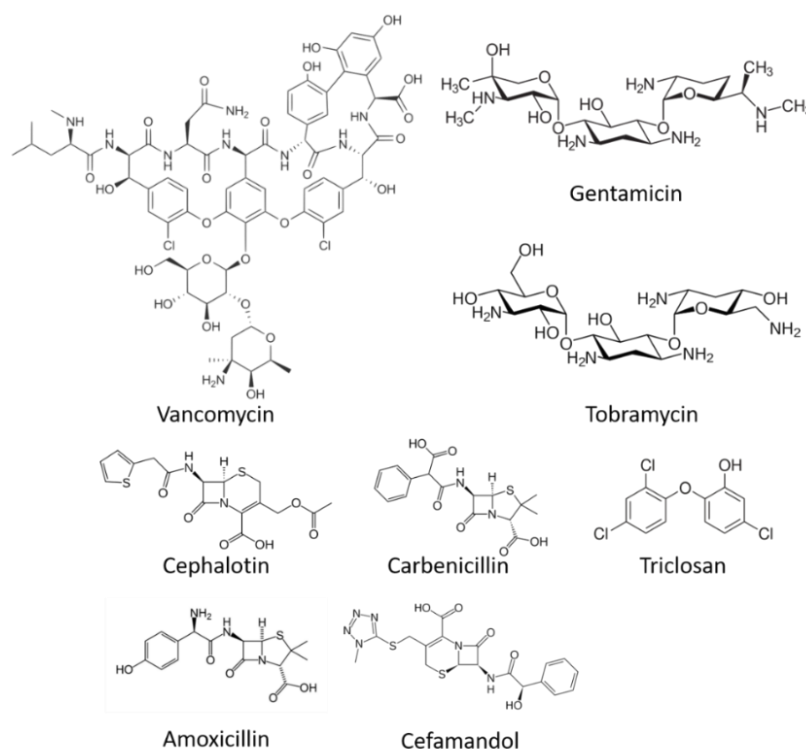
precursor plasma spraying process was used to deposit Zn- or Cu-doped hydroxyapatite on TiAlV<sup>123,126</sup>. Antibacterial activity of these coatings are not available yet.

Overall, metals are very efficient as bactericide agents, but it is necessary to control their release in body fluids to prevent any cytotoxicity, especially in the case of silver ions. However, promising strategies using additional polymeric coating or other bactericide metals like zinc have to be further investigated, notably due to the broad-spectrum activity of such agents.

#### 1.4.2.2 With organics compounds

##### 1.4.2.2.1 Antibiotics

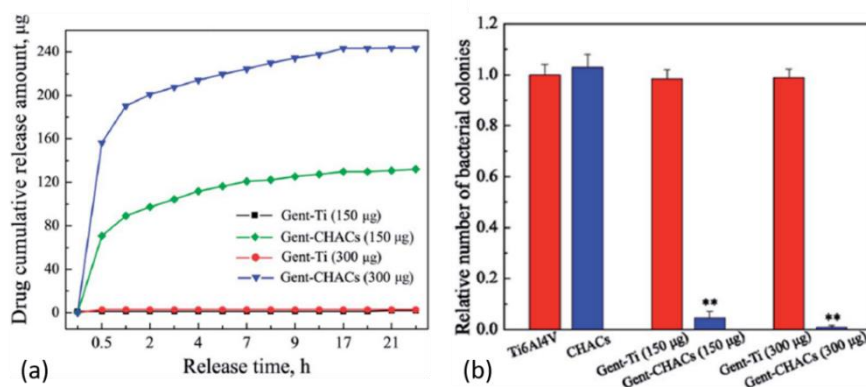
Local delivery of molecular antibiotics present at the implant surface has been widely studied over the past ten years. Antibiotics may be covalently immobilized or encapsulated in polymers or ceramics matrixes. One main disadvantage of antibiotics compared to metals ions -or NPs - and topological modifications is their narrow spectrum of efficacy. Indeed, antibiotics molecules have been developed against Gram-positive or Gram-negative bacteria, but do not have the same efficiency against both and can also show a strong strain-dependent activity. Nonetheless, some broad-spectrum antibiotics are available, a selection of which (see molecular structures on **Figure 1.25**) will be studied here for incorporation on titanium surfaces by tethering or encapsulation



**Figure 1.25** Molecular structures of some antibiotics immobilized on Ti surfaces

## 1.4.2.2.1.1 Adsorption

With the goal of combining antibacterial activity with osseointegration, loading of antibiotics within hydroxyapatite has been widely studied<sup>101,138–142</sup>. In these studies, drugs may be incorporated after in the coating by adsorption<sup>101,138,140</sup> or lyophilization<sup>141,142</sup>. The synthetic route of the hydroxyapatite coating may affect the antibiotic loading and release. Tobramycin adsorbed on plasma-sprayed HAp was released over 2 days in PBS, while release was sustained for 8 days at concentration above MIC (against *S. epidermidis*) if the drug was adsorbed on biomimetic HAp<sup>128</sup>. This was attributed to the nanoporous structure of biomimetically deposited HAp. By adsorption on such a coating, tobramycin remained active up to 6 days *in vitro* with *S. aureus* incubation every day, despite an initial burst release in the first 15 minutes<sup>138</sup>. The large amount of drug loaded allows to deliver tobramycin for 8 days with a concentration above the MIC. Adsorption of tobramycin, cephalotin, amoxicillin and gentamicin was studied on hydroxyapatite<sup>140</sup>. Coated surfaces inhibited *S. aureus* growth after 24 hours of incubation. *In vitro* release showed an initial burst release followed by a slow and reproducible release for 22 hours. Release rates indicated that the release of a therapeutically relevant dose could be achieved for about 2 days. This strategy could be useful to avoid initial contamination of the implant. The same drawback was observed when gentamicin was loaded by lyophilization on carbonated hydroxyapatite coating on TiAlV<sup>142</sup>. Macropores and mesopores of carbonated hydroxyapatite allowed to adsorb a large amount of gentamicin, but the totality of the drug was eluted after 24 hours (**Figure 1.26 (a)**). Nevertheless, this coating showed a diminution of *S. epidermidis* adhesion and prevention of biofilm formation (**Figure 1.26 (b)**).



**Figure 1.26** Cumulative amounts of gentamicin released from surfaces with adsorbed gentamicin directly on Ti (Gent-Ti), or on carbonated hydroxyapatite (Gent-CHACs) (a); Relative number of viable bacteria (*S. epidermidis*) on the different samples after culturing for 24 h (b)<sup>142</sup>

## 1.4.2.2.1.2 Encapsulation

Encapsulation of antibiotics follows the same principles than for encapsulation and release of osteogenic agents. For example, thanks to their small size, antibiotics molecules can be incorporated

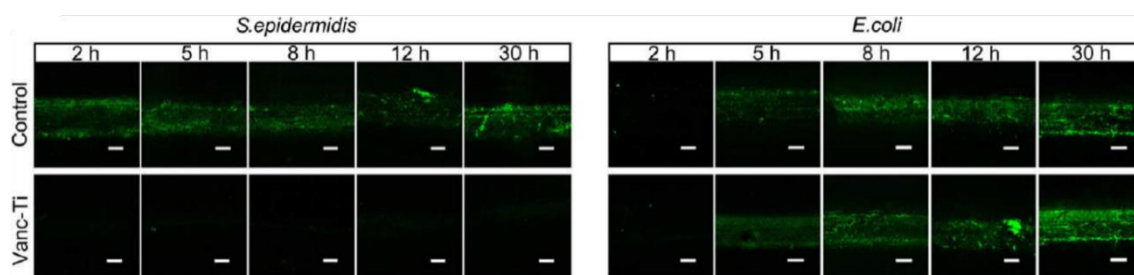
into titania nanotubes (TNTs) formed by anodization on titanium and titanium surfaces<sup>113</sup>. Filling of TNT via lyophilization allowed an uptake of gentamicin up to 600 µg for 0.5 cm x 0.5 cm surfaces. *S. aureus* adhesion was reduced by 70 % when TNTs are loaded with gentamicin, after 4 hours of incubation. However, this coating possesses a very short-term effect, as the drug is eluted in 150 min, and would be only useful to prevent initial bacterial colonization, before the adhesion and proliferation of osteoblastic cells. Another way to encapsulate antibiotics is inside a polymeric coating. Vancomycin was successfully incorporated in a PEG-poly(lactic-co-caprolactone) (PEG-PLC) hydrogel covalently bounded to Ti surface via adhesive polydopamine. Addition of starch in the coating slowed down vancomycin release *in vitro*, because of slower swelling of PEG-starch gel compared to PEG alone<sup>136</sup>. *In vivo*, vancomycin was delivered for nearly 4 weeks, with the reduction of inflammation in a rabbit model of *S. aureus* infection. Drugs can also be loaded within ceramics coatings, like silica or calcium phosphate. Triclosan was incorporated in a silica sol-gel coating on stainless steel fixation pins via sol-gel synthesis<sup>137</sup>. After an initial burst release, sustained release up to 8 weeks was observed, with elution of 33 % of the original triclosan load. An *in vivo* study in rabbits showed the ability of the coating to prevent infection and promote tissue healing.

When encapsulated in hydroxyapatite coating, antibiotic during may be added during the coating synthesis, especially for biomimetic deposition. When the molecules are added to the coating solution, they gradually become integrated within the forming calcium phosphate deposit<sup>139</sup>. For this strategy, functional groups of the antibiotic molecule is important for interaction with calcium and phosphate ions. Cephalotin and carbenicillin showed the best incorporation compared to cefamandol, amoxicillin, tobramycin and gentamicin. Looking to the antibiotic molecular structures, the incorporation efficiency seems to be related to the number of carboxylic acids, except for cephalotin that only possesses one carboxylic group. Vancomycin was poorly incorporated in the coating, probably due to its molecular size. As for their release, cephalotin was released at the slowest rate, and no more than 70 % of the loaded drug was release within 16 hours. Drug loading and release were correlated to antibacterial activity of the coating as the cephalotin-loaded deposit was the more efficient against *S. aureus*.

#### 1.4.2.2.1.2 Covalent immobilization

Tethering antibiotics has several advantages, such as long-term antibiotics effect and local activity. As the drug is in principle immobilized on the surface for the lifetime of the implant, it should be effective in case of late colonization, and also limit its toxicity to the closest tissues<sup>133</sup>. MIC is the lowest concentration at which a compound will inhibit bacterial growth when dosed against planktonic bacteria cells<sup>105</sup>. The group of Shapiro and Hickok successfully tethered different antibiotics like vancomycin and gentamycin on titanium and titanium alloy surfaces with the help of self-assembled

monolayers<sup>134,135,133</sup>. As a first step, titanium surface was etched with a mixture of  $H_2SO_4$  and  $H_2O_2$ , before covalent immobilization of silanes like aminopropyltriethoxysilane, to obtain an amine-rich surface. The antibiotics were covalently coupled in a second stage using a linker, to take the drug at a certain distance from the surface. Vancomycin-Ti surfaces significantly prevented *S. aureus* biofilm formation over 30 hours incubation, and after seven re-incubations, but did not show any activity against *E. coli* biofilm<sup>135</sup> (see **Figure 1.27**). According to the authors, this confirmed that the activity is due to the presence of the antibiotics, and not to a modification in surface roughness or chemistry, because vancomycin is only active against Gram + bacteria. Studies on osteoblasts showed the non-cytotoxicity of these coating<sup>133</sup>.



**Figure 1.27** Bacterial colonization Control and Vanc-Ti rods after 30 h of incubation with *S. epidermidis*, a gram positive organism that falls within the spectrum of activity of vancomycin, or *E. coli*, a gram negative organism that is not sensitive to vancomycin<sup>135</sup>.

Even if these coatings seem promising, few drawbacks remain. Physical and chemical stability of the coating has to be taken into account, as the forces applied to orthopedic coatings are significant and the biological fluids highly corrosive. Furthermore, their action is only directed in the space immediately adjacent to the implant, which can be either be an advantage and a disadvantage. The antibiotic cannot fight against the propagation of the infection if avoiding biofilm formation is not enough.

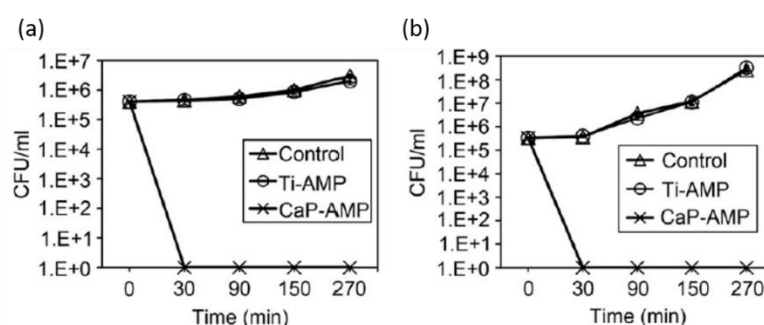
#### 1.4.2.2.2 Antimicrobial peptides

Antimicrobial peptides (AMP) are part of the immune system of numerous organisms, including humans. They possess superior antimicrobial characteristics than antibiotics, because they are broad-spectrum agents. They are active against bacterial, fungi, parasites and viruses, by targeting fundamental structures of microorganisms, like the membranes<sup>147</sup>. AMP are produced chemically or biologically using bacteria, yeast or insect cells. Advantage of biological production is the cheaper price of large-scale production.

AMP may be encapsulated in polymeric films<sup>148</sup>, or in calcium phosphate coatings<sup>149,150</sup>. Even if the incorporation is successful, the diffusion of the AMP to the surface is an issue. The outer layer is

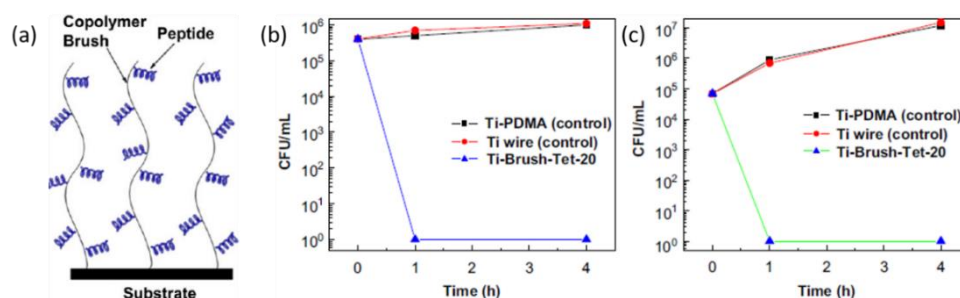


not the AMP, and bacteria adhering onto the top assembly may block AMP release. Moreover, long-term stability of the coating has to be studied. AMPs adsorbed on calcium phosphate coating were able to kill *S. aureus* and *P. aeruginosa* within 30 minutes<sup>149</sup>. Coatings remained active after four cycles of bacteria incubation, even if the activity decreased. No loading nor antibacterial activity was observed when AMPs were adsorbed on Ti surface (see **Figure 29**). To delay the AMP release from the coating, a thin phospholipid film (palmytoyl-oleoyl phosphatidyl-choline POPC) could be deposited on top of the initial calcium phosphate layer<sup>150</sup>. The presence of the film allowed a continuous drug release up to 72 hours, without initial burst release. These systems were active against *S. aureus* and *P. aeruginosa* after 24 hours of incubation.



**Figure 1.28** Antimicrobial activity of Ti-AMP and CaP-AMP against (a) *P. aeruginosa* and (b) *S. aureus*.<sup>149</sup>

For covalent binding, the titanium surface is usually functionalized with different spacers, like PEG or other “brushes”, or self-assembled monolayers, bearing reactive groups to attach the peptide onto the surface. Surface concentration of the AMP, spacer length and flexibility, as well as peptide orientation at the interface are key parameters to assure good antibacterial activity<sup>147</sup>. As an example, hydrophilic polymer brushes (N-substituted polyacrylamide PDMA/PAPMA) were used to covalently attach AMPs on titanium surface (**Figure 1.29 (a)**)<sup>151</sup>. The polymer provided protection against non-specific interaction and offered accessibility and flexibility to the AMPs. Antibacterial activity of these coatings was very efficient and fast on *P. aeruginosa* and *S. aureus* (**Figure 1.29 (b) and (c)** respectively). Biofilm resistance of the coating was attributed to effect of the anti-adhesion property of polymer brushes, combined with the bactericide activity of the peptide. Silanization of titanium surface by (3-chloropropyl)triethoxysilane (CPTES) and (3-aminopropyl)triethoxysilane (APTES) was used to functionalize the surface with an amino terminal group, in order to covalently attached AMPs<sup>152,153</sup>. These coatings were efficient against Gram-positive and Gram-negative bacteria, independently of the AMP used (melimine<sup>152</sup>, hLf1-11<sup>153</sup>).



**Figure 1.29** (a) Representation of peptide immobilized copolymer brush on surface; Antibacterial activity of peptide immobilized titanium wire against (b) *P. aeruginosa* and (c) *S. aureus*.<sup>151</sup>

#### 1.4.2.3 Antibioresistance: new antibacterial molecules from natural products

Despite the potential of local delivery of antibiotics to prevent PJI, the ongoing phenomenon of antimicrobial resistance has forced researchers to be careful while using common antibiotics. In 2018, the World Health Organization described the antibiotic resistance as “one of the biggest threats to global health, food security, and development today”<sup>143</sup>. This is not a new phenomenon, as the first drug resistant bacterial strains were discovered in the 1930s in military hospitals. Nowadays, antimicrobial resistance is responsible for almost 25000 deaths per year in Europe, and its cost is approximatively comprised between \$ 150 million and \$ 30 billion<sup>144</sup>. Resistant pathogens may be classed in three different groups. First, methicillin-resistant *Staphylococcus aureus* (MRSA) is the most spread pathogen, with 40-60 % of nosocomial *S. aureus* in the USA and UK described as MRSA. Even more dangerous than MRSA, because vancomycin is a “last chance” antibiotic, the vancomycin-resistant *S. aureus* is an emerging pathogen. The second group of resistant bacterial strains concerns multi-drug resistant (MDR) gram-negative bacteria, which are less prevalent than MRSA. *Pseudomonas aeruginosa* resistant to some (MDR) or all (pandrug-resistant) classes of antibiotics commonly used to treat Gram-negative bacteria belongs this group. The third group is the most challenging and is characterized by MDR and extensively drug-resistant strains of *Mycobacterium tuberculosis* (MDR-TB and XDR-TB), which are a rising threat in the developing world<sup>145</sup>. However, this group is outside of our study as this strain does not concern PJIs.

Antibiotics resistance is mainly due to misuse and overuse of antibiotics in western countries. 80 % of the total antibiotics consumption in the USA is used in animal food production, and almost 30 % of antibiotics prescriptions may have been inappropriate<sup>146</sup>. Resistance may appear only few years after the use of a new drug, and is spread worldwide through contact between people infected by MDR bacteria. Genes for resistance can be transferred among bacteria of different taxonomic and ecological groups. These genes are generally directed against a single family of antibiotics. In case of local delivery of antibiotics, it is important to know that very low concentration of antibiotics induces the resistance, which is correlated with sub-MIC concentration of antibiotic. To fight against antibiotics resistance, it

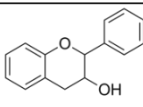
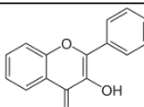
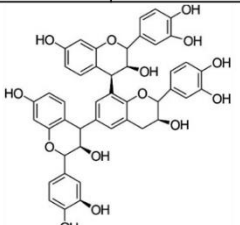

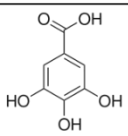
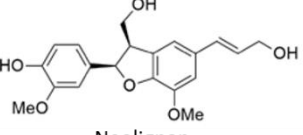


is necessary to reduce antibiotic consumption, together with a better use. Researchers need to develop new antibiotics, as only two new classes of antibiotics have reached the market since the 1970s. New antibiotics may be inspired by natural molecules, which can be used as such or improved by organic synthesis to obtain more efficient drugs<sup>145</sup>. In this part, we will focus on alternative strategies involving natural molecules. First, the use of antimicrobial peptide will be underlined, before a study of natural polyphenols extracted from natural products, known for their numerous biological properties (antibacterial, anti-viral, antioxidant, anti-inflammatory).

In order to face the development of antibacterial resistance, the use of natural products as antibacterial agents has attracted much attention in the last decades<sup>105</sup>. Phytopharmacology is used in traditional medicine over three thousand years mainly as herbal tea, but also in modern medicine since a large proportion of known drugs are molecules that have been identified in plants and used as such or as a derivative. Indeed, it is estimated that at least 25% of all modern medicines are derived, either directly or indirectly, from medicinal plants, primarily through the application of modern technology to traditional knowledge<sup>154</sup>. As a sign of this increasing interest, a list of 442 plants is included in the 2013 version of the European pharmacopoeia for their therapeutic use. A more recent approach is to focus on the most active molecules from plants. Most are secondary metabolites that serve in many cases as plant defense mechanisms against predation by microorganisms, insects and herbivores<sup>155</sup>. These molecules are responsible for plant odors (terpenoids) and colors (quinones and tannins), and most of them give the plant its flavor. Among them, polyphenols have been demonstrated to possess numerous health benefits such as antioxidation<sup>156–158</sup>, anti-inflammation<sup>159,160</sup> and antimicrobial activity<sup>157</sup>. It should be mentioned that these molecules have been investigated mainly for their use in food preservation, in the form of plant extract or essential oils, or extracted molecules<sup>161–163</sup>.

The most studied compounds include flavonoids, ubiquitous plant secondary metabolites that are known to be synthesized by plants in response to microbial infection<sup>155,164</sup>. More than 4000 flavonoids have been identified in fruits, vegetables and plant-derived beverages (tea, coffee, and wine). Flavonoids can be subdivided into many subclasses: flavonols, flavones, flavanones, anthocyanidins, flavanols, and isoflavones (**Figure 1.30**)<sup>164</sup>. Catechins and epigallocatechin gallate, mainly found in tea, are parts of the flavan-3-ol class. They are the most studied natural bioactive molecules, for their antibacterial and antifungi activities. Flavonols, such as myricetin, morin and quercetin, have received much attention thanks to their remarkable activity against both Gram-positive and Gram-negative bacteria. Flavones share a common skeleton with flavonols, without the hydroxyl on the central aromatic cycle. Baicalin and its aglycone baicalein are parts of this class (**Figure 1.31**). They are extracted from the root of the plant *Scutellaria baicalensis*, known in the Chinese pharmacopoeia for centuries for its anti-inflammatory<sup>165</sup>, antioxidant, antiviral, anticancer<sup>166</sup> and

antibacterial<sup>161,167</sup> properties. These two molecules have been characterized as ones of the most active molecules in *Scutellaria baicalensis* extracts<sup>161,167</sup>. Moreover, antibacterial activity of baicalein was tested against *S. aureus* and MRSA<sup>168,169</sup>. Baicalein alone was able to eradicate 7-days biofilm in a dose-dependent manner, for concentrations above MIC<sup>168</sup>. Use in combination with ciprofloxacin, baicalein at concentration below MIC was able to restore the antibacterial activity of ciprofloxacin against MRSA. Additionally, a synergistic effect was observed against ciprofloxacin resistant strains<sup>169</sup>.

Molecules		Biological properties
 Flavan-3-ol	 Flavonol	Antibacterial Antiviral Antifungi
 Condensed tannin		Antibacterial Antiviral
 Hydrolyzable tannin		Antibacterial Antiviral Antifungi
 Phenolic acids		Antibacterial
 Neolignan		Antibacterial

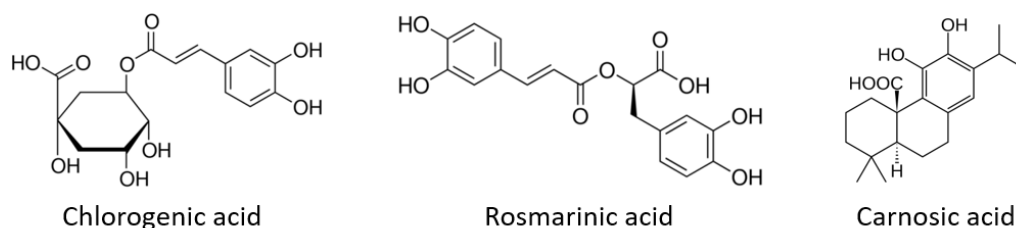
**Figure 1.30** Chemical structures of the polyphenol classes and their biological properties<sup>164</sup>



**Figure 1.31** Baicalin and baicalein structures

Another class with high biological importance includes carboxylic polyphenols such as chlorogenic acids<sup>158,170,171</sup>, gallic acid<sup>172</sup>, rosmarinic acid<sup>162</sup>, ferulic acid<sup>173</sup>, ellagic acid<sup>174</sup>, that combine polyphenol and carboxylic acid groups. Chlorogenic acids are a family of esters formed between trans-cinnamic acid and quinic acid. The most common compound is 5-O-caffeoyl-quinic acid (5-CQA), which is the only one commercially available and is therefore commonly called “chlorogenic acid”<sup>170</sup>. It can be found in many foods and beverages, mainly coffee, fruits, vegetables and lamiaceae (oregano, basil, marjoram, melissa, peppermint, rosemary, sage, spearmint and thyme). The scavenging activity and antibacterial property of methanolic extracts of fennels leaves and seeds have been attributed to chlorogenic acid<sup>157</sup>. It is also one of the major and most active components of the plant *Morina persica*<sup>175</sup>.

Finally, it is also worth mentioning the terpene family<sup>105</sup>, including carnosic acid. Carnosic acid possess one phenolic group, so that it is often classified as a polyphenol compound, but it is closer to the terpene family<sup>176</sup>. It has been described as the most active compound of rosemary essential oils for antioxidant and antibacterial activity. It is active against Gram-negative and Gram-positive bacteria.



**Figure 1.32** Molecular structures of chlorogenic, rosmarinic and carnosic acid

These examples are only a few over the wide range of natural molecules able to kill planktonic bacteria and/or to induce efficient biofilm prevention. Natural products may be used as essential oils or plant extracts, to take advantage of the synergy between compounds, or as pure compounds. An important point is that their MIC are far higher than those of common antibiotics, meaning that a higher dose is necessary to reach the antibacterial activity. As for their use in the field of body implants, only few studies but promising examples are available in the literature<sup>177–179</sup>.

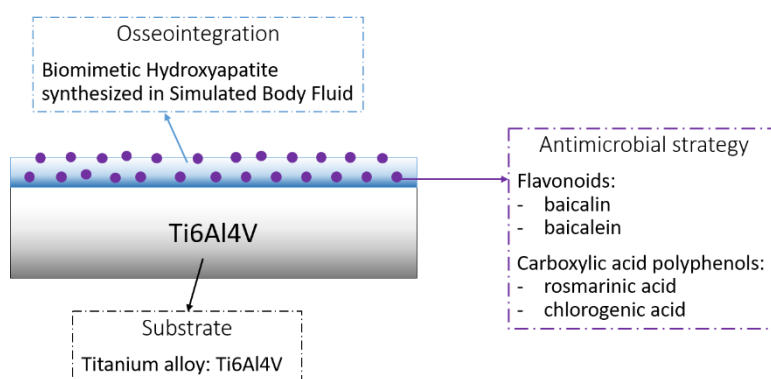
## 1.4 Conclusion: our strategy

This literature review emphasized the different strategies available to enhance osseointegration of metallic implants and to prevent the development of periprosthetic joint infections. Our goal in this PhD project was to confer both properties to titanium alloy surfaces, Ti6Al4V, the most common alloy used in total hip replacement.

As studied in this chapter, hydroxyapatite is a material that could enhance osseointegration and support to immobilize antimicrobial agents. The unique FDA approved synthesis of hydroxyapatite is the plasma spraying but coatings is inhomogeneous and the adherence to the substrate is poor. Moreover, with this method it is not possible to incorporate organic molecules like antibiotics during the process. In order to overcome the issues of plasma spraying, we decided to synthesize hydroxyapatite by a biomimetic deposition in using the Kokubo's simulated body fluid. Hydroxyapatite synthesized with this method is biomimetic in terms of chemistry and morphology, and temperature used in the process is compatible with the incorporation of organic molecules.

Several options are available to add antibacterial properties to a hydroxyapatite process, with inorganics or organics inorganics compounds. The use of metal is controversial because of the toxicity of such agents, and the issue of antibioresistance emerges with the use of antibiotics. Therefore, our choice goes on the use of natural antibacterial molecules, flavonoids and carboxylic acid polyphenols, known to be efficient against resistant-strains and never used in the field of antibacterial coatings for body implant. These four molecules possess carboxylic acid function and/or catechol functions that could significantly interact with hydroxyapatite.

In the next chapter, we will first discuss the antibacterial and antioxidant properties of selected antibiotics, as well as their interaction in solution with calcium ions, to determine which molecule would be the best choice to be associated with the hydroxyapatite coating. Spectrophotometric and spectrometric methods will be used to describe the complexation with calcium, and the behavior of molecules in aqueous solution. In a second step, the proof of concept to develop hybrid materials consisting of natural antibacterial molecules and hydroxyapatite will be presented. Antibacterial and antioxidant activity of mixed baicalein-hydroxyapatite particles will be determined. Finally, biomimetic coating of hydroxyapatite will be deposited on Ti alloy, and the incorporation of baicalein will be performed. *In vitro* antibacterial and osseointegration properties of the hybrid coating will be explored.



**Figure 1.33** Our strategy to develop a natural antibacterial molecule – biomimetic hydroxyapatite coating

## References

- 1 Y. Yang, Y. Kang, M. Sen and S. Park, in *Biomaterials for Tissue Engineering Applications*, eds. J. A. Burdick and R. L. Mauck, Springer Vienna, Vienna, 2011, pp. 179–207.
- 2 D. F. Williams, The Williams Dictionary of Biomaterials, /core/books/williams-dictionary-of-biomaterials/FFBBD9AB24857D1325171AB9E3F4827E, (accessed March 19, 2019).
- 3 A. Civantos, E. Martínez-Campos, V. Ramos, C. Elvira, A. Gallardo and A. Abarrategi, *ACS Biomaterials Science & Engineering*, 2017, **3**, 1245–1261.
- 4 Haute Autorité de Santé. Prothèses de hanche. Phase contradictoire suite à la révision d’une catégorie de dispositifs médicaux. Saint-Denis La Plaine : HAS ; 2014
- 5 S. M. Kurtz, K. L. Ong, J. Schmier, K. Zhao, F. Mowat and E. Lau, *The Journal of Arthroplasty*, 2009, **24**, 195–203.
- 6 B. Zhang, D. Myers, G. Wallace, M. Brandt and P. Choong, *International Journal of Molecular Sciences*, 2014, **15**, 11878–11921.
- 7 T. Albrektsson and C. Johansson, *European Spine Journal*, 2001, **10**, S96-S101.
- 8 R. Branemark, J. Bahuaud and M. Bertrand, *e-mémoires de l'Académie Nationale de Chirurgie*, 2006, **5** (4), 36-40.
- 9 L. Pulido, E. Ghanem, A. Joshi, J. J. Purtill and J. Parvizi, *Clinical Orthopaedics and Related Research*, 2008, **466**, 1710–1715.
- 10 G. K. Triantafyllopoulos, V. G. Soranoglou, S. G. Memtsoudis, T. P. Sculco and L. A. Poultsides, *The Journal of Arthroplasty*, 2018, **33**, 1166–1170.
- 11 J. E. Davies, *Biomaterials*, 2007, **28**, 5058–5067.
- 12 J. E. Davies, *The Anatomical Record*, 1996, **245**, 426–445.
- 13 S. A. Skoog, G. Kumar, R. J. Narayan and P. L. Goering, *Pharmacology & Therapeutics*, 2018, **182**, 33–55.
- 14 K. Anselme, M. Bigerelle, B. Noel, E. Dufresne, D. Judas, A. Iost and P. Hardouin, *Journal of Biomedical Materials Research*, 2000, **49**, 155–166.
- 15 K. Anselme, P. Linez, M. Bigerelle, D. L. Maguer, A. L. Maguer, P. Hardouin, H. F. Hildebrand, A. Iost and J. M. Leroy, *Biomaterials*, 2000, **21**, 1567-1577.

- 16 D. D. Deligianni, N. Katsala, S. Ladas, D. Sotiropoulou, J. Amedee and Y. F. Missirlis, *Biomaterials*, 2001, **22**, 1241-1251.
- 17 Q. Liu, W. Li, L. Cao, J. Wang, Y. Qu, X. Wang, R. Qiu, X. Di, Z. Wang and B. Liang, *Journal of Bionic Engineering*, 2017, **14**, 448–458.
- 18 N.-B. Li, S.-J. Sun, H.-Y. Bai, G.-Y. Xiao, W.-H. Xu, J.-H. Zhao, X. Chen, Y.-P. Lu and Y.-L. Zhang, *Nanotechnology*, 2018, **29**, 045101.
- 19 E. Chikarakara, P. Fitzpatrick, E. Moore, T. Levingstone, L. Grehan, C. Higginbotham, M. Vázquez, K. Bagga, S. Naher and D. Brabazon, *Biomedical Materials*, 2014, **10**, 015007.
- 20 R. A. Gittens, R. Olivares-Navarrete, T. McLachlan, Y. Cai, S. L. Hyzy, J. M. Schneider, Z. Schwartz, K. H. Sandhage and B. D. Boyan, *Biomaterials*, 2012, **33**, 8986–8994.
- 21 Z. Li, C. Liu, B. Wang, C. Wang, Z. Wang, F. Yang, C. Gao, H. Liu, Y. Qin and J. Wang, *RSC Advances*, 2018, **8**, 12471–12483.
- 22 F. Shahriyari, A. Razaghian, R. Taghiabadi, A. Peirovi and A. Amini, *Surface and Coatings Technology*, 2018, **353**, 148–157.
- 23 K. Ren, W. Yue and H. Zhang, *Surface and Coatings Technology*, 2018, **349**, 602–610.
- 24 B. Yue, *Journal of Glaucoma*, 2014, **23**, S20–S23.
- 25 D. Becker, U. Geißler, U. Hempel, S. Bierbaum, D. Scharnweber, H. Worch and K.-W. Wenzel, *Journal of Biomedical Materials Research*, 2002, **59**, 516–527.
- 26 U. Geißler, U. Hempel, C. Wolf, D. Scharnweber, H. Worch and K.-W. Wenzel, *Journal of Biomedical Materials Research*, 2000, **51**, 752–760.
- 27 S. Rammelt, E. Schulze, R. Bernhardt, U. Hanisch, D. Scharnweber, H. Worch, H. Zwipp and A. Biewener, *Journal of Orthopaedic Research*, 2004, **22**, 1025–1034.
- 28 M. Morra, C. Cassinelli, G. Cascardo, L. Mazzucco, P. Borzini, M. Fini, G. Giavaresi and R. Giardino, *Journal of Biomedical Materials Research Part A*, 2006, **78A**, 449–458.
- 29 B. Elmengaard, J. E. Bechtold and K. Søballe, *Biomaterials*, 2005, **26**, 3521–3526.
- 30 A. Bagno, A. Piovan, M. Dettin, A. Chiarion, P. Brun, R. Gambaretto, G. Fontana, C. Di Bello, G. Palù and I. Castagliuolo, *Bone*, 2007, **40**, 693–699.
- 31 D. M. Ferris, G. D. Moodie, P. M. Dimond, C. W. D. Giorani, M. G. Ehrlich and R. F. Valentini, *Biomaterials*, 1999, **20**, 2323–2331.

- 32 M. Schuler, G. R. Owen, D. W. Hamilton, M. de Wild, M. Textor, D. M. Brunette and S. G. P. Tosatti, *Biomaterials*, 2006, **27**, 4003–4015.
- 33 B. F. Bell, M. Schuler, S. Tosatti, M. Textor, Z. Schwartz and B. D. Boyan, *Clinical Oral Implants Research*, 2011, **22**, 865–872.
- 34 P. C. Bessa, M. Casal and R. L. Reis, *Journal of Tissue Engineering and Regenerative Medicine*, 2008, **2**, 1–13.
- 35 P. C. Bessa, M. Casal and R. L. Reis, *Journal of Tissue Engineering and Regenerative Medicine*, 2008, **2**, 81–96.
- 36 S. E. Kim, C.-S. Kim, Y.-P. Yun, D. H. Yang, K. Park, S. E. Kim, C.-M. Jeong and J.-B. Huh, *Carbohydrate Polymers*, 2014, **114**, 123–132.
- 37 S. E. Kim, Y.-P. Yun, J. Y. Lee, J.-S. Shim, K. Park and J.-B. Huh, *Journal of Tissue Engineering and Regenerative Medicine*, 2015, **9**, E219–E228.
- 38 S. E. Bae, J. Choi, Y. K. Joung, K. Park and D. K. Han, *Journal of Controlled Release*, 2012, **160**, 676–684.
- 39 C.-M. Xie, X. Lu, K.-F. Wang, F.-Z. Meng, O. Jiang, H.-P. Zhang, W. Zhi and L.-M. Fang, *ACS Applied Materials & Interfaces*, 2014, **6**, 8580–8589.
- 40 R. Guillot, F. Gilde, P. Becquart, F. Sailhan, A. Lapeyrere, D. Logeart-Avramoglou and C. Picart, *Biomaterials*, 2013, **34**, 5737–5746.
- 41 D. . Puleo, R. . Kissling and M.-S. Sheu, *Biomaterials*, 2002, **23**, 2079–2087.
- 42 S. Samavedi, A. R. Whittington and A. S. Goldstein, *Acta Biomaterialia*, 2013, **9**, 8037–8045.
- 43 M Vallet-Regi and J. M. Gonzalez-Calbet, *Progress in Solid State Chemistry*, 2004, **32**, 1–31.
- 44 L. Wang and G. H. Nancollas, *Chemical Reviews*, 2008, **108**, 4628–4669.
- 45 K. Fujisaki, S. Tadano and N. Sasaki, *Journal of Biomechanics*, 2006, **39**, 579–586.
- 46 D. Lee, C. Leroy, C. Crevant, L. Bonhomme-Coury, F. Babonneau, D. Laurencin, C. Bonhomme and G. De Paëpe, *Nature Communications*, 2017, **8**, 14104.
- 47 R. A. Surmenev, M. A. Surmeneva and A. A. Ivanova, *Acta Biomaterialia*, 2014, **10**, 557–579.

- 48 A. Bitschnau, V. Alt, F. Böhner, K. E. Heerich, E. Margesin, S. Hartmann, A. Sewing, C. Meyer, S. Wenisch and R. Schnettler, *Journal of Biomedical Materials Research Part B: Applied Biomaterials*, 2009, **88B**, 66–74.
- 49 W. S. W. Harun, R. I. M. Asri, J. Alias, F. H. Zulkifli, K. Kadirgama, S. A. C. Ghani and J. H. M. Shariffuddin, *Ceramics International*, 2018, **44**, 1250–1268.
- 50 S. Raynaud, E. Champion, D. Bernache-Assollant and P. Thomas, *Biomaterials*, 2002, **23**, 1065–1072.
- 51 L. M. Rodríguez-Lorenzo and M. Vallet-Regí, *Chemistry of Materials*, 2000, **12**, 2460–2465.
- 52 S. Sarda, F. Errassifi, O. Marsan, A. Geffre, C. Trumel and C. Drouet, *Materials Science and Engineering: C*, 2016, **66**, 1–7.
- 53 S. Diallo-Garcia, D. Laurencin, J.-M. Krafft, S. Casale, M. E. Smith, H. Lauron-Pernot and G. Costentin, *The Journal of Physical Chemistry C*, 2011, **115**, 24317–24327.
- 54 K. Achelhi, S. Masse, G. Laurent, A. Saoiabi, A. Laghzizil and T. Coradin, *Dalton Transactions*, 2010, **39**, 10644.
- 55 D. Segal, *Journal of Materials Chemistry*, 1997, **7**, 1297–1305.
- 56 Y.-G. Zhang, Y.-J. Zhu, F. Chen and J. Wu, *Materials Letters*, 2015, **144**, 135–137.
- 57 R.-L. Ying, R.-X. Sun, Q. Li, C. Fu and K.-Z. Chen, *Ceramics International*, 2019, **45**, 5914–5921.
- 58 N. Méndez-Lozano, R. Velázquez-Castillo, E. M. Rivera-Muñoz, L. Bucio-Galindo, G. Mondragón-Galicia, A. Manzano-Ramírez, M. Á. Ocampo and L. M. Apátiga-Castro, *Ceramics International*, 2017, **43**, 451–457.
- 59 J. Zhang, D. Jiang, J. Zhang, Q. Lin and Z. Huang, *Langmuir*, 2010, **26**, 2989–2994.
- 60 A. J. Nathanael, S. I. Hong, T. H. Oh, Y. H. Seo, D. Singh and S. S. Han, *RSC Adv.*, 2016, **6**, 25070–25081.
- 61 D.-M. Liu, T. Troczynski and W. J. Tseng, *Biomaterials*, 2001, **22**, 1721–1730.
- 62 I.-S. Kim and P. N. Kumta, *Materials Science and Engineering: B*, 2004, **111**, 232–236.
- 63 M. H. Fathi and A. Hanifi, *Materials Letters*, 2007, **61**, 3978–3983.
- 64 T. A. Kuriakose, S. N. Kalkura, M. Palanichamy, D. Arivuoli, K. Dierks, G. Bocelli and C. Betzel, *Journal of Crystal Growth*, 2004, **263**, 517–523.



- 65 P. Layrolle, A. Ito and T. Tateishi, *Journal of the American Ceramic Society*, 1998, **81**, 1421–1428.
- 66 D.-M. Liu, Q. Yang, T. Troczynski and W. J. Tseng, *Biomaterials*, 2002, **23**, 1679–1687.
- 67 M. Catauro, F. Bollino, E. Tranquillo, R. Tuffi, A. Dell’Era and S. V. Ciprioti, *Ceramics International*, 2019, **45**, 2835–2845.
- 68 M. G. Raucci, C. Demitri, A. Soriente, I. Fasolino, A. Sannino and L. Ambrosio, *Journal of Biomedical Materials Research Part A*, 2018, **106**, 2007–2019.
- 69 R. R. Rao, H. N. Roopa and T. S. Kannan, 8.
- 70 S.-C. Wu, H.-C. Hsu, S.-K. Hsu, Y.-C. Chang and W.-F. Ho, *Journal of Asian Ceramic Societies*, 2016, **4**, 85–90.
- 71 X. Yang and Z. Wang, *Journal of Materials Chemistry*, 1998, **8**, 2233–2237.
- 72 S.-H. Rhee, *Biomaterials*, 2002, **23**, 1147–1152.
- 73 J. M. Cao, J. Feng, S. G. Deng, X. Chang, J. Wang, J. S. Liu, P. Lu, H. X. Lu, M. B. Zheng, F. Zhang and J. Tao, *Journal of Materials Science*, 2005, **40**, 6311–6313.
- 74 B. León and J. A. Jansen, *Thin Calcium Phosphate Coatings for Medical Implants*, Springer New York, 2009.
- 75 E. Mohseni, E. Zalnezhad and A. R. Bushroa, *International Journal of Adhesion and Adhesives*, 2014, **48**, 238–257.
- 76 S. V. Dorozhkin, *Materials Science and Engineering: C*, 2015, **55**, 272–326.
- 77 H. Xu, X. Geng, G. Liu, J. Xiao, D. Li, Y. Zhang, P. Zhu and C. Zhang, *Ceramics International*, 2016, **42**, 8684–8690.
- 78 J.-M. Choi, H.-E. Kim and I.-S. Lee, *Biomaterials*, 2000, **21**, 469–473.
- 79 M.-F. Hsieh, L.-H. Perng and T.-S. Chin, *Materials Chemistry and Physics*, 2002, **74**, 245–250.
- 80 J. V. Rau, I. Cacciotti, S. Laureti, M. Fosca, G. Varvaro and A. Latini, *Journal of Biomedical Materials Research Part B: Applied Biomaterials*, 2015, **103**, 1621–1631.
- 81 D. A. Hamdi, Z.-T. Jiang, K. No, M. M. Rahman, P.-C. Lee, L. N. T. Truc, J. Kim, M. Altarawneh, L. Thair, T. A.-J. Jumaa and B. Z. Dlugogorski, *Applied Surface Science*, 2019, **463**, 292–299.

- 82 R. I. M. Asri, W. S. W. Harun, M. A. Hassan, S. A. C. Ghani and Z. Buyong, *Journal of the Mechanical Behavior of Biomedical Materials*, 2016, **57**, 95–108.
- 83 R. Bosco, M. Iafisco, A. Tampieri, J. A. Jansen, S. C. G. Leeuwenburgh and J. J. J. P. van den Beucken, *Applied Surface Science*, 2015, **328**, 516–524.
- 84 R. Drevet, A. Viteaux, J. C. Maurin and H. Benhayoune, *RSC Advances*, 2013, **3**, 11148.
- 85 D. J. Blackwood and K. H. W. Seah, *Materials Science and Engineering: C*, 2009, **29**, 1233–1238.
- 86 Y. Wang, H. Yu, C. Chen and Z. Zhao, *Materials & Design*, 2015, **85**, 640–652.
- 87 T. Kokubo, H. Kushitani, S. Sakka, T. Kitsugi and T. Yamamuro, *Journal of Biomedical Materials Research*, 1990, **24**, 721–734.
- 88 T. Kokubo, *Acta Materialia*, 1998, **46**, 2519–2527.
- 89 H. Takadama, H.-M. Kim, T. Kokubo and T. Nakamura, *Journal of Biomedical Materials Research*, 2001, **57**, 441–448.
- 90 T. Kokubo and H. Takadama, *Biomaterials*, 2006, **27**, 2907–2915.
- 91 A. Cüneyt Tas, *Biomaterials*, 2000, **21**, 1429–1438.
- 92 D. K. Pattanayak, S. Yamaguchi, T. Matsushita, T. Nakamura and T. Kokubo, *Journal of The Royal Society Interface*, 2012, **9**, 2145–2155.
- 93 A. Oyane, K. Onuma, A. Ito, H.-M. Kim, T. Kokubo and T. Nakamura, *Journal of Biomedical Materials Research Part A*, 2003, **64A**, 339–348.
- 94 E. I. Dorozhkina and S. V. Dorozhkin, *Colloids and Surfaces A: Physicochemical and Engineering Aspects*, 2002, **210**, 41–48.
- 95 D. Bayraktar and A. C. Tas, *Journal of the European Ceramic Society*, 1999, **19**, 2573–2579.
- 96 S. Jalota, S. B. Bhaduri and A. C. Tas, *Journal of Materials Science: Materials in Medicine*, 2006, **17**, 697–707.
- 97 R. S. Clavell, J. J. M. de Llano, C. Carda, J. L. G. Ribelles and A. Vallés-Lluch, *Journal of Biomedical Materials Research Part A*, 2016, **104**, 2723–2729.
- 98 N. Li, G. Xiao, B. Liu, Z. Wang, R. Zhu and Y. Lu, *Surface and Coatings Technology*, 2016, **301**, 121–125.

- 99 P. Habibovic, F. Barrère, C. A. Blitterswijk, K. Groot and P. Layrolle, *Journal of the American Ceramic Society*, 2004, **85**, 517–522.
- 100 E. I. Dorozhkina and S. V. Dorozhkin, *Journal of Biomedical Materials Research*, 2003, **67A**, 578–581.
- 101 J. Forsgren, U. Brohede, M. Strømme and H. Engqvist, *Biotechnology Letters*, 2011, **33**, 1265–1268.
- 102 H. . Wen, J. van den Brink, J. . de Wijn, F. . Cui and K. de Groot, *Journal of Crystal Growth*, 1998, **186**, 616–623.
- 103 J. Faure, A. Balamurugan, H. Benhayoune, P. Torres, G. Balossier and J. M. F. Ferreira, *Materials Science and Engineering: C*, 2009, **29**, 1252–1257.
- 104 M. A. Getzlaf, E. A. Lewallen, H. M. Kremers, D. L. Jones, C. A. Bonin, A. Dudakovic, R. Thaler, R. C. Cohen, D. G. Lewallen and A. J. van Wijnen, *Journal of Orthopaedic Research*, 2016, **34**, 177–186.
- 105 M. H. Fletcher, M. C. Jennings and W. M. Wuest, *Tetrahedron*, 2014, **70**, 6373–6383.
- 106 C.-W. Chan, L. Carson, G. C. Smith, A. Morelli and S. Lee, *Applied Surface Science*, 2017, **404**, 67–81.
- 107 M.-J. Lee, J.-S. Kwon, H. B. Jiang, E. H. Choi, G. Park and K.-M. Kim, *Scientific Reports*, , DOI:10.1038/s41598-019-39414-9.
- 108 A. Gallardomoreno, M. Pachaolivenza, L. Saldana, C. Perezgiraldo, J. Bruque, N. Vilaboa and M. Gonzalezmartin, *Acta Biomaterialia*, 2009, **5**, 181–192.
- 109 B. Valdez-Salas, E. Beltrán-Partida, N. Nedev, R. Ibarra-Wiley, R. Salinas, M. Curiel-Álvarez, Y. Valenzuela-Ontiveros and G. Pérez, *Materials Science and Engineering: C*, 2019, **96**, 677–683.
- 110 K. Modaresifar, S. Azizian, M. Ganjian, L. E. Fratila-Apachitei and A. A. Zadpoor, *Acta Biomaterialia*, 2019, **83**, 29–36.
- 111 A. Tripathy, P. Sen, B. Su and W. H. Briscoe, *Advances in Colloid and Interface Science*, 2017, **248**, 85–104.
- 112 M. Martínez-Pérez, A. Conde, M.-A. Arenas, I. Mahílllo-Fernandez, J.-J. de-Damborenea, R. Pérez-Tanoira, C. Pérez-Jorge and J. Esteban, *Colloids and Surfaces B: Biointerfaces*, 2019, **173**, 876–883.

- 113 K. C. Popat, M. Eltgroth, T. J. LaTempa, C. A. Grimes and T. A. Desai, *Biomaterials*, 2007, **28**, 4880–4888.
- 114 L. Zhao, H. Wang, K. Huo, L. Cui, W. Zhang, H. Ni, Y. Zhang, Z. Wu and P. K. Chu, *Biomaterials*, 2011, **32**, 5706–5716.
- 115 Q. Zhao, L. Yi, L. Jiang, Y. Ma, H. Lin and J. Dong, *Nanomedicine: Nanotechnology, Biology and Medicine*, 2019, **16**, 149–161.
- 116 Z. Yuan, P. Liu, Y. Hao, Y. Ding and K. Cai, *Colloids and Surfaces B: Biointerfaces*, 2018, **171**, 597–605.
- 117 Y. Evliyaoğlu, M. Kobaner, H. Çelebi, K. Yelsel and A. Doğan, *Urol Res*, 2011, **39**, 443–449.
- 118 B. Tian, W. Chen, Y. Dong, J. V. Marymont, Y. Lei, Q. Ke, Y. Guo and Z. Zhu, *RSC Advances*, 2016, **6**, 8549–8562.
- 119 L. Wang, X. Shang, Y. Hao, G. Wan, L. Dong, D. Huang, X. Yang, J. Sun, Q. Wang, G. Zha and X. Yang, *RSC Advances*, 2019, **9**, 2892–2905.
- 120 S. Shanmugam and B. Gopal, *Applied Surface Science*, 2014, **303**, 277–281.
- 121 S. Gomes, J.-M. Nedelec and G. Renaudin, *Acta Biomaterialia*, 2012, **8**, 1180–1189.
- 122 V. Stanić, S. Dimitrijević, J. Antić-Stanković, M. Mitrić, B. Jokić, I. B. Plećaš and S. Raičević, *Applied Surface Science*, 2010, **256**, 6083–6089.
- 123 R. T. Candidato, R. Sergi, J. Jouin, O. Noguera and L. Pawłowski, *Journal of the European Ceramic Society*, 2018, **38**, 2134–2144.
- 124 S. Gomes, C. Vichery, S. Descamps, H. Martinez, A. Kaur, A. Jacobs, J.-M. Nedelec and G. Renaudin, *Acta Biomaterialia*, 2018, **65**, 462–474.
- 125 S. Shanmugam and B. Gopal, *Ceramics International*, 2014, **40**, 15655–15662.
- 126 R. B. Unabia, S. Bonebeau, R. T. Candidato and L. Pawłowski, *Surface and Coatings Technology*, 2018, **353**, 370–377.
- 127 B. Desport, J. Carpena, J.-L. Lacout, D. Borschneck and J. Gattacceca, *Journal of Crystal Growth*, 2011, **316**, 164–171.
- 128 S. Gomes, A. Kaur, J.-M. Grenèche, J.-M. Nedelec and G. Renaudin, *Acta Biomaterialia*, 2017, **50**, 78–88.

- 129 M. Iafisco, C. Drouet, A. Adamiano, P. Pascaud, M. Montesi, S. Panseri, S. Sarda and A. Tampieri, *J. Mater. Chem. B*, 2015, **4**, 57–70.
- 130 J. Braux, F. Velard, C. Guillaume, M.-L. Jourdain, S. C. Gangloff, E. Jallot, J.-M. Nedelec, P. Laquerrière and D. Laurent-Maquin, *Materials*, 2016, **9**, 985.
- 131 K. A. Gross, A. Jeršova, D. Grossin, C. Rey and A. Vīksna, *IOP Conf. Ser.: Mater. Sci. Eng.*, 2012, **38**, 012032.
- 132 S. M. Hosseini, C. Drouet, A. Al-Kattan and A. Navrotsky, *American Mineralogist*, 2014, **99**, 2320–2327.
- 133 N. J. Hickok and I. M. Shapiro, *Advanced Drug Delivery Reviews*, 2012, **64**, 1165–1176.
- 134 V. Antoci, S. B. King, B. Jose, J. Parvizi, A. R. Zeiger, E. Wickstrom, T. A. Freeman, R. J. Composto, P. Ducheyne, I. M. Shapiro, N. J. Hickok and C. S. Adams, *Journal of Orthopaedic Research*, 2007, **25**, 858–866.
- 135 V. Antoci, C. S. Adams, J. Parvizi, H. M. Davidson, R. J. Composto, T. A. Freeman, E. Wickstrom, P. Ducheyne, D. Jungkind, I. M. Shapiro and N. J. Hickok, *Biomaterials*, 2008, **29**, 4684–4690.
- 136 D. Li, P. Lv, L. Fan, Y. Huang, F. Yang, X. Mei and D. Wu, *Biomater. Sci.*, 2017, **5**, 2337–2346.
- 137 H. Qu, C. Knabe, S. Radin, J. Garino and P. Ducheyne, *Biomaterials*, 2015, **62**, 95–105.
- 138 J. H. Sørensen, M. Lilja, T. C. Sørensen, M. Åstrand, P. Procter, S. Fuchs, M. Strømme and H. Steckel, *Journal of Biomedical Materials Research Part B: Applied Biomaterials*, 2014, **102**, 1381–1392.
- 139 M. Stigter, J. Bezemer, K. de Groot and P. Layrolle, *Journal of Controlled Release*, 2004, **99**, 127–137.
- 140 U. Brohede, J. Forsgren, S. Roos, A. Mihranyan, H. Engqvist and M. Strømme, *Journal of Materials Science: Materials in Medicine*, 2009, **20**, 1859–1867.
- 141 M. Lilja, J. H. Sørensen, U. Brohede, M. Åstrand, P. Procter, J. Arnoldi, H. Steckel and M. Strømme, *Journal of Materials Science: Materials in Medicine*, 2013, **24**, 2265–2274.
- 142 S. Tang, B. Tian, Q.-F. Ke, Z.-A. Zhu and Y.-P. Guo, *RSC Adv.*, 2014, **4**, 41500–41509.
- 143 M. A. Fischbach and C. T. Walsh, .
- 144 S. B. Levy and B. Marshall, *Nature Medicine*, 2004, **10**, S122–S129.
- 145 M. A. Fischbach and C. T. Walsh, *Science*, 2009, **325**, 1089–1093.

- 146 P. Holmstrup and B. Klausen, *Oral Diseases*, 2018, **24**, 291–295.
- 147 S. A. Onaizi and S. S. J. Leong, *Biotechnology Advances*, 2011, **29**, 67–74.
- 148 A. Shukla, K. E. Fleming, H. F. Chuang, T. M. Chau, C. R. Loose, G. N. Stephanopoulos and P. T. Hammond, *Biomaterials*, 2010, **31**, 2348–2357.
- 149 M. Kazemzadeh-Narbat, J. Kindrachuk, K. Duan, H. Jenssen, R. E. W. Hancock and R. Wang, *Biomaterials*, 2010, **31**, 9519–9526.
- 150 M. Kazemzadeh-Narbat, B. F. L. Lai, C. Ding, J. N. Kizhakkedathu, R. E. W. Hancock and R. Wang, *Biomaterials*, 2013, **34**, 5969–5977.
- 151 G. Gao, D. Lange, K. Hilpert, J. Kindrachuk, Y. Zou, J. T. J. Cheng, M. Kazemzadeh-Narbat, K. Yu, R. Wang, S. K. Straus, D. E. Brooks, B. H. Chew, R. E. W. Hancock and J. N. Kizhakkedathu, *Biomaterials*, 2011, **32**, 3899–3909.
- 152 R. Chen, M. D. P. Willcox, K. K. K. Ho, D. Smyth and N. Kumar, *Biomaterials*, 2016, **85**, 142–151.
- 153 M. Godoy-Gallardo, C. Mas-Moruno, M. C. Fernández-Calderón, C. Pérez-Giraldo, J. M. Manero, F. Albericio, F. J. Gil and D. Rodríguez, *Acta Biomaterialia*, 2014, **10**, 3522–3534.
- 154 M. M. Robinson and X. Zhang, THE WORLD MEDICINES SITUATION 2011/Traditional medicines: global situation, issues and challenges, <http://digicollection.org/hss/documents/s18063en/s18063en.pdf>, (accessed July 5, 2018).
- 155 M. M. Cowan, *Clin Microbiol Rev*, 1999, **12**, 564–582.
- 156 D. Procházková, I. Boušová and N. Wilhelmová, *Fitoterapia*, 2011, **82**, 513–523.
- 157 M. Salami, M. Rahimmalek and M. H. Ehtemam, *Food Chemistry*, 2016, **213**, 196–205.
- 158 B. Shan, Y. Z. Cai, M. Sun and H. Corke, *Journal of Agricultural and Food Chemistry*, 2005, **53**, 7749–7759.
- 159 H. P. Kim, K. H. Son, H. W. Chang and S. S. Kang, *Journal of Pharmacological Sciences*, 2004, **96**, 229–245.
- 160 P. Mladěnka, K. Macáková, T. Filipický, L. Zatloukalová, L. Jahodář, P. Bovicelli, I. P. Silvestri, R. Hrdina and L. Saso, *Journal of Inorganic Biochemistry*, 2011, **105**, 693–701.
- 161 Y. Lu, R. Joerger and C. Wu, *Journal of Agricultural and Food Chemistry*, 2011, **59**, 10934–10942.

- 162 J. D. Campo, C. Nguyen-The, M. Sergent and M. J. Amiot, *Journal of Food Science*, 2003, **68**, 2066–2071.
- 163 R. Ribeiro-Santos, D. Carvalho-Costa, C. Cavaleiro, H. S. Costa, T. G. Albuquerque, M. C. Castilho, F. Ramos, N. R. Melo and A. Sanches-Silva, *Trends in Food Science & Technology*, 2015, **45**, 355–368.
- 164 M. Daglia, *Current Opinion in Biotechnology*, 2012, **23**, 174–181.
- 165 B. Dinda, S. Dinda, S. DasSharma, R. Banik, A. Chakraborty and M. Dinda, *European Journal of Medicinal Chemistry*, 2017, **131**, 68–80.
- 166 Y. Gao, S. A. Snyder, J. N. Smith and Y. C. Chen, *Medicinal Chemistry Research*, 2016, **25**, 1515–1523.
- 167 X. Shang, X. He, X. He, M. Li, R. Zhang, P. Fan, Q. Zhang and Z. Jia, *Journal of Ethnopharmacology*, 2010, **128**, 279–313.
- 168 Y. Chen, T. Liu, K. Wang, C. Hou, S. Cai, Y. Huang, Z. Du, H. Huang, J. Kong and Y. Chen, *PLOS ONE*, 2016, **11**, e0153468.
- 169 B. C. L. Chan, M. Ip, C. B. S. Lau, S. L. Lui, C. Jolival, C. Ganem-Elbaz, M. Litaudon, N. E. Reiner, H. Gong, R. H. See, K. P. Fung and P. C. Leung, *Journal of Ethnopharmacology*, 2011, **137**, 767–773.
- 170 M. N. Clifford, *J. Sci. Food Agric.*, 1999, **79**, 362–372.
- 171 M. Kalinowska, E. Bajko, M. Matejczyk, P. Kaczyński, B. Łozowicka and W. Lewandowski, *International Journal of Molecular Sciences*, 2018, **19**, 463.
- 172 B. Badhani, N. Sharma and R. Kakkar, *RSC Advances*, 2015, **5**, 27540–27557.
- 173 H. Kikuzaki, M. Hisamoto, K. Hirose, K. Akiyama and H. Taniguchi, *Journal of Agricultural and Food Chemistry*, 2002, **50**, 2161–2168.
- 174 N. Seeram, L. Adams, S. Henning, Y. Niu, Y. Zhang, M. Nair and D. Heber, *The Journal of Nutritional Biochemistry*, 2005, **16**, 360–367.
- 175 A. Mocan, G. Zengin, A. Uysal, E. Gunes, A. Mollica, N. S. Degirmenci, L. Alpsoy and A. Aktumsek, *Journal of Functional Foods*, 2016, **25**, 94–109.
- 176 S. Birtić, P. Dussort, F.-X. Pierre, A. C. Bily and M. Roller, *Phytochemistry*, 2015, **115**, 9–19.
- 177 E. Tranquillo, F. Barrino, G. Dal Poggetto and I. Blanco, *Materials*, 2019, **12**, 155.

- 178 A. Córdoba, M. Satué, M. Gómez-Florit, M. Hierro-Oliva, C. Petzold, S. P. Lyngstadaas, M. L. González-Martín, M. Monjo and J. M. Ramis, *Advanced Healthcare Materials*, 2015, **4**, 540–549.
- 179 M. I. Alvarez Echazú, C. E. Olivetti, C. Anesini, C. J. Perez, G. S. Alvarez and M. F. Desimone, *Materials Science and Engineering: C*, 2017, **81**, 588–596.



## Chapter 2

Molecular study: interactions  
between calcium and  
biologically-active molecules



## 2. Molecular study: interactions between calcium and biologically-active molecules

### Outline

2. Molecular study: interactions between calcium and Biologically-active molecules.....	65
2.2 Introduction.....	69
2.3 Antibacterial and antioxidant activities of BAMs. ....	69
2.4 Interactions of calcium with natural polyphenols exhibiting antioxidant properties.....	72
2.4.1 Introduction.....	72
2.4.2 Experimental .....	73
2.4.3 Results and discussion.....	74
2.4.4 Conclusion .....	87
2.5 Stability of baicalin and baicalein at different pH and effect on calcium complexation.....	88
2.5.1 Introduction.....	88
2.5.2 Stability of baicalin and baicalein at different pH .....	89
2.5.3 Interaction with calcium.....	97
2.5.4 Conclusions.....	106
2.6 General conclusions .....	107
References.....	108



## 2.2 Introduction

In this first part of my PhD project, we attempted to understand the interaction between calcium and four biologically active molecules (BAMs) in solution at different pHs. The four BAMs studied along this chapter, and the entire thesis, are polyphenols and flavonoids: rosmarinic acid (RA), chlorogenic acid (CA), baicalin (BA) and baicalein (BE). As already discussed in the Literature review (Chapter 1), these molecules are potent antibacterial and/or antioxidant agents to be used in the field of bone implants. In a first instance, the characterization of the antibacterial and antioxidant activities of these molecules will be presented. Secondly, the interaction between rosmarinic and chlorogenic acids with calcium at different pHs will be investigated. As we intent to incorporate BAMs in hydroxyapatite, the interaction with calcium should be considered. This work conducted to the submission of a full paper, presented in the paragraph 2.4. In a third step, the *in vitro* fate of baicalin and baicalein at different pHs, as well as their interaction with calcium will be studied. In particular, the degradation of both molecules has been mentioned several times in the literature, but without further characterizations. We will try to better understand this phenomenon in the paragraph 2.5. and study how it affects their calcium-binding affinity.

## 2.3 Antibacterial and antioxidant activities of BAMs

The antibacterial activity of RA, CA, BA and BE was characterized by the measure of the minimum inhibitory concentration (MIC), against four bacterial strains: a Gram negative, *Pseudomonas aeruginosa* ATCC 27853, and three Gram positive, *Listeria ivanovii* Li4(pvS2), *Staphylococcus epidermidis* CIP 68.21 and *Staphylococcus aureus* ATCC 6538. Minimum inhibitory concentration of the molecules was measured by the microdilution method in 96-wells plates. Mueller-Hilton broth (MH) was used for culture of *S. epidermidis*, Brain Heart Infusion broth (BHI) for *L. ivanovii* and Lysogeny broth (LB) was used for *S. aureus* and *P. aeruginosa*. For each tested strain, a bacterial inoculum of  $1 \times 10^6$  cfu/mL was prepared by diluting an overnight culture in sterile MH. BAM solutions (100  $\mu$ L of 10 mg.mL<sup>-1</sup> stock solution in DMSO) were allotted in a 96-well microplate by two fold serial dilutions. Growth of bacterial strains was *de visu* assessed after 24 hours incubation at 37°C. MIC was defined as the minimal concentration of the tested compound that completely inhibited cell growth. BAM were tested at final concentrations ranging from 16 to 0.4 mg.mL<sup>-1</sup> for RA and CA, 40.96 to 0.01 mg.mL<sup>-1</sup> for BA and 1.35 to 0.033 mg.mL<sup>-1</sup> for BE. The highest final DMSO concentration used (10 % v/v) induced no significant bacterial growth inhibition. MIC determination of ciprofloxacin (0.0625  $\mu$ g.mL<sup>-1</sup> for *S. epidermidis* CIP 68.21 and 0.5  $\mu$ g.mL<sup>-1</sup> for *S. aureus* ATCC 7574) was performed as a control on each microplate. The accepted variance on MIC value can be estimated to a 2-fold difference due to the

microdilution method used. Experiments were performed in duplicate. Results are gathered in **Table 2.1**.

First, a difference is noticeable between Gram-positive and Gram-negative bacteria. The MIC of the four molecules against *P. aeruginosa* is outside the range of tested concentrations, while it was possible to measure MIC for the three other bacteria strains. This suggests that the four molecules are more active against Gram-positive bacteria than Gram-negative. Against the three Gram-positive bacteria, baicalein is the molecule with the lowest MIC, at 34 µg/mL against *S. epidermidis* and *L. ivanovii* and 17 µg/mL against *S. aureus*, meaning that it is the molecule with the best antibacterial activity. Chlorogenic acid is the less active molecule against the three tested bacteria strains, with a MIC of 2043 µg/mL against *L. ivanovii*, 4087 µg/mL against *S. aureus* and higher than 4087 against *S. epidermidis*. Baicalin and rosmarinic acid have intermediary MIC comprised between 512 and 1024 µg/mL depending on the bacteria.

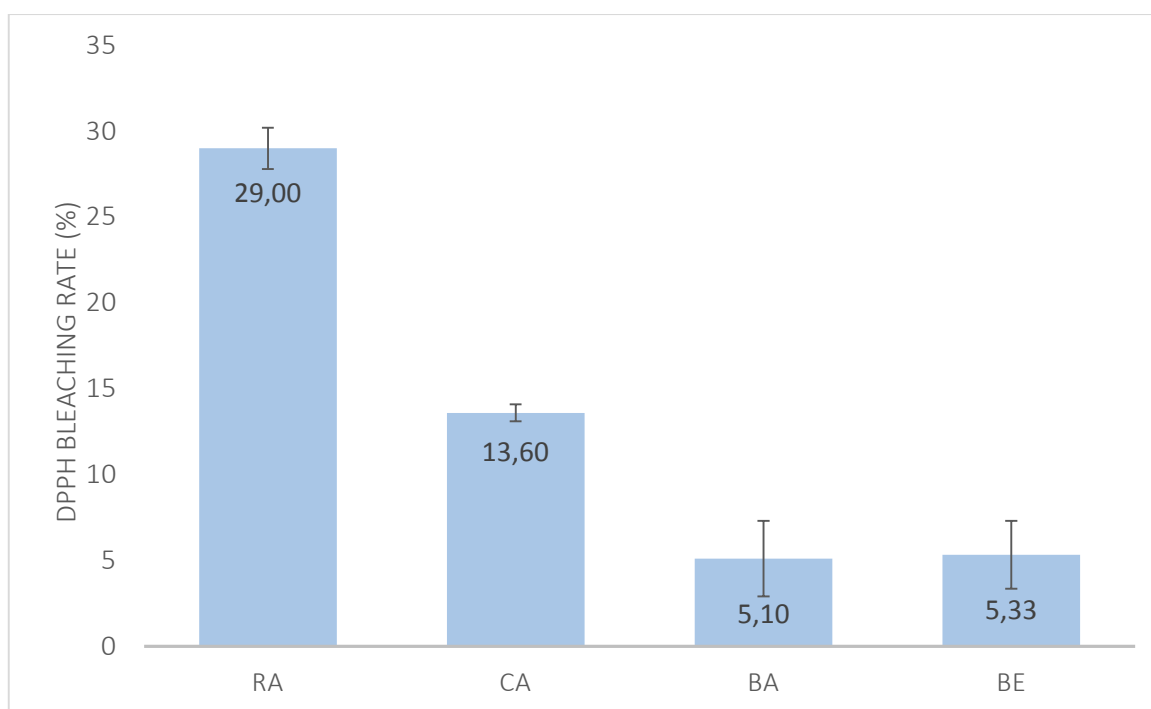
MIC (µg/mL)	<i>S. epidermidis</i> CIP 68.21	<i>S. aureus</i> ATCC 6538	<i>L. ivanovii</i> Li4(pvS2)	<i>P. aeruginosa</i> ATCC 27853
Rosmarinic acid	512	4087	512	> 4087
Chlorogenic acid	> 4087	4087	2043	> 4087
Baicalin	1024	256	512	> 2048
Baicalein	34	34	17	> 68

**Table 2.1** Antibacterial activity of the four biologically active molecules against four bacterial strains

Thereafter, the antioxidant activity of the four molecules was also tested. It was assayed by the measure of the scavenging activity on the stable free radical DPPH with a modified Blois' method in which the bleaching percentage of DPPH is monitored at a characteristic wavelength in presence of the sample<sup>1</sup>. The assay was performed as follows: 100 µL of BAM solution (concentration 50 µM) in ammonium carbonate pH 7.7 were mixed with 400 µL of Tris buffer pH 7.4 and 500 µL of fresh solution of DPPH at 100 µM in ethanol. Absorbance was measured at 517 nm after 20 minutes of reaction in the dark. DPPH inhibition was calculated by the equation:

$$\% \text{ inhibition} = [1 - (A_{\text{sample}} / A_{\text{DPPH solution}})] \times 100, \text{ with } A \text{ the measured absorbance.}$$

**Figure 2.1** Antioxidant activity of the four biologically active molecules **Figure 2.1** presents the DPPH bleaching percentage of the four BAMs. RA is the molecule with the best antioxidant activity, with a radical scavenging activity of 29 %. BE and BA have the same antioxidant activity, with a DPPH bleaching rate of ca. 5 %. CA have an intermediary behavior with 13.6 % of bleaching rate.



**Figure 2.1** Antioxidant activity of the four biologically active molecules

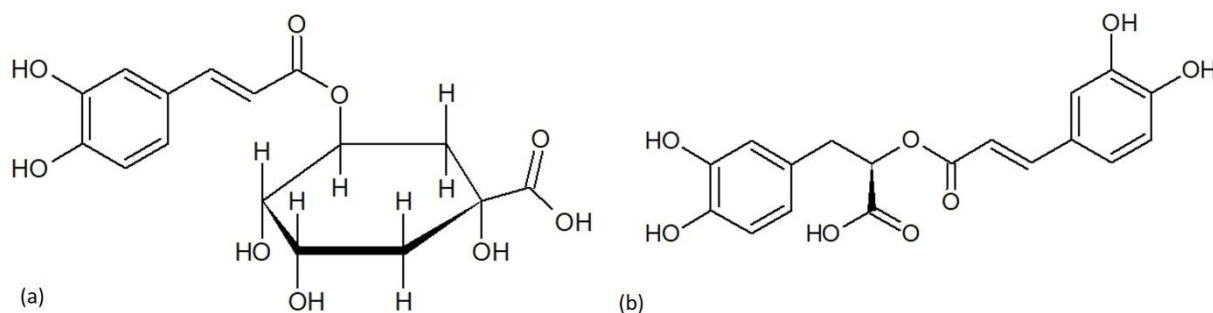
To conclude, baicalein is the molecule with the best antibacterial activity against the four tested bacterial strains, while chlorogenic acid is the one with the worst. On the contrary, baicalein has the weakest antioxidant activity, together with baicalin. Rosmarinic acid has an antioxidant activity 6-times higher than baicalin and baicalein, and twice that of chlorogenic acid. Rosmarinic is then the best antioxidant molecule in our study.

## 2.4 Interactions of calcium with natural polyphenols exhibiting antioxidant properties

### 2.4.1 Introduction

Phytopharmacology has attracted much attention in the research field in the last decades not only because of its use as in traditional medicine over three thousand years mainly as herbal tea, but also in modern medicine since a large proportion of known drugs are molecules which have been identified in plants and used as such or as a derivative. Indeed, it is estimated that at least 25% of all modern medicines are derived, either directly or indirectly, from medicinal plants, primarily through the application of modern technology to traditional knowledge<sup>2</sup>. As a sign of this increasing interest, a list of 442 plants is included in the 2013 version of the European pharmacopoeia for their therapeutic use. However, control quality to ensure safety and efficacy in production of traditional medicines is difficult, thus precluding from ensuring the efficiency of a drug based on a plant extract. A more recent approach is to focus on the most active molecules from plants. Among them, polyphenols have been demonstrated to possess numerous health benefits such as antioxidation<sup>3–5</sup>, anti-inflammation<sup>6,7</sup> and antimicrobial activity<sup>4</sup>. The most studied compounds include in particular flavonoids, ubiquitous plant secondary metabolites, whose activity is, at least partly, associated with their chelation of transition metals ions<sup>8</sup>. Such a complexation can not only lead to increased solubility, hydrophilicity and bioavailability, but the metal complexes may also possess different biological properties than the ligand alone<sup>7,9,10</sup>. In particular, iron<sup>7,11–13</sup> and copper<sup>9,11,14–16</sup> playing a key role in living systems, their complexes with flavonoids have been widely studied<sup>17</sup>. Another class with high biological importance includes carboxylic polyphenols such as chlorogenic acids<sup>5,18,19</sup>, gallic acid<sup>20</sup>, rosmarinic acid<sup>21</sup>, ferulic acid<sup>22</sup> and ellagic acid<sup>23</sup>. Complexation with transition metals ions was also largely studied, in particular for caffeic acid derivatives<sup>24–26</sup>. In aqueous solutions at neutral pH polyphenolic molecules usually bind to the metal or alkali metal ion by one or more  $-OH$  (and  $-COO^-$ , if present), usually resulting in the formation of weak mono-nuclear complexes<sup>27</sup>. However, their calcium complexes have been poorly characterized, despite the presence of this ion in biological fluids and therefore their possible relevance for pharmaceutical applications as antibacterial or antioxidant compounds. In this context, this study aimed at a detailed *in vitro* evaluation of calcium complexes of chlorogenic acid and rosmarinic acid (denoted biological active molecules (BAM) in the text) (**Figure 2.2**).





**Figure 2.2** Molecular structures of (a) chlorogenic acid and (b) rosmarinic acid

Several spectroscopic methods have been used to investigate a possible complexation between these catechol derivatives and calcium. The pH being of particular importance on both the formation and the stability of the complexes, a preliminary study of the UV-vis absorbance of the BAMs was undertaken. Particular attention was devoted to the determination of the stoichiometry of complexes and to the identification of complexing sites using mass spectrometry (MS) and NMR spectroscopy. Effect of calcium complexation on antioxidant activity of both molecules was also assessed. Taken together, these data reveal the large diversity of possible complexation modes of calcium ions with these molecules and their noticeable dependence on pH. However, little if any variation of their biological activity could be evidenced. This suggests that, compared to other inorganic ions, interactions of calcium ions with these molecules should not play a major role in their antioxidant efficiency but may nevertheless be taken into account for their *in vivo* fate.

## 2.4.2 Experimental

### 2.4.2.1 Chemicals

Chlorogenic acid (CA) and rosmarinic acid (RA) was purchased from Carbosynth Limited (Compton, Berkshire, UK). Calcium chloride dihydrate was obtained from Jessen Chemica. Phosphate buffer (PB) 0.1 M was prepared by mixing potassium phosphate monobasic and potassium phosphate dibasic at pH 7.2.

### 2.4.2.2 Spectroscopic and spectrometric measurements

The formation of complexes between the BAMs and calcium was investigated with several methods. UV-Visible spectroscopy was performed on a Libra Biochrom S60 spectrometer, between 250 and 600 nm. Electrospray ionization mass spectrometry (ESI-MS) studies were conducted on a LTQ orbitrap mass spectrometer, with a capillary voltage of 20 V and tube lens voltage of 70 V, in positive ion mode. Resonant excitation was carried out using collision-induced dissociation (CID), normalized collision energies (NCE) were between 5 and 30 %. All data analysis was performed using Thermo Xcalibur™ software. Samples were introduced at the rate of 20  $\mu\text{L} \cdot \text{min}^{-1}$  with a 500  $\mu\text{L}$  syringe. Solutions were prepared in ammonium carbonate buffer 1 mM at pH 7.8, from stock solutions of BAM in

methanol. Complexation of calcium with rosmarinic and chlorogenic acids was studied by  $^1\text{H}$  and  $^{13}\text{C}$  NMR, on a Bruker 300 MHz spectrometer equipped with a BBFO probe. Rosmarinic acid and chlorogenic acid were dissolved in  $\text{D}_2\text{O}$  in the presence of calcium chloride with ratio BAM /Ca = 0.1, and pH was adjusted to 7 with NaOD 0.01 M.

#### 2.4.2.3 Antioxidant activity assays

The scavenging activity on the stable free radical DPPH was assayed by the modified Blois' method in which the bleaching percentage of DPPH is monitored at a characteristic wavelength in presence of the sample<sup>1</sup>. The assay was performed as follows: 100  $\mu\text{L}$  of BAM solution (concentration 50  $\mu\text{M}$ ) in ammonium carbonate pH 7.7 were mixed with 400  $\mu\text{L}$  of Tris buffer pH 7.4 and 500  $\mu\text{L}$  of fresh solution of DPPH at 100  $\mu\text{M}$  in ethanol. Absorbance was measured at 517 nm after 20 minutes of reaction in the dark. DPPH inhibition was calculated by the equation:

$$\% \text{inhibition} = [1 - (A_{\text{sample}} / A_{\text{DPPH solution}})] \times 100,$$

with **A** the measured absorbance. For calcium effect testing, a ratio of 0.1 (BAM/Ca) was used, and solution of BAM with calcium was prepared 5 hours before the assay.

### 2.4.3 Results and discussion

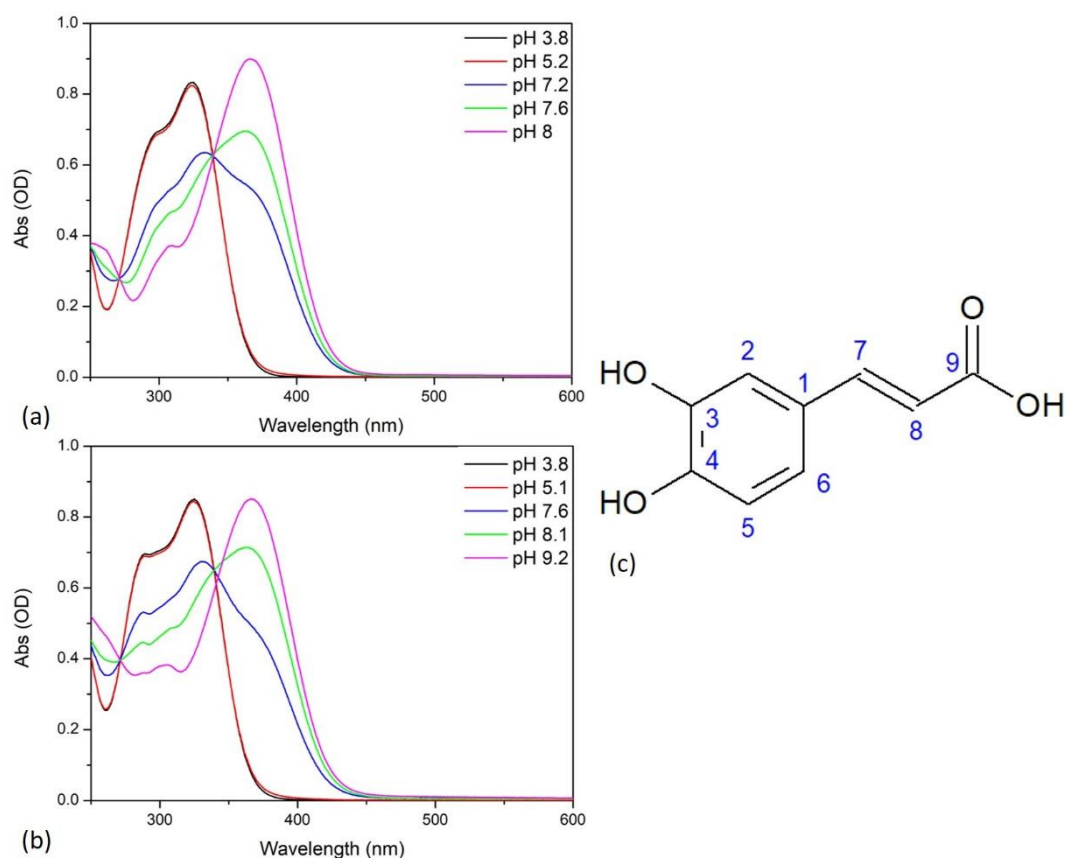
#### 2.4.3.1 Spectroscopic studies of calcium-polyphenol interaction

##### 2.4.3.1.1 UV-visible spectroscopy

Because of its sensitivity to the protonation state of catechol as well as to the influence of the presence of metal ions, UV-vis spectroscopy is a method of choice to study both free polyphenols and their complexes<sup>1,12,15,28,29</sup>.

The absorbance of carboxylic polyphenols recorded in the 250-600 nm range significantly varies with pH, as shown on **Figure 2.3**. The position of the bands as well as their shift with pH are very similar for RA and CA (**Figure 2.3 (a), (b)**), which share the same caffeic acid moiety (**Figure 2.3 (c)**). In acidic pH, a maximum is observed at 325 nm for RA together with a shoulder at 288 nm (see **Figure 2.3 (b)**). At basic pH, the absorption maximum showed a bathochromic shift up to 365 nm. In addition, a new shoulder was observed around 307 nm. In parallel, an additional absorption band is visible at c.a. 255 nm at pH 8. Evolution of absorption behavior of RA is consistent with previous reports by Danaf *et al.*<sup>30</sup>. The bathochromic shift visible when increasing pH from acidic to basic values was ascribed to the deprotonation of the hydroxyl on the position 3 of the caffeic acid part, whose pKa is reported to be at 8.36, based on potentiometric titration and Density Function Theory calculations.<sup>30</sup> Another clue for a relationship between the absorbance modification and deprotonation of a catechol hydroxyl group

is the observed isobestic point at 271 nm and, at lower extent, at 340 nm suggesting that a unique reaction is occurring within this pH range.

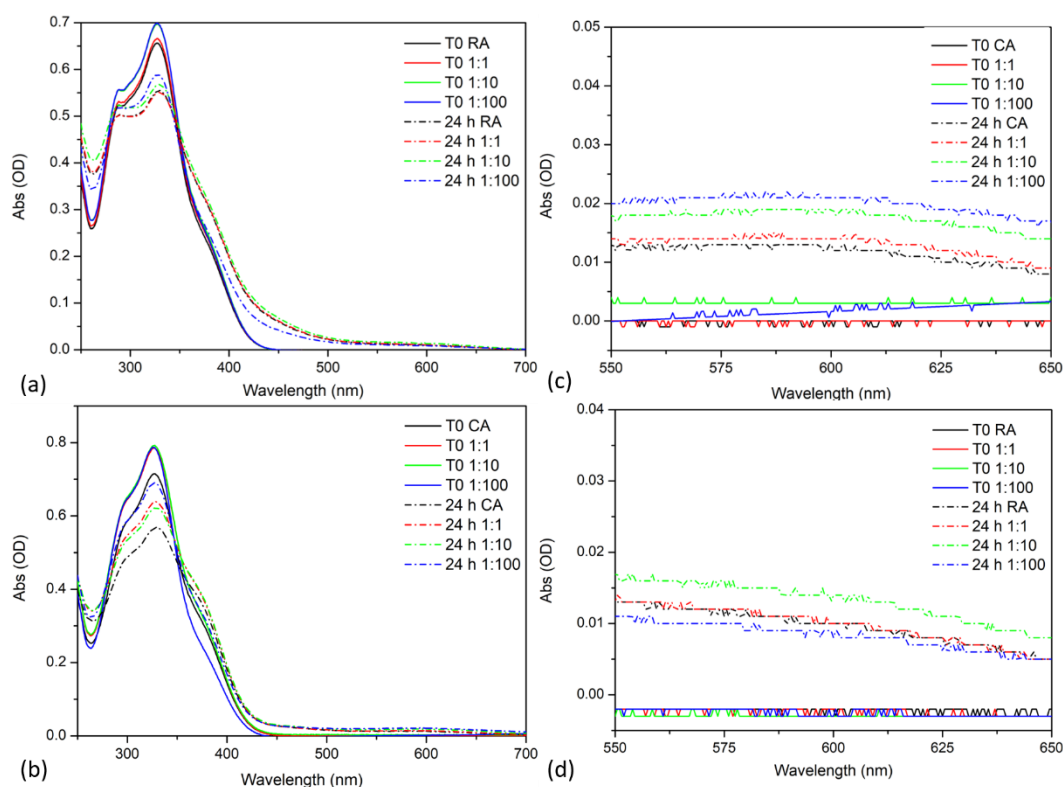


**Figure 2.3** UV-Visible spectra of (a) chlorogenic acid and (b) rosmarinic acid at different pHs, BAM concentration  $50 \mu\text{mol.L}^{-1}$ ; (c) structure of caffeic acid

Modifications of the absorption spectrum of CA with pH are very similar to those observed for RA (see **Figure 2.3 (a)**). At acidic pH, a maximum is observed at 323 nm with a shoulder at 300 nm. A bathochromic shift up to 365 nm is observed at basic pH, in addition with a new shoulder around 307 nm. As for RA, an additional absorption band is visible at ca. 255 nm. The presence of two isobestic points at 270 and 339 nm, together with the bathochromic shift, suggests the deprotonation of one of the catechol groups of CA at high pH, in agreement with the pKa of the hydroxyl group on position 3 of the caffeic acid moiety, calculated to be at 9.32 (calculation made with ACDLab software).

Noticeably no modification between absorption spectra at pH 3.8 and pH 5.1 are observed for CA, even though the pKa of the carboxylic acid was calculated at 3.90. This is in agreement with previous observations by Cornard *et al.*<sup>29</sup> and consistent with the position of the carboxylic group that it is carried by the quinic acid moiety and is not conjugated with the catechol ring. Similarly, for RA no difference could be observed on absorption spectra between pH 3 and pH 5, in accordance with the fact that its carboxylate group is not conjugated to the catechol rings.

As we intended to investigate the antioxidant properties of the BAM, the study of complexes formation between BAM and calcium was performed at pH 7.8, near physiological conditions. **Figure 2.4** displays the absorbance of mixtures of BAM and calcium chloride at three different BAM:Ca molar ratios 1, 0.1 and 0.01 recorded in ammonium carbonate buffer, immediately after mixture and 24 hours later.



**Figure 2.4** UV-Visible spectra of (a) chlorogenic acid and (b) rosmarinic acid with calcium at pH 7.8 in  $(\text{NH}_4)_2(\text{CO}_3)$  1mM, BAM concentration 50  $\mu\text{M}$ , molar ratios BAM:  $\text{Ca}^{2+}$ . (c) and (d) inset between 550 and 650 nm

In an ammonium carbonate buffer of pH 7.8, the initial spectrum of CA is quite similar to the one recorded in unbuffered solution at pH 5, except for an additional shoulder at ca. 380 nm. When compared to **Figure 2.3**, it suggests an apparent pH between 5 and 7, demonstrating the strong sensitivity of the UV-vis spectrum to the solution content. Upon CA addition in the 1:1 and 1:10 ratio, the two main bands at 300 nm and 323 nm rise in intensity while the shoulder at 380 nm remains unmodified. In the presence of a higher proportion of calcium (CA: $\text{Ca}^{2+}$  ratio 1:100), the intensity of these two bands does not evolve but the shoulder is less intense. After 24 h, the absolute and relative intensity of the two high-energy bands are modified while that of the low-energy shoulder has increased. Moreover, a new broad band also appears at ca. 600 nm. Quite similar observations prevail

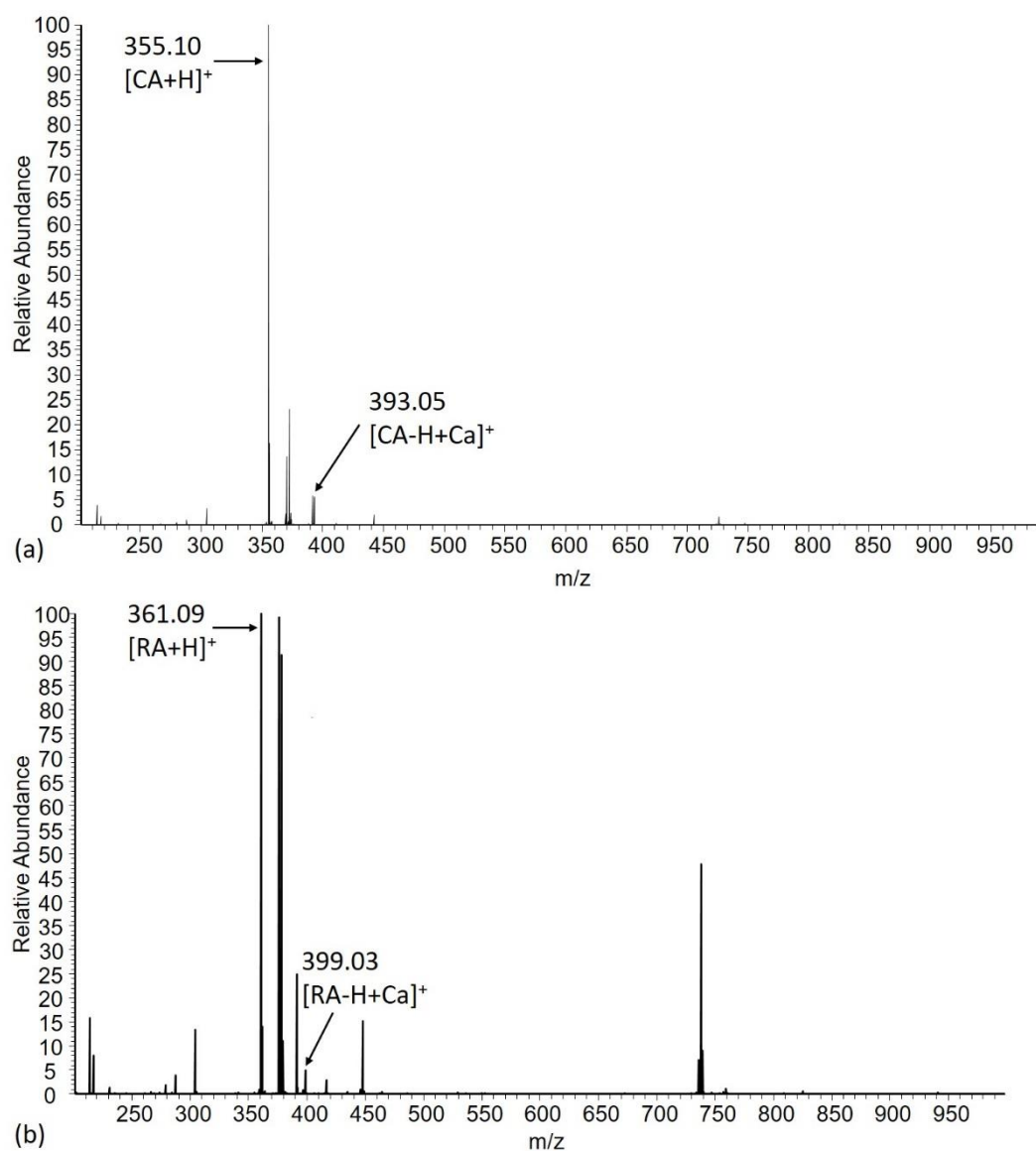
for RA, except that the 290 nm band intensity decreases to a limited extent only while the 365 nm shoulder varies more significantly with time.

From these data, one could hypothesize that calcium ions interact with CA and RA. Such interactions affect several bands of the UV-visible spectra, indicating that the chromophore part of the molecules, *i.e.* the caffeic group, is involved in the reaction. The decrease in the intensity of the bands in the 250-350 nm range and the increased intensity of the 390 nm band in the presence of calcium could indicate a deprotonation event. This, and the appearance of a new band at 600 nm, is therefore in favor of the formation of a BAM-Ca<sup>2+</sup> complex involving the catechol ring. However, because carboxylic acids of CA and RA are not conjugated to the caffeic moiety, their possible involvement in such a complexation cannot be put aside.

#### 2.4.3.1.2 Electrospray mass spectrometry

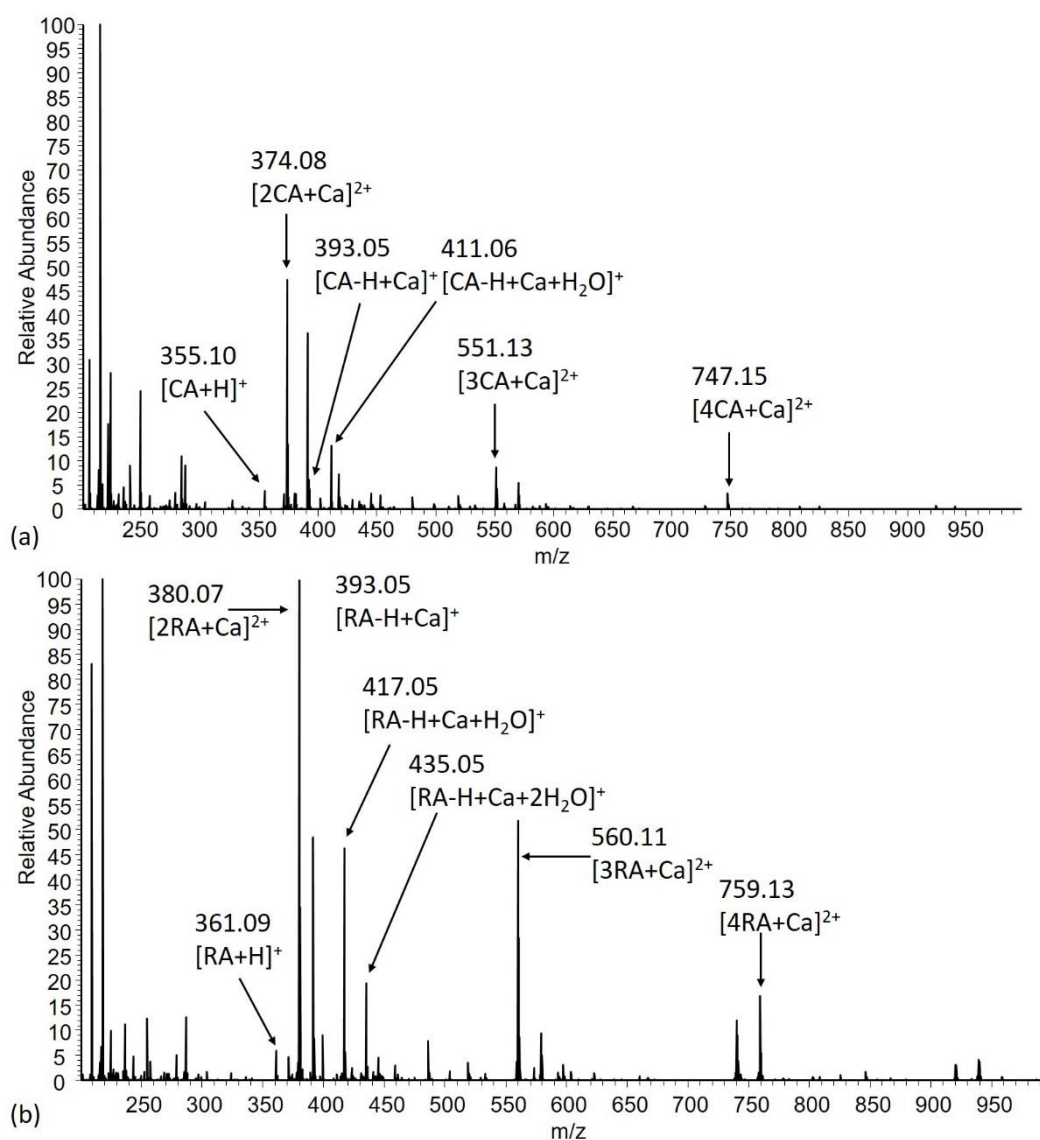
Electrospray ionization mass spectrometry (ESI-MS) has previously shown to provide direct evidence for the formation of the complexes based upon the masses and fragmentation ions of the complex<sup>11,31</sup>. The presence of calcium-BAM complexes was thus investigated by ESI-MS in positive mode. **Figure 2.5** shows mass spectra of equimolar solutions of BAMs with calcium at pH 7.8 in ammonium carbonate buffer. Rosmarinic acid and chlorogenic acid spectra exhibit the peak corresponding to the protonated molecule, at  $m/z$  361.09 ([RA+H]<sup>+</sup>) and 355.10 ([CA+H]<sup>+</sup>), respectively, as the main peak. In addition, [BAM-H+Ca]<sup>+</sup> species were detected for CA and RA at  $m/z$  394.10 and 393.05, respectively, with a significant intensity ( $\approx 5$  % of that of the main peak). Additional peaks on **Figure 2.5 (a) and (b)** can be attributed to RA or CA species associated with ammonium.

Complementary studies were conducted at pH 5 in ultrapure water allowed the detection of additional peaks - compared to that identified at pH 7- that can be assigned to BAM/Ca<sup>2+</sup> complexes (**Figure 2.6**). In details,  $m/z$  380.07 and  $m/z$  374.08 ascribed to [2RA+Ca]<sup>2+</sup> and [2CA+Ca]<sup>2+</sup>, respectively, are the main peaks found in an equimolar solution of CaCl<sub>2</sub> and rosmarinic acid or chlorogenic acid, respectively. In these conditions, additional ions at  $m/z$  417.05 and  $m/z$  411.06 corresponding to [RA-H+Ca]<sup>+</sup> and [CA-H+Ca]<sup>+</sup>, respectively are also formed as well as their mono hydrated adducts (+nH<sub>2</sub>O). Complexes with more than two BAM per calcium ion are also found at  $m/z$  560.11 and 759.13 ([3RA+Ca]<sup>2+</sup> and [4RA+Ca]<sup>2+</sup>) and  $m/z$  551.13 and 747.15 ([3CA+Ca]<sup>2+</sup> and [4CA+Ca]<sup>2+</sup>). Stability of the monomolecular and bimolecular complexes formed at pH 5 was estimated by the calculation of CE<sub>50</sub>, *i.e.* the energy required to dissociate 50 % of the original complex. Monomolecular complexes formed by deprotonated RA and CA and one calcium have a similar stability, with a CE<sub>50</sub> of 13 eV and 12 eV, respectively Bimolecular complexes involving one calcium ion are of comparable stability with CA (11 eV) but much less stable with RA (5.6 eV).



**Figure 2.5** MS spectra of chlorogenic **(a)** acid and rosmarinic **(b)** acids with calcium (AM/Ca = 1) at pH

7.8



**Figure 2.6** MS spectra of chlorogenic acid **(a)** and rosmarinic **(b)** acids with calcium (BAM/Ca = 1) at pH 5

Altogether, MS data confirm that at pH  $\approx 7$ , calcium ions can form complexes with CA and RA. Moreover, in acidic conditions, a much wider range of complexes are formed. Noticeably, monomolecular complexes have a similar stability for the two BAMs, which would suggest that the catechol ring, that is present on both CA and RA, are mainly involved in their formation. In contrast, the stability of the bimolecular complexes is very different for the two BAMs, which would suggest that carboxylate groups are also involved in  $\text{Ca}^{2+}$  coordination.

#### 2.4.3.1.3 NMR spectroscopy

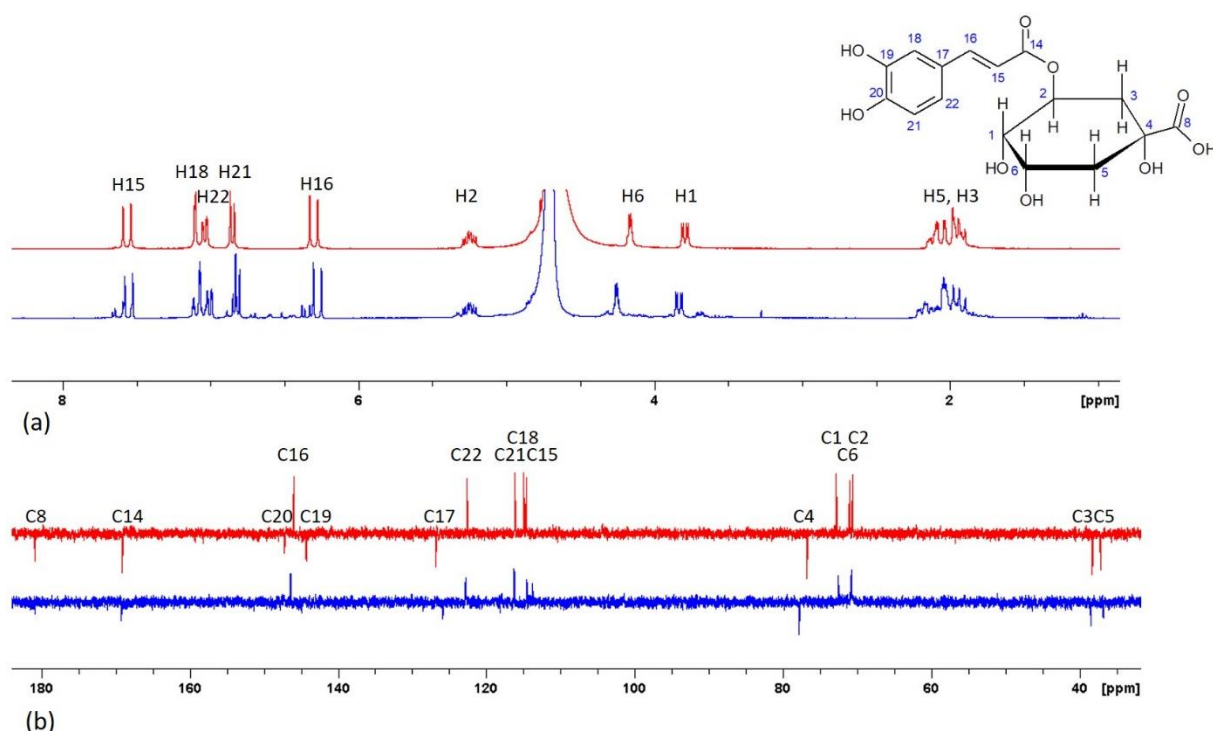
NMR spectroscopy was performed in order to gather more information on potential complexation site between BAM and calcium<sup>13,17,32</sup>. We studied solutions of calcium and BAM with a ratio BAM:Ca = 0.1, as this is the ratio where effects of complexation are visible on the UV-Vis absorption spectra. <sup>1</sup>H and <sup>13</sup>C NMR spectra of CA and RA without or with calcium were recorded in D<sub>2</sub>O at pH 7, and corresponding chemical shifts were assigned in comparison with literature<sup>33–35</sup>.

For CA, H2 was the only proton not affected by the presence of calcium (**Figure 2.7**). Aromatic and vinylic protons were shifted up-field, while protons from the quinic part of the molecule were shifted low-field. A complexation of calcium at the carboxylic acid site leading to an electron-withdrawing effect on the adjacent carbons of the quinic moiety of CA, can explain the up-field shift of the corresponding protons. In parallel, a deprotonation/complexation at the catechol site of the molecule could explain the low-field shift of aromatic and vinylic protons. Indeed, a facilitated deprotonation of one hydroxyl group complexed with calcium would induce a positive mesomeric effect along the conjugated moiety of the molecule.

<sup>13</sup>C NMR studies confirmed the presence of the two complexation sites. Mesomeric effect to the conjugative part of the molecule lead to the shifting low-field of carbons in ortho and para positions compared to the deprotonated hydroxyl, and the shifting up-field of meta position. High low-field shift (1.06 ppm) of C4 is a sign for the complexation around the carboxylate, that we can assume to be between the hydroxyl group of C4 and hydroxyl group of C8 (4-hydroxy-8-hydroxy site), which is consistent with the fact that this site is commonly mentioned as a site of complexation for metals on CA<sup>36</sup>.

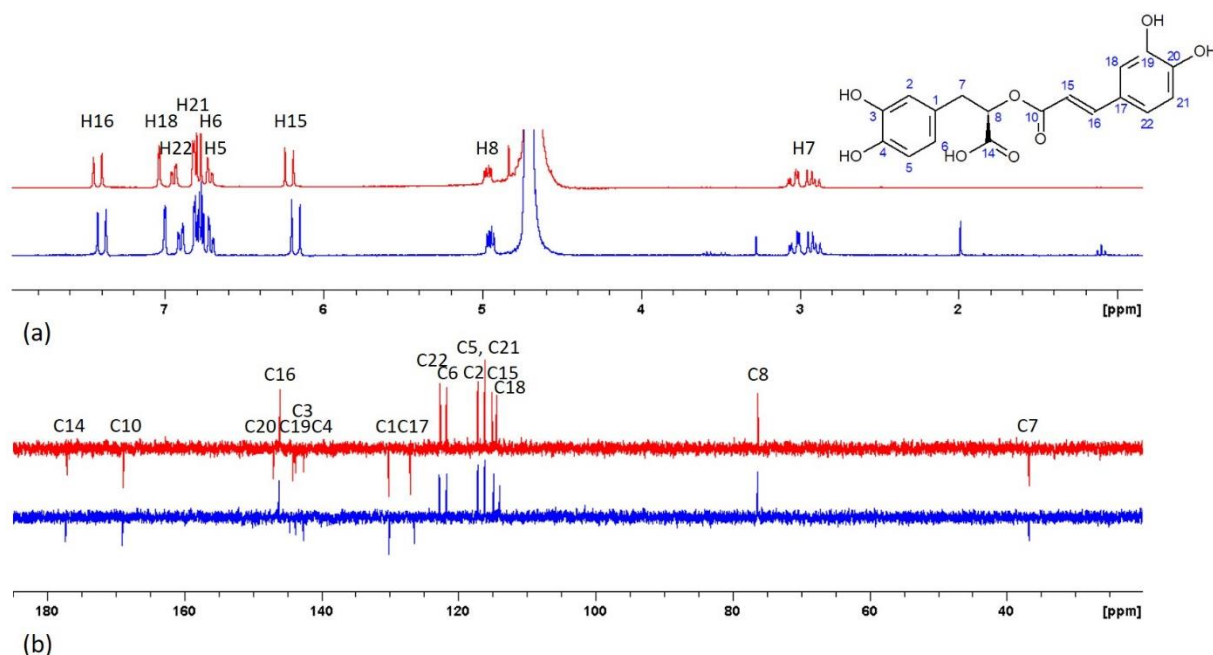
It is noteworthy that intensity of both C20 and C19 as well as C8 signals were strongly decreased, which could sign for the complexation on the catechol or on the carboxylate groups. However, such modifications could also be induced by some relaxation issues, so that they cannot unequivocally be assigned to a complexation process.





**Figure 2.7**  $^1\text{H}$  (a), and  $^{13}\text{C}$  (b) NMR spectra of chlorogenic acid pure (red line) and in presence of calcium,  $\text{CA}/\text{Ca} = 0.01$  (blue line)

$^1\text{H}$  spectrum of RA in presence of calcium was calibrated assuming that H7 is not affected by the complexation. With such an assumption, all vinylic and aromatic protons were shifted up-field while chemical shift of H8 is identical to the one without calcium (**Figure 2.8**). Complexation would therefore preferably take place on one or the other of catechol sites. In the  $^{13}\text{C}$  spectrum, C19 was shifted down-field (+0.4 ppm), in line with a possible complexation on the catechol site, further confirmed by the observed high up-field shifting of C17 and C18 (-0.57 and -0.45 ppm, respectively) that could be explained by a mesomeric effect, and to a lower extent to the shift of the vinylic carbons. Some modifications of the C3-C4 catechol signal was also observed, but to a lesser degree (only 0.06 ppm shift). Finally, a 0.2 ppm shift of C14 signal was observed, which could be an indication the carboxylate group could also be involved in the complexation, although this hypothesis is not confirmed by  $^1\text{H}$  NMR results.

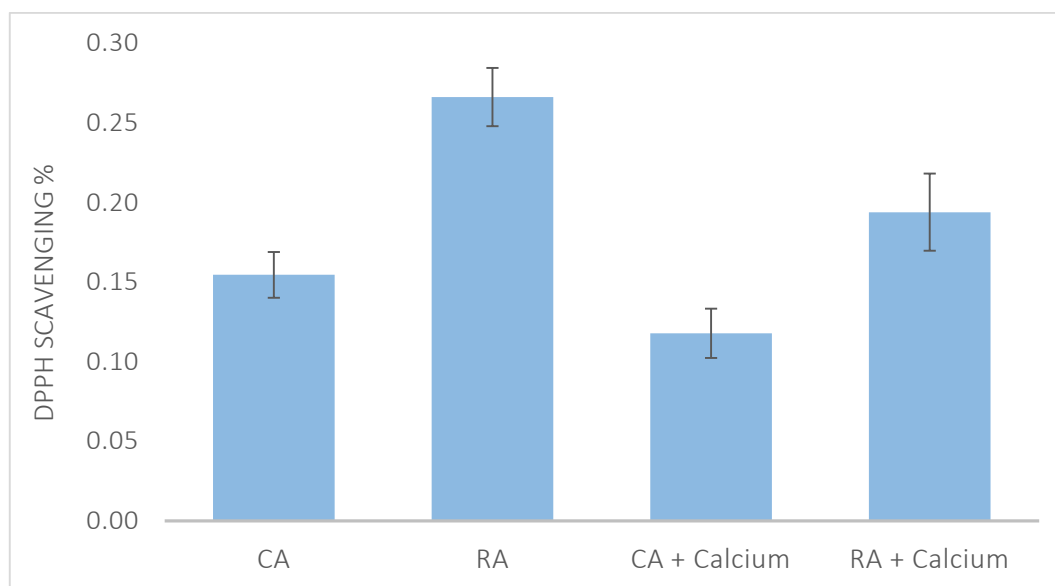


**Figure 2.8**  $^1\text{H}$  (a), and  $^{13}\text{C}$  (b) NMR spectra of rosmarinic acid pure (red line) and in presence of calcium, RA/Ca = 0.01 (blue line)

Altogether, NMR studies suggest that both catechol and carboxylate groups may act as binding sites for calcium for both BAM at pH 7, although the former seems highly favored for RA.

#### 2.4.3.2 Effect of complexation upon antioxidant activity

The effect of calcium chelation on antioxidant activity was assessed according to the DPPH radical scavenging method (**Figure 2.9**), for 0.1 molar ratio (BAM/Ca). Rosmarinic acid is the best antioxidant molecule, with a DPPH bleaching percentage of 27 %, followed by chlorogenic acid (13.6%). The presence of calcium does not affect the antioxidant activity of chlorogenic acid, while the DPPH bleaching percentage is decreased by 29 % for RA. Antioxidant activity is recognized in the literature<sup>37</sup> to arise from the oxidation potential of hydroxyl groups, namely the catechol ones for RA. Therefore, the effect of the presence of calcium on the antioxidant activity of RA designates the catechol as the preferential site for the complexation. Conversely, as there is no effect of the complexation on the antioxidant activity for chlorogenic acid, it could be assumed that the catechol group is less involved in complexation for CA and thus that the carboxylate could be the preferred site of complexation.



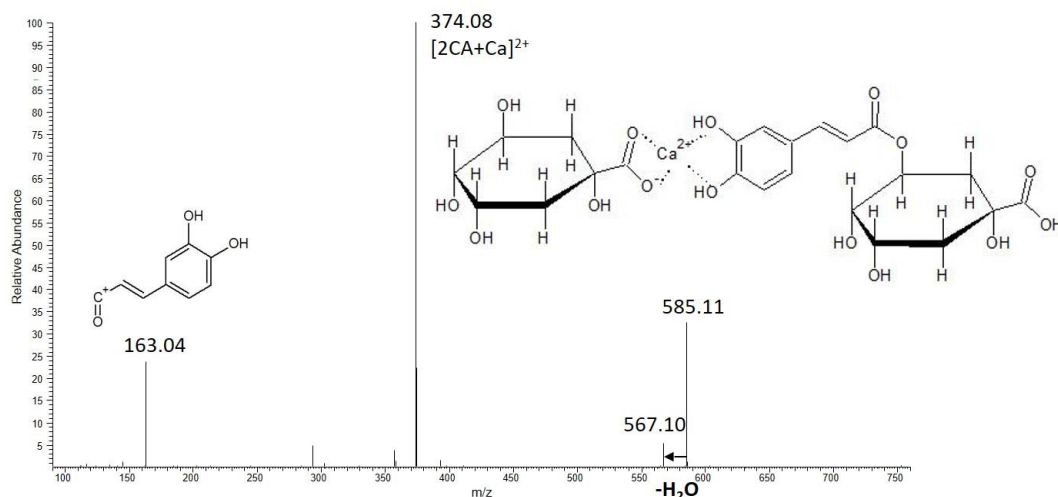
**Figure 2.9** Antioxidant activity of BAM alone or in presence of calcium (molar ratio BAM/Ca 0.1)

#### 2.4.3.3 Discussion

UV-visible spectroscopy analysis of chlorogenic acid and rosmarinic acid in the presence of calcium ions near neutral pH have evidenced modification of the intensity of several absorption bands and appearance of an additional one, suggesting that complexation does occur and is correlated with partial deprotonation of the catechol ring. However, because the carboxylate groups of both BAMs are not conjugated with the caffeic moiety, this technique did not allow us to conclude on the possible involvement of these groups in the complexation reaction. MS studies confirmed that both molecules can form mononuclear complexes with calcium near neutral pH and evidenced that, at pH 5, multimolecular complexes could also be obtained. The difference in stability of the bimolecular complexes formed with CA and RA suggested that carboxylate groups could also be involved in calcium complexation. Finally,  $^1\text{H}$  and  $^{13}\text{C}$  NMR indicated that both catechol and carboxylate groups could interact with calcium at pH 7, although the later appears significantly more efficient in CA than in RA.

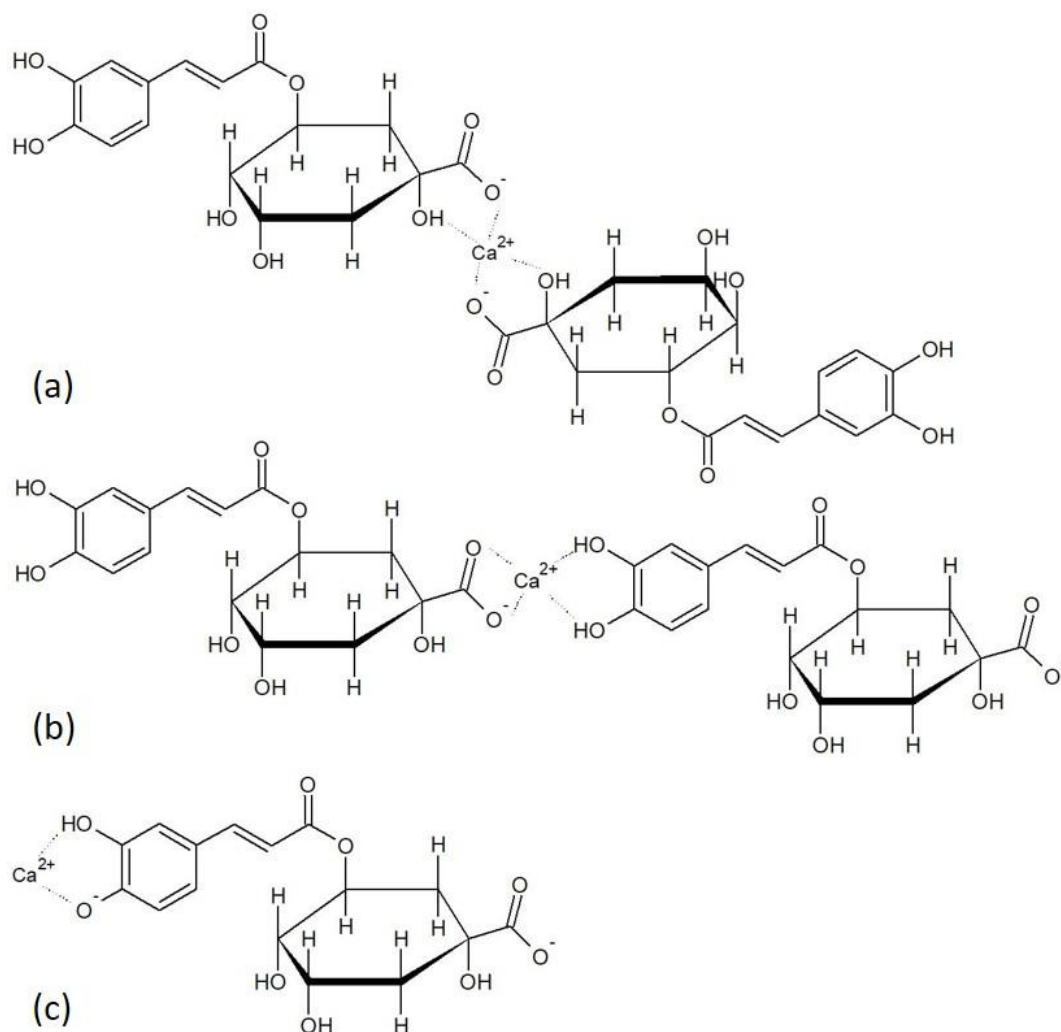
In the case of chlorogenic acid, Cornard *et al.* have shown that carboxylate is first involved in the complexation of  $\text{Pb}^{2+}$  ions, followed by the catechol<sup>29</sup>. For quinic acid, i.e. one of the structural moiety of chlorogenic acid, it is known that two polyol sites : the 1-hydroxy-6-hydroxy and the 4-hydroxy-8-hydroxy<sup>36</sup> are likely to chelate metals. In our study, we noticed that the behavior of the molecule regarding calcium ion is different at pH 5 and pH 7.8 in ammonium carbonate buffer. At pH 5, when carboxylate is deprotonated several complexes are detected with ESI-MS, but  $[\text{2CA}+\text{Ca}]^{2+}$  and  $[\text{CA}-\text{H}+\text{Ca}]^+$  are the more intense ones. Additional fragmentation experiments performed for  $[\text{2CA}+\text{Ca}]^{2+}$  showed the formation of two ions following the hydrolysis of the ester function: (i) a complex constituted by one CA, the calcium ion and the quinic moiety of the second CA, and (ii) the

caffeic acid part of the second CA (**Figure 2.10**). Calcium would therefore be complexed on the quinic acid part of the molecule, meaning on the carboxylate or on the 4-hydroxy-8-hydroxy site, as shown on **Figure 2.11 (a)**. It is also possible that one molecule chelates the calcium by one of these sites, and the other by the catechol (**Figure 2.11 (b)**).



**Figure 2.10** MS/MS spectrum of chlorogenic acid with calcium (CA: Ca = 1),  $m/z = 374.08$

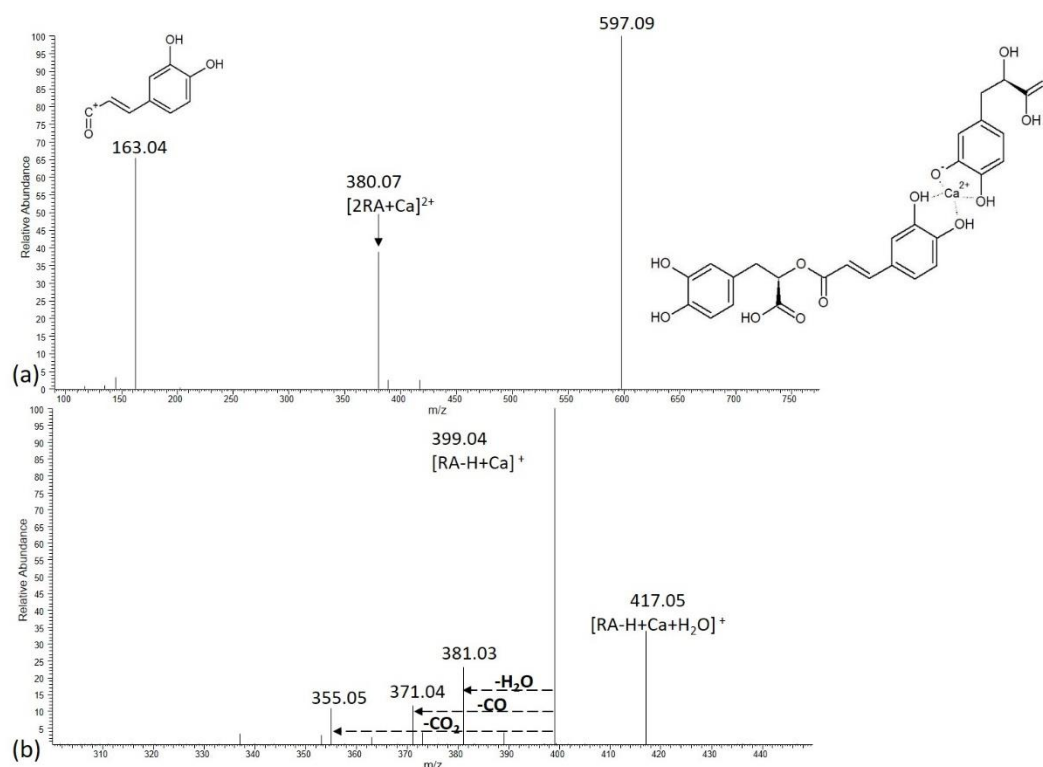
Unlike what happens at pH 5, only the  $[CA-H+Ca]^+$  complex is formed at pH 7.8. The shoulder at 410 nm on UV-Vis absorption spectra in presence of calcium indicates a modification similar to deprotonation that becomes less important at high calcium proportion. This suggests a preferred complexation on the catechol ring, as it starts to be deprotonated at this pH ( $pK_a = 9.38$ ) (**Figure 2.11 (c)**). This is consistent with NMR studies that showed the shift of protons and carbons signals from the caffeic part of the molecule, close to the catechol. Even if visible, the shift of carbons and protons NMR peaks from the quinic part of the molecule are less intense than for the caffeic part. Additional complexation on the carboxylate or on the 4-hydroxy-8-hydroxy site is indeed in line with the slight observed modifications of UV-Vis spectrum at high calcium content. We can also note that calcium coordination at the 1-hydroxy-6-hydroxy is very unlikely, as no clear shift of protons and carbons NMR signals on 1 and 6 positions is observed. At pH 7.8, the calcium complexation does not modify the antioxidant activities of chlorogenic acid. This suggests that the polyol cycle of the quinic acid moiety is involved in the antioxidant activity, even if the catechol is involved in complexation.



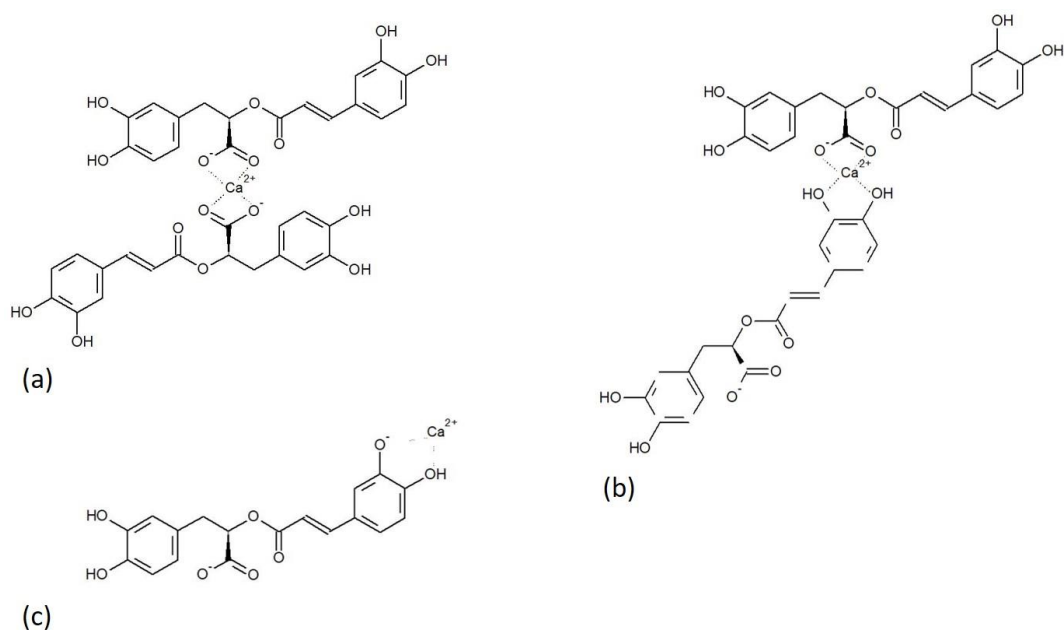
**Figure 2.11** Calcium complexation by chlorogenic acid at pH 5 (a) and (b), and pH 7.8 (c)

Behavior of rosmarinic acid with calcium depending of pH and medium conditions is quite similar to chlorogenic acid, as their structures are close. Three sites are possible for chelation, two catechols and the carboxylate. Among the several complexes that can be formed at pH 5, as shown by ESI-MS experiments, the two main ones are  $[2\text{RA}+\text{Ca}]^{2+}$  and  $[\text{RA}-\text{H}+\text{Ca}]^+$ . Fragmentation of  $[2\text{RA}+\text{Ca}]^{2+}$  leads to the formation of two ions resulting from the hydrolysis of the ester function of RA (**Figure 2.12**). The first one is composed by one RA molecule chelating  $\text{Ca}^{2+}$  with the (3,4 dihydroxyphenyl) lactic acid part of a second RA. The second fragmentation ion consists of the caffeic part of the second molecule. In this complex, the calcium can be located either on the carboxylate or on the catechol C3-C4 of the first molecule, and either on the carboxylate or on one or the other catechol for the second, as shown in **Figure 2.10** (a), (b). Moreover the fragmentation of  $[\text{RA}-\text{H}+\text{Ca}]^+$  indicates the loss of  $\text{H}_2\text{O}$ ,  $\text{CO}$  and  $\text{CO}_2$ , i.e. the loss of the carboxylate (**Figure 2.12**), suggesting that the calcium is not complexed by the carboxylate. Chelation with a stoichiometry 1-1 would therefore occur preferentially on the catechol C19-C20 (on the caffeic part of RA), as it is the one with the lower pKa (**Figure 2.13** (c)).

Moreover, this complex is the only one that can be formed at pH 7.8, and NMR studies at this pH show that the complexation is more likely to occur on this site. Indeed, all peaks for protons corresponding to one or the other aromatic cycle are shifted, but those of carbons C19-C20 are more shifted than C3-C5.  $^{13}\text{C}$  NMR study also reveals that the carboxylate is involved at this pH, with the shift of C14 peak. From UV-Vis absorption studies at pH 7.8 in presence of calcium we know that calcium complexation induces a modification of the spectrum similar to deprotonation, which is less important at high calcium dosages. In conclusion, the complexation at pH 7.8 is more likely to take place on the catechol C19-C20, and the carboxylate is involved only if the concentration of calcium rises. Effects on the antioxidant activity, which is lowered in presence of calcium, strengthens this hypothesis. Unlike for chlorogenic acid, only two catechols of RA are responsible for the antioxidant activity so the complexation of one of them should have a strong effect on the antioxidant activity of the molecule.



**Figure 2.12** MS/MS spectrum of rosmarinic acid with calcium (RA: Ca = 1), (a) m/z = 380.07, (b) m/z = 399.04



**Figure 2.13** Calcium complexation by rosmarinic acid at pH 5 (a) and (b); and pH 7.8 (c)

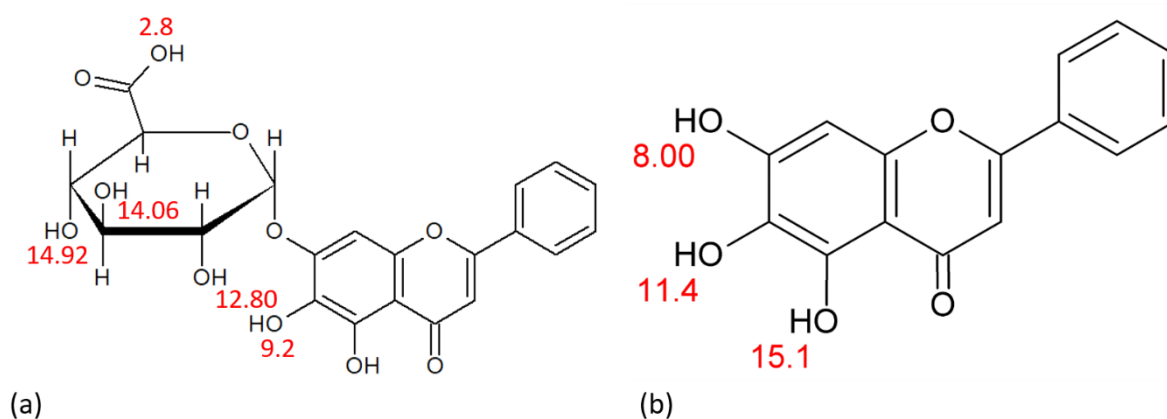
#### 2.4.4 Conclusion

The ability of two natural polyphenols, chlorogenic acid and rosmarinic acid to chelate calcium ions and the impact of such a complexation on their anti-oxidant activity was studied. Complexation was found highly pH-dependent, with monomolecular complexes formed at neutral pH and bimolecular complexes at acidic pH. Monomolecular complexes formed with deprotonated molecules possess the best stability. Both catechol and carboxylate groups are able to act as binding sites for calcium. Only the antioxidant activity of rosmarinic acid was decreased in the presence of calcium, due to the inactivation of the catechol moiety. Considering that calcium level in blood is ca. 1 mM, such interactions may play a role in bio-availability and in vivo efficiency of both rosmarinic and chlorogenic acid

## 2.5 Stability of baicalin and baicalein at different pH and effect on calcium complexation

### 2.5.1 Introduction

Baicalin (BA) and baicalein (BE) (**Figure 2.14**) are two flavonoids extracted from the root of the plant *Scutellaria baicalensis*. As mentioned in the literature review ([Chapter 1](#)), they are interesting for their antibacterial and antioxidant activity. However, several papers<sup>38,39</sup> mentioned their degradation *in vivo*, supposedly via an oxidation process, by analogy with the well-characterized oxidation of others flavonoids (quercetin, fisetin)<sup>40–42</sup>. The final product of degradation of both molecules has not been yet undoubtedly identified. Nevertheless, the degradation was found to be very sensitive to pH, temperature and presence of other flavonoids in solution. In this chapter, we will study the fate of BA and BE at pH 5 and pH 7.8. UV-Vis spectroscopy was used, because both molecules are two colored molecules. We also performed electrospray mass spectrometry (ESI-MS) to determine the molecular mass of the product in solution as well as their potential product of degradation. We were able to propose a scheme for the degradation and oxidation of baicalin and baicalein. With the oxidation of BE and BA in mind, we studied their interaction with calcium at pH 5 and pH 7.8, with the same characterization techniques. The effect of interaction with calcium on the biological activity of baicalein and baicalin was also investigated.



**Figure 2.14** Molecular structures with pKa (calculated with ADC iLab software) of baicalin (a) and baicalein (b)

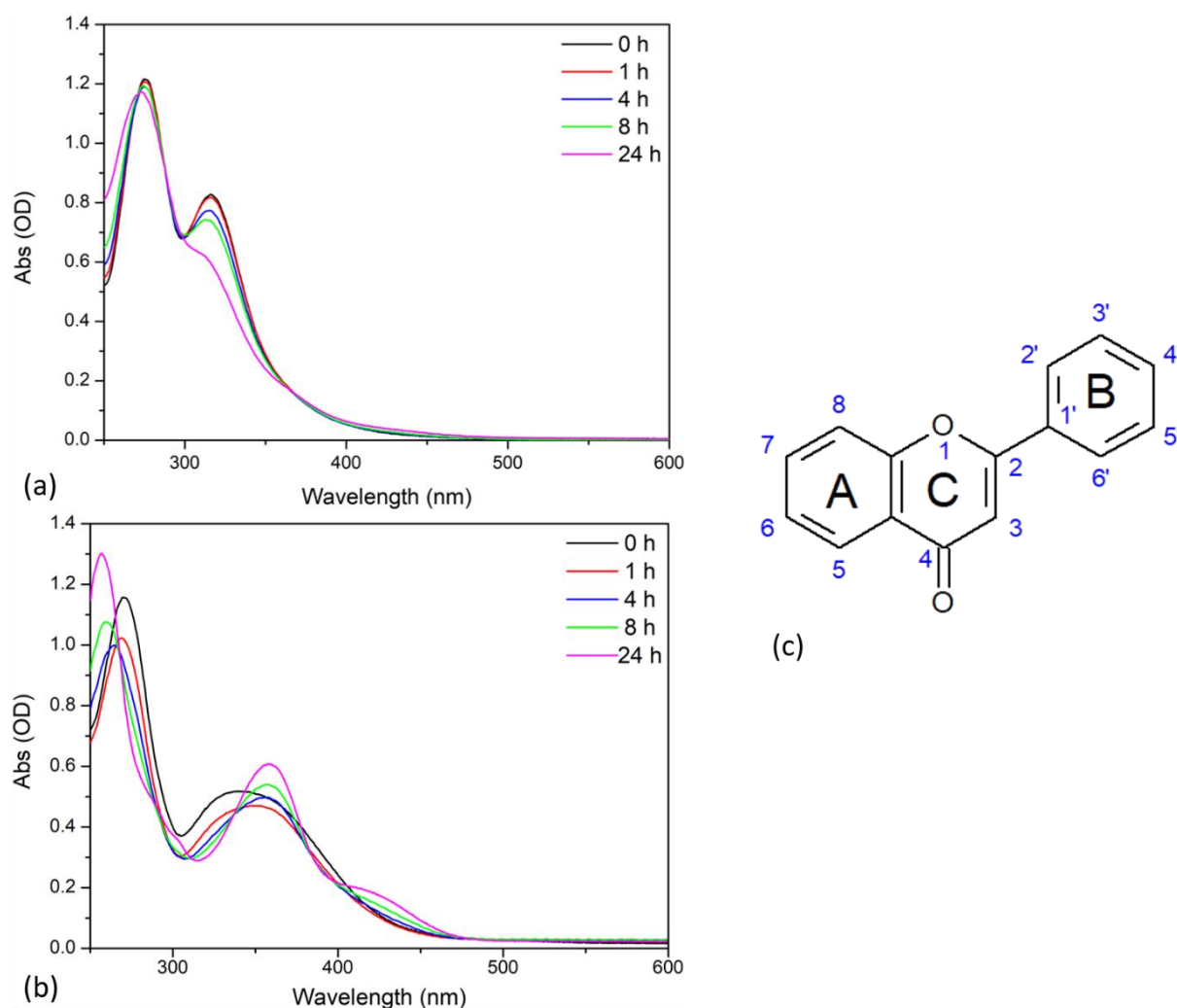


## 2.5.2 Stability of baicalin and baicalein at different pH

### 2.5.2.1 UV-visible spectroscopy

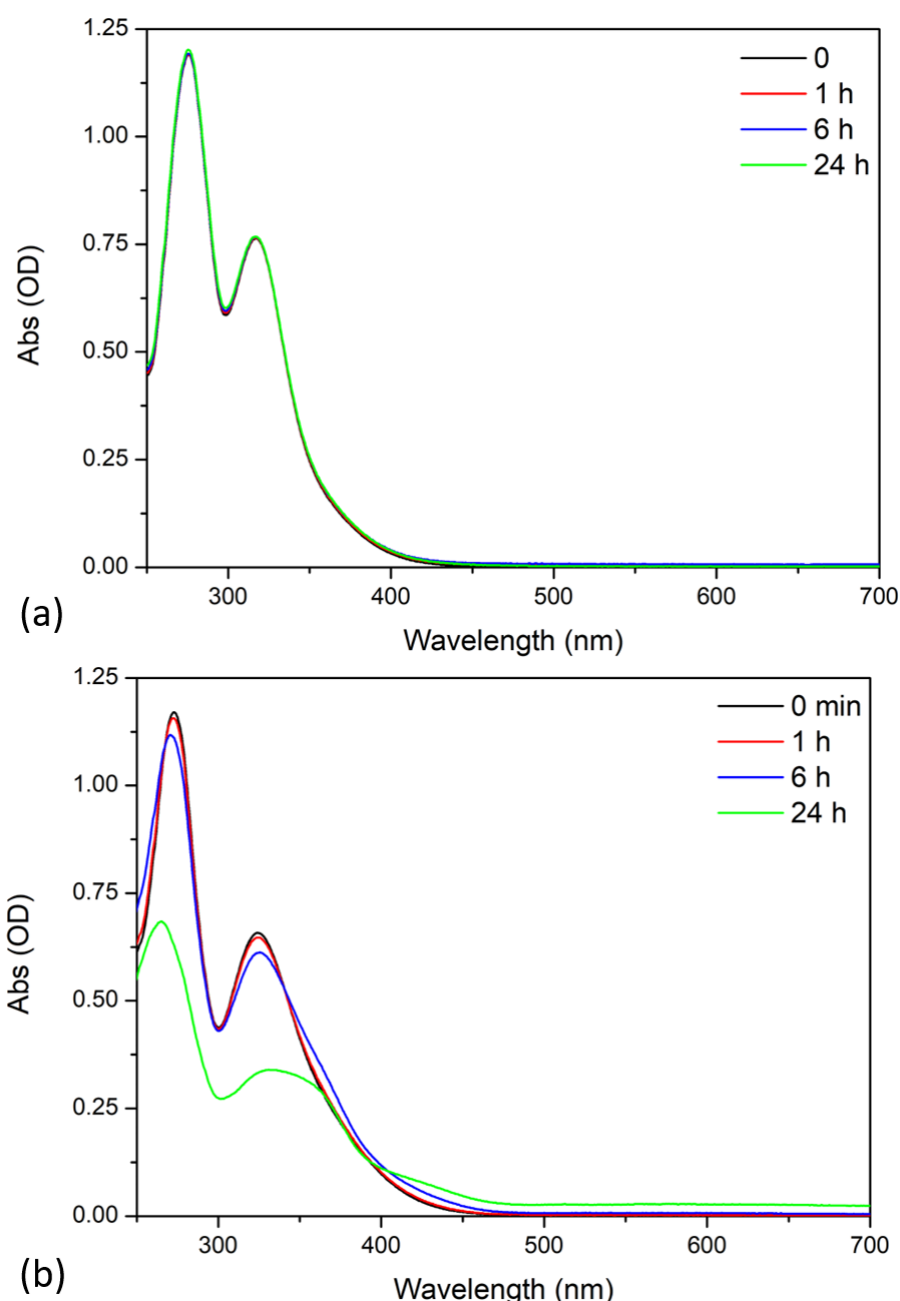
As the literature reports that baicalin and baicalein are likely to undergo degradation in aqueous solution<sup>38</sup>, their stability was assayed over time in phosphate buffer at pH 7.2. Neutral pH was chosen because it is representative of the physiological pH, *i.e.* conditions where BA and BE biological activity is relevant. In freshly-prepared solutions, both BA and BE UV-visible spectra (**Figure 2.15**) exhibit two main bands positioned at 275 and 316 nm, and 271 and 340 nm, respectively, in accordance with literature data. Indeed, flavones are reported to show two major absorption bands in the UV-visible region<sup>1,12,43</sup>, band I and II. Band I, in the range of 300–400 nm, arises from the absorption of B-ring conjugated with carbonyl of ring C (cinnamoyl system, see **Figure 2.15 (c)**). Band II, between 240–300 nm, is related to conjugated system between ring A and carbonyl of ring C (benzoyl system, see **Figure 2.15 (c)**). Z.S. Markovic et al<sup>1</sup> published an experimental UV spectrum of BE at pH 7 with two main peaks at 264 and 359 nm, which is consistent with our observations.

At pH 7.2, the BA spectrum remained unchanged after one hour at pH 7.2. Then, a slight blue-shift of band II was observed after more than 4 hours in solution, while band I intensity progressively decreased with time. After 24 hours, band I was only a shoulder. On BE spectrum, a clear blue shift of the band II over time was observed from 271 to 257 nm on BE spectrum (**Figure 2.15 (b)**). Simultaneously, band I was shifted towards longer wavelengths from 340 to 360 nm after 24 hours in solution, giving simultaneous rise to a new adsorption band whose intensity is higher after 24 h than the one of the initial BE band I. Moreover, an additional shoulder was observed around 420 nm. These modifications over time were very slightly visible after a 1 hour-old BE solution. It could therefore be concluded that even if BE was slightly less stable than BA, both molecules remains unchanged in solution after one hour at pH 7.2. Further experiments as a function of pH were consequently performed with solutions initially prepared for less than one hour.



**Figure 2.15** Stability of baicalin (a) and baicalein (b) as a function of time in 0.1 M PBS pH 7.2, at a concentration of  $50 \mu\text{mol.L}^{-1}$ , and structure of flavonoids (c)

It is commonly found in the literature that BE and BA are more stable at acidic pH<sup>38</sup>. UV-Vis spectra of BE and BA at pH 5 in ultrapure water was monitored, and displayed in **Figure 2.16**. Spectrum of baicalin at this pH remained unchanged over time. On the contrary to BA, the BE spectrum evolved during the time of experiment. Band I is shifted to 265 nm after 24 hours. Band II is shifted from 324 to 325 nm besides the appearance of a shoulder at 365 nm after 6 hours. After 24 hours, a new shoulder is visible at 438 nm. Absorption intensity slightly decreased from 0 to 6 hours, and drastically between 6 and 24 hours. It can thus be concluded that baicalein is unstable at pH 5 in ultrapure water, although the degradation kinetics is slower than at pH 7.2. BA is stable over 24 hours in ultrapure water at pH 5.



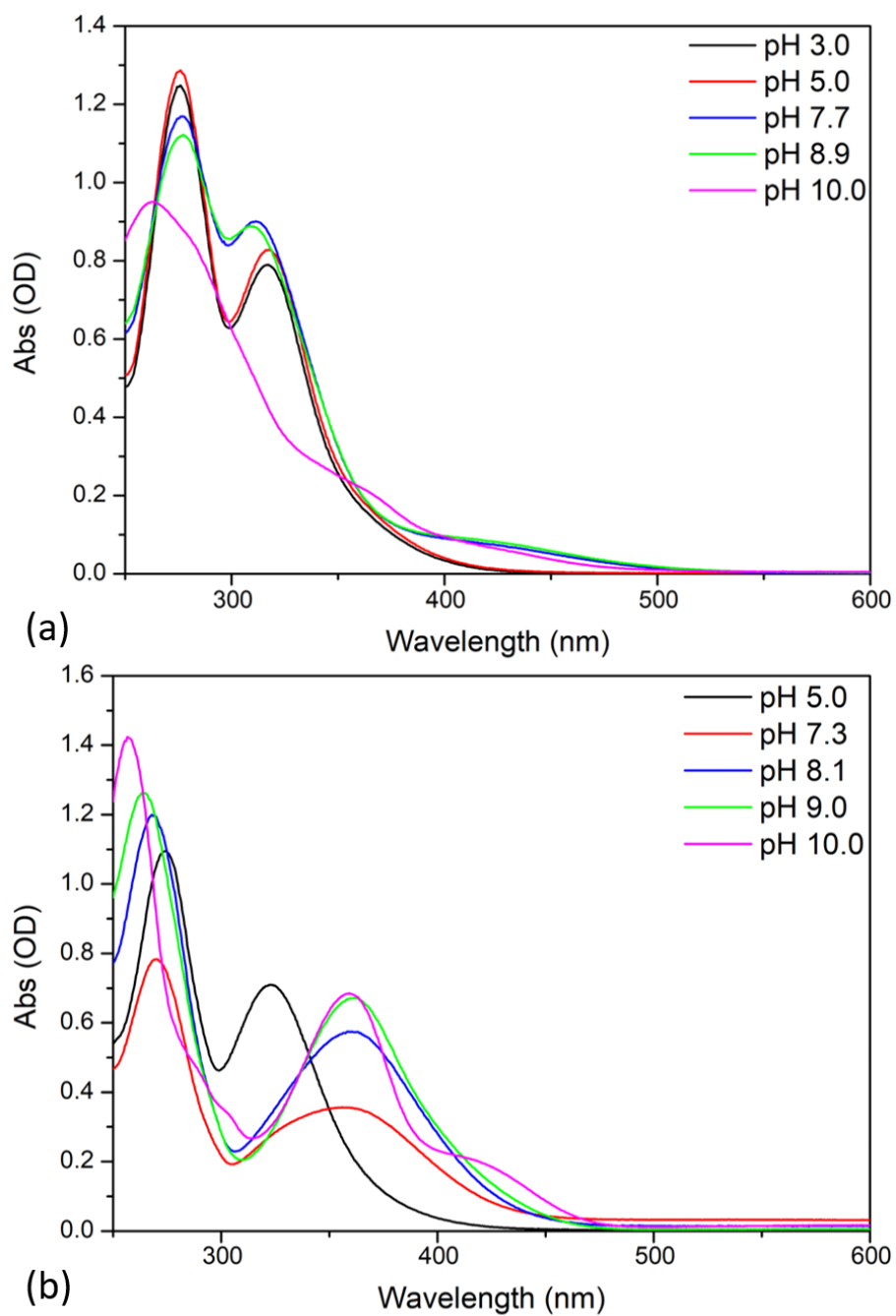
**Figure 2.16** Stability of baicalin (a) and baicalein (b) as a function of time in ultrapure water, at a concentration of  $50 \mu\text{mol.L}^{-1}$

The evolution of UV-Vis spectra of BA and BE were recorded more systematically as function of pH. For baicalin (**Figure 2.17 (a)**), an increase of the pH clearly led to the collapse of band I (317 nm) above pH 7 while band slightly decreases II (276 nm) in intensity. In addition, a new band with a maximum at 432 nm appears, which could sign for the deprotonation of the catechol with the lowest pKa that is 9.2 (**Figure 2.14** Molecular structures with pKa (calculated with ADC iLab software) of baicalin (a) and baicalein (b). For baicalein (**Figure 2.17 (b)**), band II (274 nm) undergoes a progressive slight red-shift while band I (323 nm) shifts towards longer wavelengths ( $\Delta\lambda \approx 50 \text{ nm}$ ), according to the

supposed facilitated deprotonation of catechol<sup>12</sup>. A new shoulder near 450 nm is observed at pH 10. Deprotonation of the carboxylic acid of BA is not visible on the UV-Vis absorption spectra, although its pKa was calculated at 3.8. This is consistent with the assumption that the glycosidic part of BA is not conjugated with rings A and C.

We have to be very careful with the interpretation of the evolution of UV-Vis spectra as a function of pH because of the degradation of both molecules at  $\text{pH} \approx 7$ . For baicalin, we know that the degradation starts after 4 hours at neutral pH. Consequently, we can assume that spectra recorded within 1 hour at pH 5 and 7.2 can be compared on the basis of pH evolution. In case of baicalein however, the degradation takes place before 4 hours. It is therefore difficult to assign the evolution of the UV-Vis spectrum only to the rise of the pH. We are probably looking at two events at the same time, the evolution due to pH, and the degradation of the molecule.

To conclude, baicalin and baicalein are both unstable in aqueous solution, with different kinetics. Baicalin is stable at acidic pH, and starts to be degraded after 4 hours at  $\text{pH} \approx 7$ . Baicalein is degraded at neutral pH within 1 hour, while at pH 5 the degradation has been evidenced only 6 hours after solubilization of the molecule. We have thus to be careful while studying events involving baicalein because of its quick degradation in aqueous medium. Further experiments as a function of pH were consequently performed with solutions prepared for less than one hour.



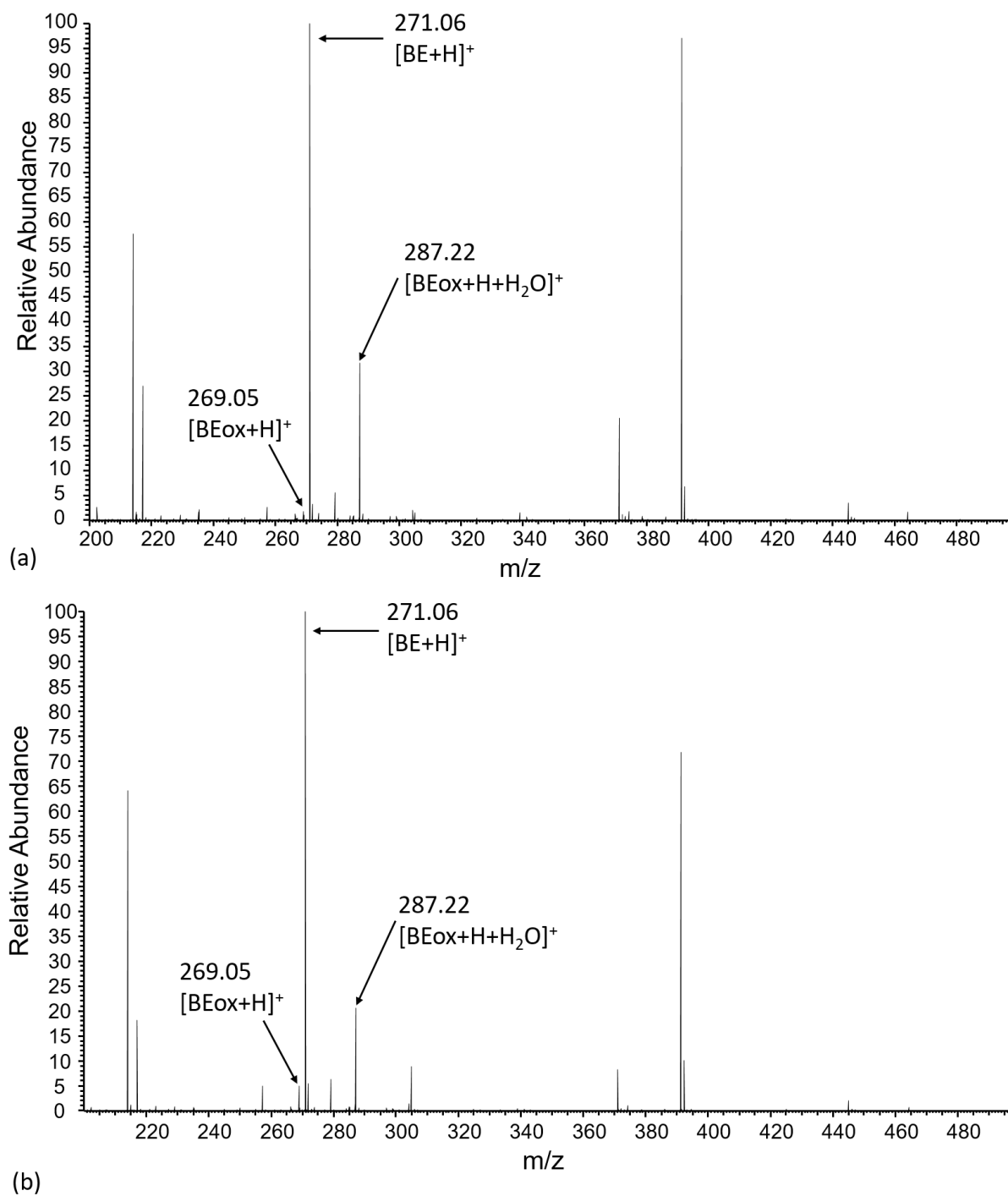
**Figure 2.17** UV-Visible spectra of (a) baicalin and (b) baicalein at different pHs, BAM concentration 50  $\mu\text{mol.L}^{-1}$

### 2.5.2.3 Mass spectrometry

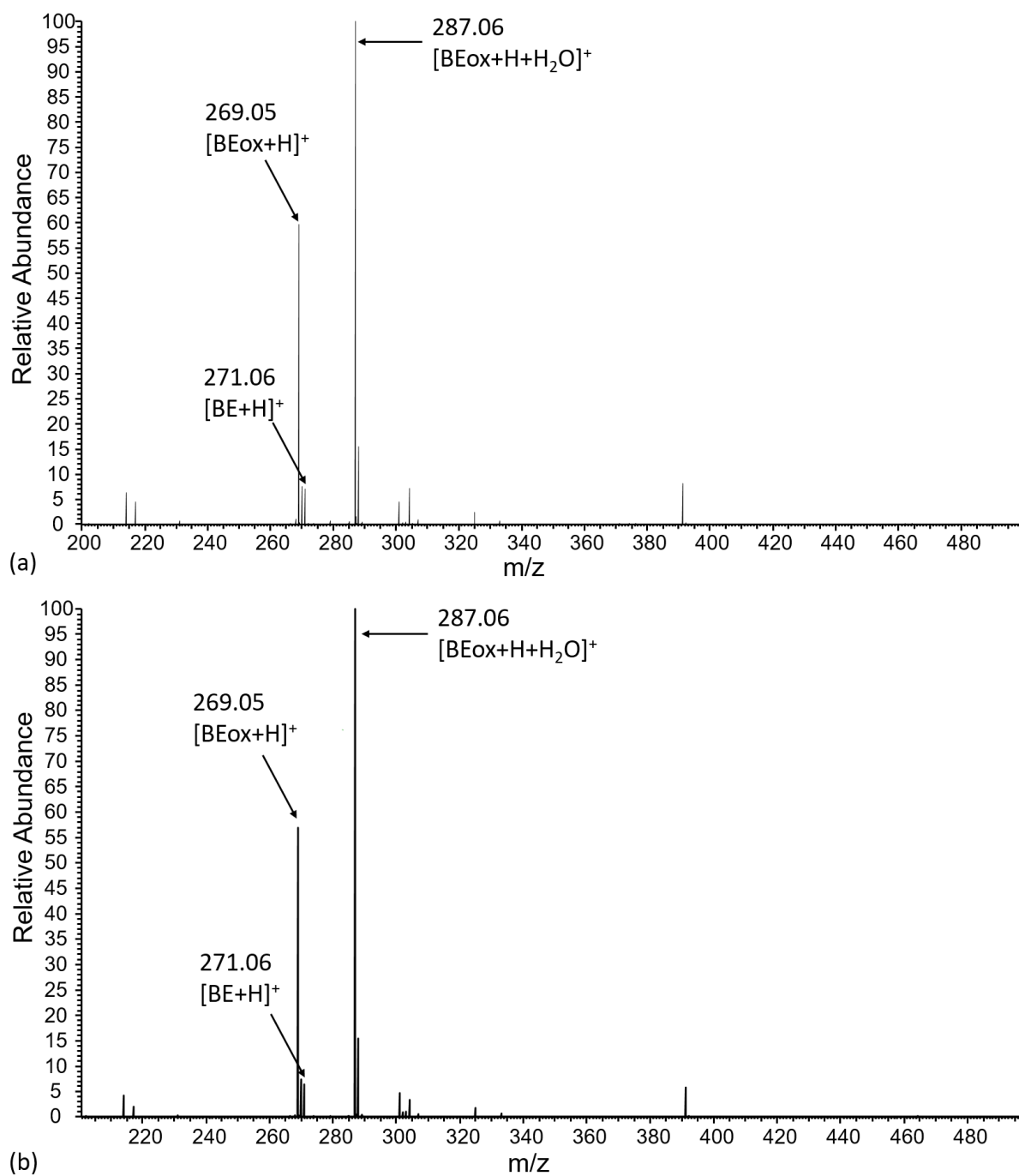
The degradation of baicalein was studied by electrospray mass spectrometry (ESI-MS) in positive mode, at pH 5 in ultrapure water and pH 7.8 in ammonium bicarbonate buffer  $(\text{NH}_4)_2(\text{HCO}_3)$ . Baicalein was solubilized at  $0.01 \text{ mol.L}^{-1}$  in methanol before the dilution in water or buffer at  $50 \text{ }\mu\text{M}$ . ESI-MS experimental parameters were the same than presented in paragraph 2.4.2.2. Mass spectra were recorded shortly after preparation of BE solution or 20 hours later.

**Figure 2.18** presents mass spectra at pH 5. Shortly after preparation (**Figure 2.18 (a)**), the main peak is detected at  $m/z$  271.06, corresponding to a protonated adduct of baicalein  $[\text{BE}+\text{H}]^+$ . Besides this peak, a peak with low relative abundance is present at  $m/z$  269.05, ascribed to a molecule of baicalein that would have lost two protons. The hydrated adduct of this molecule is also found at  $m/z$  287.22, with a higher relative abundance, suggesting that the modified BE is more stable when hydrated. Spectrum after 20 hours (**Figure 2.18 (b)**) is very similar. The only difference is the relative abundance of the peak at  $m/z$  269.05 that is slightly higher than in **Figure 2.18 (a)**. Spectra at pH 7.8 are presented in **Figure 2.19**. The same peaks than in pH 5 are present, with different relative abundances. The main peak is at  $m/z$  285.05 that corresponds to adduct of BE that would have lost two protons and  $\text{H}_2\text{O}$ . No difference between the two spectra are visible, meaning that the degradation of the molecule in ammonium carbonate buffer at pH 7.8 occurs within the time of preparation of the solution and injection in mass spectrometer.

Overall, three peaks are detected for BE, with relative abundance depending on the pH of the solution. The degradation of the molecule corresponds to the loss of two protons, and the degraded molecule seems to be stabilized by one molecule of  $\text{H}_2\text{O}$ . With data from UV-Vis spectroscopy, we assumed that the degradation takes place at the catechol level. A loss of two protons is consistent with this assumption, as BE can lose protons only on hydroxyl groups. An oxidation of the catechol group in a quinoic derivative could explain the loss of two protons, as it is presented in **Figure 2.20**. This is in accordance to the work of Xing *et al.*<sup>40</sup> dealing with the degradation process of baicalin (BA) at pH 9.0. ESI-MS results confirm the quick degradation of BE in ammonium carbonate buffer, as the oxidation takes place within few minutes. We can also notice the presence of the oxidized molecule at pH 5, even shortly after the preparation of the solution, whereas in this condition the UV-Vis spectrum of BE remains unchanged.

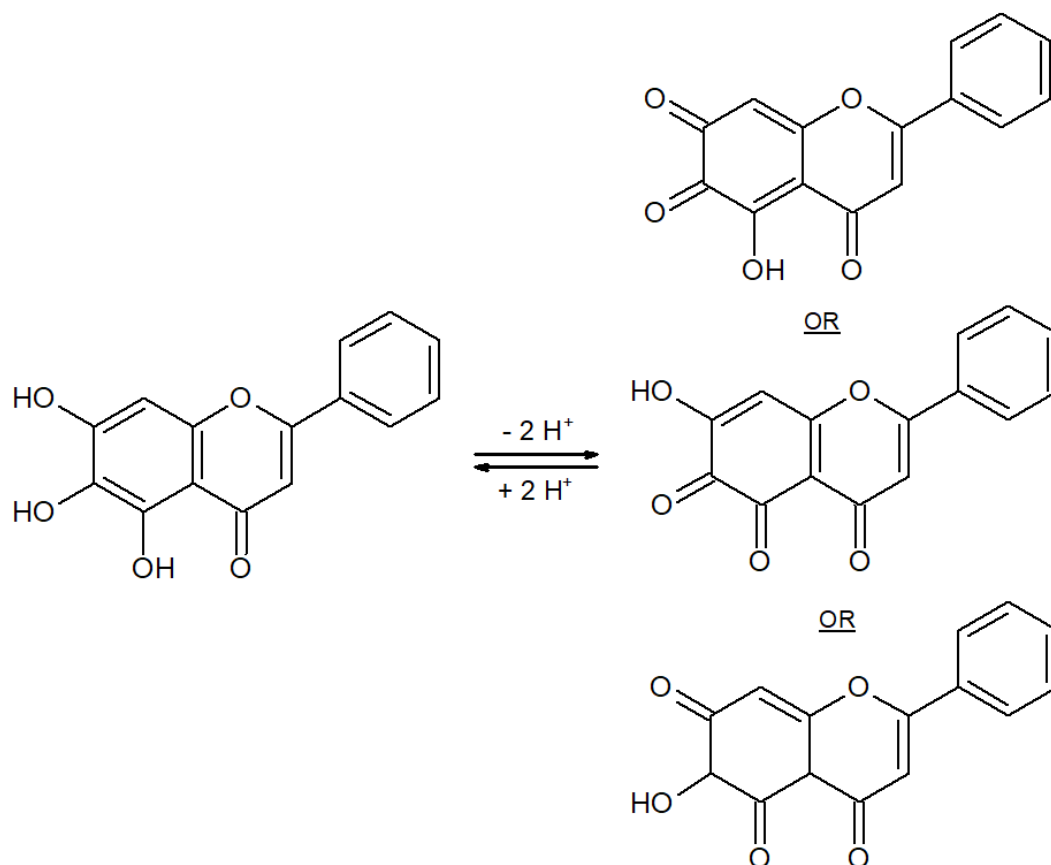


**Figure 2.18** ESI-MS spectra of baicalein in ultrapure water at pH 5 shortly after preparation of the solution (a) and 20 hours after (b). BE concentration = 50  $\mu$ M



**Figure 2.19** ESI-MS spectra of baicalein in 1 mM ammonium carbonate buffer ( $(\text{NH}_4)_2(\text{HCO}_3)$ ) at pH 7.8 shortly after preparation of the solution (a) and 20 hours after (b). BE concentration = 50  $\mu\text{M}$





**Figure 2.20** Proposed oxidation scheme of baicalein

## 2.5.3 Interactions with calcium

### 2.5.3.1 Spectroscopic and spectrometric measurements

#### 2.5.3.1.1 UV-Vis spectroscopy

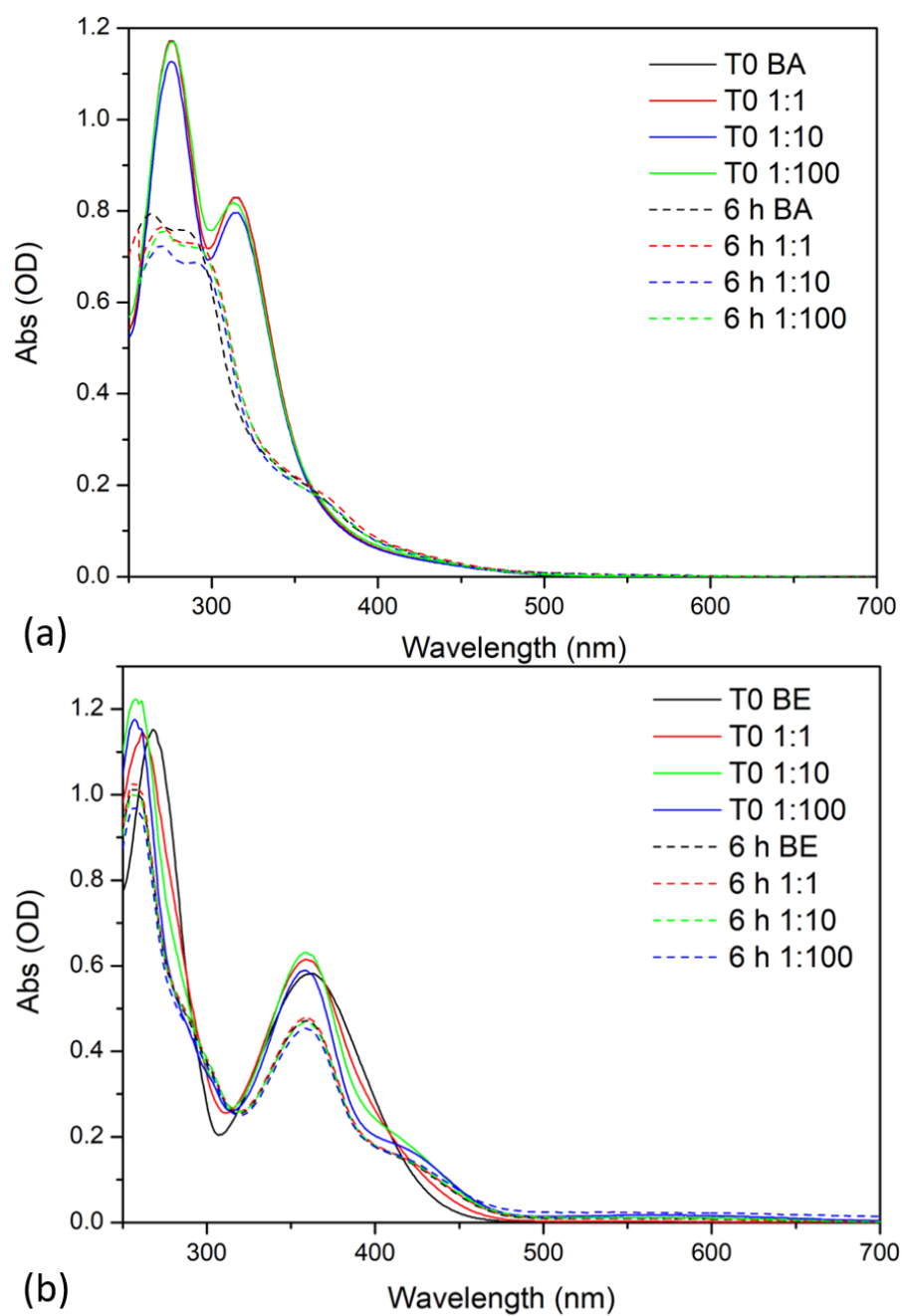
As we intended to investigate the antimicrobial and anti-oxidant properties of flavonoids, the study of complexes formation between BAM and calcium was performed near physiological pH, at pH 7.8 in our experiments. **Figure 2.21** displays the UV-vis absorbance spectra of mixtures of BE or BA and calcium chloride at three different BAM:Ca molar ratios 1, 0.1 and 0.01 recorded in ammonium carbonate buffer, immediately after mixture and 6 hours later.

In the case of BA (**Figure 2.21 (a)**), the presence of  $\text{Ca}^{2+}$  at pH 7.8 does not modify the UV-visible spectrum shortly after the addition of calcium, whatever the BA/Ca ratio tested. After 6 h, spectra are very similar to the one obtained for pure baicalin at pH 10 without calcium, with a drop of the intensity of main absorption band. However, this effect cannot be related to calcium complexation, as the evolution is the same for pure baicalin and baicalin in presence of calcium whatever the BA/Ca ratio. Given the evolution of UV-Vis spectrum of BA at pH 7.8 after 8 hours, we can assume that the degradation is pH-dependent, but also buffer-dependent. Indeed, the degradation at pH 7.2 in

phosphate buffer involves only a shift of band II near 270 nm within 8 hours (see **Figure 2.15 (a)**). In ammonium bicarbonate buffer at pH 7.8, the degradation is quicker, occurring within 6 hours, with a more important modification of the UV-Vis spectrum. The degradation is similar to a deprotonation, which could be related to an event at the catechol group in ring A.

For BE (**Figure 2.21 (b)**), there is a clear effect of presence of calcium immediately after its addition with a red-shift of the 270 nm peak and the emergence of the 420 nm band that are both enhanced as the BAM:Ca decreases, suggesting the transitory formation of specific complexes. After 6 h, no further band II shift is observed but the overall spectra intensity decreases while a shoulder appears at 293 nm. This modification is not dose-dependent as the spectra are identical whatever the BAM/calcium ratio tested mixtures. Given the degradation of BE at pH 7.2 in phosphate buffer (**Figure 2.15 (b)**), after 6 hours, we are probably only looking at the degradation of the molecule, with no effect of the presence of calcium. We can also notice that the spectrum of the degraded molecule is similar to the one of BE at pH 10. Degradation has the same effect than deprotonation, suggesting an event at the catechol site.

To conclude, we tried to observe a complexation between calcium and BE or BA at pH 7.8 in ammonium carbonate buffer. As for baicalin, no effect of interaction with calcium was visible, neither at short-term nor at long-term. After 6 hours, the only event is the degradation of the molecule that we assumed to be quicker at pH 7.8 in ammonium carbonate buffer than in phosphate buffer at pH 7.2. For baicalein, a modification of the UV-Vis spectrum on the short-term for molar ratio BE/Ca 1:10 and 1:100 suggests an interaction with calcium. However, after 6 hours, the degradation of the molecule overwhelmed any interaction with calcium. For both molecules, the degradation indices the same modification of the UV-Vis spectrum than the one observed when increasing pH, thzt was interpreted as a deprotonation.



**Figure 2.21** UV-Visible spectra of baicalin (a) and baicalein (b) with calcium at pH 7.8 in 1mM of buffer  $(\text{NH}_4)_2(\text{CO}_3)$  immediately after mixture and after 6 hours. BAM concentration 50  $\mu\text{M}$ ; molar ratios are expressed regarding BAM: Ca concentration

## 2.5.3.1.2 Mass spectrometry

The complexation with calcium was investigated by ESI-MS in positive mode, at pH 5 and pH 7.8. Equimolar solutions of BA or BE with calcium at 50  $\mu$ M were prepared in ultrapure water or ammonium bicarbonate buffer. ESI-MS spectra of BA and BE in presence of calcium at pH 5 are presented in **Figure 2.22 (a)** and **(b)** respectively.

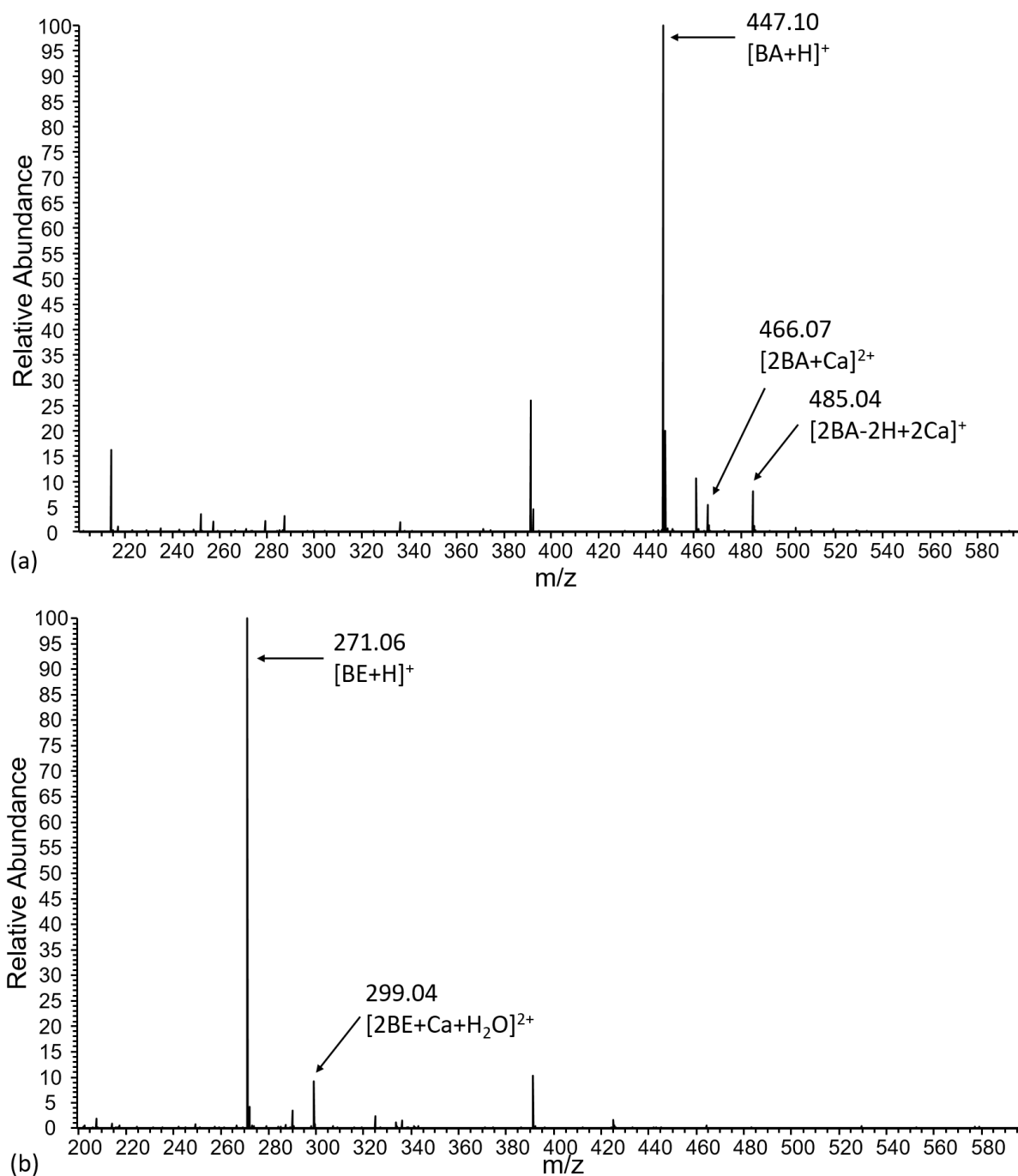
For baicalin, in addition to the peak of the protonated molecule at  $m/z$  447.10, two peaks are observed, at  $m/z$  466.07 with  $z = 2$  and at  $m/z$  485.04 with  $z = 1$ . The first peak corresponds to a complex  $[2BA+Ca]^{2+}$  with a 2 : 1 stoichiometry (BA:Ca) and the second to a complex  $[2BA-2H+2Ca]^+$  with a 2 : 2 stoichiometry (BA:Ca). This latter complex could be formed by two deprotonated baicalin, or by a fully protonated baicalin and an oxidized form of the molecule, as it was observed for baicalein.

For baicalein, the main peak is the protonated molecule at  $m/z$  271.06, as observed before. Another peak is observed at  $m/z$  299.04 with  $z = 2$ . This peak corresponds to the adduct  $[2BE+Ca+H_2O]^{2+}$ . Overall, both baicalin and baicalein are able to form complexes with calcium at pH 5. Stability of complexes was estimated by the calculation of  $CE_{50}$ , the necessary energy to dissociate 50 % of the complex. For BA, an intermediate value is obtained for  $[2BA+Ca]^{2+}$  (9.0 eV) whereas the complex formed by two deprotonated BA (or one BA and one BAox) and two calcium ions  $[2BA+2Ca-2H]^+$  was found more stable (11.4 eV). Note that such a calculation was not possible for  $[2BE+Ca+H_2O]^{2+}$  as this complex was detected in very low amount and revealed to be highly unstable.

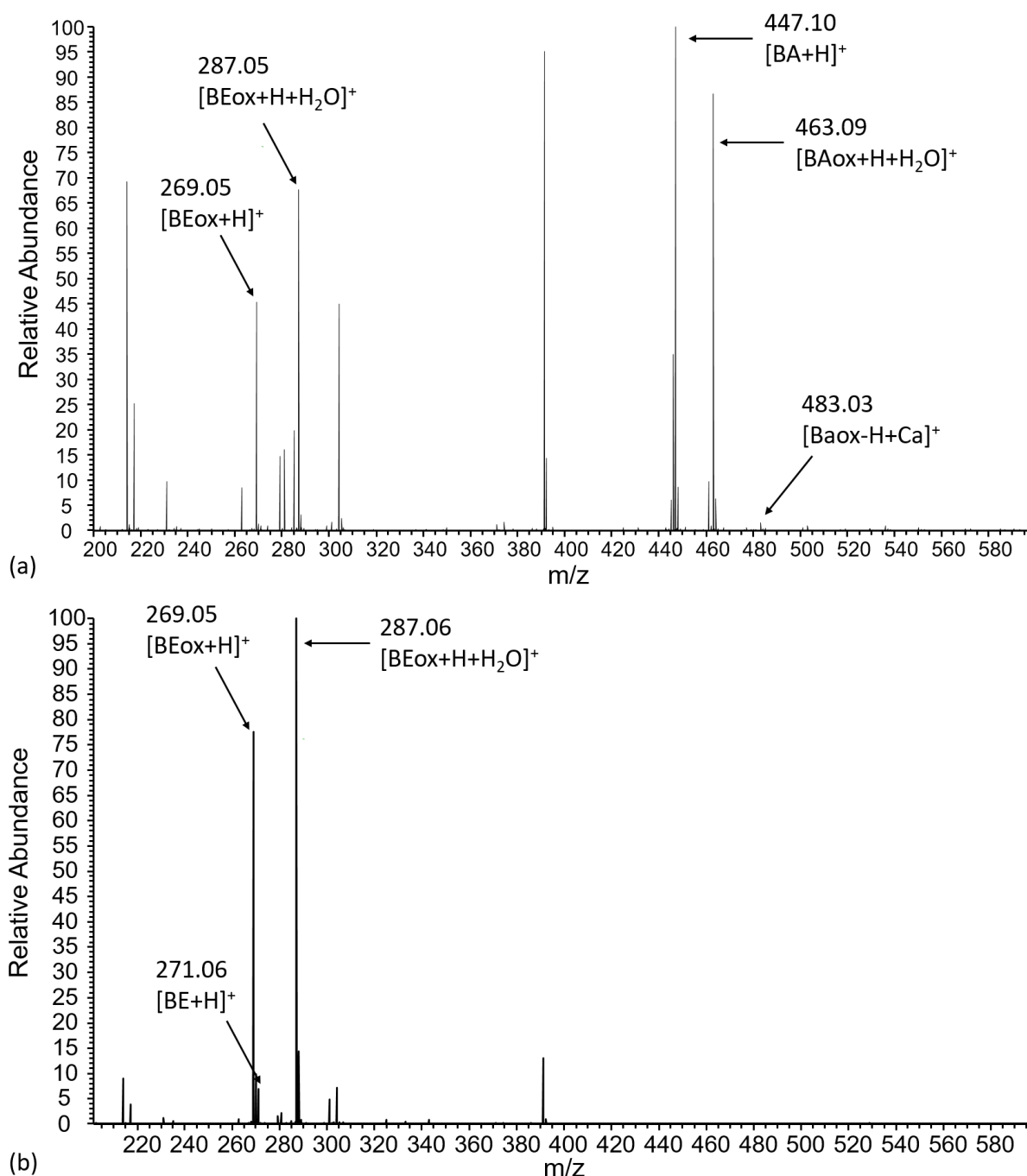
At pH 7.8, baicalin exhibits only one peak corresponding to a complex with calcium, with a very low relative abundance, at  $m/z$  483.03 (**Figure 2.23 (a)**). It corresponds to a complex formed with calcium and BA that lost two protons, in other words an oxidized BA. The complex would have the formula  $[BAox-H+Ca]^+$ . Other peaks in the spectrum are assigned to the protonated molecule at  $m/z$  447.10 ( $[BA+H]^+$ ), an hydrated adduct of the oxidized molecule at  $m/z$  463.09 ( $[BAox+H+H_2O]^+$ ), and two peaks corresponding to oxidized BE at  $m/z$  269.05 and 287.05 ( $[BEox+H]^+$  and  $[BEox+H+H_2O]^+$ , respectively). This is in agreement with the fact that baicalin is unstable at pH 7.8, and that the sugar moiety is hydrolyzed during degradation, as suggested by Xing *et al.*<sup>40</sup> On the ESI-MS spectrum of baicalein at pH 7.8 (**Figure 2.23**), no peak corresponding to a complex between BE or its oxidized form with calcium is detected. The same three peaks that were observed on the ESI-MS spectrum of BE at pH 7.8 without calcium are detected:  $[BE+H]^+$ ,  $[BEox+H]^+$  and  $[BEox+H+H_2O]^+$ , at  $m/z$  271.06, 269.06 and 287.22 respectively.

Overall at pH 7.8, the oxidation process strongly decreases the calcium-binding efficiency of BA and BE. Oxidized BA seems to be unstable, as its final products of degradation ( $BEox+H$ )<sup>+</sup> and

([BEox+H+H<sub>2</sub>O]<sup>+</sup>) are observed in large quantity. The oxidized molecule is only stabilized by adduct with water or calcium.



**Figure 2.22** ESI-MS spectra of baicalin (a) and baicalein (b) in ultrapure water at pH 5 in presence of calcium at ratio BAM/Ca = 1:1. BAM concentration = 50  $\mu$ M

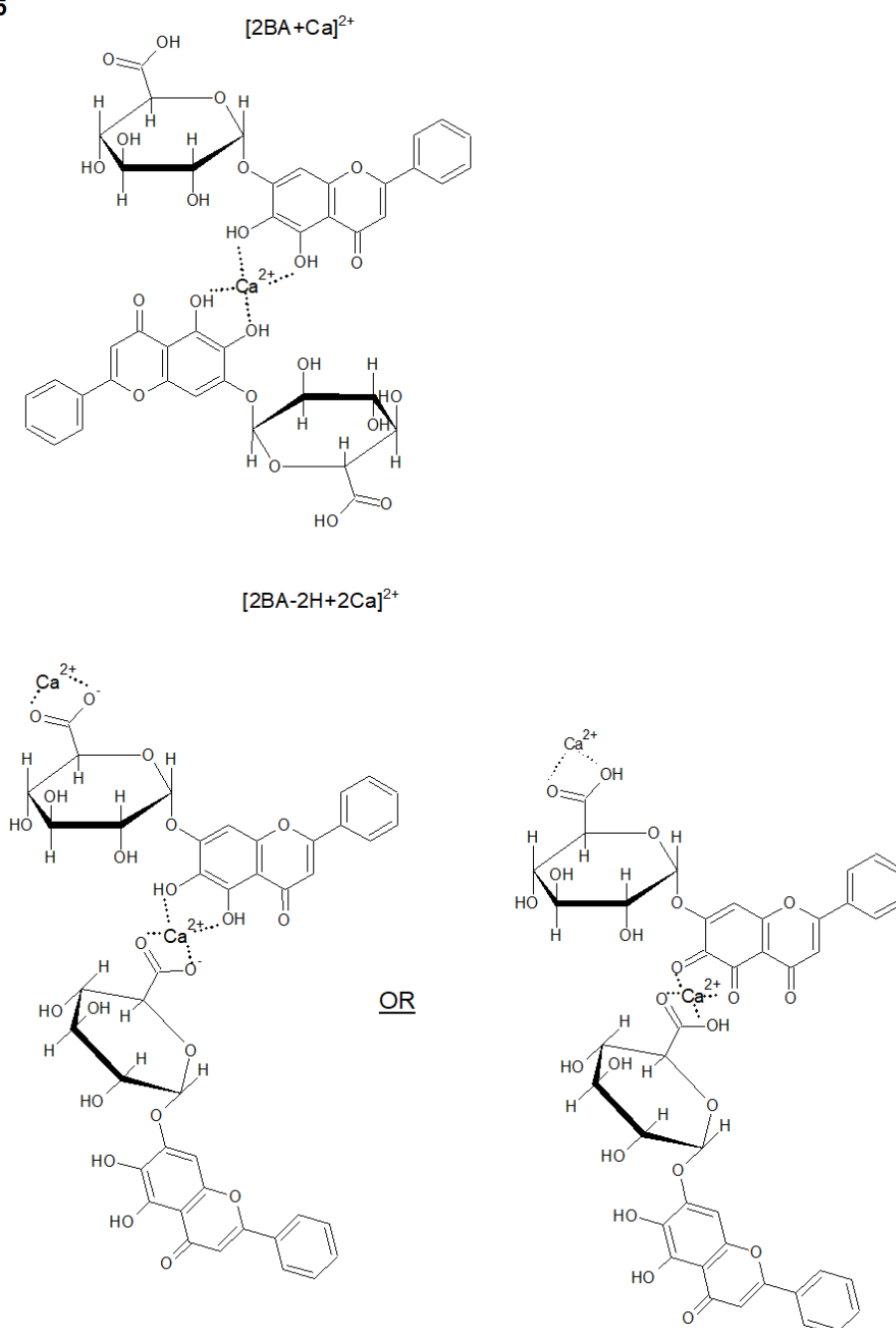


**Figure 2.23** ESI-MS spectra of baicalin (a) and baicalein (b) in ammonium bicarbonate buffer at pH 7.8 in presence of calcium at ratio BAM/Ca = 1:1. BAM concentration = 50  $\mu$ M

To conclude, the complexation with calcium is pH-dependent and varies with the oxidation of BA and BE. At pH 5, BA chelates calcium with a ratio 2:1 and 2:2, with the 2:2 complex being more stable than the 2:1. The 2:2 complex may be constituted by two deprotonated BA or by one fully-protonated BA and one oxidized BA (see **Figure 2.24**). For BE, a 2:1 hydrated complex is formed. At pH 7.8, the oxidation process overwhelmed the complexation with calcium. Oxidized BE is not able to form

chelate calcium, and only one complex with oxidized BA is formed. However, oxidized BA is unstable and degradation products of BA have been detected by mass-spectroscopy. It is stabilized by adducts with water or calcium. The oxidation of BA was also observed by UV-Vis spectroscopy at pH 7.8, but we were not able to detect any possible complexation in the presence of calcium with this method. Complexation site could thus take place on the carboxylate that is not in the conjugated part of the molecule. On the contrary we observed a sign of interaction with calcium in the UV-Vis spectrum of BE while nothing is detected by mass spectrometry.

pH 5



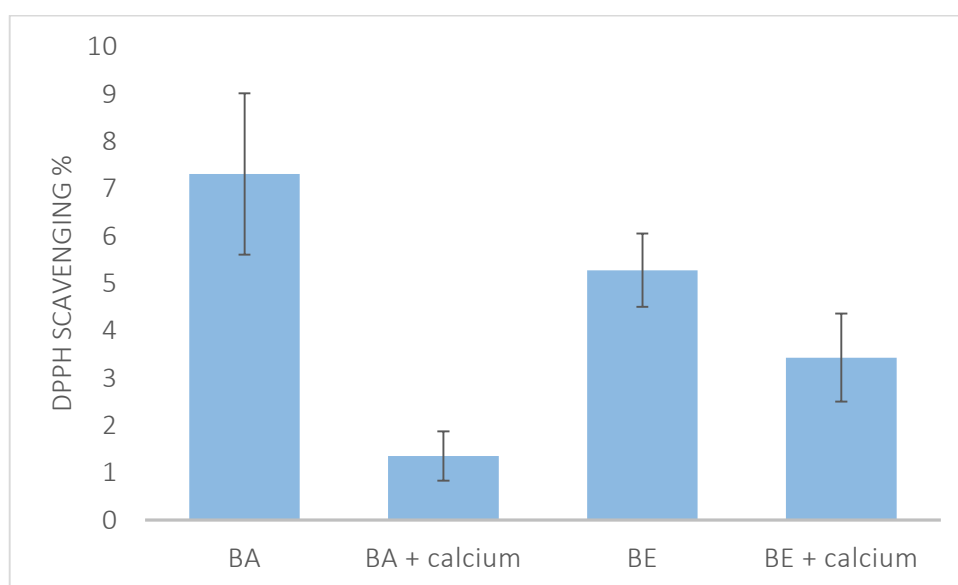
**Figure 2.24** Complexes formed by baicalein and calcium at pH 5

### 2.5.3.2 Effect of complexation on the biological activity

The effect of the presence of calcium on the antioxidant and antibacterial activities of baicalin and baicalein was finally studied

#### 2.5.3.2.1 Antioxidant activity

The antioxidant activity was tested as presented in the paragraph 2.3, to the exception that for the solution with calcium, mixture were preapred 6 hours before the DPPH assay. Results are presented in **Figure 2.25**. The antioxidant activity of baicalein is similar with or without calcium. The low activity is related to the fact that in this solution, BE is fully oxidized even without calcium. Antioxidant activity of BA drastically decreases after 6 hours in presence of calcium. Given the fact that baicalin is oxidized at p 7.8 in 6 hours, we can assume that the reduction of it radical scavenging activity is more likely due to its oxidation rather than an effect of calcium complexation.



**Figure 2.25** Antioxidant activity of BA and BE alone or in presence of calcium (molar ratio BAM/Ca 0.1), at pH 7.8

#### 2.5.3.2.2 Antibacterial activity

The antibacterial activity of BA and BE in presence of calcium was studied, against *S. epidermidis* CIP 68.21, *S. aureus* ATCC 6538, *L. ivanovii* Li4(pvS2) and *P. aeruginosa* ATCC 27853. Calcium was added in equimolar concentration compared to BA or BE. From **Table 2.2**, we observe that MIC in presence of calcium are identical to MIC of pure BA or BE, within the experimental error, except in two cases. MIC of BA was decreased by 8 fold (from 1024 to 128  $\mu\text{g.mL}^{-1}$ ) against *S. epidermidis* in presence of calcium. Although significant because above the experimental error, such a decrease remains modest. Similarly, MIC of BE was reduced from 34 to 8.5  $\mu\text{g.mL}^{-1}$  against *S. aureus*. It is important to note that BE and BA are oxidized in culture medium.



MIC ( $\mu\text{g/mL}$ )	<i>S. epidermidis</i> CIP 68.21	<i>S. aureus</i> ATCC 6538	<i>L. ivanovii</i> Li4(pvS2)	<i>P. aeruginosa</i> ATCC 27853
Baicalin	1024	256	512	> 2048
Baicalein	34	34	17	> 68
Baicalin + calcium	128	128	1024	2048
Baicalein + calcium	17	8,5	17	> 68

**Table 2.2** Minimum inhibitory concentration of baicalin and baicalein against four bacterial strains, alone and in presence of calcium (molar ratio 1:1)

#### 2.5.3.2.3 Conclusions

Biological activities of baicalin and baicalein appear more dependent on their oxidation state than on the presence of calcium. Indeed, calcium does not have any effect on the antioxidant activity of BA and BE. The presence of calcium does not affect MIC of BA and BE against *L. ivanovii* and *P. aeruginosa*. Nevertheless, the MIC of BA is decreased by 8-fold against *S. epidermidis*. Thus, it appears that the presence of calcium does not affect, or slightly positively affects the antimicrobial activity of the flavonoids. This result is encouraging from the perspective of using the product as an antibacterial agent in a living organism, therefore in the presence of calcium

#### 2.5.3.3 Conclusions

Baicalin and baicalein are two flavonoids, with two main sites for calcium complexation, the catechol on the A-ring and the 5-hydroxy-4-keto site. In addition, baicalin is a glucuronic acid derivative, so the carboxylate group on the sugar ring is also a potential site for calcium binding. Interaction between baicalin and calcium is pH-dependent. At pH 5, ESI-MS studies revealed the presence of two complex between calcium and the molecule,  $[2\text{BA}+\text{Ca}]^{2+}$  and  $[2\text{BA}-2\text{H}+2\text{Ca}]^+$  (constituted by two deprotonated BA or one BA and one oxidized BA). At pH 7.8, none of these complexes are formed, but the complex  $[\text{BAox}-\text{H}+\text{Ca}]^+$ , *i.e.* a complex between the oxidized molecule and the calcium, is detected, besides the non-oxidized non-complexed molecule. Oxidized BA coexists with non-oxidized BA, but only when stabilized by water or calcium; otherwise it is degraded in BEox. We can assume that complexation with calcium occurs immediately after oxidation; otherwise a peak corresponding to BAox would be detected. No effect of complexation is visible on UV-Vis absorption spectra, which can be explained by considering that complexation occurs at the carboxylate site, which is not conjugated with the chromophore part of the molecule. Concerning the biological activities of BA, its antioxidant activity is only affected by the oxidation and not the complexation with calcium. Besides the decrease of MIC of BA against *S. epidermidis*, complexation of calcium does not affect the antibacterial activity of BA.

Baicalein, which is the aglycone of baicalin, oxidizes faster than baicalin and at a lower pH. At pH 5, the oxidized molecule is detected, as well as a  $[2\text{BE}+\text{Ca}+\text{H}_2\text{O}]^{2+}$  complex in a very small quantity compare to the native molecule. As complexation occurs with both baicalin and baicalein at this pH, we can assume that the catechol and 5-hydroxy-4-keto sites are also the preferred complexation sites for baicalin at this pH. At pH 7.8, the entire molecule is oxidized, as shown by ESI-MS and UV-Vis absorption experiments. A small effect of calcium complexation is visible in the first times of UV-Vis studies, but no complex is detected by mass spectrometry. As soon as the complex is formed, baicalein oxidizes, and the calcium leaves the molecule, so no complex can be detected by mass spectrometry. It therefore seems that the oxidation of the complex is in competition with the oxidation of the non-complexed molecule, the former being faster. The absence of complex at pH 7.8 with BE supports our previous assumption that, for baicalin at this pH, calcium interacts with the carboxylate moiety. Finally, there is no effect of the presence of calcium on the antioxidant activity, as the molecule spontaneously oxidized in the medium, even without calcium. There is no significant effect of calcium on the antibacterial activity of BE, except a 4-fold decrease of the MIC against *S. aureus*.

#### 2.5.4 Conclusions

In this section, we aimed at investigate the fate of baicalin and baicalein at different pH, and their interaction with calcium at neutral pH. The degradation of both molecules has already been mentioned, but not deeply investigated. Literature only focused on how to avoid this degradation, and oxidation was only suggested. Here, we show that baicalin is oxidized and hydrolyzed in baicalein at pH 7.8, but remains stable at pH 5. On the contrary, baicalein is more unstable, and is oxidized at pH 5. The oxidation was proven by ESI-MS, with the loss of two protons. Both BE and BA have a weak antioxidant activity at neutral pH, because they already fully oxidized. On the contrary, their antibacterial activity does not vary with oxidation. We can even assumed that the active molecule is the oxidized one in the case of BE, because the oxidation of the molecule is almost immediate at physiological pH. Moreover, the antibacterial assays are performed at 37 °C, which probably increases the kinetics of the reaction. The calcium complexation is pH-dependent. At pH 5, both BE and BA may chelate calcium, but at pH 7.8 complexation is hindered by the oxidation reaction. Oxidized BE cannot chelate calcium, and only a small fraction of oxidized BA form a complex. For BA, oxidation overwhelms the complexation because there is no trace of a complex with non-oxidized BA while there is still a peak of non-oxidized BA alone. Given the information of complexation of both molecules at pH 5 and 7.8, we can assumed that at pH 5, the complexation site is on the catechol or the 5-hydroxy-4-keto site, because both molecules chelate calcium. After oxidation, only BA can form complex, so the site of complexation is more likely the carboxylate, as it is absent on BE that does not form any complex. Calcium complexation does not have an important effect on the antibacterial activity of baicalin and

baicalein. The presence of calcium does not interfere with the biological activity of both molecules, which is encouraging for their utilization *in vivo* as potent antibacterial agents.

## 2.6 General conclusions

In this chapter, we decided to study four biologically active molecules, chosen for their antibacterial and antioxidant activities. Chlorogenic and rosmarinic acids are two polyphenols that share the same caffeic acid moiety. As for baicalin and baicalein, they are two flavonoids, baicalein being the aglycone form of baicalin. Among the four molecules, baicalein was characterized to be the best antibacterial agent, while rosmarinic acid is the best antioxidant molecule. The interaction of the four molecules with calcium was investigated by UV-Vis spectroscopy and mass spectrometry. For chlorogenic and rosmarinic acid, complexation was found highly pH-dependent, with monomolecular complexes formed at neutral pH and bimolecular complexes at acidic pH. Monomolecular complexes formed with deprotonated molecules possess the best stability. We tried to determine the site of complexation of calcium by NMR, but we were not able to discriminate between catechol and carboxylate groups. Finally, the effect of calcium complexation on the antioxidant activity was studied, but only a slight decrease of the activity of rosmarinic acid was observed. For baicalin and baicalein, we were first concerned by their degradation at physiological pH, as it was already mentioned in the literature. We highlighted the oxidation of both molecules, with different kinetics of degradation. BE is more unstable than BA, it oxidizes at pH 5, while BA only starts to oxidize at pH 7.2. The kinetics of degradation is pH-dependent and medium-dependent. Given the oxidation of the molecules, we can assume that the active form of baicalein is the oxidized one. The complexation with calcium was investigated, knowing that both molecules are degraded at neutral pH. Complexation is possible at pH 5, but in competition with the oxidation at pH 7.8. Indeed, oxidized BE cannot chelate calcium, while the presence of calcium allows the stabilization of oxidized BA that is otherwise degraded in oxidized BE.

To conclude, we studied the complexation of chlorogenic and rosmarinic acid with calcium, as well as its effect on the antioxidant activity of both molecules. The oxidation and degradation of baicalin and baicalein, and their interaction with calcium were investigated depending on pH. Complexation with calcium should play a role for the *in vivo* fate of the molecules, but the effect on their biological activity was not marked. As we want to associate these molecules in hydroxyapatite, knowing their interaction with calcium could be useful to understand their behavior towards the targeted material. In the next chapter, we will first focus on the preparation of biologically active molecules-hydroxyapatite hybrid nanoparticles.

## References

- 1 L.-G. Gao, H. Wang, X.-L. Song and W. Cao, *Journal of Molecular Structure*, 2013, **1034**, 386–391.
- 2 M. M. Robinson and X. Zhang, THE WORLD MEDICINES SITUATION 2011/Traditional medicines: global situation, issues and challenges, <http://digicollection.org/hss/documents/s18063en/s18063en.pdf>, (accessed July 5, 2018).
- 3 D. Procházková, I. Boušová and N. Wilhelmová, *Fitoterapia*, 2011, **82**, 513–523.
- 4 M. Salami, M. Rahimmalek and M. H. Ehtemam, *Food Chemistry*, 2016, **213**, 196–205.
- 5 B. Shan, Y. Z. Cai, M. Sun and H. Corke, *Journal of Agricultural and Food Chemistry*, 2005, **53**, 7749–7759.
- 6 H. P. Kim, K. H. Son, H. W. Chang and S. S. Kang, *Journal of Pharmacological Sciences*, 2004, **96**, 229–245.
- 7 P. Mladěnka, K. Macáková, T. Filipský, L. Zatloukalová, L. Jahodář, P. Bovicelli, I. P. Silvestri, R. Hrdina and L. Saso, *Journal of Inorganic Biochemistry*, 2011, **105**, 693–701.
- 8 P. Mladěnka, L. Zatloukalová, T. Filipský and R. Hrdina, *Free Radical Biology and Medicine*, 2010, **49**, 963–975.
- 9 M. Říha, J. Karlíčková, T. Filipský, K. Macáková, L. Rocha, P. Bovicelli, I. P. Silvestri, L. Saso, L. Jahodář, R. Hrdina and P. Mladěnka, *RSC Adv.*, 2014, **4**, 32628–32638.
- 10 R. Ravichandran, M. Rajendran and D. Devapiriam, *Food Chemistry*, 2014, **146**, 472–478.
- 11 M. T. Fernandez, M. L. Mira, M. H. Florêncio and K. R. Jennings, *Journal of Inorganic Biochemistry*, 2002, **92**, 105–111.
- 12 J. M. Dimitrić Marković, Z. S. Marković, T. P. Brdarić, V. M. Pavelkić and M. B. Jadranin, *Food Chemistry*, 2011, **129**, 1567–1577.
- 13 C. A. Perez, Y. Wei and M. Guo, *Journal of Inorganic Biochemistry*, 2009, **103**, 326–332.
- 14 N. N. Trofimova, E. V. Stolpovskaya, V. A. Babkin, S. V. Fedorov, G. A. Kalabin, S. V. Goryainov, E. E. Zolotarev, A. Y. Safronov, A. V. Kashevskii and R. G. Zhitov, *Russian Journal of Bioorganic Chemistry*, 2015, **41**, 745–752.
- 15 J. Yang, Y. Xu, H.-Y. Liu, R.-M. Han, J.-P. Zhang, L. Skibsted, J. Yang, Y. Xu, H.-Y. Liu, R.-M. Han, J.-P. Zhang and L. H. Skibsted, *Molecules*, 2017, **22**, 1757.

- 16 Q. K. Panhwar, S. Memon and M. I. Bhanger, *Journal of Molecular Structure*, 2010, **967**, 47–53.
- 17 M. Samsonowicz and E. Regulska, *Spectrochimica Acta Part A: Molecular and Biomolecular Spectroscopy*, 2017, **173**, 757–771.
- 18 M. N. Clifford, *J. Sci. Food Agric.*, 1999, **79**, 362–372.
- 19 M. Kalinowska, E. Bajko, M. Matejczyk, P. Kaczyński, B. Łozowicka and W. Lewandowski, *International Journal of Molecular Sciences*, 2018, **19**, 463.
- 20 B. Badhani, N. Sharma and R. Kakkar, *RSC Advances*, 2015, **5**, 27540–27557.
- 21 J. D. Campo, C. Nguyen-The, M. Sergent and M. J. Amiot, *Journal of Food Science*, 2003, **68**, 2066–2071.
- 22 H. Kikuzaki, M. Hisamoto, K. Hirose, K. Akiyama and H. Taniguchi, *Journal of Agricultural and Food Chemistry*, 2002, **50**, 2161–2168.
- 23 N. Seeram, L. Adams, S. Henning, Y. Niu, Y. Zhang, M. Nair and D. Heber, *The Journal of Nutritional Biochemistry*, 2005, **16**, 360–367.
- 24 S. Z. Milić, N. I. Potkonjak, S. Ž. Gorjanović, S. D. Veljović-Jovanović, F. T. Pastor and D. Ž. Sužnjević, *Electroanalysis*, 2011, **23**, 2935–2940.
- 25 A. Beneduci, E. Furia, N. Russo and T. Marino, *New Journal of Chemistry*, 2017, **41**, 5182–5190.
- 26 S. Chan, S. Kantham, V. M. Rao, M. K. Palanivelu, H. L. Pham, P. N. Shaw, R. P. McGeary and B. P. Ross, *Food Chemistry*, 2016, **199**, 185–194.
- 27 B. Kutus, D. Ozsvár, N. Varga, I. Pálínkó and P. Sipos, *Dalton Transactions*, 2017, **46**, 1065–1074.
- 28 M. Samsonowicz, E. Regulska and M. Kalinowska, *Chemico-Biological Interactions*, 2017, **273**, 245–256.
- 29 J.-P. Cornard, C. Lapouge, L. Dangleterre and C. Allet-Bodelot, *The Journal of Physical Chemistry A*, 2008, **112**, 12475–12484.
- 30 N. A. Danaf, R. A. Melhem, K. I. Assaf, W. M. Nau and D. Patra, *Journal of Luminescence*, 2016, **175**, 50–56.
- 31 Y. Wei and M. Guo, *Biological Trace Element Research*, 2014, **161**, 223–230.
- 32 H. Bazin, G. Descotes, A. Bouchu and M. Petit-Ramel, *Canadian Journal of Chemistry*, 1995, **73**, 1338–1347.

- 33 C. J. Kelley, R. C. Harruff and M. Carmack, *The Journal of Organic Chemistry*, 1976, **41**, 449–455.
- 34 F. K. Ticli, L. I. S. Hage, R. S. Cambraia, P. S. Pereira, Â. J. Magro, M. R. M. Fontes, R. G. Stábéli, J. R. Giglio, S. C. França, A. M. Soares and S. V. Sampaio, *Toxicon*, 2005, **46**, 318–327.
- 35 T. Lopez-Arnaldos, M. Lopez-Serrano, A. R. Barcelo, A. A. Calderon and J. M. Zapata, *Fresenius Journal of Analytical Chemistry*, 1995, **351**, 311–314.
- 36 S. E. Castillo-Blum and N. Barba-Behrens, *Coordination Chemistry Reviews*, 2000, **196**, 3–30.
- 37 Z. Gao, K. Huang, X. Yang and H. Xu, *Biochimica et Biophysica Acta*, 1999, **1472**, 643–650.
- 38 Z. Feng, J. Zhou, X. Shang, G. Kuang, J. Han, L. Lu and L. Zhang, *Pharmaceutical Biology*, 2017, **55**, 1177–1184.
- 39 J. Xing, X. Chen and D. Zhong, *Journal of Pharmaceutical and Biomedical Analysis*, 2005, **39**, 593–600.
- 40 Š. Ramešová, R. Sokolová, I. Degano, J. Bulíčková, J. Žabka and M. Gál, *Analytical and Bioanalytical Chemistry*, 2012, **402**, 975–982.
- 41 Š. Ramešová, R. Sokolová and I. Degano, *Electrochimica Acta*, 2015, **182**, 544–549.
- 42 R. Sokolová, Š. Ramešová, I. Degano, M. Hromadová, M. Gál and J. Žabka, *Chemical Communications*, 2012, **48**, 3433.
- 43 G. Dehghan and Z. Khoshkam, *Food Chemistry*, 2012, **131**, 422–426.







## Chapter 3

# Formation of hybrid hydroxyapatite – biologically active molecule nanoparticles



## 3. Formation of hybrid hydroxyapatite – biologically active molecule nanoparticles

### Outline

3. Formation of hybrid hydroxyapatite – biologically active molecule nanoparticles .....	115
3.1 Introduction.....	117
3.2 Hydroxyapatite synthesis .....	117
3.3 Incorporation of BAMs .....	118
3.3.1 Post synthesis adsorption.....	118
3.3.2 In situ synthesis .....	125
3.3.3 Comparison of incorporation methods.....	130
3.4 Biological activity of hydroxyapatite – baicalein hybrid particles obtained by adsorption .....	134
3.4.1 Introduction.....	134
3.4.1 Baicalein release <i>in vitro</i> .....	134
3.4.2 Antioxidant activity.....	135
3.4.4 Antibacterial activity.....	137
3.4.5 Conclusions.....	141
3.5 Conclusions.....	141
References.....	143



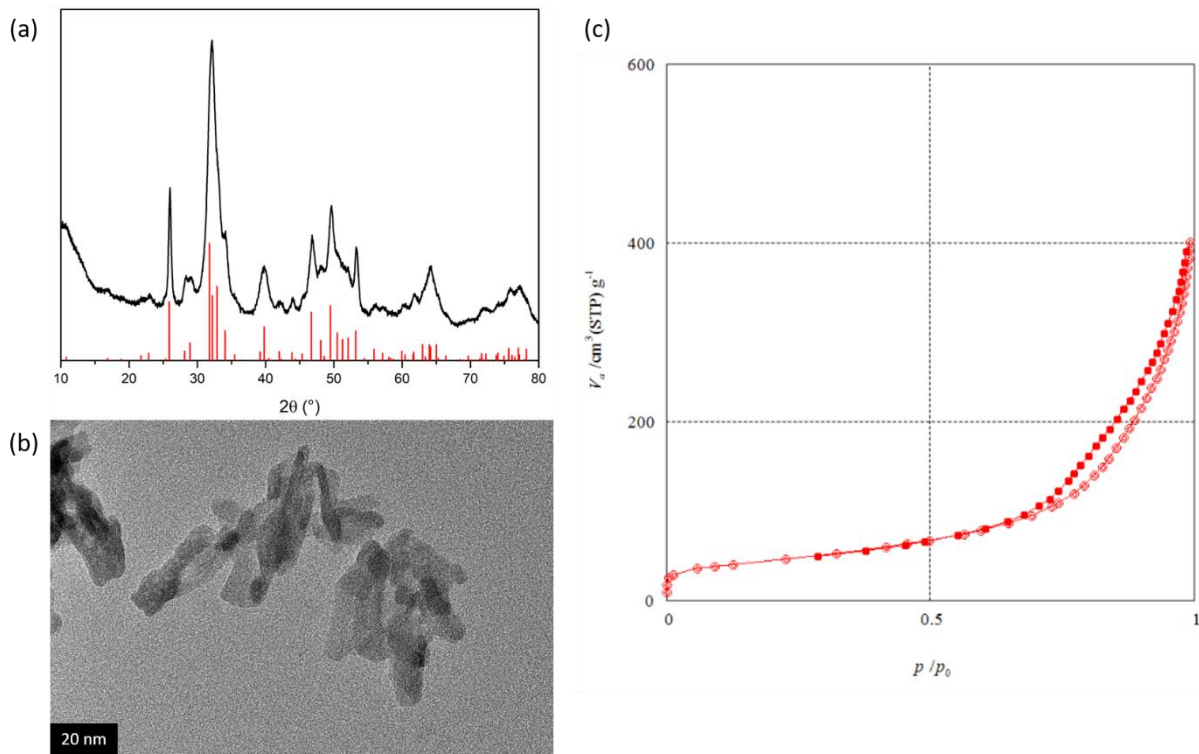
### 3.1 Introduction

In the previous chapter, we evidenced that the four natural biologically active molecule (BAM), rosmarinic acid, chlorogenic acid, baicalin and baicalein could interact with calcium at different levels. Rosmarinic and chlorogenic acid formed monomolecular complexes at both pH 5 and 7.8, while the oxidation of baicalin overwhelmed the complexation at neutral pH. Baicalein was the molecule with the lowest affinity for  $\text{Ca}^{2+}$ . Keeping these informations in mind, we here tried to associate these molecules with hydroxyapatite nanoparticles in order to achieve their controlled release in a biological medium. Two strategies were considered, adsorption on pre-formed hydroxyapatite nanoparticles or incorporation of BAMs in the reaction medium during hydroxyapatite synthesis. Considering the size of BAMs compared to the crystal lattice of hydroxyapatite, in both cases BAM would be adsorbed on the surface of HAp particles, and/or in the interparticulate porosity. In the first section, the synthesis and characterization of hydroxyapatite nanoparticles will be described, before reporting the investigation of the two methods for incorporating the molecules in the material. Then, the antibacterial and antioxidant properties of hydroxyapatite nanoparticles incorporating baicalein will be studied.

### 3.2 Hydroxyapatite synthesis

Hydroxyapatite was synthesized by co-precipitation following the neutralization method<sup>1</sup>. Briefly, 0.1 mol of  $\text{Ca}(\text{OH})_2$  (7.4 g) was dissolved in 100 mL of distilled water during 1h30, and 0.06 mol (6.9 g) of  $\text{NH}_4\text{H}_2\text{PO}_4$  was dissolved in 50 mL of water. Ammonium dihydrogenophosphate solution was added to calcium solution, and the medium was left to react for 48 h at 25 °C under stirring. Temperature was controlled by a thermostat bath. After reaction, white particles were recovered by centrifugation at 5000 rpm for 5 minutes, followed by three washing with distilled water. The powder was dried in a oven at 100 °C for 24 hours. Particles were characterized by X-ray powder diffraction (XRD) and Transmission Electron Microscopy (TEM).  $\text{N}_2$  physisorption was used to determine the specific area of the powder and its porosity.

The yield of synthesis, as determined by weighting the final powder, was 60 % assuming that only hydroxyapatite was formed. The X-ray diffractogramm (**Figure 3.1 (a)**) confirmed this hypothesis, by comparison with the PDF card 00-064-0738. TEM image as seen in **Figure 3.1 (b)** showed plate-like nanoparticles  $31 \pm 6$  nm in length and  $9 \pm 3$  nm in width. Specific surface area calculated with the BET method was  $160 \text{ m}^2 \cdot \text{g}^{-1}$ . The average pore diameter of the powder, corresponding to interparticle space, was 15 nm (see the isotherm of  $\text{N}_2$  physisorption on **Figure 3.1 (c)**).



**Figure 3.1** X-ray diffractogram (a), TEM image (b), and N<sub>2</sub> physisorption isotherm of synthesized hydroxyapatite particles

Crystallite size may be calculated using Debye-Scherrer's formula (**Equation 3.1**). We used the peak at 26 °, corresponding to the plan (002) due to its adequate resolution and loss of interference.

$$D = \frac{K \times \lambda}{\beta \times \cos(\theta)}$$

**Equation 3.1** Scherrer's formula

In the formula, D is the crystallite size, K is a dimensionless shape factor with a typical value of 0.9,  $\lambda$  is the X-ray wavelength, in our case 1.54 Å (Cu K $\alpha$  wavelength),  $\beta$  is the full width at half maximum (radians), and  $\theta$  is the diffraction angle of the corresponding reflection (°). Using this formula, calculated crystallite size for HAp was 21±2 nm.

### 3.3 Incorporation of BAMs

#### 3.3.1 Post synthesis adsorption

As previously mentioned, BAM were selected in particular for their carboxylic acid and catechol functions, presumed to interact with the hydroxyapatite surface. In a first approach, a two-step method was used to synthesize the hybrid particles.

In this approach, 10 mg of ground HAp particles were re-suspended in a 200 mL solution of BAM in distilled water (pH  $\approx$  5). The BAM concentration was set to 0.05 mM as it is near the limit of solubility of BA and BE, corresponding to an initial molar ratio between Ca and BAM of 1. After 24 hours of contact under stirring at room temperature, particles were recovered by filtration, and dried at 100 °C for 24 hours. The quantity of adsorbed BAM was estimated by TGA and/or UV-Visible spectroscopy. For the UV-Vis method, absorbance of the solution was checked before and after adsorption, and the difference between the two values was used to estimate the adsorbed quantity. Morphology of particles after adsorption was also observed with TEM.

Incorporated quantity measured by TGA and UV-Vis spectroscopy, expressed in mg of incorporated molecule by g of HAp, and particle size as obtained from TEM are gathered in **Table 3.1**.

Sample	Incorporated quantity (mg.g <sup>-1</sup> ) (UV)	Incorporated quantity (mg.g <sup>-1</sup> ) (TGA)	Incorporated quantity (molecules.nm <sup>-2</sup> ) (TGA)	Particle length/width (nm)	Crystallite size (nm) (XRD)
HAp-RA	20	31	0.3	31 $\pm$ 10/8 $\pm$ 2	21 $\pm$ 5
HAp-CA	10	27	0.3	43 $\pm$ 11/12 $\pm$ 1	23 $\pm$ 5
HAp-BE	89	63	0.9	33 $\pm$ 10/15 $\pm$ 3	24 $\pm$ 5
HAp-BA	60	37	0.3	27 $\pm$ 4/8 $\pm$ 3	24 $\pm$ 5
HAp	-	-	-	31 $\pm$ 6/9 $\pm$ 3	21 $\pm$ 2

**Table 3.1** Estimation of adsorbed quantity of BAM on HAp measured by TGA or UV-Vis spectroscopy and particle dimension as obtained from TEM

From UV-vis and TGA, baicalein is the molecule with the highest adsorption rate. Nonetheless, it is important to note the difference in the adsorbed quantity if measured by UV or by TGA. For baicalin and baicalein, the reason is probably the beginning of degradation of the molecule after 24 hours, which modifies the UV-vis spectrum and therefore induces an error in the estimation.

The variation of pH at the beginning and end of the adsorption process was also monitored (**Table 3.2**). In all situations, the initial mixture is acidic and the pH is higher after adsorption, close to neutrality.

	HAp	HAp-RA	HAp-CA	HAp-BA	HAp-BE
BAM (mM)	0	0.05	0.05	0.05	0.05
Initial pH	4.7	3.7 (3.5)	4.6 (4.1)	4 (4.05)	5
Final pH	6.6	7.2	7.1	6.6	7

**Table 3.2** Initial and final pH of HAp suspensions alone or in the presence of BAMs. Calculated pH with the weak acid dissociation equation under brackets for RA, CA and BA.

$$\text{pH} = \frac{1}{2}(\text{pka} - \log C)$$

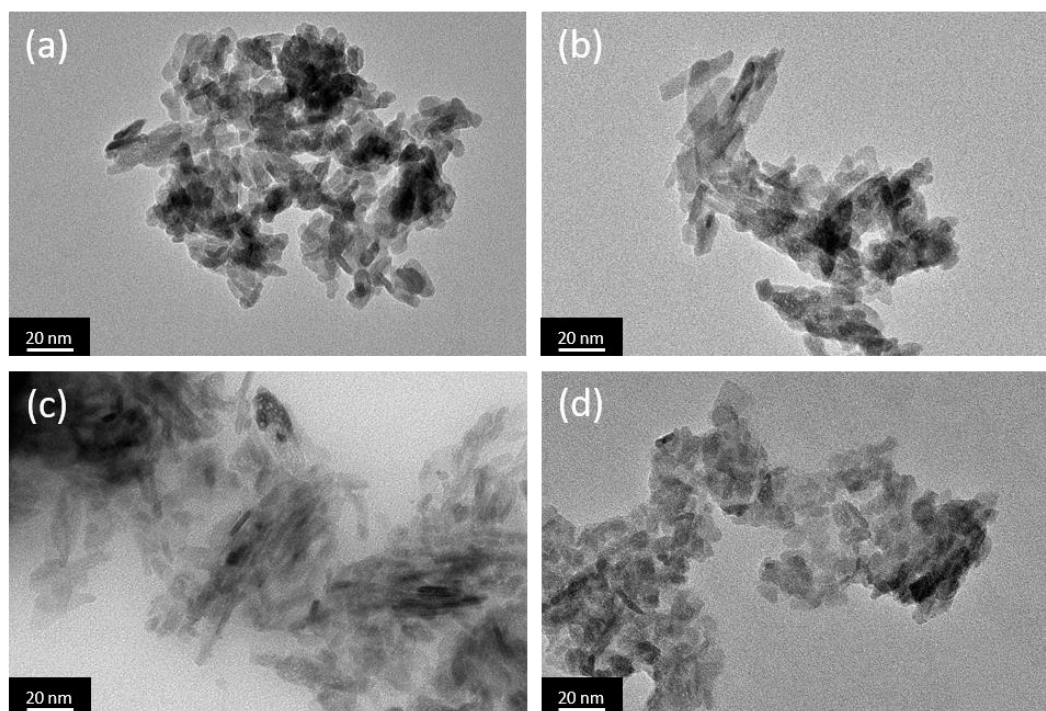
**Equation 3.2** Weak acid dissociation

In more details, all initial values are close or lower to the control sample, in agreement with the acidic nature of BAMs. We calculated the theoretical pH for a solution of RA, CA or BA, thanks to the equation of weak acid dissociation (see **Equation 3.2**). Considering final values, they are larger than for pure HAp, except for BA. The increase of pH observed when the dried HAp powder is placed in an acidic aqueous environment was previously reported<sup>2</sup> and attributed to the protonation of phosphate groups on the HAp surface and possible release of OH<sup>-</sup> and carbonate species. This previous work also evidenced that the final pH could be modified if adsorbing molecules were present. Here, a final higher pH compared to HAp alone may indicate that the adsorption process involves a deprotonation of the BAM.

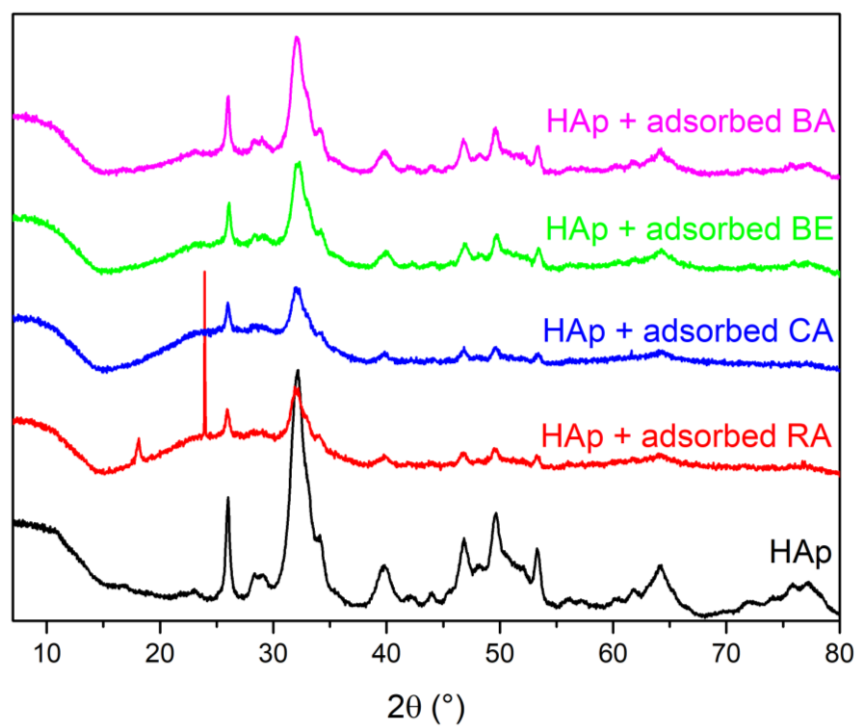
As seen in the TEM images presented in **Figure 3.2** adsorption of BAM did not modify the platelet-shape aspect of HAp particles. Determination of particle width and length by image analysis confirmed that adsorption did not significantly modify particles dimension (**Table 3.1**).

As seen in **Figure 3.3**, X-ray diffractograms after adsorption are similar to pure HAp, confirming TEM observations. The crystallite size, calculated and gathered in **Table 3.1** are similar to the one of HAp before adsorption. The background noise is higher for particles after adsorption because the quantity of powder used for the measurement was very small. We can note two remarkable peaks on the diffractogram of HAp + adsorbed RA, at 18 ° and 24 °. The peak at 18 ° deserves our attention. We assigned it to Ca(OH)<sub>2</sub>, but we cannot give an explanation to the presence of calcium hydroxide in these conditions. This must be checked with another batch of hydroxyapatite after adsorption. The peak at 24 ° is probably an artefact of the sample holder, due to the small quantity of analyzed powder.



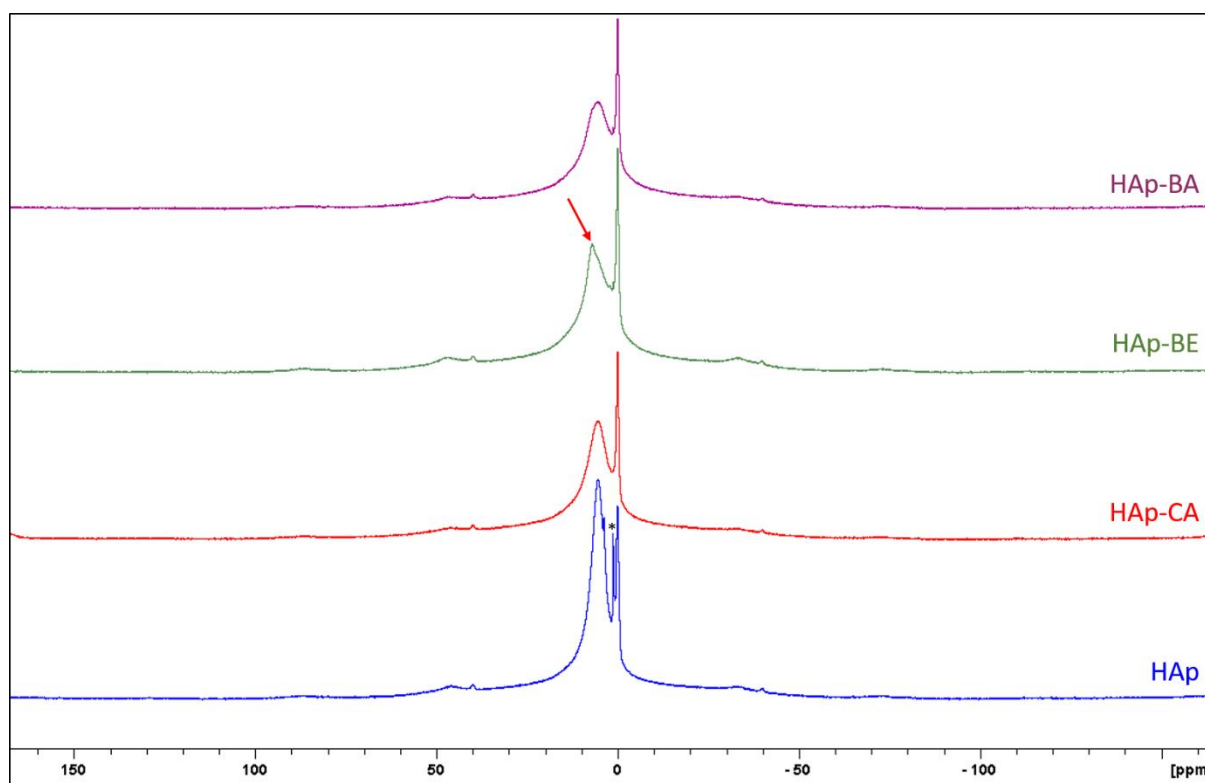


**Figure 3.2** TEM image of hydroxyapatite after adsorption of (a) rosmarinic acid, (b) chlorogenic acid, (c) baicalein and (d) baicalin



**Figure 3.3** X-ray diffractograms of HAp particles after adsorption of BAM

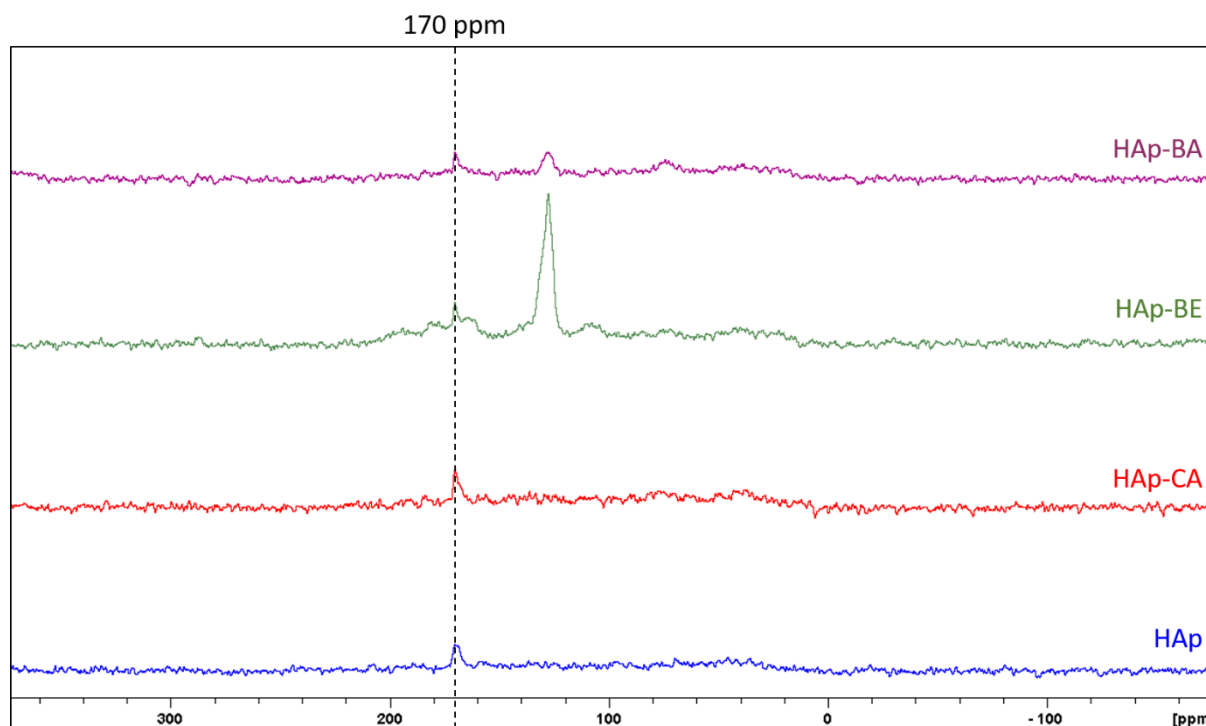
$^1\text{H}$ ,  $^{13}\text{C}$  and  $^{31}\text{P}$  solid-state CP-MAS NMR experiments were performed on HAp-CA, HAp-BE and HAp-BA (initial BAM concentration = 0.05 mM) and compared with pure HAp. HAp-RA was not studied, as the adsorbed quantity is comparable to the one in HAp-CA, with close molecular structure and weight. Superimposition of  $^1\text{H}$  spectra is presented in **Figure 3.4**. On the spectrum of pure HAp, we can notice the common signal of protons in HAp, with the very narrow peak at 0 ppm characteristic of protons in the crystal lattice, and the broader peak at 5.6 ppm characteristic of disordered protons at the HAp surface<sup>3</sup>. Similar spectra are observed for HAp-CA and HAp-BA, except that the high ppm peak is broader. On the HAp-BE spectrum we can distinguish a shoulder at 7.2 ppm indicated by a red arrow, probably corresponding to the aromatic protons of baicalein.



**Figure 3.4**  $^1\text{H}$  solid-state NMR spectra of HAp, HAp-CA, HAp-BE and HAp-BA (initial concentration for adsorption = 0.05 mM) (\* indicates residual peaks of acetone and ethanol)

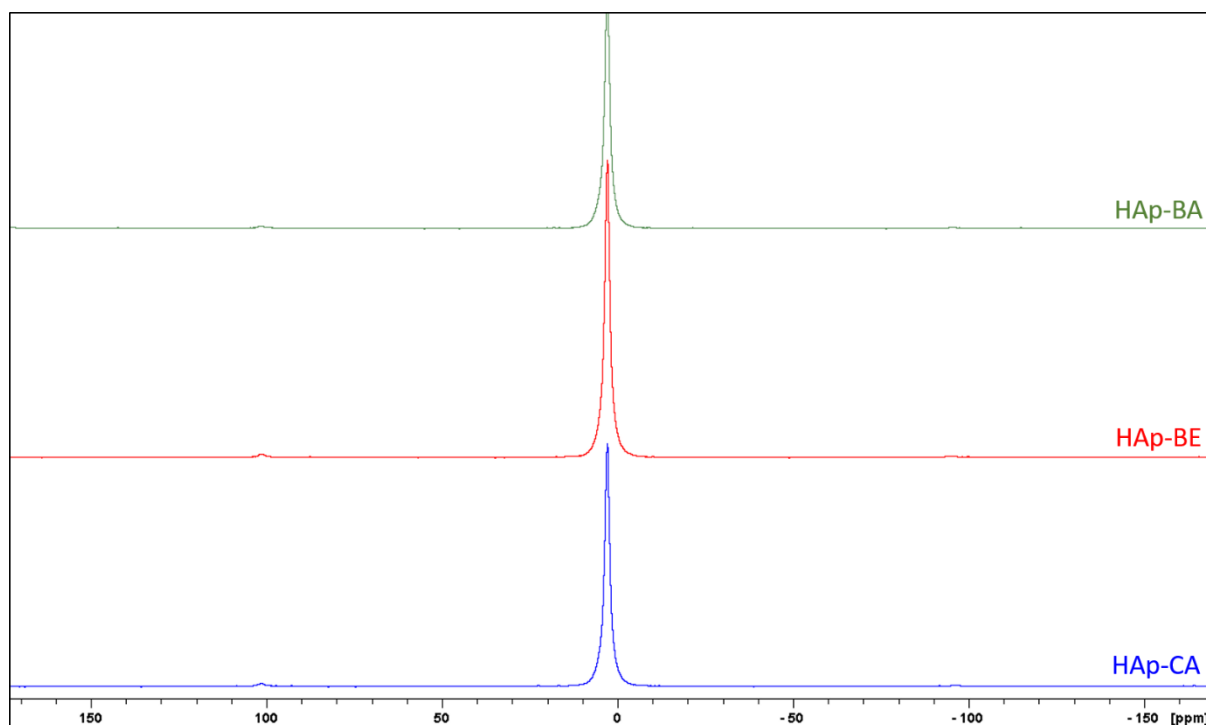
The  $^{13}\text{C}$  spectrum of HAp (**Figure 3.5**) is characterized by a broad peak of weak intensity at 170 ppm corresponding to carbonates. Carbonates are also visible on the spectra of HAp-CA, HAp-BE and HAp-BA. However, the peak is dissymmetrical, with a more intense part above 170 ppm, which would suggest a type B substitution<sup>4</sup>. In HAp lattice, carbonates can substitute the hydroxyl, which is called an A-type substitution, or the phosphate that is called a B-type substitution. In addition, an intense peak at approximately 120 ppm is seen on the HAp-BE spectrum, and, to lesser extent, on the one of HAp-BA. This peak corresponds to aromatic carbons of baicalein and baicalin. As NMR is not a very sensitive characterization method, only adsorbed baicalein and baicalin are detected because they are

adsorbed in a larger quantity than CA. These data also confirm the higher affinity of BE for HAp compared to BA and CA.



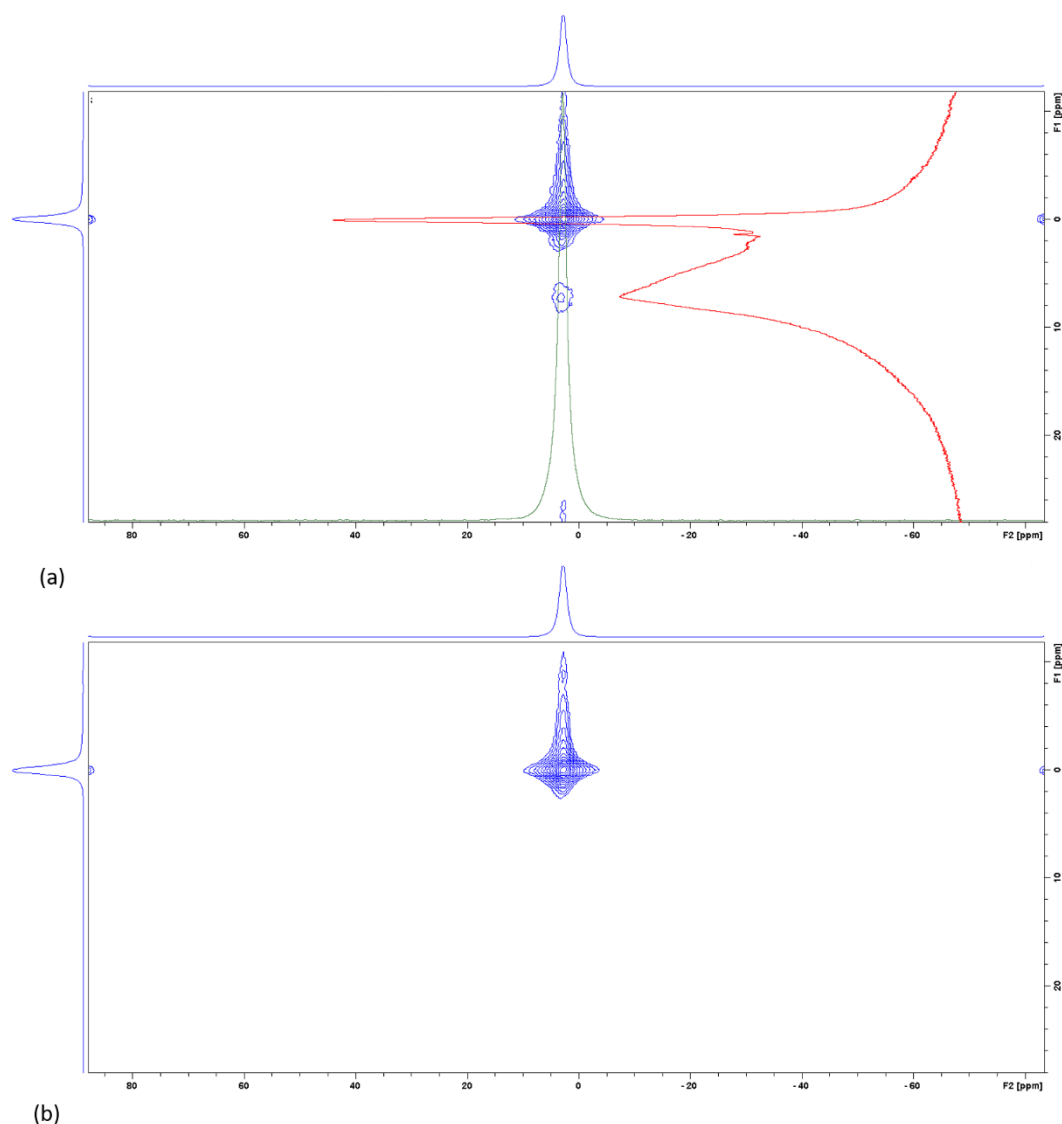
**Figure 3.5**  $^{13}\text{C}$  cp-mas solid-state NMR spectra of HAp, HAp-CA, HAp-BE and HAp-BA (initial concentration for adsorption =  $0.05 \text{ mmol.L}^{-1}$ ). NS = 47752, d1 = 1s, p15 = 2 ms.

The  $^{31}\text{P}$  spectrum of HAp (**Figure 3.6**) is characterized by an unique peak at 2.7 ppm corresponding to phosphorous in the apatitic structure. The position and width of the peak is the same for the three samples with adsorbed BAMs.



**Figure 3.6**  $^{31}\text{P}$  solid-state NMR spectra of HAp, HAp-CA, HAp-BE and HAp-BA (initial concentration for adsorption =  $0.05 \text{ mmol.L}^{-1}$ ).

A 2D correlation map between  $^1\text{H}$  and  $^{31}\text{P}$  of HAp-BE was recorded. A three units sequence was used, with 1- a saturation on  $^{31}\text{P}$  to remove noise coming from dephasing, 2- an Hahn echo to filter the contribution of amorphous OH in  $^1\text{H}$  spectrum and 3- acquisition  $^{31}\text{P}$  with cross-polarization. During a cross-polarization experiment,  $^1\text{H}$  is magnetized, before contact with  $^{31}\text{P}$  during the contact time, and then spectrum is acquired on  $^{31}\text{P}$ . We tested four contact times (p15) for cross-polarization, and we decided to focus on the 10 ms condition (**Figure 3.7 (a)**). The correlation between crystalline  $^{31}\text{P}$  and aromatic  $^1\text{H}$  is visible at 2.7 ppm for  $^{31}\text{P}$  and 7.1 ppm for  $^1\text{H}$ . This correlation is the sign of the adsorption of BE on HAp. The same correlation map was recorded for pure HAp as reference (**Figure 3.7 (b)**). The only correlation visible is at 2.7 ppm for  $^{31}\text{P}$  and 0 ppm for  $^1\text{H}$ , which corresponds to the correlation between OH in apatitic structure and crystalline phosphorous, that is also visible on HAp-BE spectrum.



**Figure 3.7** 2D hetero correlation map  $^1\text{H}$ - $^{31}\text{P}$  of HAp-BE (a) and HAp (b). NS = 256, d1 = 1 s, p15 = 10 ms, TD = 180

### 3.3.2 *In situ* synthesis

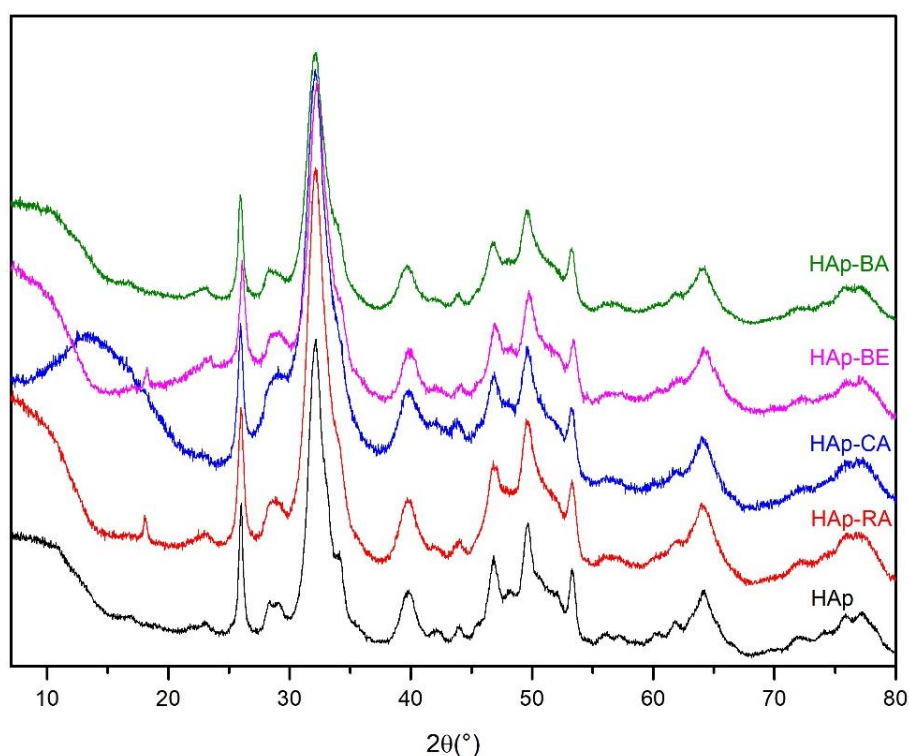
The second attempt to incorporate the four natural BAM in hydroxyapatite was by incorporation during synthesis. The protocol was the same as for pure hydroxyapatite, except that 100 times smaller concentrations of inorganic precursors were used, molecules were added in the calcium hydroxide solution and the solution left under stirring for 1 h 30 before adding the dihydrogenophosphate solution. Two ratios between calcium and BAMs were studied, 0.0075 and 0.075 (BAM : calcium), except for baicalin for which the highest ratio was 0.04 due to solubility issues. Colored particles were obtained, with color depending on the incorporated molecule. The crystalline phase of the precipitated powder was first checked by XRD. The morphology of the synthesized

particles was studied by TEM. Quantity of incorporated molecule was measured by thermogravimetric analysis (TGA).

We will first describe the synthesis with the molar ratio BAM:Ca = 0.0075. **Table 3.3** gathers the yield of the reaction, calculated from recovered powder weight assuming that hydroxyapatite was the only formed phase, the particle dimension as obtained from TEM, the crystallite size obtained from XRD, the incorporated quantity of BAM measured by TGA and the molar ratio BAM: Ca in the materials, calculated from the incorporated quantity of BAM measured by TGA.

Sample	Yield (%)	Particle length/width (nm)	Crystallite size (nm)	Incorporated quantity (mg.g <sup>-1</sup> )	Final molar ratio BAM : Ca
HAp	90	30±7/8±4	15±3	-	-
HAp-RA	46	14±2/4.2±0.5	16±1	52	0.015
HAp-CA	56	19±2/6±2	15±1	42	0.011
HAp-BE	53	17±3/7±1	17±1	52	0.02
HAp-BA	46	13±2/4.2±0.5	13±2	54	0.012

**Table 3.3** Yield of the synthesis, particle and crystallite size, incorporated quantity of BAM and final molar ratio BAM:Ca of HAp-BAM (BAM: Ca = 0.0075).



**Figure 3.8** XRD pattern of hydroxyapatite particles synthesized in the presence of rosmarinic acid (HAp-RA), chlorogenic acid (HAp-CA), baicalein (HAp-BE) and baicalin (HAp-BA) (BAM:Ca = 0.0075)

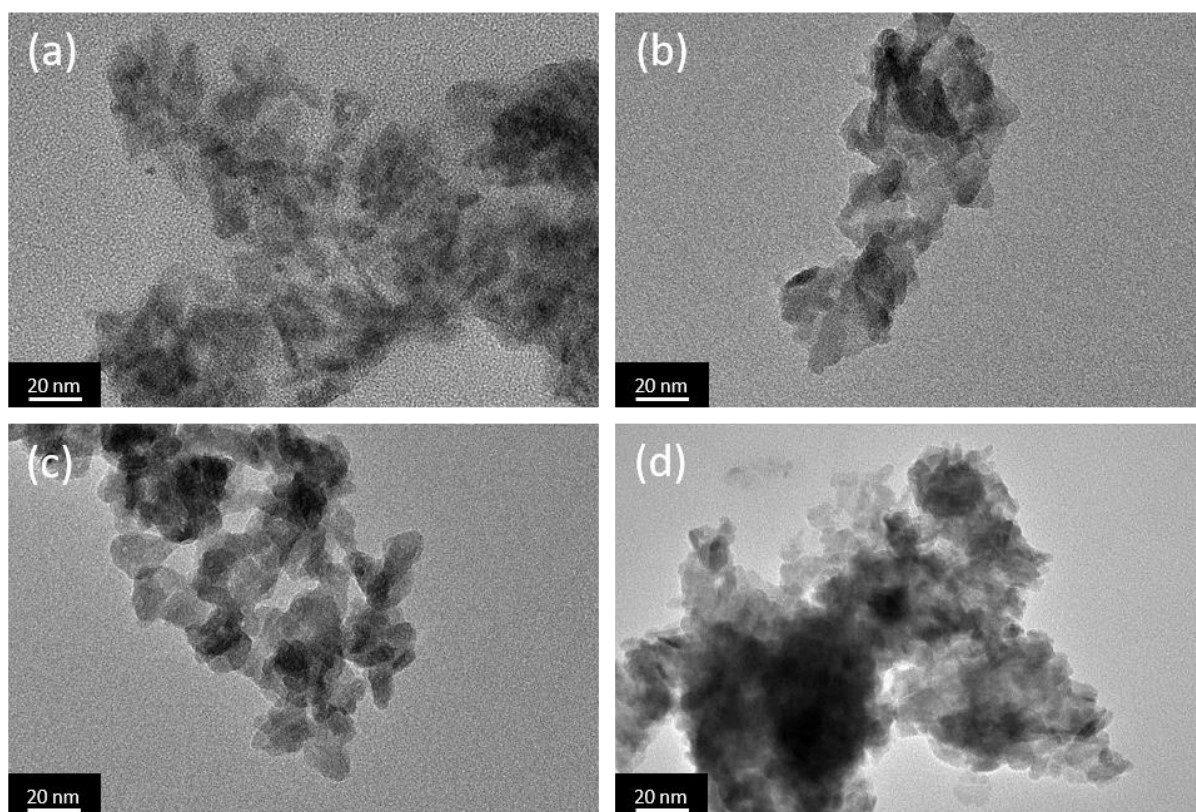
From XRD, it is possible to evidence the formation of hydroxyapatite in all conditions (**Figure 3.8**). The calculated crystallite size of pure hydroxyapatite is 15 nm and is not significantly modified in the presence of BAMs at this concentration. It is also important to notice that in the low  $2\theta$  domain, diffractograms of HAp-RA and HAp-BE show an additional peak at *ca.*  $2\theta = 18^\circ$ . This peak may correspond to the (001) diffraction peak of  $\text{Ca(OH)}_2$ , which is the most intense for this structure. This peak is not observed for BA and CA.

In parallel, the yield of the hydroxyapatite formation decreases with the incorporation of the BAM, from 90 % for pure HAp, to  $50 \pm 5$  % in the presence of BAMs (**Table 3.4**). Therefore, the presence of BAMs seems to inhibit the formation of HAp. The amount of incorporated BAM is higher than in the case of adsorption, except for baccalain. However, from the measure of the incorporated quantity, we can calculate the final molar ratio between BAM and Ca in the hybrid material. It is 0.011 for HAp-CA, 0.015 for HAp-RA, 0.02 for HAp-BE and 0.01 for HAp-BA. The highest ratio is again obtained for BE, as observed in the adsorption process. Thus, there is an enrichment in BAM within the material compared to the initial molar ratio in solution (0.0075).

TEM images of HAp-CA and HAp-BA (**Figure 3.9 (b) and (d)**) show platelet-shaped particles, similar to pure HAp, but apparently more aggregated. HAp-RA and HAp-BE have a less defined shape. The particles in the four samples are significantly smaller (**Table 3.3**) than pure hydroxyapatite, which is consistent with crystallite size calculated from XRD data. However, while crystallite size varied only in a non-significant amount, size variation as measured from TEM evidence a noticeable difference between HAp-RA and HAp-CA, and HAp-BA and HAp-BE.

Altogether, BAMs at low concentration decrease the amount of formed hydroxyapatite nanoparticles and the crystallite size, these two parameters being apparently correlated (i.e. lowest yields (RA, BA) are obtained for the smallest particles). The amount of incorporated BAM can also vary, but clear correlation with the other studied factors is not straightforward: for instance BE leads to the highest BAM:Ca ratio but the yield is not very different from other BAMs. Importantly XRD suggests that other phases are present in the final powder, and especially  $\text{Ca(OH)}_2$ .





**Figure 3.9** TEM images of (a) HAp-RA, (b) HAp-CA, (c) HAp-BE and (d) HAp-BA

In order to evaluate better the effect of BAM on the hydroxyapatite synthesis, a higher molar ratio was studied for RA, CA and BE, BAM: Ca = 0.075, and, due to solubility limitation, BAM: Ca = 0.04 for BA. Apparent (*i.e.* on hydroxyapatite basis) yields of the reactions, crystallite size (from XRD), incorporated quantity and BAM: Ca molar ratio in the materials are gathered in **Table 3.4**.

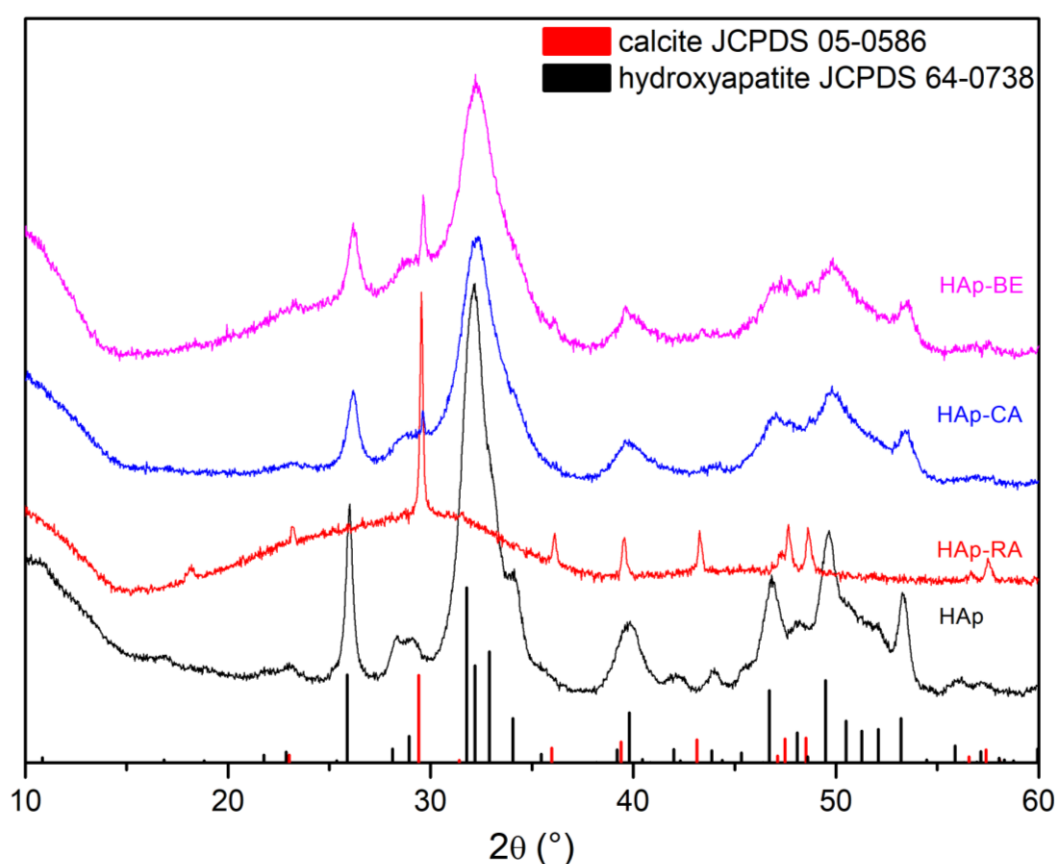
Sample	Yield (%)	Crystallite size (nm)	Incorporated quantity (mg.g <sup>-1</sup> )	Final molar ratio BAM : Ca
HAp	90	15±3	-	-
HAp-CA	43	14±2	73	0.02
HAp-BE	42	14±3	135	0.05
HAp-BA	50	18±2	111	0.025

**Table 3.4.** Apparent yield of the synthesis, crystallite size and incorporated quantity of BAM and of HAp-BAM (BAM: Ca = 0.075).

The synthesis with rosmarinic acid was difficult to handle. After washing, almost no powder was collected. Synthesized particles seemed to redissolve in distilled water, so it was impossible to calculate the yield of the reaction and to measure the incorporated quantity of RA by TGA. In order to recover few mg of powder to perform XRD, the washing step was skipped.

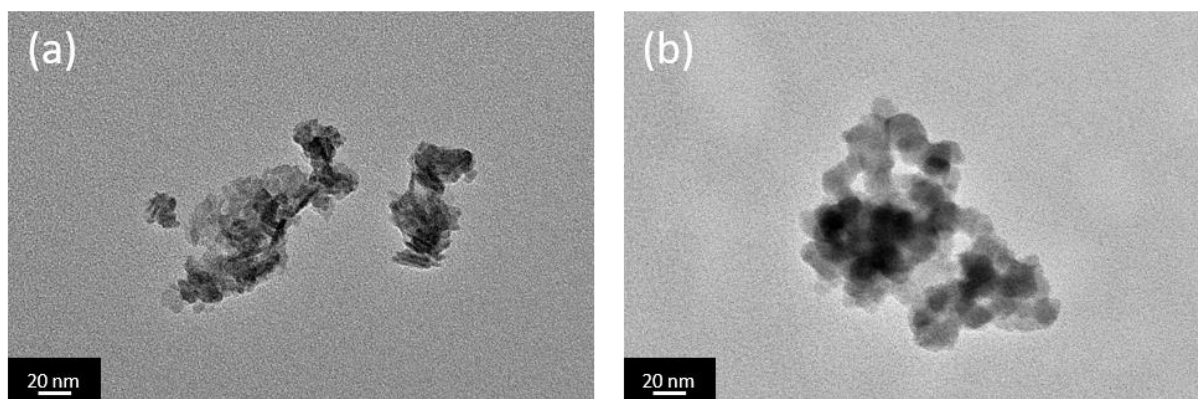


XRD patterns presented in **Figure 3.10** showed the presence of hydroxyapatite for HAp-BE, HAp-CA and HAp-BA. Calculated crystallite sizes are similar to the one calculated for HAp particles synthesized in the presence of BAMs with the molar ratio 0.0075, *i.e* around 15 nm. In presence of RA, the diffractogram is not the one of hydroxyapatite, therefore we decided to name this compound CaP(for calcium phosphate)-RA. However, after comparison with database, it could be assigned to the calcium carbonate ( $\text{CaCO}_3$ ) calcite phase. As a matter of fact, the main diffraction peak of calcite at *ca.*  $29^\circ$  is also visible on the diffractogram of HAp-BE, and to a lesser extent in the one of HAp-CA but not with BA. The presence of calcite would explain the redissolution of CaP-RA in water during washing, as calcite is quite soluble in water near neutral pH. Therefore HAp formation seems totally inhibited by the presence of rosmarinic acid.



**Figure 3.10** XRD pattern of hydroxyapatite particles synthesized in the presence of rosmarinic acid (HAp-RA), chlorogenic acid (HAp-CA), and baicalein (HAp-BE) (Ca:BAM = 0.075), and comparison with patterns of hydroxyapatite (JCPDS 64-0738) and calcite (JCPDS 05-0586)

TEM images of HAp-BE and CaP-RA are presented in **Figure 3.11**. It is clearly visible that particles in presence of RA are different from the ones of HAP-BE, the latter being similar to previous samples. They are larger, and rectangular-shaped, compared to the small platelet-like particles of HAp-BE. These observations therefore confirm results from XRD.



**Figure 3.11** TEM images of (a) HAp-BE and (b) CaP-RA (initial BAM:Ca = 0.075)

For CA and BE incorporating particles, we have noticed that the apparent yield was lower than with the ratio 0.0075. Thus, a larger quantity of BAM seemed to inhibit HAp formation more. In parallel, incorporated quantity of BAMs was higher, with  $73 \text{ mg.g}^{-1}$  of incorporated CA and  $135 \text{ mg.g}^{-1}$  of incorporated BE. Yet, whereas the initial solutions were 10 times more concentrated in BAM, the final incorporated quantity is not 10 times higher than the quantity incorporated when the BAM: Ca ratio was 0.0075. The final loadings were at least twice that obtained at the lower ratio but smaller than the initial solution content. Again, BE was the most efficiently incorporated molecule.

Overall, the synthesis of hydroxyapatite in presence of BAM is possible for low molecular ratio between BAM and calcium, even if, when synthesized in the presence of organic molecules, the yield of the reaction decreases and HAp crystals are smaller. At higher ratio, the synthesis is totally inhibited in presence of rosmarinic acid while, despite a stronger effect compared to lower ratio, HAp is still obtained for the other BAMs

Variations in yields, as calculated from the weight of recovered powder, must be taken carefully as other phases,  $\text{Ca(OH)}_2$  at low molar ratio and  $\text{CaCO}_3$  at high ratio, were also evidenced. These phases may also be taken into account when calculating the amount of BAM per g of hydroxyapatite. However, it can at least be stated that bacalein is the most efficiently retained BAM in the final product.

### 3.3.3 Comparison of incorporation methods

We developed two methods to associate BAMs with HAp, either by post-synthesis adsorption or incorporation during synthesis. The first method leads to adsorption of all BAMs without significant modification of the HAp nanoparticles structure, with highest loading being obtained for BE. The second method allows to obtain hybrid nanoparticles for all BAMs and two sets of concentrations, except for RA at the highest BAM:Ca ratio. However, the reaction yield of hydroxyapatite formation is

decreased compared to the one of pure HAP synthesis and other phases are recovered in almost all samples.

#### *Adsorption method*

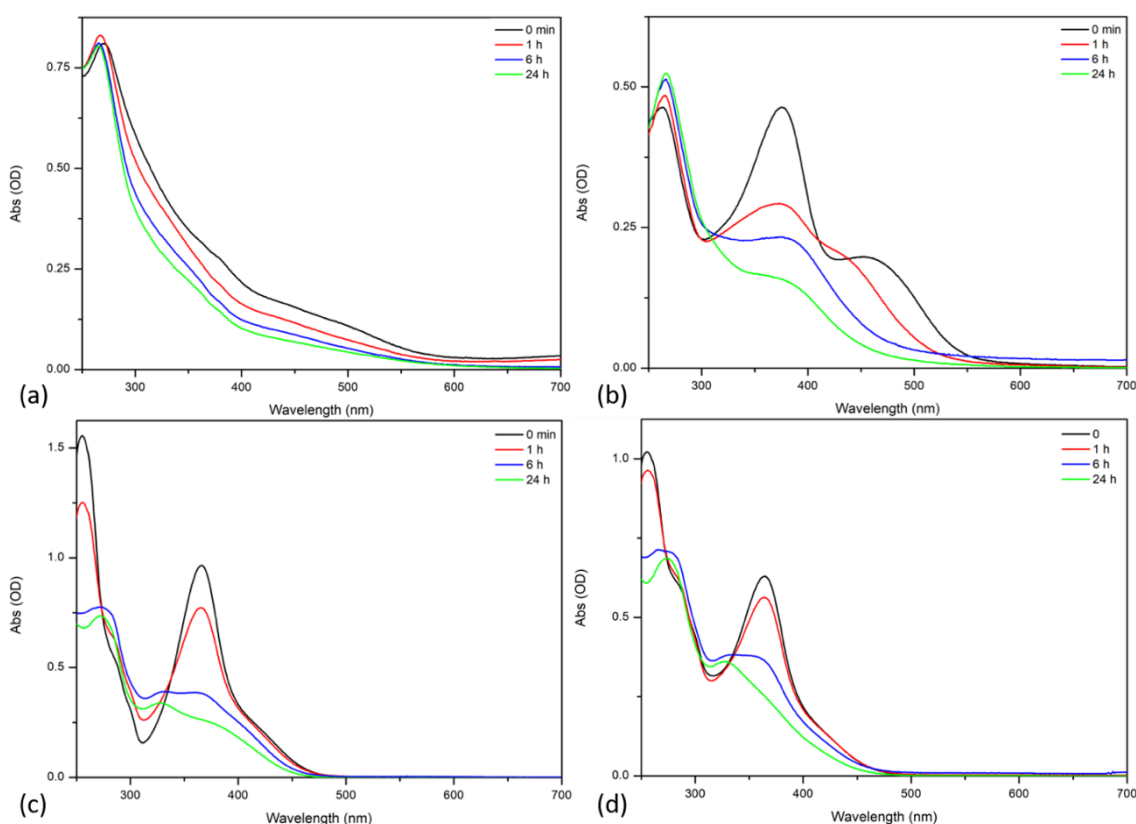
Because the underlying mechanisms are expected to be simpler, we can first discuss the second method. Adsorption of biologically active molecules on hydroxyapatite have already been reported in the literature, for delivering antibacterial agents or osteogenic components. For instance, antibiotics such as gentamicin, tobramycin, or gentamicin have been efficiently adsorbed on hydroxyapatite nanoparticles or coatings<sup>5–9</sup>. Others examples are anticancer<sup>10</sup>, anti-inflammatory<sup>11</sup> or hemostatic<sup>12</sup> molecules. Overall, three kind of interactions can be expected between the molecules and the surface: (1) electrostatic, (2) hydrophilic/hydrophobic and (3) complexation with the calcium ions. The first two ones are highly correlated to the surface charge of HAp: at pH below its isoelectric point (IEP), the surface is positively-charged and has good affinity for anionic species, while the mirror situation occurs at pH above IEP. Near the IEP, the HAP surface has a marked hydrophobic character.

The IEP of hydroxyapatite can range between 7 and 8, being therefore positively-charged in the sorption conditions in this work. We measured the pKa of the carboxylic acid of RA, CA and BA by titration with NaOH. For the three molecules, carboxylic acid is deprotonated at pH 5 in distilled water, suggesting that attractive electrostatic interactions can drive their adsorption on the HAp surface. Surprisingly, baicalein appears to have the strongest affinity for HAp, although being neutral at pH 5. Moreover, it did not show any interaction with calcium ion in our previous molecular study (see [Chapter 2](#)). This result can be interpreted in light of a study by Chirdon et al.<sup>13</sup> that showed that catechol and pyrogallol adsorbed more readily and strongly on HAp surfaces than phenol and carboxylic acids. The proposed explanation is based on cooperative hydrogen-bond interactions thanks to the presence of two or three close phenol groups. The fact that BA is less efficiently adsorbed than BE evidence that the loss of one available OH group on the pyrogallol ring is not compensated by the presence of an additional carboxylate group on the sugar moiety. Accordingly, the catechol ring present on CA and RA is less efficient than the pyrogallol ring of BE to interact with the HAp surface. Noticeably, it seems that the ability of the BAM to form complexes with  $\text{Ca}^{2+}$  is not relevant to explain the results obtained by the adsorption process. As discussed above, the main reason is that other interactions are also driving the BAM affinity for the HAp surface. Another point to consider is that the coordination sphere of calcium ions within HAp is already occupied by phosphate and hydroxyl groups, limiting its chelation by the BAM ligands.

*In situ method*

In contrast, the formation of BAM- $\text{Ca}^{2+}$  could be expected to be relevant for the first *in situ* method since it involves a preliminary step where  $\text{Ca}(\text{OH})_2$  is dissolved in the presence of the bioactive molecules. However, two points are to be considered. The first one is related to the pH conditions that are highly alkaline (pH 12). On the one hand, such conditions should favor highly deprotonated forms of the molecules, which should enhance their interaction with calcium ions. On the other hand, experiments described in Chapter 2 made us expect that some degradation of the BAM could occur in these pH conditions.

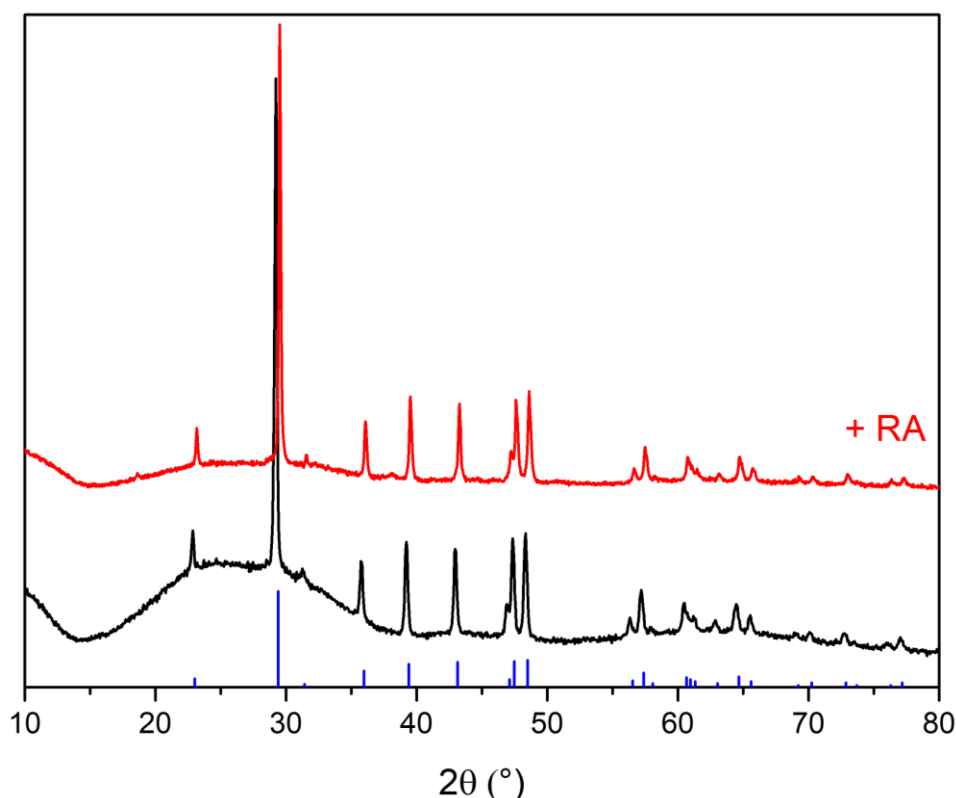
To check this hypothesis, we investigated the stability of the BAMs at pH 12 by UV-Vis spectroscopy (Figure 3.12). It is clear that the spectrum at pH 12 for the four molecules is different from the one at pH 5 (see Chapter 2), and that spectra evolve with time. For BE and BA, we assume that oxidation is the privileged degradation pathways, as it was described in Chapter 2 for degradation of these molecules at pH 7. As for RA and CA, we assume that the ester function would be hydrolyzed. Therefore, it is very likely that the structure of BAMs involved in the HAp growth process is different from the one investigated in Chapter 2 during studies in solution, and that the identified complexes are not fully relevant to understand their influence on the *in situ* process.



**Figure 3.12** Stability of (a) RA, (b) CA, (c) BE and (d) BA at pH 12.

The second point to consider is that BAM may also influence  $\text{Ca(OH)}_2$  dissolution and/or favor  $\text{CaCO}_3$  formation. Indeed, for RA, the  $\text{Ca(OH)}_2$  diffraction peak observed on particles synthesized with the ratio 0.0075 is the highest and  $\text{CaCO}_3$  formation is the most favored when ratio is 0.075, while for BA, no  $\text{Ca(OH)}_2$  peak is observed at low ratio and no  $\text{CaCO}_3$  is found at high ratio.

To understand better this phenomenon, some additional experiments were performed. First, the evolution of the  $\text{Ca(OH)}_2$  solution in the absence or presence of RA was followed by XRD measurements. In the first case, after 15 minutes, a very low amount of powder could be recovered, suggesting fast dissolution of calcium hydroxide. After 30 minutes, the solid content of the solution was much more significant and XRD indicate that it consists of pure  $\text{CaCO}_3$ . Formation of calcite in these conditions is very favorable and already reported in the literature. A similar evolution was found in the presence of RA, except for a trace of remaining  $\text{Ca(OH)}_2$  after 30 min. This would indicate that RA has only a minor influence on  $\text{Ca(OH)}_2$  dissolution. It is also important to keep in mind that upon ammonium phosphate addition, without BAM, only HAp is formed while in the presence of RA at high concentration only  $\text{CaCO}_3$  is identified with intermediate situations, *i.e.* both  $\text{CaCO}_3$  and HAp being present, for other BAMs. Therefore RA may either inhibit  $\text{CaCO}_3$  dissolution or inhibit HAp formation.



**Figure 3.13** XRD of powder recovered after 30 min in solution of  $\text{Ca(OH)}_2$  and  $\text{Ca(OH)}_2 + \text{RA}$ ., and comparison with XRD of calcite (PDF card 05-0586)

One important information is that the crystallite sizes are similar for HAp and HAp-CA/BE/BA, while all BAMs induce a decrease in particle size, as estimated on TEM images. If we make the hypothesis that in a first approximation, the crystallite size is the size of the first objects that are formed in solution, if the crystallites have the same size whatever the synthesis condition, this can be interpreted considering that HAp nucleation is not perturbed. If we continue the hypothesis with the fact that the particle size reflects the growth phase, if the particle size is decreased when incorporation of CA, BA and BE, we can suggest that these molecules inhibit the growth of HAp. Such a growth limitation can result either from adsorption of the BAMs on the surface of growing particles of HAp or a depletion in available  $\text{Ca}^{2+}$ . The first possibility is very unlikely, because when we tried to adsorb BAMs on HAp particles, BE was the molecule with the highest affinity for HAp surface while it does not show a particular inhibiting effect here. Accordingly, RA did not exhibit a specifically high affinity for HAp surface but has the highest inhibiting action on precipitation. Altogether, this would favor the hypothesis that the underlying mechanism is mainly related to BAM interactions with  $\text{CaCO}_3$  that would limit its dissolution. It has been shown that for selected organics at concentrations lower than  $0.01 \text{ mol.L}^{-1}$  the dissolution of  $\text{CaCO}_3$  is inhibited in alkaline pH<sup>14,15</sup>. Inhibition was attributed to the blocking of dissolution sites by adsorbed carboxylates. RA, with one carboxylate and two catechol functions may act as strong adsorbent on  $\text{CaCO}_3$ , preventing from its dissolution.

## 3.4 Biological activity of hydroxyapatite – baicalein hybrid particles obtained by adsorption

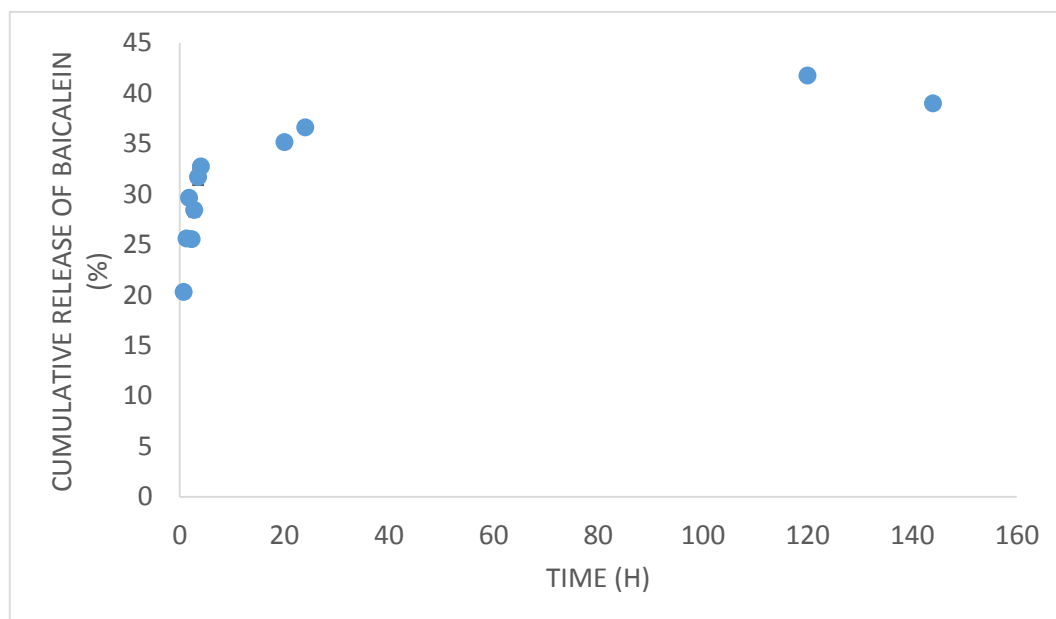
### 3.4.1 Introduction

In this part, the biological activity of hydroxyapatite nanoparticles with BAM will be investigated. We decided to focus only on the hybrid hydroxyapatite particles with baicalein. Indeed, as seen in Chapter 2, it is the molecule with the best antibacterial activity. Moreover, it is the molecule with the best incorporation in hydroxyapatite, either by adsorption or during synthesis. As we saw that baicalein is degraded in pH 12 during synthesis of hydroxyapatite, we decided to study only particles after adsorption. First, the release of baicalein from HAp coatings was studied by HPLC, before the study of their antioxidant and antibacterial activities.

#### 3.4.1 Baicalein release *in vitro*

This work was initiated during my stay in the team of Pr M.F. Desimone at the Universidad de Buenos Aires. Baicalein release from HAp particles (after adsorption) in PBS was studied by HPLC. 10 mg of particles were suspended in 2 mL of PBS at pH 7.4, and 0.5 mL of supernatant was removed at different times for HPLC analysis, and replaced by fresh PBS. Baicalein release was studied over 6 days.

HPLC analysis was performed with reverse phase on a C18 column. Cumulative release profile, in percentage of the total adsorbed amount, is presented in **Figure 3.14**.



**Figure 3.14** Cumulative release of baicalein

Release profile is characterized by a rapid burst release, with 20 % of the total amount of adsorbed baicalein released in the first 45 minutes. Thereafter, release rate is slower during 24 hours, to reach 36 %. After 6 days, 40 % of baicalein is released from the hydroxyapatite particles. This suggests that a noticeable amount of baicalein strongly binds to hydroxyapatite.

The release profile of baicalein follows a classic profile of drug release from nanoparticles, consisting in initial burst release followed by a slower and more controlled phase<sup>6,7,9,10,16</sup>. The initial release may be longer or shorter, from a few minutes<sup>7</sup> to several hours<sup>9</sup>, depending on the affinity of the molecule for the substrate, and the design of nanoparticles. Our nanoparticles reached a plateau in 24 hours, which is approximatively in the average of systems found in the literature. In some cases, the total quantity is released in few hours<sup>6,7</sup>, while others may achieve a sustained release over several days<sup>10,16</sup>. In the literature, sustained release of baicalein was achieved by encapsulation in organic polymers matrixes, like chitosan nanoparticles<sup>17</sup> or polymers micelles<sup>18</sup>. When encapsulated in such chitosan nanoparticles, baicalein is entirely released after 14 days of experiments.

### 3.4.2 Antioxidant activity

As seen in [Chapter 2](#), baicalein is a flavonoid with a significant antioxidant activity, thanks to its pyrogallol group. The antioxidant activity relies on the quenching of the reactive oxygen species (ROS) that are involved in the development of diseases such as cancer, and inflammation.

This work was also initiated during my stay in the team of Pr M.F. Desimone at the Universidad de Buenos Aires. Antioxidant activity of HAp particles with adsorbed baicalein was tested with the DPPH radical scavenging testing, derived from Blois<sup>19,20</sup>. It is based on the DPPH• scavenging through donation of a hydrogen, which is followed by the reduction of the absorption band at 517 nm, as already seen in [Chapter 2](#). 10 mg of particles were suspended in a 1:1 (v/v) mixture of TRIS buffer at pH 7.4 and DPPH solution in ethanol (100 µM). Samples were let to react for 20 minutes in the dark before centrifugation and recovering of the solution and measure of the absorbance of the solution at 517 nm. In order to see the effect of baicalein release, particles after DPPH testing were incubated in PBS for 24 hours before going to a second DPPH assay. After recovery of the particles they were again placed in fresh PBS. This was done every 24 hours for 5 days. Antioxidant activity of each supernatant was also tested. DPPH bleaching rates of particles are gathered in **Table 3.5**.

First, it is important to mention that the release medium did not show any antioxidant activity, despite the fact that baicalein is released by 40 %. Two explanations are possible: either the released quantity is too low for detection of antioxidant activity, or baicalein released in PBS is degraded and not active any more. Indeed, as said in [Chapter 2](#), oxidized baicalein does not have antioxidant properties. On the contrary, particles have a radical scavenging activity of about 80 % after the first test. After 24 hours in PBS, particles are still active, with an antioxidant activity of about 50 %. Particles loose a part of their activity in PBS, as after 4 days in PBS activity is only 18 %. Interestingly, at day 5, one day after the previous testing, activity reaches again 50 %. To conclude, immobilized baicalein is still active, and a sufficient quantity remains after release to maintain the antioxidant activity of particles. It is worth to note that the antibacterial activity of hydroxyapatite particles without baicalein should be tested shortly.

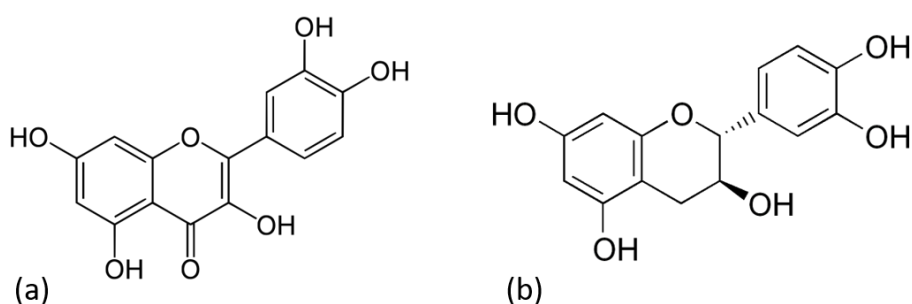
Time (days)	DPPH bleaching percentage (%)
0	80
1	47
4	18
5	51

**Table 3.5** Antioxidant activity of HAp – adsorbed baicalein particles before and after immersion in PBS (m = 10 mg).

Incorporation in HAp of flavonoids was already reported with quercetin, which is a hydroxyflavone<sup>21</sup>. After incorporation of the molecule in hydroxyapatite particles during synthesis,



radical scavenging activity of the hybrid material was reduced to 50 % compared to pure quercetin. Authors interpret that results as a consequence of the oxidation of quercetin, which loss its antioxidant activity. On the contrary, materials synthesized by phase transition, meaning first the synthesis of monetite ( $\text{Ca}(\text{HPO}_4)$ ), another calcium phosphate synthesized at acid pH, in which quercetin is stable, before phase transition to hydroxyapatite in ammonia, have an antioxidant activity close to pure quercetin. Quercetin is not oxidized during the latte synthesis, so it keeps its antioxidant activity. Only a few other examples of hybrid hydroxyapatite nanoparticles with antioxidant activity using flavonoids were reported and it is the first time with baicalein. Besides quercetin mentioned before<sup>16,21</sup>, catechin was also used<sup>22</sup> (**Figure 3.15**). Catechin covalently linked to nanoscale hydroxyapatite showed an antioxidant activity higher than pure catechin, which is attributed to the accumulation of the molecules on the particles surface.



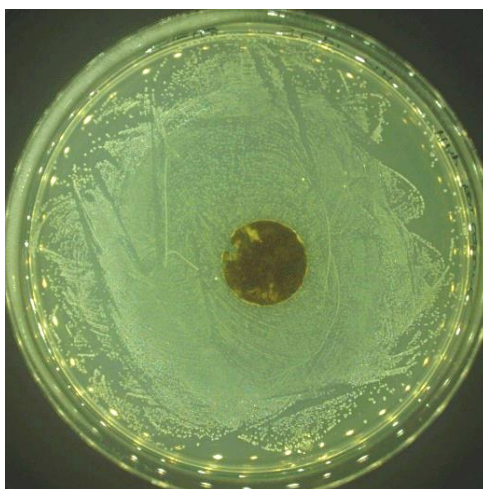
**Figure 3.15** Structure of (a) quercetin and (b) catechin

### 3.4.4 Antibacterial activity

In order to check if the molecule is still active after oxidation, we tested its antibacterial activity after 24 hours of oxidation in the culture medium. The MIC was measured as presented before in [Chapter 2](#). We observed that the MIC after oxidation of the molecule is the same than the value obtained with a fresh solution of BE, *i.e.* 34  $\mu\text{g}/\text{mL}$ . This is not surprising, because we saw that the oxidation of baicalein in these conditions is very fast. In fact, the molecule oxidized in the first hour in the culture medium, so it was already oxidized in the test using a freshly prepared BE solution. This implies that the weak antibacterial activity of the hydroxyapatite particles with adsorbed baicalein is not due to a loss of activity by baicalein after release.

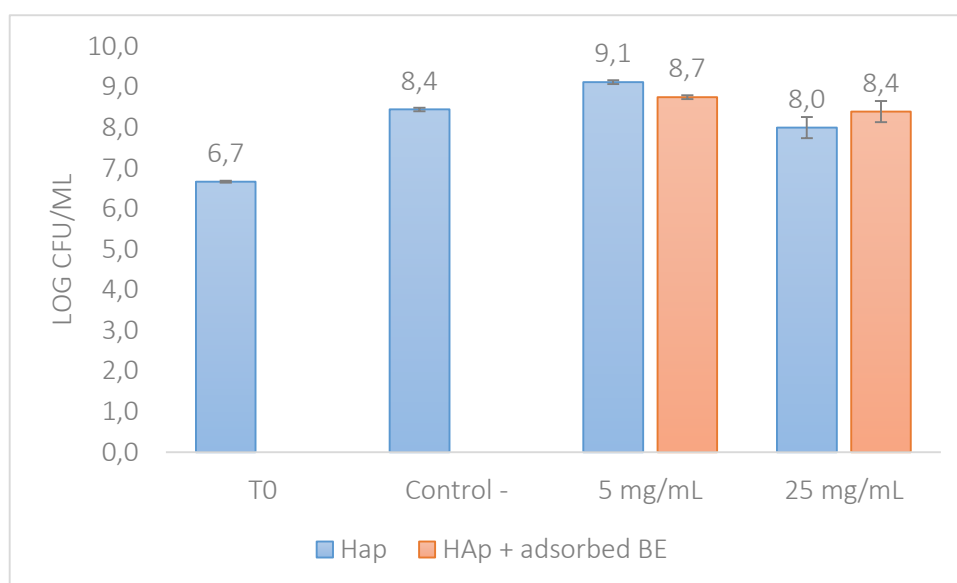
Antibacterial activity of particles with adsorbed baicalein was first tested with an adapted disk-diffusion method. In the classic disk diffusion method, a paper disk is impregnated with a suspension of particles, and deposited on an agar plate where bacteria are spread<sup>23</sup>. Here, particles were put under the form of pellet of approximatively 10 mg. The pellet was then deposited on a MH-agar plate with spread *Staphylococcus epidermidis* CIP 68.21. As seen in **Figure 3.16**, no diffusion disk is visible around

the pellet. We assumed that the pellet did not have any antibacterial activity because baicalein could not diffuse from the particles, due to the compact form of the pellet. We decided to move to testing in liquid medium.



**Figure 3.16** Disk diffusion assay on a MH-agar plate seeded with *S. epidermidis* CIP 68.21

For the testing in liquid medium, particles were incubated with a *S. epidermidis* CIP 68.21 suspension at  $10^6$  CFU/mL in MH for 24 hours at 37 °C, under rotary stirring at 30 rpm. Suspension were recovered and diluted in PBS for plate counting. Two concentrations of particles were tested, 5 and 25 mg/mL. Pure hydroxyapatite particles at the same concentrations were used as control. Results after testing in MH are presented in **Figure 3.17**, and compared with the initial number of bacteria in solution (T0) and the negative control (Control -) that corresponds to bacteria alone in solution.

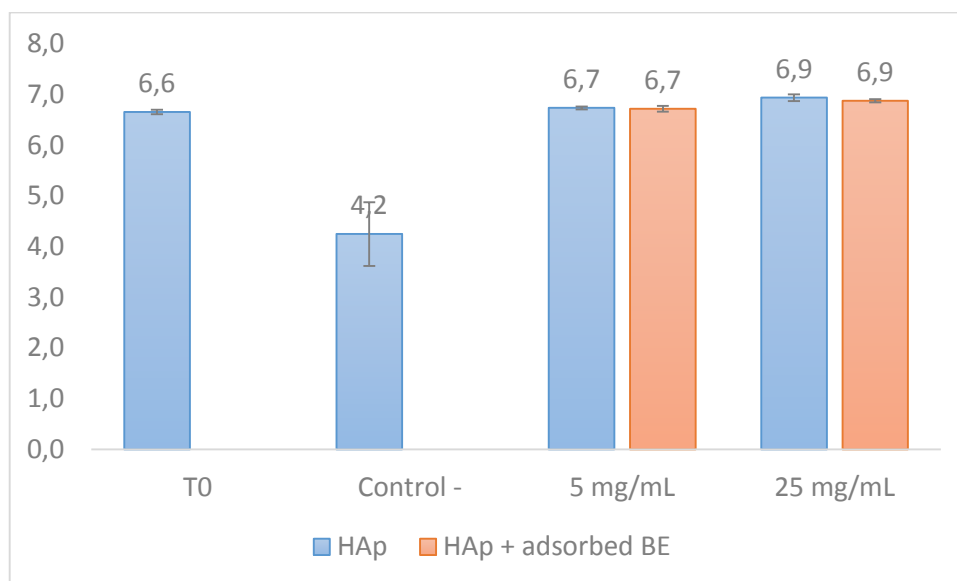


**Figure 3.17** Antibacterial activity of HAp particles with adsorbed baicalein, test in MH

First and foremost, we can see that the concentration of bacteria after incubation with hydroxyapatite particles with or without adsorbed baicalein is similar to the one of the negative control, whatever the quantity of particles tested. Hybrid particles do not prevent the growth of *S. epidermidis* in these conditions.

In order to see if our particles possess a bactericidal effect, we tested their antibacterial activity in PBS. In this medium, the bacterial growth is inhibited. The number of bacteria is supposed to be constant during the time of the experiment. The protocol was the same than used for testing in MH. Results are presented in **Figure 3.18**.

First, we can observe that the number of bacteria after incubation in PBS is the same for hydroxyapatite particles and hydroxyapatite particles with adsorbed baicalein, whatever the tested amount of particles. This suggests that particles with adsorbed baicalein do not have any bactericidal effect, otherwise a reduction of the counted number of bacteria would have been observed. Surprisingly, the number of bacteria in the negative control is lower than the number at t0, suggesting that a certain quantity of bacteria died during the experiment.

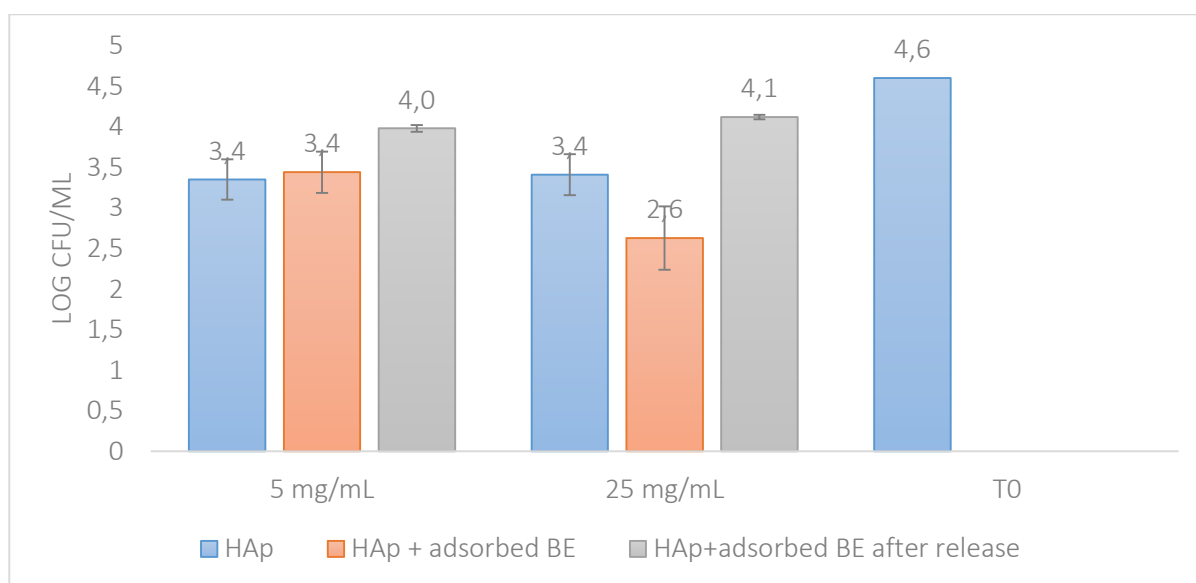


**Figure 3.18** Antibacterial activity of HAp particles with adsorbed baicalein, test in PBS

Based on the release assay, and the quantity of particles used for antibacterial testing, the theoretical concentration of baicalein in solution would be 0.1 mg/mL at 5 mg/mL of particles and 0.6 mg/mL for 25 mg/mL, which is far above the MIC (34 µg/mL). If the MIC of particles is reached in solution, bacterial growth should be inhibited. We have already checked that baicalein is still active

after oxidation in culture broth, so the absence of activity of hybrid particles cannot be explained by the loss of activity of baicalein after release in solution.

We thought that maybe the initial quantity of bacteria was too important for the activity of baicalein. We decided to perform the same test than the one in MH and PBS, but starting from a lower concentration of *S. epidermidis*. We chose  $10^4$  CFU/mL as the initial concentration of bacteria in solution. During the same experiments we tested the antibacterial activity of particles after 24 hours release of baicalein in PBS. Particles were incubated 24 hours in PBS at room temperature, and after recovery by centrifugation, their antibacterial activity in liquid medium was tested as presented before. Two concentrations were tested, 5 and 25 mg/mL. Results obtained after testing in PBS and their comparison with the antibacterial activity measured without incubation in PBS are presented in **Figure 3.19**. The concentration of bacteria for particles with adsorbed baicalein and adsorbed baicalein after incubation in PBS are similar to the one of hydroxyapatite particles. The concentration is lower than initial concentration, but unfortunately we do not have the data concerning the negative control, meaning the concentration of bacteria after 24 hours of incubation in PBS. Nevertheless, this result suggests that even with a lower initial concentration of bacteria, particles with baicalein do not exhibit any antibacterial activity.



**Figure 3.19** Antibacterial activity of HAp particles with adsorbed baicalein, before and after incubation in PBS, test in PBS

In contrast to other drug-release hydroxyapatite systems reported in the literature, particles with baicalein are no clear antibacterial activity. Indeed, porous hydroxyapatite nanoparticles loaded with tetracycline, a broad-spectrum antibiotic, was shown to inhibit *E. coli* growth in 2 hours, and remained active for several days<sup>26</sup>. Antibacterial activity was tested following the disk diffusion

method, with particles shaped as pellets. This antimicrobial testing method was also used to evaluate the activity of hydroxyapatite nanoparticles loaded with vancomycin, against laboratory strains of *S. aureus* and *E. coli*, and MRSA<sup>27</sup>. Particles were active for 7 days against MRSA, and for more than 20 days against the other strains. In both cases, the antibacterial activity is related to the diffusion of the antibiotics outside the hydroxyapatite pellet. In the first study, hydroxyapatite particles are porous, made from stoichiometric HAp. Porous nanoparticles allow a large loading of antibiotics, and its sustained release. In the second study, vancomycin is loaded in commercial HAp, in a large amount (160 mg/g). The difference of activity between these systems and ours should also be strongly linked to the intrinsic antibacterial activity of the used molecules. These studies described hydroxyapatite loading with classic broad-spectrum antibiotic (vancomycin and tetracyclin), with MIC much below that of baicalein (MIC < 1 µg/mL compared to 34 µg/mL for BE ).

### 3.4.5 Conclusions

In this part, we investigated the biological activity of hydroxyapatite with adsorbed baicalein. *In vitro* release, radical scavenging activity and antimicrobial activity against *S. epidermidis* were tested. Baicalein release follows a typical profile consisting of initial burst release and slower phase. The maximum quantity released is 40 % of the total amount of baicalein adsorbed, meaning 25 mg of baicalein for 1 g of particles. After adsorption of baicalein on hydroxyapatite, the molecule remains partly active as hybrid particles exhibit antioxidant activities. We assumed that adsorbed baicalein is responsible for both activities, rather than the released baicalein in solution. Released baicalein, oxidized at physiological pH, should lose its antioxidant activity, while particles with adsorbed baicalein exhibit a significant activity for several days. As far as the antibacterial activity is concerned, our system is unfortunately not efficient against *S. epidermidis* CIP 68.21. These particles are less effective than other antibacterial drug release system with hydroxyapatite found in the literature, but the later use antibiotics such as vancomycin or tetracycline, with MIC below the MIC of baicalein.

### 3.5 Conclusions

In this chapter, we wanted to determine if it is possible to associate rosmarinic acid, chlorogenic acid, baicalin and baicalein with hydroxyapatite nanoparticles. Two methods of incorporation were tested, post-synthesis adsorption and direct synthesis with incorporation of BAM in the reaction medium. Hydroxyapatite nanoparticles were synthesized by precipitation in aqueous medium. We evidenced that the *in situ* incorporation of molecules is possible, but the presence of organics at high concentration partially or totally inhibited the crystallization of hydroxyapatite. Moreover, BAM being degraded at alkaline pH, the real form of incorporated molecules is not known. On the contrary, post-synthesis adsorption did not modify the morphology nor the size of

hydroxyapatite crystals. Among the four molecules tested, baicalein was the one with the best affinity for hydroxyapatite, despite the fact that no complex with calcium was identified during the molecular study. As it is the molecule with the lowest MIC towards bacteria of interest, we decided to test the antibacterial and antioxidant activities of baicalein associated with hydroxyapatite nanoparticles. Particles with adsorbed baicalein showed a significant antioxidant activity, with 80 % of DPPH radical scavenging. The antioxidant activity was maintained over a week, after baicalein release in PBS. However, the release medium did not show any antioxidant activity, because the molecule oxidized in PBS. Unfortunately, our particles do not possess any antibacterial activity against *S. epidermidis* CIP 68.21, in the tested conditions. Compared to other systems consisting of hydroxyapatite nanoparticles with incorporated natural molecules, our system is promising in regards to radical scavenging activity, as the activity is sustained over days after incubation in PBS.

To conclude, this chapter aimed at providing a proof of concept for the development of hybrid materials consisting of hydroxyapatite and natural biologically-active molecules. It is the first report of baicalein-integrated hydroxyapatite, with antioxidant properties. These particles may be used in the field of body implant if coated on metallic substrates. However, as the organic molecule is degraded at high temperature, low temperature processes are required.

## References

- 1 K. Achelhi, S. Masse, G. Laurent, A. Saoiabi, A. Laghzizil and T. Coradin, *Dalton Transactions*, 2010, **39**, 10644.
- 2 H. Bouyarmane, S. E. Asri, A. Rami, C. Roux, M. A. Mahly, A. Saoiabi, T. Coradin and A. Laghzizil, *Journal of Hazardous Materials*, 2010, **181**, 736–741.
- 3 F. Pourpoint, C. Gervais, L. Bonhomme-Coury, T. Azaïs, C. Coelho, F. Mauri, B. Alonso, F. Babonneau and C. Bonhomme, *Appl Magn Reson*, 2007, **32**, 435–457.
- 4 K. Beshah, C. Rey, M. J. Glimcher, M. Schimizu and R. G. Griffin, *Journal of Solid State Chemistry*, 1990, **84**, 71–81.
- 5 J. Forsgren, U. Brohede, M. Strømme and H. Engqvist, *Biotechnology Letters*, 2011, **33**, 1265–1268.
- 6 U. Brohede, J. Forsgren, S. Roos, A. Mihranyan, H. Engqvist and M. Strømme, *Journal of Materials Science: Materials in Medicine*, 2009, **20**, 1859–1867.
- 7 M. Lilja, J. H. Sörensen, U. Brohede, M. Åstrand, P. Procter, J. Arnoldi, H. Steckel and M. Strømme, *Journal of Materials Science: Materials in Medicine*, 2013, **24**, 2265–2274.
- 8 J. H. Sörensen, M. Lilja, T. C. Sörensen, M. Åstrand, P. Procter, S. Fuchs, M. Strømme and H. Steckel, *Journal of Biomedical Materials Research Part B: Applied Biomaterials*, 2014, **102**, 1381–1392.
- 9 S. Tang, B. Tian, Q.-F. Ke, Z.-A. Zhu and Y.-P. Guo, *RSC Adv.*, 2014, **4**, 41500–41509.
- 10 M. Betsiou, G. Bantsis, I. Zoi and C. Sikalidis, *Ceramics International*, 2012, **38**, 2719–2724.
- 11 Y. Ryabenkova, N. Jadav, M. Conte, M. F. A. Hippler, N. Reeves-McLaren, P. D. Coates, P. Twigg and A. Paradkar, *Langmuir*, 2017, **33**, 2965–2976.
- 12 S. Sarda, F. Errassifi, O. Marsan, A. Geffre, C. Trumel and C. Drouet, *Materials Science and Engineering: C*, 2016, **66**, 1–7.
- 13 W. M. Chiridon, W. J. O'Brien and R. E. Robertson, *Journal of Biomedical Materials Research Part B: Applied Biomaterials*, 2003, **66**, 532–538.
- 14 Richard G. Compton and C. A. Brown, *Journal of Colloid and Interface Science*, 1995, **170**, 586–590.
- 15 K. Burns, Y.-T. Wu and C. S. Grant, *Langmuir*, 2003, **19**, 5669–5679.

- 16 M. Patra, R. Mukherjee, M. Banik, D. Dutta, N. A. Begum and T. Basu, *Colloids and Surfaces B: Biointerfaces*, 2017, **154**, 63–73.
- 17 V. Nipun Babu and S. Kannan, *International Journal of Biological Macromolecules*, 2012, **51**, 1103–1108.
- 18 H. Shen, Y. Liu, H. Zhang, P. Ding, L. Zhang, L. Zhang and J. Ju, *Journal of Pharmacy and Pharmacology*, 2019, **71**, 765–773.
- 19 M. S. Blois, *Nature*, 1958, **181**, 1199–1200.
- 20 M. I. Alvarez Echazú, C. E. Olivetti, C. Anesini, C. J. Perez, G. S. Alvarez and M. F. Desimone, *Materials Science and Engineering: C*, 2017, **81**, 588–596.
- 21 L. Forte, P. Torricelli, E. Boanini, M. Gazzano, K. Rubini, M. Fini and A. Bigi, *Acta Biomaterialia*, 2016, **32**, 298–308.
- 22 E. Sistanipour, A. Meshkini and H. Oveisi, *Colloids and Surfaces B: Biointerfaces*, 2018, **169**, 329–339.
- 23 P. Phatai, C. M. Futralan, S. Kamonwannasit and P. Khemthong, *J Sol-Gel Sci Technol*, 2019, **89**, 764–775.
- 24 V. M. Wu, S. Tang and V. Uskoković, *ACS Appl. Mater. Interfaces*, 2018, **10**, 34013–34028.
- 25 R. V. Chernozem, M. A. Surmeneva, B. Krause, T. Baumbach, V. P. Ignatov, O. Prymak, K. Loza, M. Eppe, F. Ennen-Roth, A. Wittmar, M. Ulbricht, E. A. Chudinova, T. Rijavec, A. Lapanje and R. A. Surmenev, *Materials Science and Engineering: C*, 2019, **97**, 420–430.
- 26 L. Ploux, M. Mateescu, L. Guichaoua, J. Valentin, J. Böhmeler, K. Anselme, E. Champion, N. Pécourt, R. Chotard-Ghodsni and M. Viana, *J Mater Sci*, 2016, **51**, 8861–8879.
- 27 J.-L. Jiang, Y.-F. Li, T.-L. Fang, J. Zhou, X.-L. Li, Y.-C. Wang and J. Dong, *Inflamm. Res.*, 2012, **61**, 207–215.







## Chapter 4

Elaboration of hybrid  
hydroxyapatite – biologically  
active molecules coating on  
Ti6Al4V titanium alloys



## 4. Elaboration of hybrid hydroxyapatite – biologically active molecules coatings on Ti6Al4V titanium alloys

### Outline

4. Elaboration of hybrid hydroxyapatite – biologically active molecules coatings on Ti6Al4V titanium alloys.....	149
4.1 Introduction.....	151
4.2 Deposition of biomimetic hydroxyapatite in SBF.....	151
4.2.1 Elaboration of the method.....	151
4.2.2 Characterization of SBF deposited in 1.5-SBF on Ti6Al4V.....	162
4.3 Incorporation of biologically active molecules.....	166
4.3.1 Introduction.....	166
4.3.2 Incorporation of BAM during the synthesis.....	166
4.3.3 Post-synthesis adsorption of BAM.....	173
4.3.4 Conclusions.....	178
4.4 Biological activity of hydroxyapatite-baicalein coatings.....	180
4.4.1 Introduction.....	180
4.4.2 Antioxidant activity.....	180
4.4.3 Antibacterial activity.....	181
4.4.4 Preliminary testing of the cytotoxicity of hybrid coatings.....	186
4.5 Conclusions.....	190
4.6 Summary.....	191
References.....	195



## 4.1 Introduction

In this chapter, we will focus on the development of a hybrid coating deposited on Ti6Al4V titanium alloy consisting of hydroxyapatite and natural biologically-active molecules. The chosen method has been to form hydroxyapatite from a supersaturated solution called Simulated Body Fluid (SBF) whose composition was directly derived from the one used by Kokubo et al<sup>1</sup>. These authors have shown that the obtained hydroxyapatite was suitable with osteoblast growth, so that the material was qualified as biomimetic. SBF closely resemble the inorganic composition and concentration of blood plasma. The presence of ions such as  $\text{Na}^+$  and  $\text{Mg}^{2+}$ , and  $\text{CO}_3^{2-}$  induces substitutions, leading to a carbonated calcium-deficient hydroxyapatite. This method of deposition is widely used in the literature, but with different parameters depending of the authors. Surface pretreatment, temperature of deposition, composition and concentration of the solutions, are particularly discussed in the literature<sup>2-5</sup>. In this chapter, we will investigate different surface treatments with the composition of SBF derived from the one used by Kokubo et al<sup>1</sup>, in order to determine the best suited for HAP deposition and adhesion. Secondly, the composition of the solution will be modified, mainly the carbonate content. The biomimetic coating has been deeply characterized. The second part of this chapter deals with the incorporation of BAM (rosmarinic and chlorogenic acids, baicalin and baicalein). In [Chapter 3](#), we proved that the incorporation of BAM is possible either concomitantly with HAp synthesis or by adsorption on pre-synthesized HAp. The same methodology will be used here. First, the incorporation of BAM during synthesis by adding the molecules directly in the SBF will be investigated. Then, the post-synthesis adsorption of baicalin and baicalein on deposited HAp coatings has been performed. Hybrid coatings synthesized following both methods will be characterized and compared. The last part of this chapter is the characterization of the biological properties of the hybrid materials. Drug release, antioxidant and antibacterial activities will be investigated. A preliminary study of osteoblasts adhesion and proliferation will also be presented.

## 4.2 Deposition of biomimetic hydroxyapatite in SBF

### 4.2.1 Elaboration of the method

Two parameters are important for the deposition of biomimetic hydroxyapatite in SBF: the formulation of the SBF solution and the pre-treatment of the surface of the alloy. In the literature, it is commonly reported that an alkali-heat treatment, consisting of first hydroxylation of Ti in NaOH as a first step followed by an annealing one at high temperature to crystallize titanium oxide, favors the deposition of HAp<sup>1,2</sup>. In this work, we have studied the effect of the annealing step on the deposition of HAp in a SBF whose composition is similar to the Kokubo's formulation of SBF<sup>1</sup> but 1.5 fold concentrated (1.5-SBF). The latter modification is expected to improve the deposition rate.

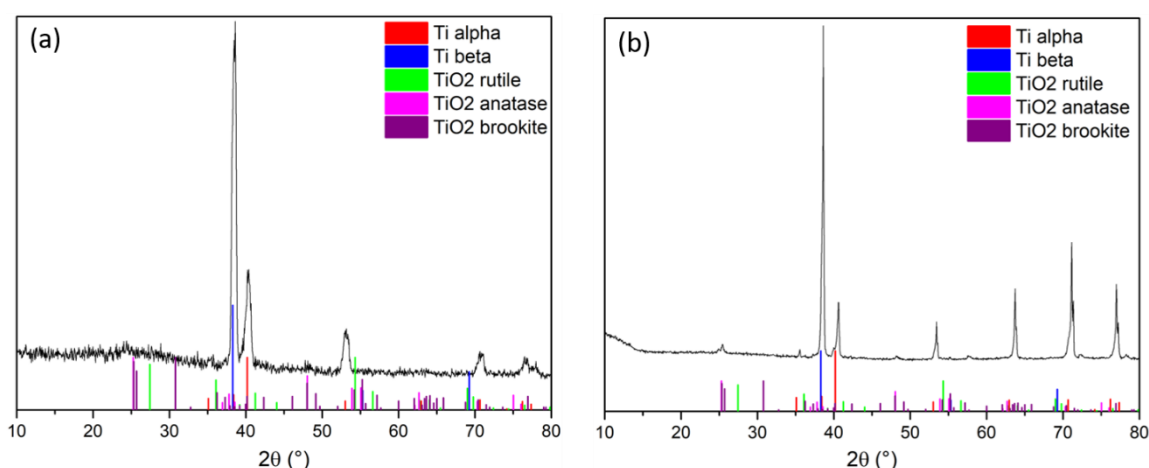
As mentioned in the literature review (Chapter 1), besides the original Kokubo's preparation of SBF, many derived composition have been used<sup>3,6,7</sup>. The main variable is the carbonate concentration. Consequently, we decided to compare the HAp deposition process using 1.5-SBF or a carbonate more concentrated solution. These two studies allowed us to determine the best parameters to obtain a thick and homogeneous layer of hydroxyapatite on the surface of the Ti alloy Ti6Al4V. The deposition duration and the renewal of the solution was also taken into account.

#### 4.2.1.1 Surface pre-treatment

##### 4.2.1.1.1 Surface preparation

Square plates of Ti6Al4V (1 cm<sup>2</sup>, provided by GoodFellow) were used as substrate for the deposition of HAp. They were polished at three different grid with silicon carbide papers (# 500, # 800 and # 1200). Plates were then soaked in a 5 M NaOH solution, at 60 °C for 24 hours (30 mL of solution for 8 plates). After this alkaline treatment, they were washed three times in distilled water and finally left 24 h in water at room temperature, before drying 24 h at 37 °C. For annealing process, alkali-treated samples were heated at 600 °C for 1 h under air, with a ramp of 5 °C/min, before cooling in the furnace.

**Figure 4.1** shows the X-ray diffraction pattern of plates before and after annealing. Diffraction peaks corresponding to  $\alpha$ -titanium and  $\beta$ -titanium are visible for the plate after alkali treatment. After annealing, the diffraction pattern of sample signs for a more crystalline materials, with narrower peaks and a better signal to noise ratio. Peak at 25 ° is characteristics of TiO<sub>2</sub> in an anatase and brookite mixture, both being “kinetics” phases of titanium oxide. Peaks are weak because titanium oxide is only present at the surface of the substrate. No peak of TiO<sub>2</sub> rutile are detected, probably because the duration of annealing treatment was not enough to transform anatase to rutile.

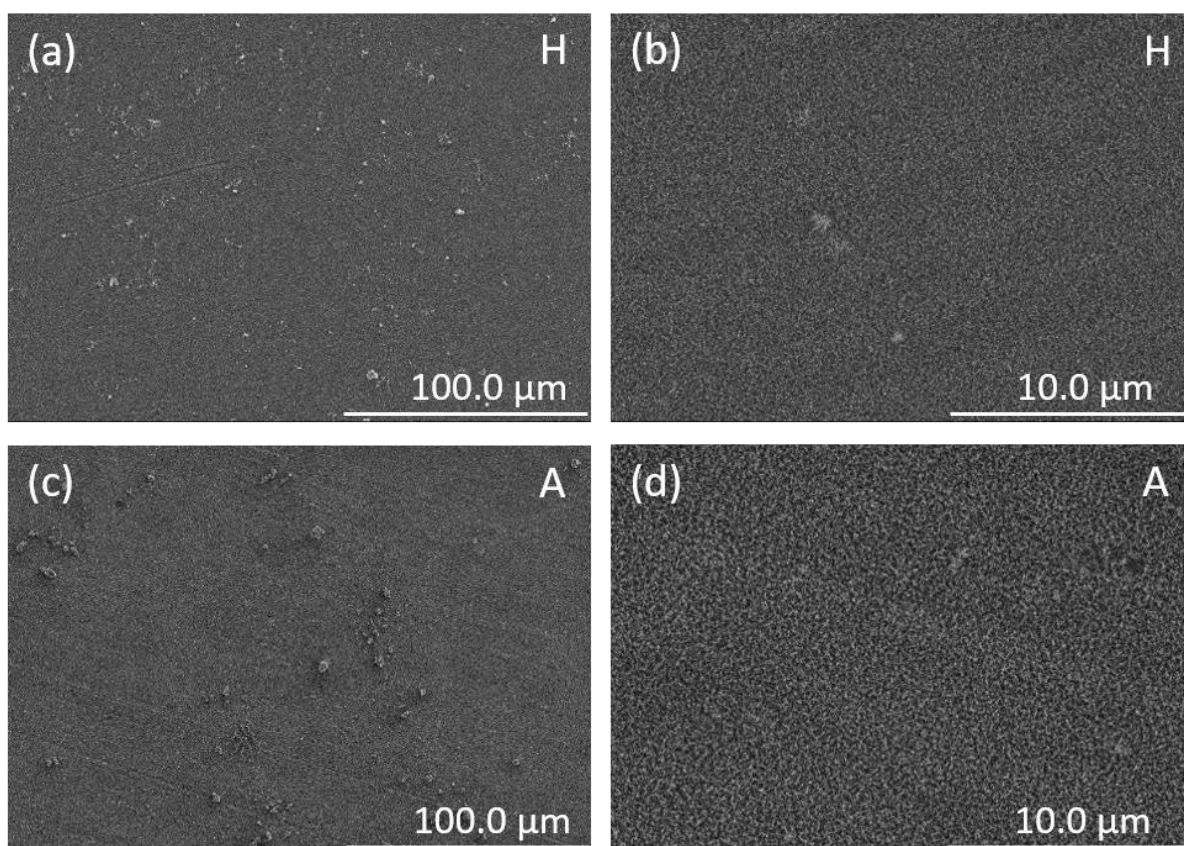


**Figure 4.1** X-ray diffraction patter of alkali-treated Ti6Al4V samples (a) before and (b) after annealing

The morphology of the substrates before and after annealing was observed by SEM (**Figure 4.2**). There is no notable difference between the surfaces. At low magnification, both surfaces are rather flat



(Figure 4.2 (a) and (c)). At higher magnification, surfaces appear porous, probably as a consequence of NaOH pretreatment (Figure 4.2 (b) and (d)).



**Figure 4.2** SEM images of hydroxylated Ti6Al4V surfaces (a,b) before and (c,d) after annealing.

(H = hydroxylated; A = annealed)

#### 4.2.1.1.2 Deposition of hydroxyapatite

After surface pre-treatment, hydroxyapatite was deposited on the substrates in SBF concentrated 1.5 fold (1.5-SBF). We chose to concentrate the soaking solution in order to speed up the process. Samples were immersed vertically in the solution, with ratio surface/volume ratio  $S/V = 25 \text{ mL.cm}^{-2}$ . As samples are suspended vertically, the deposition of hydroxyapatite is possible on both faces of the substrate. The composition of SBF is reminded in **Table 4.1**. SBF was prepared in ultrapure water, and the pH was checked to be between 7.4 and 7.6. The amount of each constituent required for the preparation of the solution for 1 L is described in **Table 4.2**, with order of addition of the reagents. Deposition was performed in high density polyethylene bottles (Thermo Scientific™ Nalgene™ Wide-Mouth HDPE Packaging Bottles), because hydroxyapatite may crystallize on the surface of glass bottles. The solution of deposition was renewed every 48 h by freshly prepared SBF. Plates were withdrawn from the medium after either 7 days or 14 days of deposition. They were washed three times in distilled water,

and dried 24 h at 37 °C. The morphology of the deposited layer was observed by SEM, and the crystalline phase was controlled by XRD and Raman spectroscopy.

Concentration (mmol.L <sup>-1</sup> )	Na <sup>+</sup>	K <sup>+</sup>	Ca <sup>2+</sup>	Mg <sup>2+</sup>	Cl <sup>-</sup>	HCO <sub>3</sub> <sup>2-</sup>	HPO <sub>4</sub> <sup>2-</sup>	SO <sub>4</sub> <sup>2-</sup>
Blood plasma	142.0	5.0	2.5	1.5	103.0	27.0	1.0	0.5
SBF <sup>1</sup>	142.0	5.0	2.5	1.5	147.8	4.2	1.0	0.5

**Table 4.1** Ionic composition of SBF and comparison with blood plasma

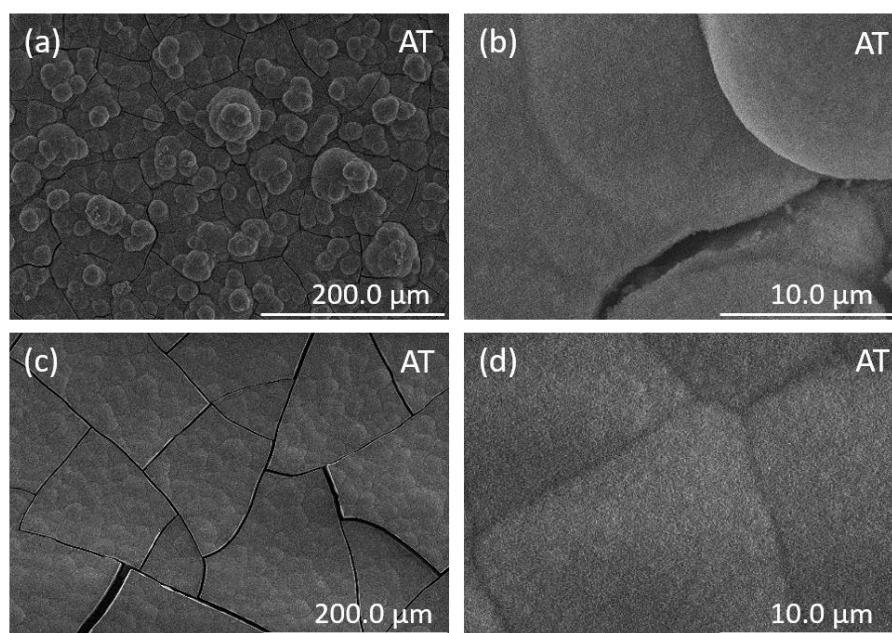
Product	Weight (g)
NaCl	12.054
NaHCO <sub>3</sub>	0.528
KCl	0.338
KH <sub>2</sub> PO <sub>4</sub>	0.248
Mg <sub>2</sub> Cl <sub>2</sub> , 6 H <sub>2</sub> O	0.466
HCl 1M	15 mL
CaCl <sub>2</sub> , 2 H <sub>2</sub> O	0.582
Na <sub>2</sub> SO <sub>4</sub>	0.108
TRIS	9.046
HCl 1M	50 mL

**Table 4.2** 1.5-SBF preparation for 1 L of solution

**Figure 4.3** and **Figure 4.4** show the deposited layer of material after immersion in 1.5-SBF of the hydroxylated surfaces and the hydroxylated/annealed surfaces, respectively. After 7 days of deposition on the non-heat-treated surface (**Figure 4.3 (a)**), we observe a bottom layer covered by a cauliflower-shaped material, more visible on the image at higher magnification (**Figure 4.3 (b)**). After 14 days (**Figure 4.3 (c)**), the material is denser, consisting of plates separated by cracks. The cauliflower shape is still visible, but the surface is fairly flat, compare to the surface after 7 days of deposition. The image at higher magnification (**Figure 4.3 (d)**) show the morphology of the head of the cauliflower. Some cracks are formed after 14 days, probably due to drying of a very dense and thick layer. The material grows from the bottom to the top, which is visible on **Figure 4.3 (a)**. Between 7 days and 14 days, this growing material densifies at the surface. The morphology is typical for hydroxyapatite synthesized in supersaturated solutions<sup>1,2,6</sup>. As described by Kokubo, hydroxyapatite is formed by the crystallization at the surface of the substrate. Erreur ! Source du renvoi introuvable. **Figure 4.4 (a)** shows the alkali-treated and annealed surface after 7 days of deposition. It is visible that the surface is not homogeneously covered, as the deposited material is only located at the center of the image, looking like a small island. The thickness of the material increases from the edges of the spot to the center. We

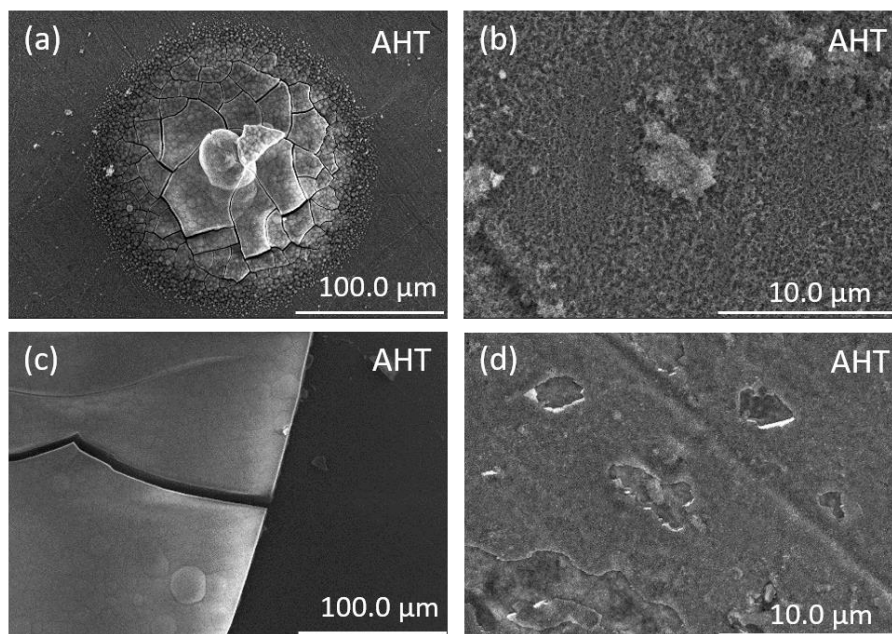
can recognize the cauliflower-shaped material at the center, with plates of dense material in the middle-height of the small island. At the edges, on the bottom, small round particles are visible. On this image, we can observe all the steps of the formation of the synthesized material after deposition in SBF. The image at higher magnification (**Figure 4.4 (b)**) shows a non-covered part. The morphology is the same than the Ti6Al4V surface after hydroxylation and annealing, before deposition, showing that no material has been deposited. **Figure 4.4 (c)**, showing the annealed surface after 14 days of deposition, is split in two parts. On the left side, we can observe a layer of deposited material, with a crack between two dense plates. The right side of the image consists of the non-covered surface of Ti6Al4V. A difference in height between the two parts of the image is clearly visible, suggesting that the deposited layer is thick. **Figure 4.4 (d)** shows a plate with very thin layer of material, and some small spots of deposited material, that charge under the electronic flow of the microscope.

From the observation of the images presented in **Figure 4.4**, we can conclude that the annealing step does not favor the uniform deposition of hydroxyapatite. Surfaces are not fully covered by the material but a very dense and thick layer can be formed locally. On the contrary, surfaces that were only hydroxylated are fully covered with a homogeneous layer of material (**Figure 4.3**).



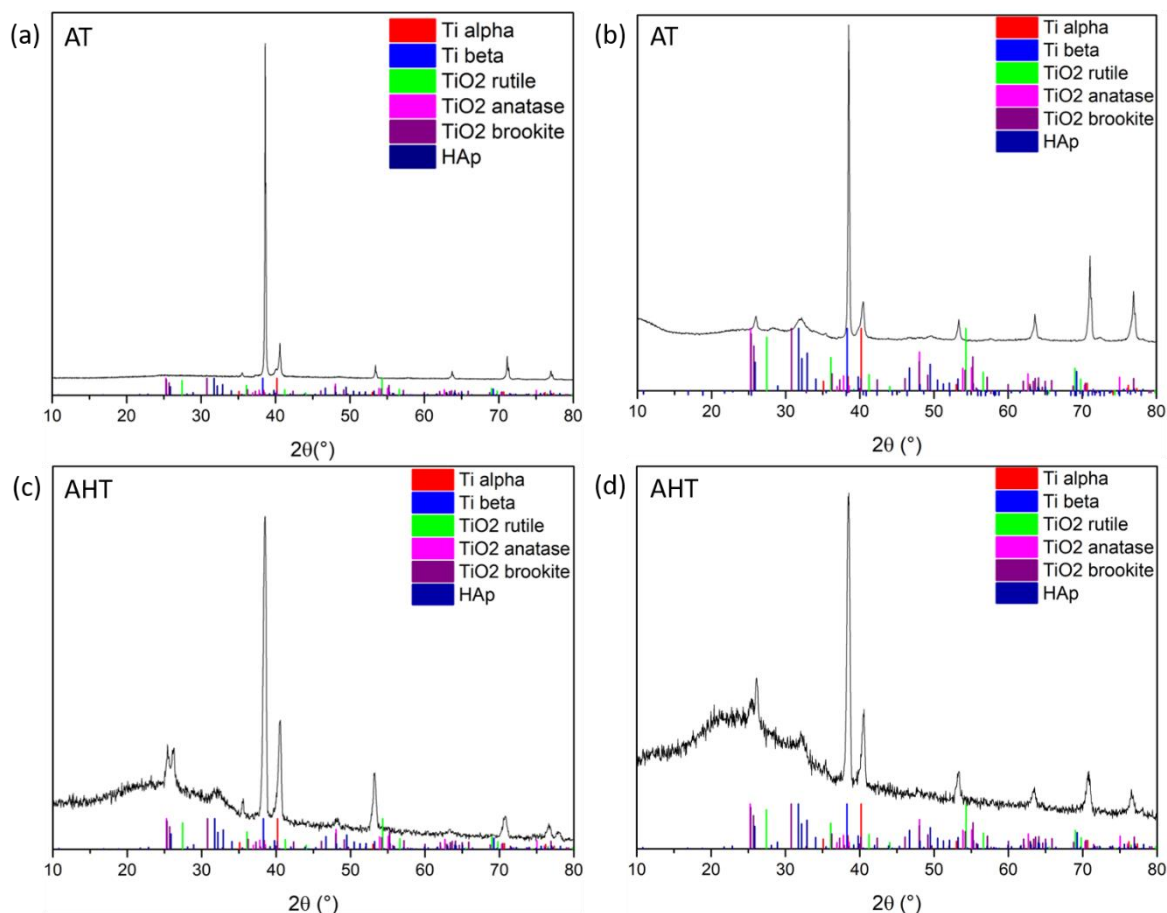
**Figure 4.3** SEM images of hydroxylated Ti6Al4V plates after (a,b) 7 days and (c,d) 14 days of soaking in 1.5-SBF





**Figure 4.4** SEM images of hydroxylated and annealed Ti6Al4V surfaces after 7 days (a), (b) or 14 days (c), (d) of soaking in 1.5-SBF

X-ray diffractograms of surfaces after deposition are presented in **Figure 4.5**. Diffraction peaks of  $\alpha$ -Ti and  $\beta$ -Ti are visible on all the surfaces, as well as peaks of  $\text{TiO}_2$  anatase and brookite for annealed substrates (**Figure 4.5 (c) and (d)**). After 7 days of soaking of the alkali-treated plate, no peak of hydroxyapatite is visible (see **Figure 4.5 (a)**), whereas after 14 days (see **Figure 4.5 (b)**) diffraction peaks are visible at  $26^\circ$  and  $31^\circ$ , confirming the deposition of hydroxyapatite. On the alkali-treated and annealed substrate, peaks of HAp are visible at  $31^\circ$  and  $26^\circ$  for both soaking duration (**Figure 4.5 (c) and (d)**). In addition, there is a broad band between  $20$  and  $35^\circ$  on both diffractograms after 7 and 14 days. This commonly refers to an amorphous contribution, probably an amorphous calcium phosphate in that case. From XRD results, it can be concluded that 14 days of soaking on non-annealed substrates seems to be the most effective method to obtain pure hydroxyapatite.

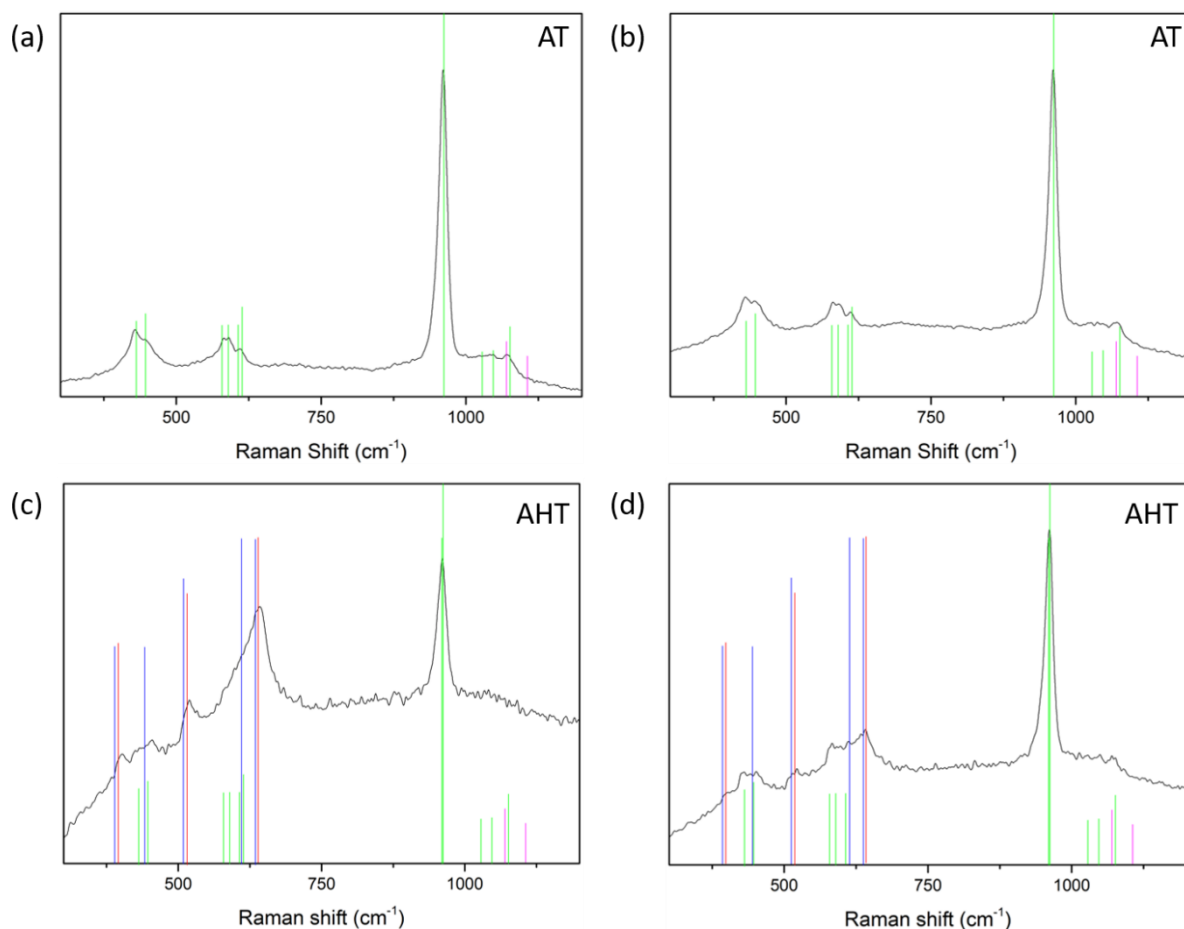


**Figure 4.5** X-ray diffractograms of substrates after 7 days (a,c) and 14 days (b,d) of deposition in 1.5-SBF: (a) and (b) alkali-treated Ti6Al4V; (c) and (d) alkali-treated and annealed Ti6Al4V.

(AT= alkali-treated; AHT = alkali-heat-treated)

Raman spectra of surfaces after deposition are presented in **Figure 4.6**. The apparatus used is equipped with an optical microscope and an optical fiber, which allows precise control of the surface area to be analyzed. As previously pointed out on the SEM images, we know that annealed substrates lead to the formation of un-homogeneous surfaces after soaking. This was confirmed by optical microscopy analyses. However, thanks to the optical fiber, Raman analyses were performed only areas with deposited material. Spectra after deposition for 7 days on the non-annealed substrates and annealed substrates are similar (see **Figure 4.6 (a) and (b)**), characterized by the intense phosphate vibration  $\nu_1$  at  $960\text{ cm}^{-1}$ , typical of hydroxyapatite. Other phosphate vibrations in HAp are also visible, at  $430$  and  $448\text{ cm}^{-1}$  ( $\nu_2$ ), between  $579$  and  $591\text{ cm}^{-1}$  ( $\nu_4$ ), and at  $1048$  and  $1075\text{ cm}^{-1}$  ( $\nu_3$ )<sup>8</sup>. A peak at  $1070\text{ cm}^{-1}$ , corresponding to the  $\nu_1$  vibration of  $\text{CO}_3^{2-}$  is found, indicating the presence of type B carbonate substitution<sup>9</sup>. The intense  $\nu_1$  vibration at  $960\text{ cm}^{-1}$  is also visible on spectrum after 7 days of deposition on annealed substrates (see **Figure 4.6 (c) and (d)**). We can note the presence of the vibrations corresponding to  $\text{TiO}_2$ , anatase and brookite. Peaks of carbonate are absent. After 14 days

of deposition, signals of  $\text{TiO}_2$  are still present, but with a weaker relative intensity. Besides the  $\nu_1$  phosphate vibration,  $\nu_2$ ,  $\nu_3$  and  $\nu_4$  vibrations are also visible. Carbonates are hardly detected. Altogether, Raman analysis confirms that the deposition of HAp is more efficient on non-annealed surfaces.



**Figure 4.6** Raman spectra of substrates after 7 days (a), (c) or 14 days (b), (d) of deposition in 1.5-SBF: (a) and (b) alkali-treated Ti6Al4V; (c) and (d) alkali-treated and annealed Ti6Al4V.

Green lines: phosphate vibration of hydroxyapatite<sup>8</sup>; pink lines: carbonates vibration in carbonated hydroxyapatite<sup>10</sup>; blue and red lines: vibrations of titanium oxide (brookite and anatase respectively<sup>11</sup>).

(AT= alkali-treated; AHT = alkali-heat-treated)

#### 4.2.1.1.3 Conclusion: choice of the surface pretreatment

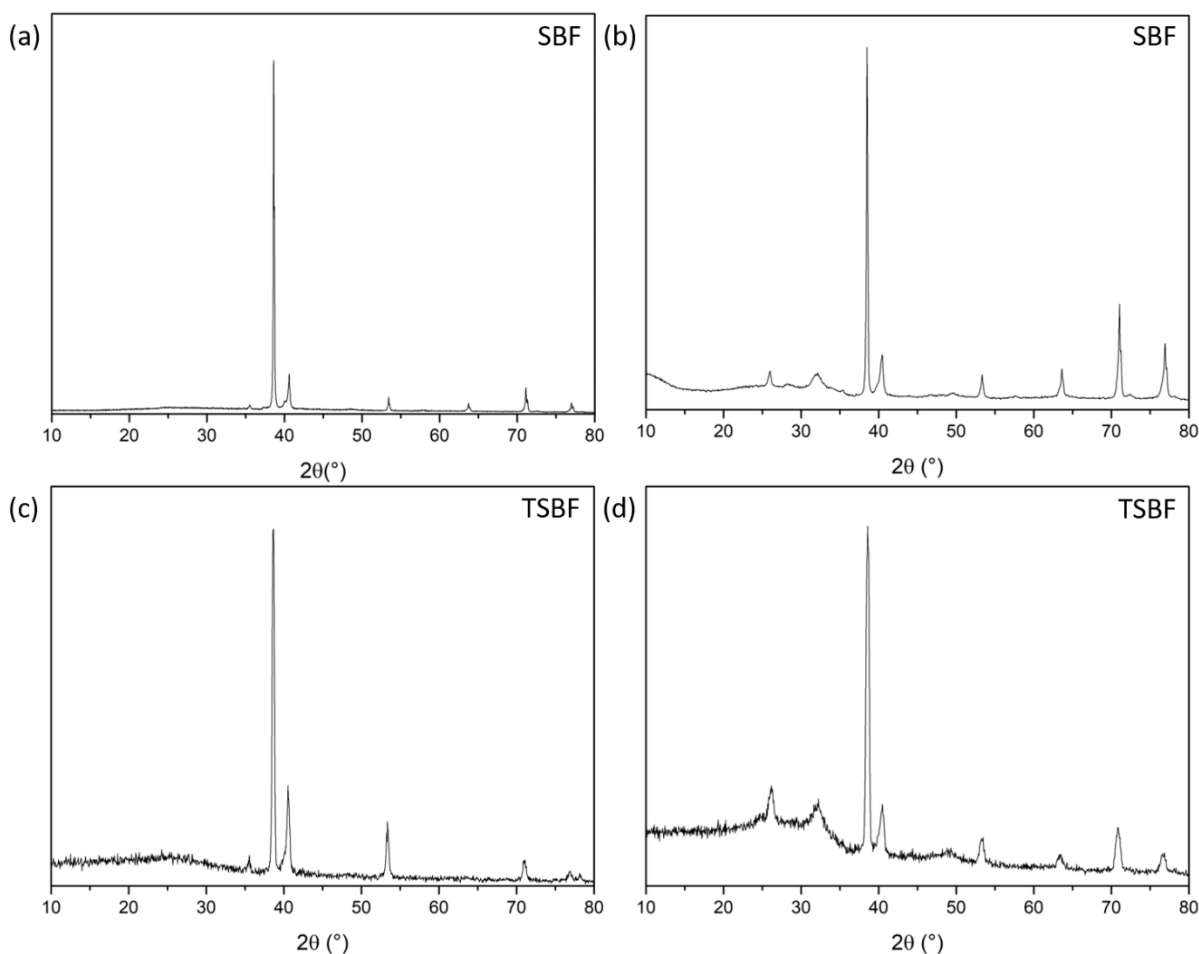
In the latter part of the work we have investigated the effect of alloy surface pretreatment on the deposition of hydroxyapatite from SBF. In the literature, it is commonly assumed that the hydroxylation of Ti in NaOH allows a good crystallization of hydroxyapatite on the surface, thanks to the exchange of  $\text{Na}^+$  ions with  $\text{Ca}^{2+}$ <sup>1,2</sup>. Post hydroxylation annealing at high temperature is sometimes suggested, in order to crystallize an intermediate amorphous sodium titanate layer into titanium oxide.

Here, after annealing, we obtained a mixture of anatase and brookite. Crystallization of  $\text{TiO}_2$  was visible on the X-ray diffractogram, and the mixture of phases was also seen on the Raman analysis. In contact with 1.5-SBF, hydroxylated surfaces were fully homogeneously covered with hydroxyapatite while deposition on annealed surface was not efficient. Our results are slightly different from those obtained in the systematic study from Pattanayak *et al.*<sup>2</sup>. The authors varied the pretreatment step pH from acidic to alkaline, and the effect of heat treatment of the titanium plates. For an alkaline pretreatment, they observed the deposition of hydroxyapatite in SBF, which is consistent with our study. The difference with our findings deals with the heat treatment: despite the fact we used the same conditions, they reported that a thicker layer of hydroxyapatite was deposited on heat treated plates. In our study, heat treatment is unfavorable, because the deposited layer is not homogeneous.

#### 4.2.1.2 Influence of the composition of the soaking solution

The conventional composition of SBF contains 147.8 mM of  $\text{Cl}^-$  and 4.2 mM of  $\text{CO}_3^{2-}$ <sup>12</sup>. The latter carbonate concentration is lower than the one in blood plasma (i.e. 27 mM), and was modified by several authors. For instance, Tas *and coll.*<sup>6</sup> suggested that 27 mM and 103 mM of  $\text{CO}_3^{2-}$  and  $\text{Cl}^-$  respectively led to increase the deposition rate of a biomimetic hydroxyapatite. Consequently, we decided to compare two different soaking solution: SBF concentrated 1.5 fold (1.5-SBF) and the solution used by Tas and coll. (TSBF) concentrated 1.5 fold (1.5-TSBF). Solutions were renewed every 48 h with freshly prepared 1.5-SBF and 1.5-TSBF. Plates were withdrawn after 7 and 14 days of soaking and characterized by XRD and Raman spectroscopy.

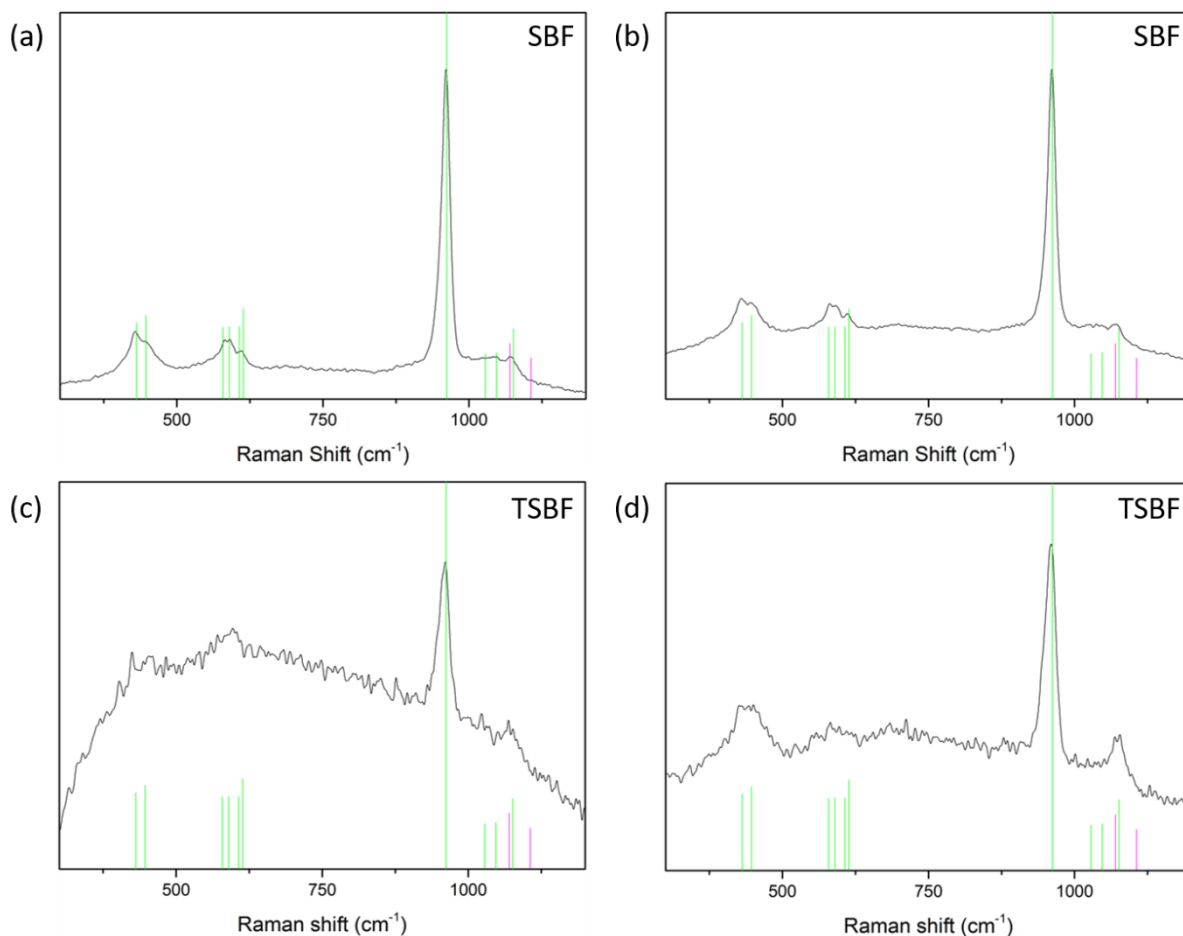
First of all, we observed by optical microscopy that surfaces after deposition in 1.5-TSBF were not homogeneously covered with the deposited material. X-ray diffractograms of surfaces after deposition in 1.5-TSBF are presented in **Figure 4.7**, and compared with surfaces after deposition in 1.5-SBF (**Figure 4.7 (a)** and **(b)** already shown in 4.2.1.1.2). After 7 days of deposition, diffraction peak of HAp at  $26^\circ$  and  $31^\circ$  are absent from the diffractogram (see **Figure 4.7 (c)**), that may be explained by several hypotheses: either the deposited layer is too thin or amorphous. More, as evidenced by optical microscopy analysis, the layer was not continuous. The amount of calcium phosphate deposited on the surface was maybe too small to be detected by diffraction. On the contrary, after 14 days of soaking, HAp peaks at  $26^\circ$  and  $31^\circ$  are clearly visible (see **Figure 4.7 (d)**), suggesting a significant deposition of HAp.



**Figure 4.7** X-ray diffractograms of substrates after 7 days (a), (c) or 14 days (b), (d) of deposition in 1.5-SBF (a), (b) or 1.5-TSBF (c), (d)

The Raman signature of samples after soaking in 1.5-TSBF are significantly different from those obtained after deposition in 1.5-SBF, as seen in **Figure 4.8**. On both spectra after 7 days and 14 days, **Figure 4.8 (c) and (d)** respectively, the noise is very important. After 7 days, the  $\nu_1$  vibration of phosphate is distinguishable, while other phosphate vibrations are absent, or merged in the noise. After 14 days, besides the  $\nu_1$  vibration at  $960\text{ cm}^{-1}$ ,  $\nu_2$  vibration at  $430\text{ cm}^{-1}$  and  $\nu_3$  vibration at  $1075\text{ cm}^{-1}$  are visible. The absence of clear peaks at  $1103\text{ cm}^{-1}$  and  $1070\text{ cm}^{-1}$  after 7 days indicates that carbonates are not incorporated into the hydroxyapatite in significant amounts. This is surprising, as carbonate concentration is higher in 1.5-TSBF than in 1.5-SBF: 27.0 mM and 4.2 mM, respectively. However, carbonate peaks may be evidenced after 14 days of soaking in SBF.





**Figure 4.8** Raman spectra of substrates after 7 days (a), (c) or 14 days (b), (d) of deposition 1.5-SBF (a), (b) or 1.5-TSBF (c), (d). Green lines: phosphate vibration of hydroxyapatite; pink lines: carbonates vibration in carbonated hydroxyapatite

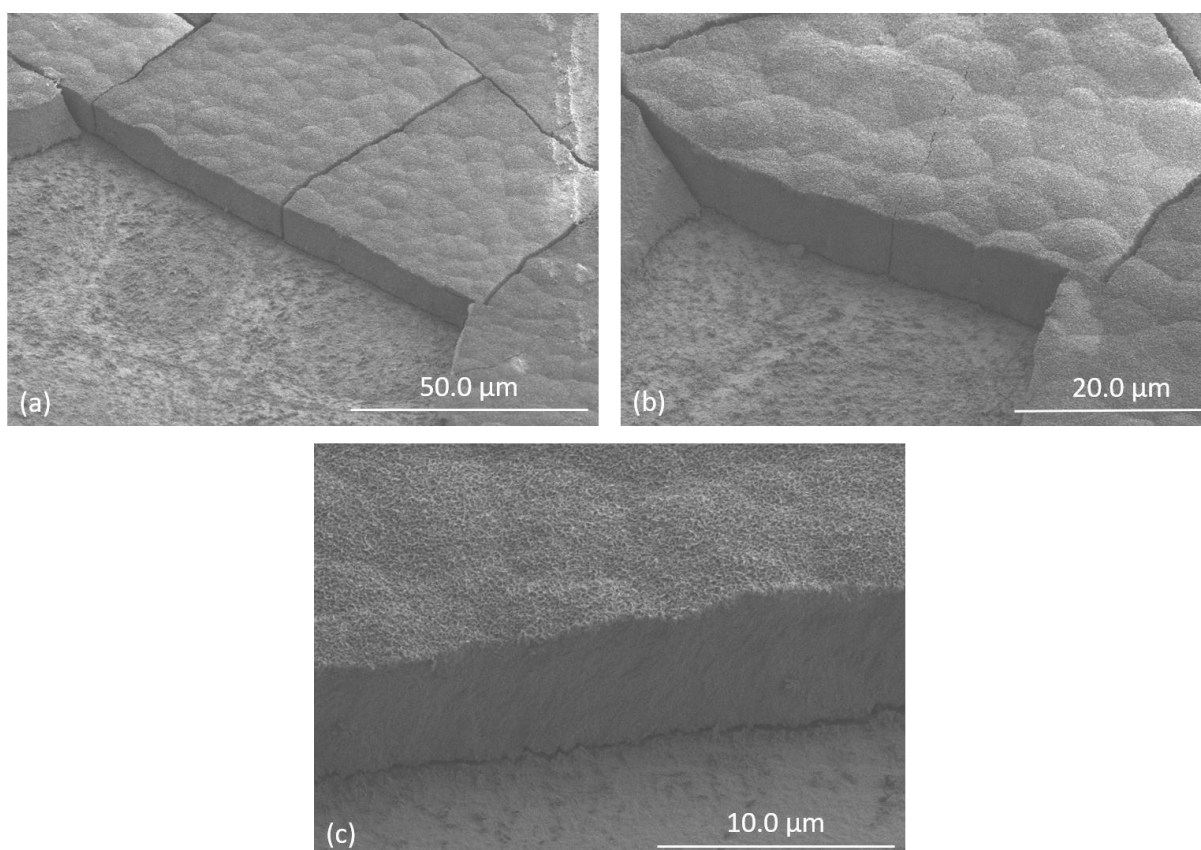
#### 4.2.1.1.3 Conclusion: choice of the composition of the SBF solution

Surfaces coated by deposition in 1.5-TSBF were not observed by SEM as we have already seen that they were not homogeneously covered by optical microscopy. Contrary to what it is reported by Jalota et al.<sup>6</sup>, we did not find that a higher concentration of carbonates was favorable to deposit HAp. The most plausible explanation is that the 1.5-TSBF solution was highly unstable, and a calcium phosphate material started to crystallize homogeneously in the solution, besides the heterogeneous crystallization on Ti alloy surfaces. On this basis, we decided to keep the conventional composition of SBF to deposit HAp on Ti surfaces for subsequent experiments.

#### 4.2.2 Characterization of SBF deposited in 1.5-SBF on Ti6Al4V

After the choice of the surface pretreatment of the substrate and the composition of the supersaturated soaking solution, HAp was synthesized in these conditions, i.e. alkali treatment of the plate before soaking in 1.5-SBF and further characterized.

To determine the thickness of the layer, scratches were made with a scalpel on the edges of the coating, in order to peel it off from the substrate. Samples were then observed by SEM-FEG, with an acceleration voltage of 1 keV, on a tilted sample-holder of 45 °, in order to observe the cross-section of the coating. Images at magnification x1k, x2k and x10k are presented in **Figure 4.9 (a), (b) and (c)** respectively. Taking into account the tilt angle (45°) of the measure ( $\text{thickness} = \frac{\text{measured distance}}{\sin 45}$ ), layer thickness is about 12  $\mu\text{m}$ . The layer is thicker than thin films deposited with sol-gel methods, but much thinner than what is deposited with plasma-spray deposition<sup>13</sup>. It is in the average of deposition from supersaturated biomimetic solutions.

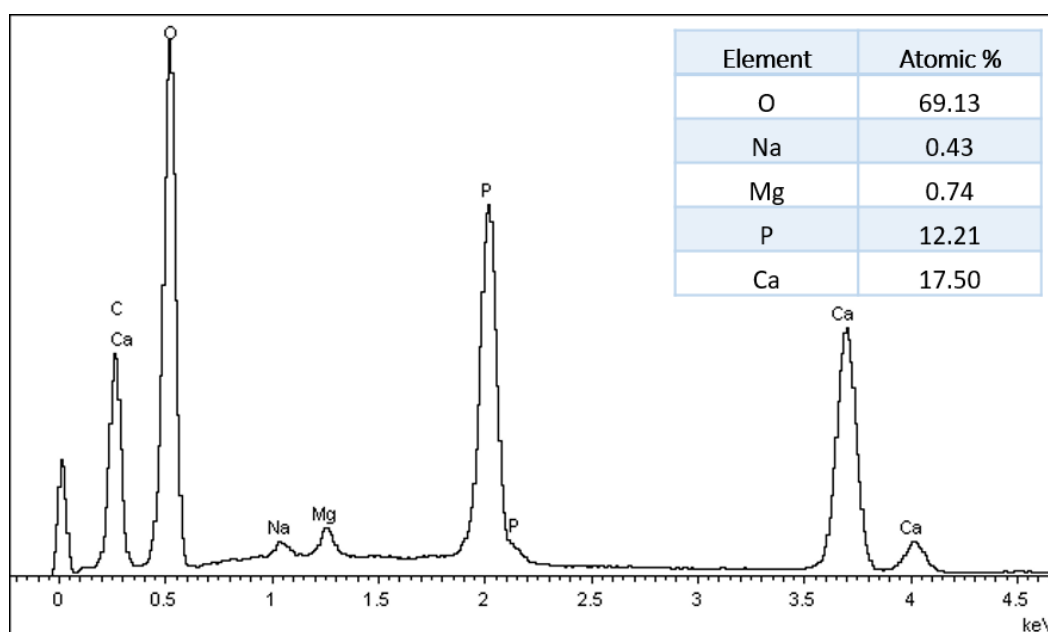


**Figure 4.9** SEM images of HAp layer after 14 days of deposition of Ti6Al4V, tilt = 45 °. Magnification = x1k (a), x2k (b) and x10k (c)

The fine microstructure of the coating is visible on **Figure 4.9 (c)**. Spheroids at the top of the dense coatings are composed by needle-like particles. The cross-section of the coating shows a dense

microstructure without the presence of pores inside the layer, but it may be an artefact due to the scratching.

Energy-dispersive X-ray spectrum of HAp coating is presented in **Figure 4.10**. The absence of Ti peak confirmed the thickness of the coating is above 1 – 2  $\mu\text{m}$ , as it is the depth penetration of this analytical technique. The presence of Na and Mg peaks indicates that the HAp layer may be substituted. It is possible to calculate the ratio Ca/P in the coating, which is 1.4. As HAp might be substituted, we can also calculate the ratio cations/P, i.e.  $(\text{Ca}+\text{Na}+\text{Mg})/\text{P}$ , which is 1.5<sup>14</sup>. A stoichiometric hydroxyapatite possesses a Ca/P ratio of 1.67, and in biological HAp, the ratio is closer to 1.5. This suggests that HAp is calcium-deficient, with a biomimetic composition.



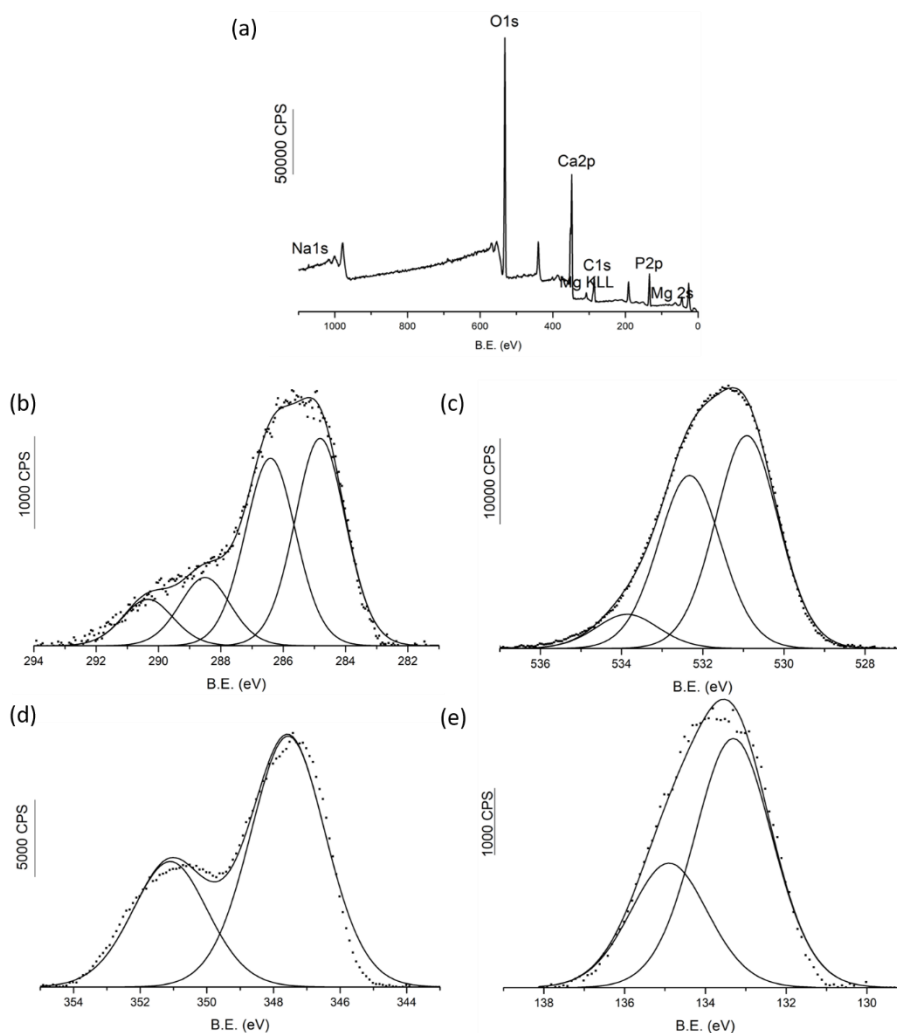
**Figure 4.10** EDS spectrum of HAp layer

The composition of the upper surface was characterized by X-ray Photoelectron spectroscopy (**Figure 4.11**). On the survey spectrum (**Figure 4.11 (a)**), we detect the presence of oxygen, carbon, calcium, phosphorous and magnesium. The presence of sodium and magnesium indicates a substitution of the upper layer of hydroxyapatite coating. Positions and atomic percentages of elements found in the HAp coatings are reported in **Table 4.3**. Calculated ratio Ca/P and Ca/O are compared with the one in stoichiometric HAp ( $\text{Ca}_{10}(\text{PO}_4)_6(\text{OH})_2$ ). The position of peaks of Ca and P are consistent with the position of peaks reported in the literature for stoichiometric HAp<sup>15</sup>. Ca/P ratio in HAp coating is comprised between 1.3 (**Table 4.3**) and 1.6 depending on the sample. It is lower than the one of stoichiometric hydroxyapatite (1.67). The ratio calculated by XPS reflects the upper surface of the material, which explains why the Ca/P ratio is lower than the one calculated from EDS. However, it confirms that the layer is calcium-deficient. On the contrary, the ratio Ca/O is equal to the ratio Ca/O in stoichiometric

hydroxyapatite. The presence of carbon, which is normally absent in hydroxyapatite, may be due from the presence of adventitious organic contamination, because samples were stored in air after synthesis, or from the presence of carbonates. The peak of C 1s is composed by four contributions: C-C and C-H at 284.8 eV, C-O at 286.4 eV, C=O at 288.5 eV and metal carbonates at 290.3 eV. The contribution of metal carbonates represents 9.1 % of the total peak of carbon in the hydroxyapatite layer. It means that the adventitious carbon contamination represents 90.9 % of the total of carbon. Considering the atomic percentage of carbon in the hydroxyapatite layer, the percentage of adventitious carbon contamination is 14.2 % of the total amount of atoms in hydroxyapatite layer. Moreover, the presence of carbonates confirms the carbonation of the hydroxyapatite coating synthesized in 1.5-SBF. Ca2p has spin-orbit components with Ca 2p<sub>1/2</sub> at 352 eV and Ca 2p<sub>3/2</sub> at 347 eV. P 2p has closely spaced spin-orbit components, responsible for the asymmetric peak envelope, and visible on the decomposition, with 2p<sub>1/2</sub> at 134.2 eV and 2p<sub>3/2</sub> at 133 eV.

Element	Sample	C 1s	O 1s	Ca 2p <sub>3/2</sub>	P 2p	Mg 1s	Na 1s		
BE (eV)	HAp	286.0	532.0	347.6	134.0	1304.2	1072.0	Ca/P	Ca/O
	Stoichiometric HAp <sup>15</sup>	285.4* (± 0.2)	531.8 (± 0.2)	347.8 (± 0.2)	133.8 (± 0.2)	-	-		
% At	HAp	15.6	50.4	19.3	14.5		0.2	1.3	0.4
	Stoichiometric HAp	-	59.1	22.7	13.6	-	-	1.67	0.4

**Table 4.3** Position and atomic percentages of carbon, oxygen, calcium, phosphorous, magnesium and sodium in hydroxyapatite coatings and comparison with stoichiometric hydroxyapatite<sup>15</sup> (\*carbon from adventitious organic contamination)



**Figure 4.11** X-ray photoelectron spectrum (a) survey, (b) C1s, (c) O1s, (d) Ca2p, and (e) P2p

Overall, we managed to synthesize a hydroxyapatite layer with biomimetic characteristics. The spheroids morphology observed with SEM is classical for hydroxyapatite deposited in supersaturated biomimetic solutions<sup>5</sup>. XRD and Raman spectroscopy confirmed the deposition of hydroxyapatite, with a certain extent of carbonatation, as it was visible on the Raman spectrum and XPS decomposition of carbene. EDX spectroscopy showed that the presence of Na and Mg in the deposited hydroxyapatite. That was expected, as we used the SBF solution containing  $\text{Na}^+$  and  $\text{Mg}^{2+}$  ions. From EDX, we calculated a ratio  $(\text{Ca}+\text{Mg}+\text{Na})/\text{P}$  of 1.5, which is also a biomimetic characteristic. The HAp in the coating is calcium-deficient, and substituted. The ratio was also calculated from XPS for the upper surface, and it is comprised between 1.3 and 1.5. XPS confirmed the carbonatation of hydroxyapatite, and revealed an important adventitious contamination.

## 4.3 Incorporation of biologically active molecules

### 4.3.1 Introduction

The incorporation of biologically active molecules in hydroxyapatite (or calcium phosphate) coatings has been well investigated in the last decades. Osteogenic factors, or antibacterial agents are incorporated with the goal to improve the properties of the inorganic material <sup>4,16–21</sup>. Several approaches are possible to incorporate molecules: incorporation during synthesis, post-synthesis covalent grafting, or adsorption. In this work, we decided to functionalize HAp coatings either by incorporation during synthesis, or by adsorption on the preformed HAp layer. Hydroxyapatite coatings were obtained after 14 days of deposition in 1.5-SBF on alkali-treated Ti6Al4V. Physicochemical properties of the obtained coatings are compared, then their antibacterial activities.

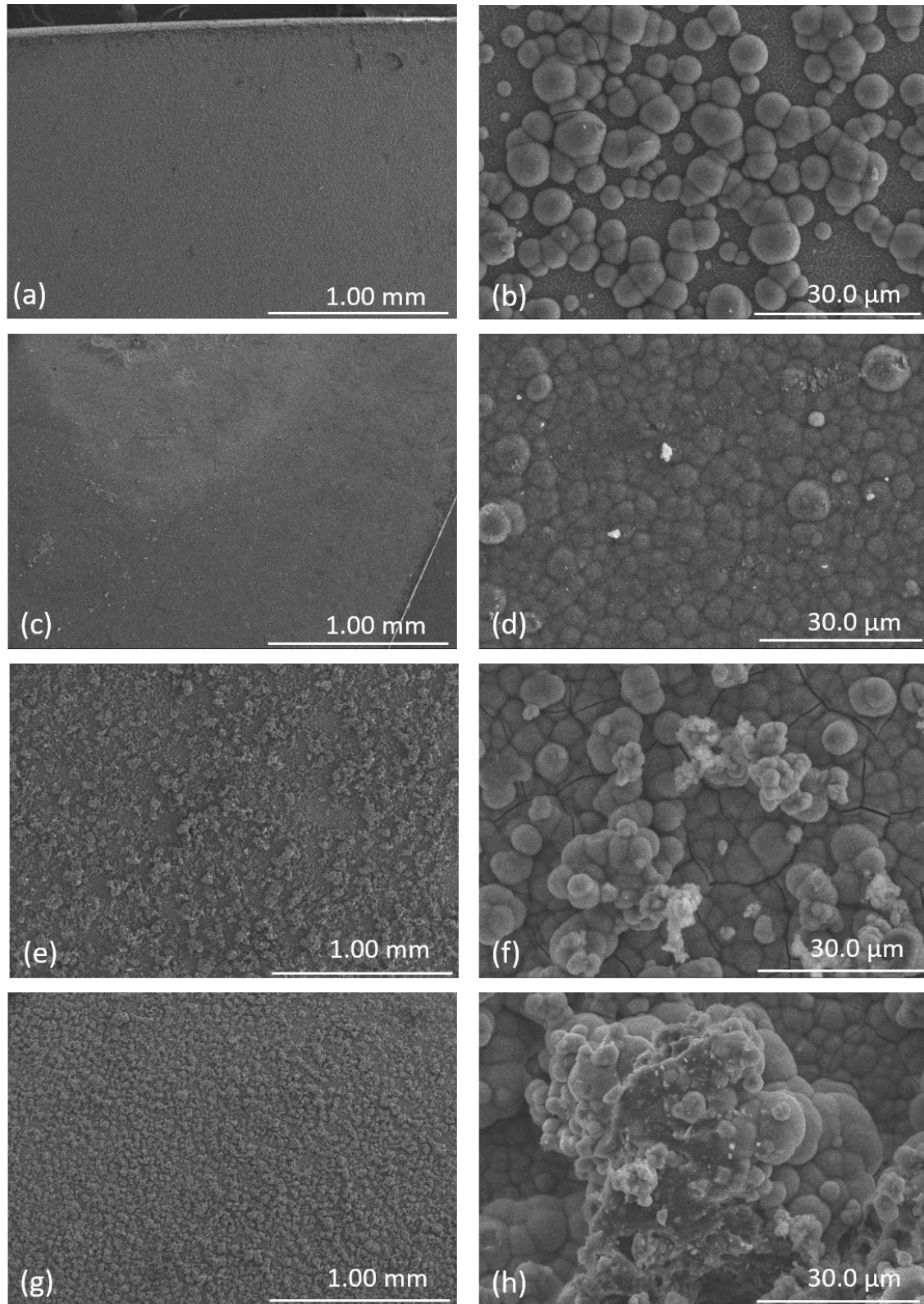
### 4.3.2 Incorporation of BAM during the synthesis

Rosmarinic and chlorogenic acids, baicalin and baicalein were incorporated in the hydroxyapatite coatings in a one-pot synthesis, by addition of the molecule in the SBF solution. Due to solubility issues, only one ratio between BAM and calcium have been tested, BAM:CA = 0.0075 that is comparable with the lowest ratio used for the incorporation of BAM on the HAp nanoparticles (see [Chapter 3](#)). This ratio corresponds to a BAM concentration in SBF of 0.019 mM. During 1.5-SBF preparation, BAM is the last component to be incorporated. It was checked that the presence of BAM did not modify the pH of the solution (pH  $\approx$  7.7). After 14 days of soaking of the plates in the solution which was renewed every 48 hours, morphology of the coatings were observed with SEM, and the crystallinity of the deposited mineral was checked by XRD.

On the SEM images at low magnification (**Figure 4.12 (a), (c), (e) and (g)**), it is visible than the quantity of deposited material is more important when baicalein and baicalin are present, compared to rosmarinic and chlorogenic acids. In presence of RA, the surface is not fully covered with material, as seen on **Figure 4.12 (b)** at 1.5 k of magnification. However, the spheroid morphology is comparable to HAp deposited in the absence of BAM. The coating formed in presence of CA covers the entire surface, with a spheroid-like morphology (**Figure 4.12 (d)**). With baicalin and baicalein, the surface is also fully covered (**Figure 4.12 (e) – (h)**). The bottom layers of both coatings are dense and homogeneous, with the spheroid morphology. However, the top surface is inhomogeneous. More, a disordered toping is visible in the presence of BA. It may be the sign of the reprecipitation of BA on the HAp layer (**Figure 4.12 (h)**).

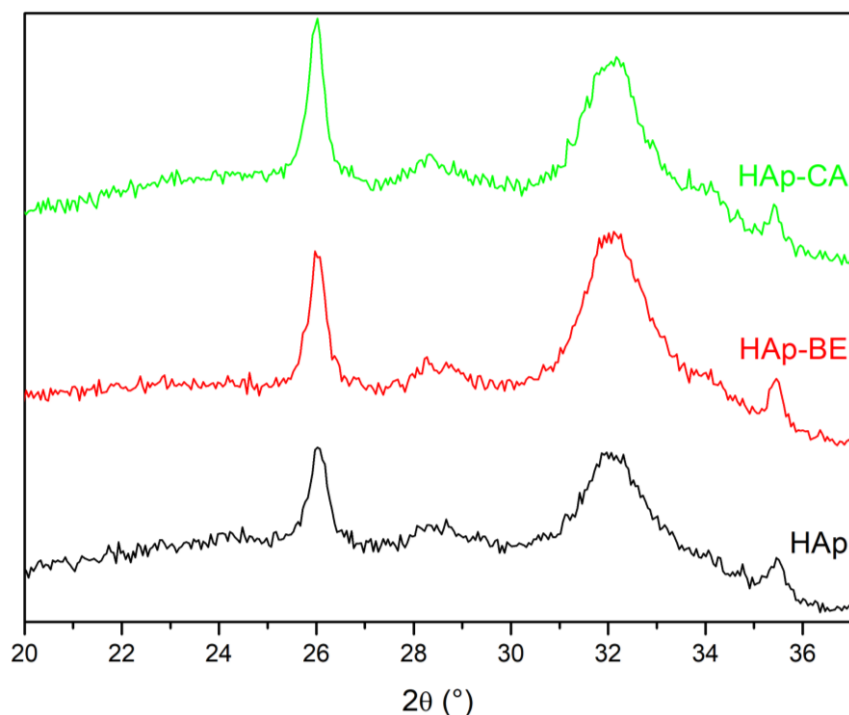
We tried to measure the thickness of the coating with BE by peeling, but it was not possible to perform the scratches, because the layer is more friable than pure HAp coatings.





**Figure 4.12** SEM images of HAp coatings with BAM incorporation: rosmarinic acid (a), (b); chlorogenic acid (c), (d); baicalein (d), (e); and baicalin (g), (h).

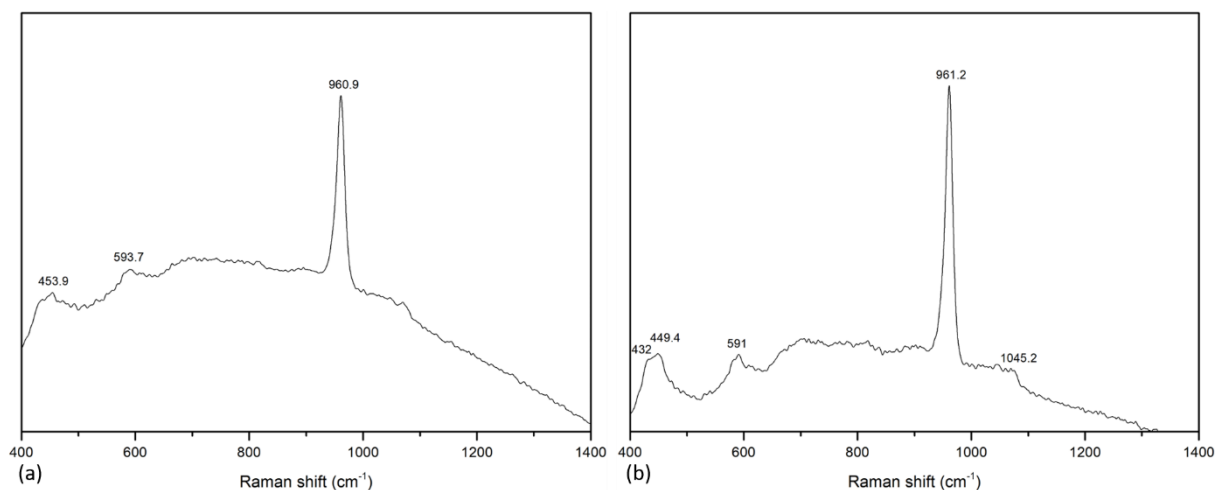
X-ray diffraction was performed to verify the crystalline phase of the deposited coating with chlorogenic acid and baicalein. **Figure 4.13** presents the X-ray diffractograms between 20 and 37 ° of HAp-CA and HAp-BE compared with pure HAp. For both coatings with BAM, the peak at 26 ° and the range at 32 ° are present. No difference between the three coatings are visible. The deposition of hydroxyapatite in presence of BAM is therefore confirmed.



**Figure 4.13** X-ray diffractograms of hydroxyapatite deposited on Ti alloy in presence of chlorogenic acid and baicalein, and comparison with pure hydroxyapatite.  $2\theta = 20 - 37^\circ$

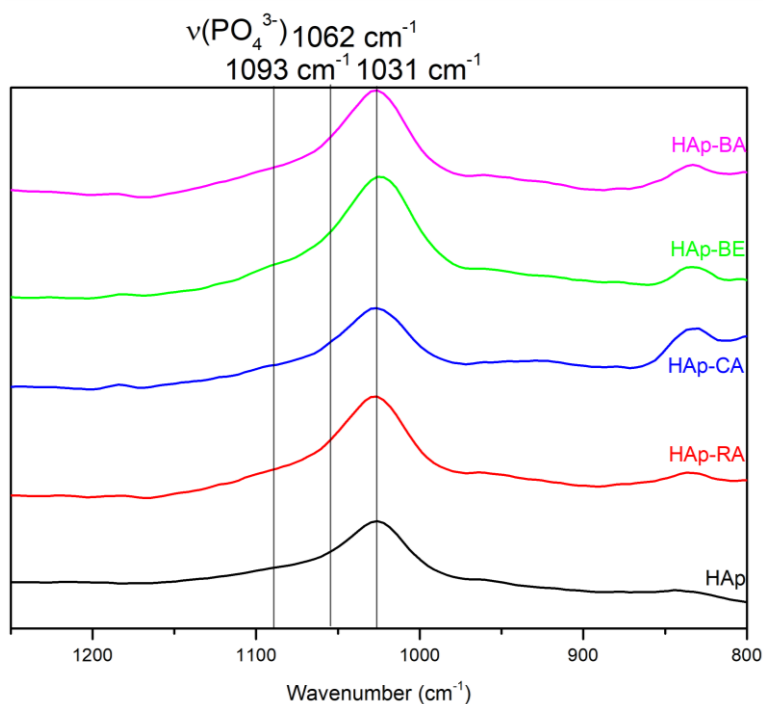
Raman spectroscopy was also used to analyse the coating deposited at the surface in presence of BAMs. However, it is worth noting that rosmarinic acid and baicalein are fluorescent under the Raman laser irradiation, and thus Raman analysis is not possible with those molecules. Nevertheless, Raman spectra of HAp-CA and HAp-BA presented in **Figure 4.14 (a)** and **(b)**, respectively, showed the phosphates vibrations in HAp, at c.a.  $450\text{ cm}^{-1}$ ,  $590\text{ cm}^{-1}$ ,  $960\text{ cm}^{-1}$  and  $1045\text{ cm}^{-1}$ <sup>8</sup>. This confirms the deposition of hydroxyapatite on Ti6Al4V alloy in presence of CA or BA in the 1.5-SBF solution.





**Figure 4.14** Raman spectra of HAp coatings deposited (a) in presence of chlorogenic acid (HAp-CA) and (b) baicalin (HAp-BA)

As Raman spectroscopy could not be performed for coatings deposited in presence of rosmarinic acid nor baicalein, InfraRed spectroscopy in attenuated total reflectance (ATR-FTIR) was used. **Figure 4.15** presents the overlay of spectra between 800 and 1300  $\text{cm}^{-1}$  for coatings deposited with the four molecules, and their comparison with pure HAp coating. The presence of the most intense phosphate vibration of HAp at 1031  $\text{cm}^{-1}$  is present on all spectra, as well as shoulder at 1062  $\text{cm}^{-1}$ . This confirms the deposition of hydroxyapatite in presence of BAM.



**Figure 4.15** ATR-IR spectra of BAM-incorporating HAp coatings, and comparison with pure HAp coating

The ratio Ca/P of hydroxyapatite deposited with BAM was measured by XPS for the top surface (analyzed depth < 11 nm) of the coatings. Ratio are equivalent for the 4 coatings, comprised between 1.1 and 1.2 (see **Table 4.4**). The ratio is decreased compared to the biomimetic HAp coating (*ca.* 1.5), meaning that either the calcium is enriched with phosphorous or depleted with calcium.

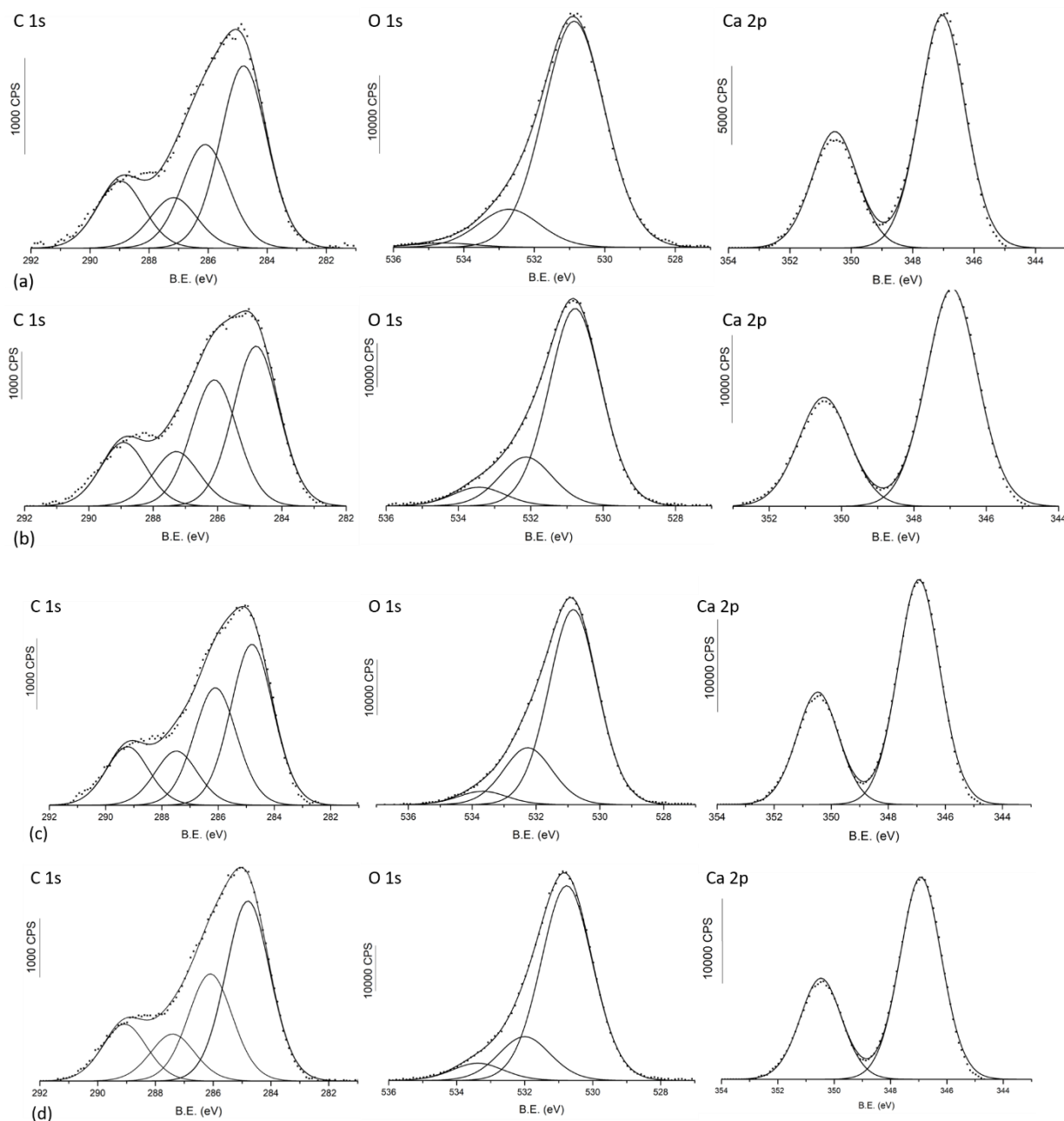
Sample	% At C	% At O	% At Ca	% At P	% At Ti	% At Mg	% At Na	Ca/P
HAp	15.6	50.4	19.3	14.5	0	3.4	0	1.3
HAp-RA	16.1	48.5	17.2	15.4	4.6	2.1	0	1.1
HAp-CA	18.8	48.0	17.9	14.8	0	0.5	0	1.2
HAp-BE	15.8	48.7	18.1	16.5	0	2.3	0	1.1
HAp-BA	16.4	48.9	18.9	15.4	0	2.9	0	1.2

**Table 4.4** Atomic % from XPS spectra for HAp-RA, HAp-CA, HAp-BE and HAp-BA coatings

The presence of Ti in the spectrum of HAp-RA confirmed SEM observations. Depth of analysis with of XPS being approximatively 10 nm, the HAp-RA coating is either ultra-thin, or inhomogeneous with the presence of non-coated areas. In accordance with SEM, the more probable hypothesis is the inhomogeneity of the coating.

C 1s and O 1s signals of coatings with BAM are similar to pure HAp coating, in their position and atomic percentages. Because of the important adventitious carbon contamination, the signal of carbon is difficult to compare between samples and analyze. Adventitious contamination is also comprised in oxygen spectra, which can explain the difficulties to compare between samples, especially because BAM are organic molecules that are in the same region than contamination. It would have been easier to see the incorporation of BAM if they possessed a heteroatom such as nitrogen, or chloride.

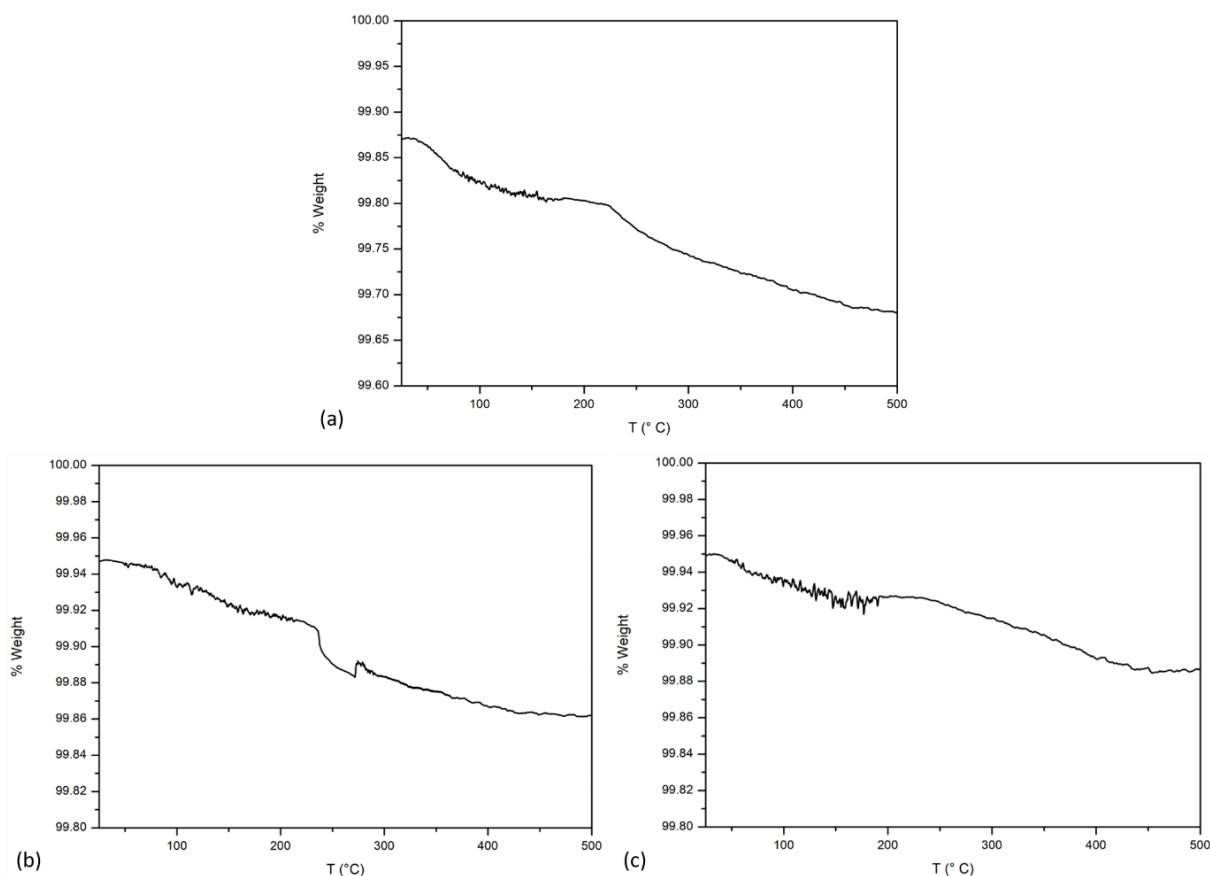
Overall, XPS indicate that, in presence of BAMS, the Ca/P ratio is significantly decreased compared to the pure HAp coating. One possibility to explain the decrease of Ca/P ratio is that, because of the lowest availability of calcium ions forming complexes, a P-rich calcium phosphate is formed. However it should be amorphous and in low amounts as it could not be evidenced by XRD nor by Raman.



**Figure 4.16** XPS spectra of HAP-RA (a), HAP-CA (b), HAP-BE (c), and HAP-BA (d) coatings

We tried to measure the incorporated quantity of BAM in the coating by thermogravimetric analysis, with the use of a TGA sorption/desorption apparatus. The loss of weight between room temperature and 600 °C was investigated. However, the weight difference is measured on the whole sample, meaning the substrate, the coating and the incorporated BAM. Considering the very low quantity of molecule that can be expected to be incorporated, the loss of weight is almost negligible. Moreover, unfortunately, the signal was very noisy, as seen in **Figure 4.17** for HAP-BE and HAP-BA. Moreover, the measured loss of weight was higher in the case of pure HAP coating than for coatings

containing BE or BA. From several measurements, we could estimate an incorporated quantity of baicalein of 0.2 mg for one coating but did not analyze further the other coatings.



**Figure 4.17** Thermogravimetric analysis of coatings on Ti6Al4V (a) pure Hap, (b) HAp-BE, and (c) HAp-BA

To sum up, the incorporation of BAM in HAp coating was possible via a one-pot synthesis, with incorporation of BAM directly in the deposition medium. The presence of BAM in the solution does not prevent the crystallization of hydroxyapatite, but some differences exist between pure HAp coating and coatings deposited with BAM. First of all, the morphology of coating is different, with a more fragile and thinner layer that does not cover the entire surface in the case of rosmarinic acid. XRD and Raman spectroscopy suggested the presence of hydroxyapatite as the only calcium phosphate phase, even if the Ca/P ratio calculated by XPS for the top surface of the coating is lower than for pure HAp. Unfortunately, the quantification of BAM incorporated in the coating was not possible, as detection techniques are missing. The traditional technique consisting in measuring the UV-Vis spectrum before and after synthesis is not very feasible, as the synthesis occurs in 14 day with renewal of the solution every 48 hours. Moreover, as BAM are not very stable at physiological pH, especially baicalin and baicalein, UV signatures of the molecules are not reliable. In addition, the homogeneous precipitation of BAM is visible in the deposition vessel, meaning that a measure of BAM concentration in solution after synthesis would misrepresent the real incorporated quantity. Another possibility would be to

dissolve the HAp to release the molecule, before measuring the concentration by analytical technique such as HPLC.

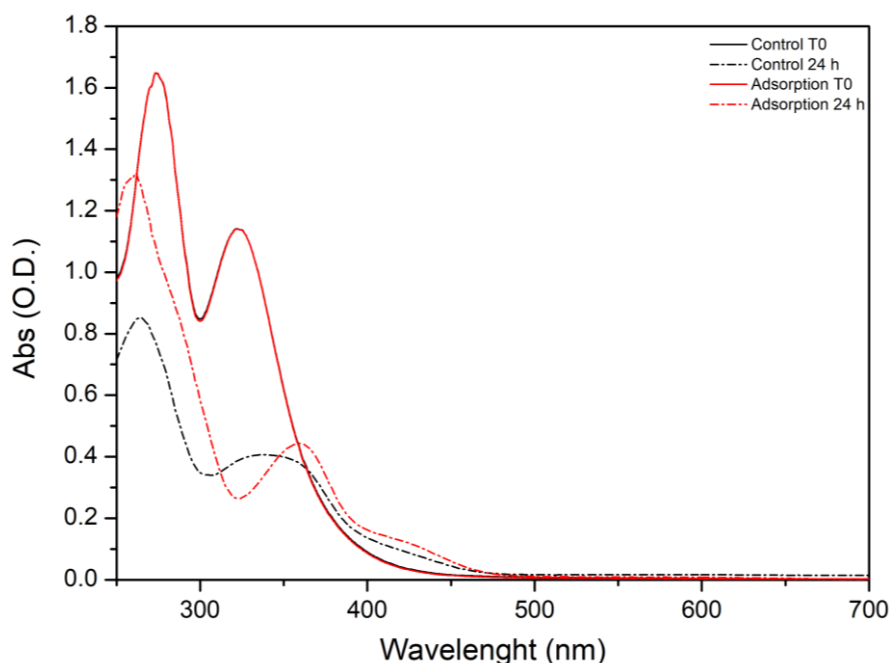
### 4.3.3 Post-synthesis adsorption of BAM

The second method to add biological function to hydroxyapatite coatings is the adsorption of biologically active agents on the hydroxyapatite. This technique is widely used to incorporate antibiotics to obtain antibacterial coatings<sup>4,16,18</sup>. Adsorption force depends on the interaction between the organic molecules and hydroxyapatite. Antibiotics presenting carboxylic acid or catechol functions are supposed to have a strong affinity for hydroxyapatite<sup>18</sup>. We already shown in Chapter 3 than the adsorption of the four BAM used, chlorogenic and rosmarinic acids, baicalin and baicalein is possible on hydroxyapatite nanoparticles. In this part, we propose to investigate the adsorption of BAM on hydroxyapatite coatings synthesized in 1.5-SBF on Ti6Al4V alloys. With the purpose of using these hybrid coatings for their antibacterial properties, we decided to only study the adsorption of baicalein and baicalin on HAp coatings, as these molecules have the highest antibacterial properties.

Hydroxyapatite coatings were synthesized in 1.5-SBF on alkali-treated Ti6Al4V substrates, as presented in 3.2.2. For the adsorption, Ti alloy plates coated with hydroxyapatite are immersed in an 2 mL/plate aqueous solution of either BA or BE at  $1.10^{-4}$  mol.L<sup>-1</sup> for 24 hours. At this concentration, and for this volume, the quantity of BA or BE in solution is  $2.10^{-7}$  mol for one sample. Ti alloy plates dimensions are 1 cm<sup>2</sup> for each face. As plates are soaked vertically in the 1.5-SBF, both faces are coated with HAp, so the total surface covered with HAp available for adsorption is 2 cm<sup>2</sup>, if we neglect the specific surface area of the hydroxyapatite layer, as it appears very dense. To sum up, the theoretical quantity of BA or BE that can be incorporated is  $1.10^{-7}$  mol.cm<sup>-2</sup>, i.e.  $6.10^2$  molecules.nm<sup>-2</sup>.

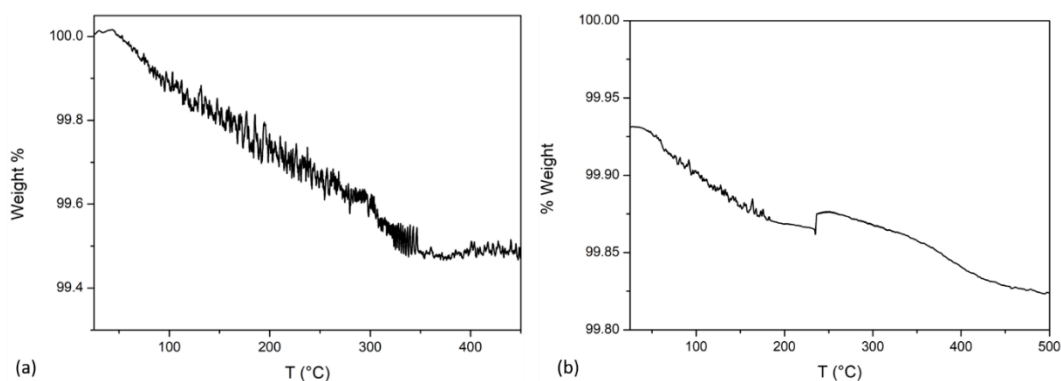
Several attempts were made to measure the adsorbed quantity, with the same issues encountered than for the quantification when BAM are incorporated during the synthesis. UV-Visible spectroscopy was first used to measure the concentration of BE or BA in solution before and after adsorption. However, as expected, the UV-Vis spectrum after 24 hours is different from “fresh” solutions of the molecules. Moreover, the spectrum of BE after adsorption does not exhibit the same maxima than the one of BE after 24 hours in water, as seen in **Figure 4.18**. After 24 h in water, the peak at 274 nm is shifted at 264 nm, and the peak at 323 nm is shifted at 350 nm, with a broadening. This is consistent with the observations made in Chapter 2 about the degradation of baicalein in solution. After adsorption, the peak at 323 nm is shifted at 360 nm, which is similar with baicalein at pH 10 or after total degradation. For both spectra, the shoulder at 420 nm is visible. Two events happen at the time, the degradation of the molecule in water, and the release of ions from hydroxyapatite, notably OH<sup>-</sup>, contributing to increase the pH of the solution, and thus modifying the state of the molecule. Due

to all of these considerations, the quantification of the quantity of the adsorbed molecule was not possible by UV-Vis method.



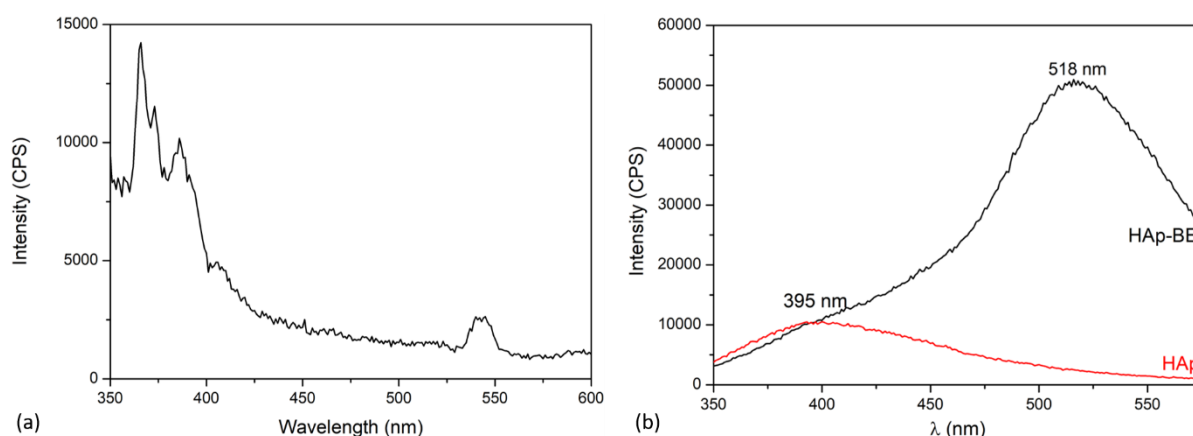
**Figure 4.18** UV-Vis spectra of baicalein in solution before and after 24 h adsorption on HAp coatings, and comparison with baicalein 24 h in water. Initial concentration:  $1.10^{-4}$  mol.L $^{-1}$

Similarly to incorporation of BAM during synthesis, we tried to detect the adsorbed molecule with thermogravimetric analysis. The loss of weight between 25 °C and 500 °C was measured. The signal is again very noisy, as seen in **Figure 4.19** for HAp with adsorbed baicalein **(a)** and adsorbed baicalin **(b)**. For both coatings, we can estimate an adsorbed quantity of 0.1 mg adsorbed. For baicalein, this quantity is overvalued, as the maximal quantity that can be adsorbed is  $2.10^{-7}$  mol, corresponding to 0.05 mg. It is also overvalued in the case of baicalin, as  $2.10^{-7}$  mol corresponds to 0.09 mg, but the error is less important. Once again, this method is not adapted to measure the adsorbed quantity of molecule on hydroxyapatite coatings, because the loss of weight due to the molecule is very low.



**Figure 4.19** Thermogravimetric analysis of HAp coatings after adsorption of BE (a) and BA (b)

For baicalein, we decided to take advantage of its fluorescence properties and measure the fluorescence response of coatings to detect its presence on the coating surface. First, the fluorescence signal of baicalein in solution in DMSO was measured, with an excitation wavelength at 320 nm. The fluorescence spectrum of baicalein exhibit several peaks (**Figure 4.20 (a)**) at 366, 373, 386 and 540 nm. In the spectrum of the hydroxyapatite with adsorbed baicalein (HAp-BE, **Figure 4.20 (b)**), the peak at 518 nm was assigned to BE. The shift from 540 to 518 nm probably results from the modification of the environment of the molecule on the hydroxyapatite surface, compared to in a DMSO solution. HAp has an intrinsic fluorescence at 395 nm, as seen on **Figure 4.20 (b)**, which is also visible on the spectrum of HAp with adsorbed baicalein. Thus, fluorescence spectroscopy confirms the adsorption of baicalein on the hydroxyapatite surface. However, even if the incorporation of baicalein is visible, fluorescence does not allow the measure of the exact adsorbed quantity.

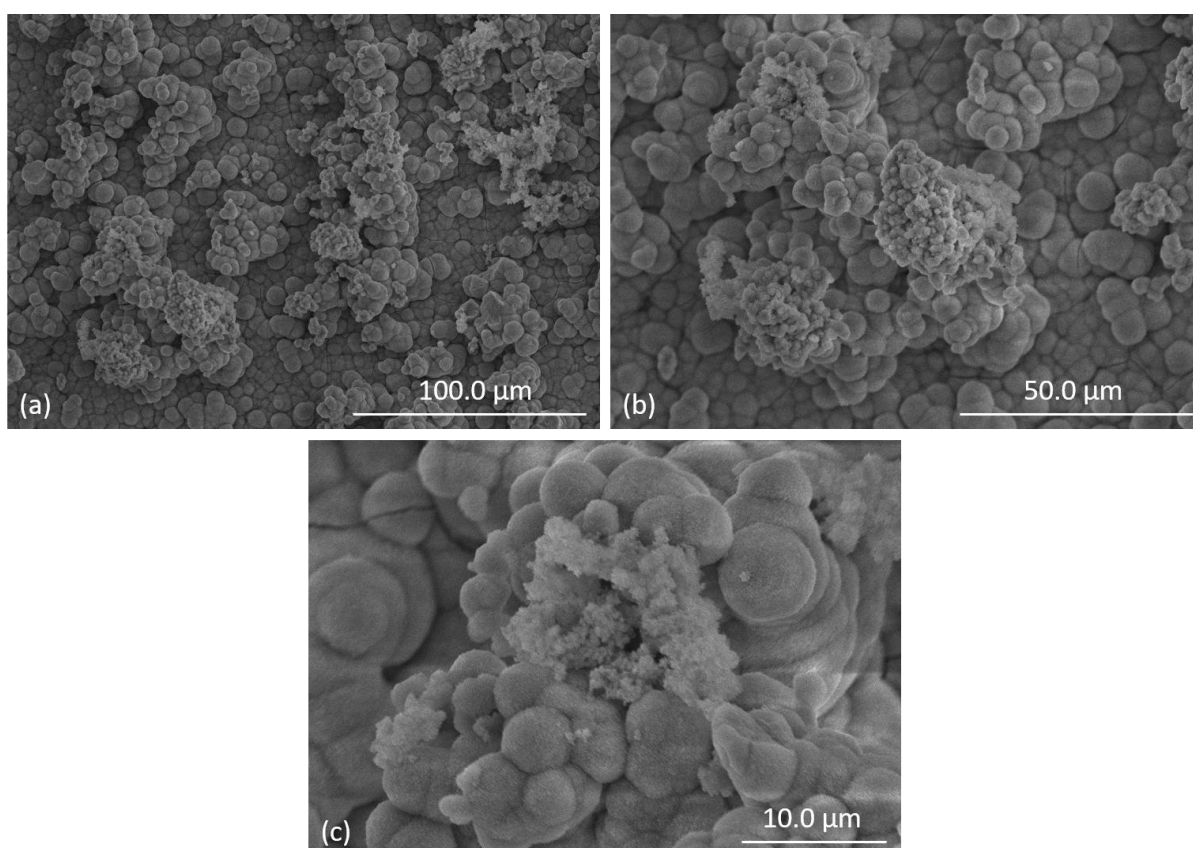


**Figure 4.20** Fluorescence spectra of (a) baicalein 50 μM in DMSO,  $\lambda_{\text{ex}} = 320$  nm and (b) hydroxyapatite coatings before and after adsorption of baicalein,  $\lambda_{\text{ex}} = 300$  nm

**Figure 4.21** presents the SEM images of the hydroxyapatite coating after adsorption of baicalein, when the adsorption is made with the plate placed horizontally in the vessel. On the image at low magnification (**Figure 4.21 (a)**) two distinct layers of the coating are visible. The lower layer is representative of hydroxyapatite coating, with a dense and homogeneous layer composed by spheroids. Above this layer, the spheroid morphology is visible, but particles cover non-uniformly the surface. This would suggest that the hydroxyapatite layer was dissolved during the adsorption process. If we observe the same area at higher magnification (**Figure 4.21 (b)** and **(c)**), two different morphologies appear for the second layer. Smaller particles are deposited on the big “cauliflower-like” particles. These smaller particles do not look like the rest of the coating, so we can assume that they are not constituted by hydroxyapatite. An important charging effect is visible on **Figure 4.21 (c)**, when the enlargement is made on the small particles. This charging effect suggests that these smaller particles are composed by a material more insulating than hydroxyapatite, which would be the

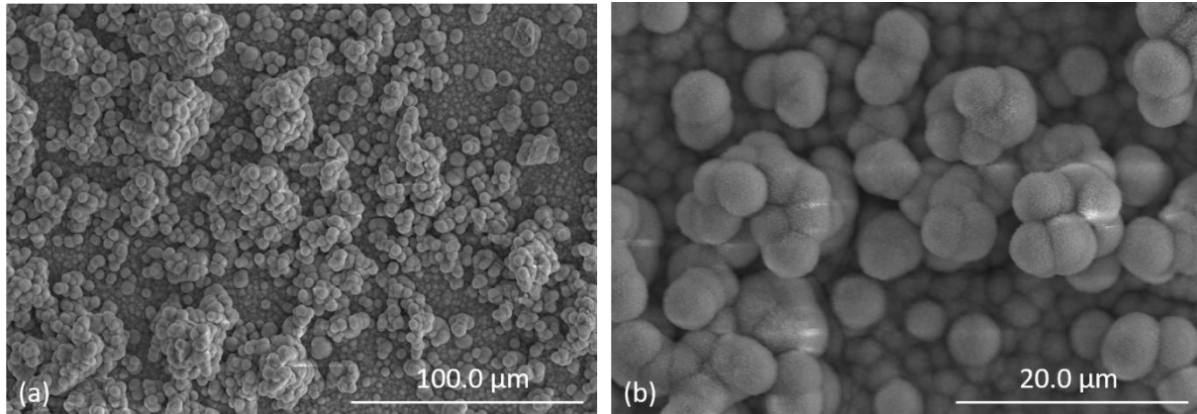


expected case of organic molecules. We can therefore assume that small particles are composed by baicalein, which precipitated on the hydroxyapatite surface during the adsorption step, or by a calcium phosphate material, with a morphology and a composition different from hydroxyapatite. To answer this question, EDX spectroscopy may be useful, in order to detect the presence or absence of calcium and phosphate in this area. As a comparison, images of hydroxyapatite coating after adsorption when the plate is vertically placed are presented in **Figure 4.22**. At the lowest magnification, the morphology is similar to that for horizontal adsorption. However, at higher magnification, the second type of particles is not present. This strengthens the hypothesis that they are composed of precipitated baicalein, that settle on the surface when the latter is placed horizontally, whereas when it is placed vertically the deposition is not possible.



**Figure 4.21** SEM images of hydroxyapatite coating on Ti6Al4V after horizontal adsorption of baicalein. Magnification: 500 (a), 1.00 k (b) and 3.00 k (c)

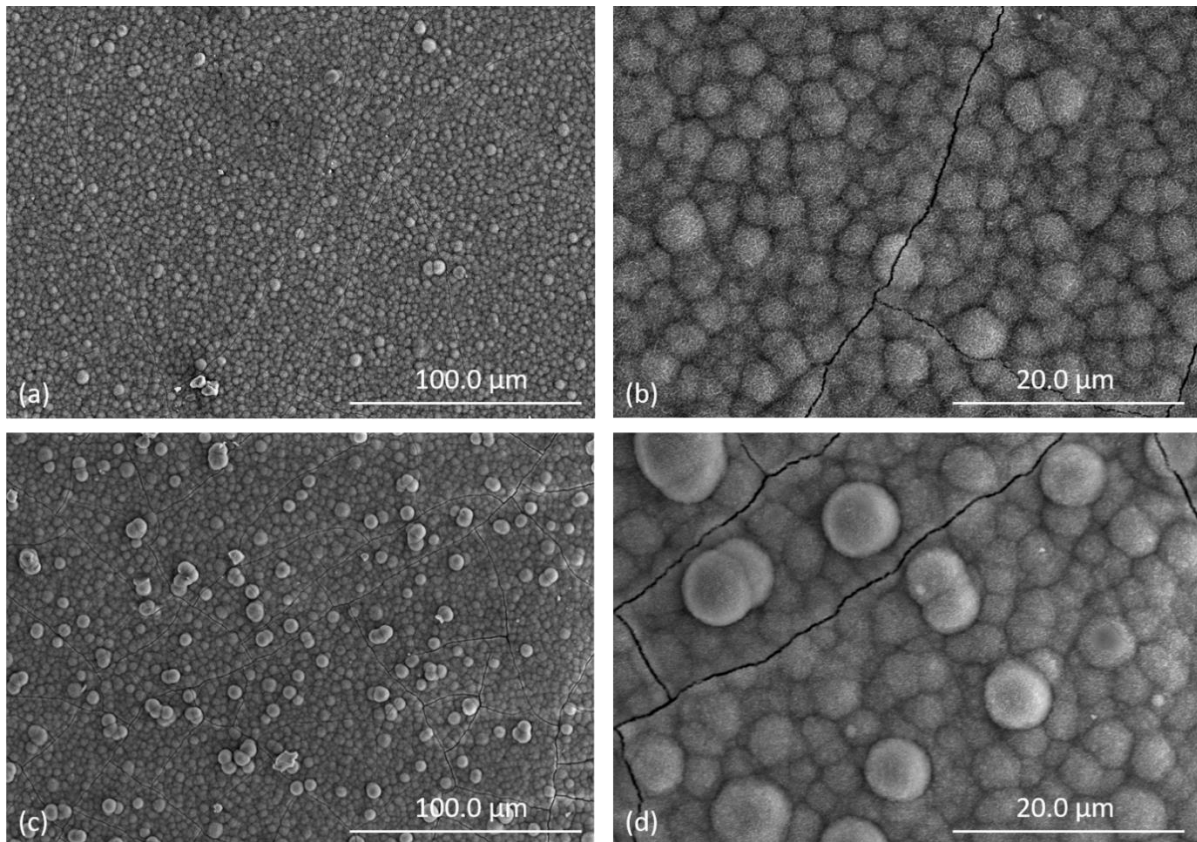




**Figure 4.22** SEM images of hydroxyapatite coating on Ti6Al4V after vertical adsorption of baicalein.

Magnification: 500 (a) and 2.5 k (b)

In order to verify that the “dissolution” of the coating is actually due to the adsorption process, a control of adsorption was performed and sample were observed with SEM. Briefly, Ti alloy plates with hydroxyapatite coatings synthesized in SBF were placed either horizontally or vertically in a vessel, a immersed in water for 24 hours. Their morphology was then observed, and is presented in **Figure 4.23 (a), (b)** for the horizontal adsorption, and **(c), (d)** for vertical adsorption.



**Figure 4.23** SEM images of hydroxyapatite coatings on Ti6Al4V after immersion in water for 24 hours, horizontally (a), (b), or vertically (c) and (d). Magnification: 500 (a), (c) and 2.5 k (b) and (d)

The morphology is similar for both horizontal and vertical controls. It consists of the dense and homogeneous layer of spheroids typical for hydroxyapatite. This suggests that the immersion of coatings in water is not responsible for the dissolution of the coating during adsorption. Therefore, baicalein adsorption seems to induce a remodeling of the surface, characterized by a dissolution of the hydroxyapatite coating, and the precipitation of baicalein if adsorption is performed horizontally.

To conclude, baicalin and baicalein were adsorbed on hydroxyapatite coatings on Ti6Al4V surfaces. SEM showed that the adsorption is responsible for a remodeling of the surface, and that the molecule precipitates again on the surface if the adsorption is performed in a horizontal configuration. Vertical adsorption would thus be privileged. XPS was useful to determine that baicalein interacts with both calcium and phosphorous on the surface, which was not seen in the case of incorporation during synthesis. However, despite the number of characterization techniques used, we cannot quantify the adsorption. We are still searching for an efficient quantification method.

### 5.3.4 Conclusions

In this part, we investigated the incorporation of BAM on the hydroxyapatite coatings by two methods, incorporation during synthesis of HAp or post-synthesis adsorption on pre-formed HAp layers. For the first method, BAM were incorporated in the 1.5-SBF prepared for the deposition of hydroxyapatite, with a ratio in solution between calcium and BAM  $\text{BAM: Ca} = 0.0075$ . Hydroxyapatite is efficiently synthesized in these conditions, even if the presence of BAM induces some changes in the morphology of the material. With all BAMs, the layer is thinner and more fragile for all molecules, and does not cover the entire surface with rosmarinic acid. The ratio  $\text{Ca/P}$  calculated from XPS data is lower than the ratio of pure hydroxyapatite coating, suggesting the presence of BAM at the hydroxyapatite surface and/or precipitation of a P-rich amorphous calcium phosphate phase. Unfortunately, it was not possible to quantify the incorporated amount of molecules in the coatings.

The second method used is the post-synthesis adsorption. After hydroxyapatite deposition in 1.5-SBF, samples were immersed in an aqueous solution of baicalein (or baicalin) for 24 hours. We observed by SEM that the adsorption induces a remodeling of hydroxyapatite surface. Fluorescence spectroscopy confirmed the incorporation of baicalein in the coating. However, we were not able to quantify the adsorbed amount of the molecule on the hydroxyapatite surface, due to a lack of quantification technique. HPLC would be an effective technique to measure the remaining concentration of baicalein in solution, but we were not able to perform this experiment, notably due to a lack of sensitivity of our apparatus.

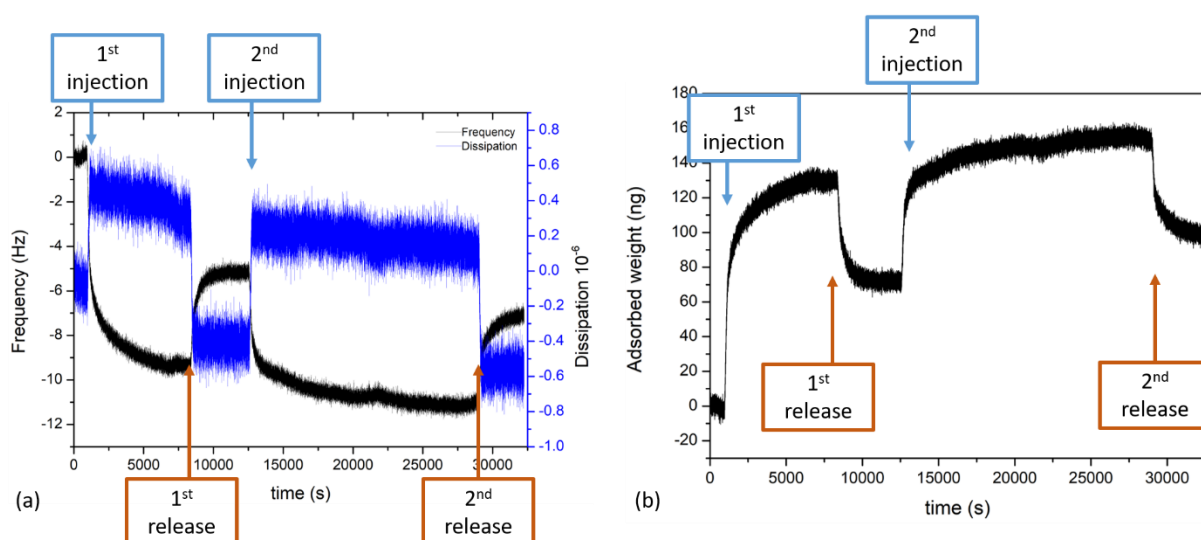
Quartz crystal microbalance experiments were undertaken. For the first, we have established the feasibility of measuring the adsorption of baicalein by this method by adsorbing baicalein on

hydroxyapatite coated quartz used as received from the supplier. **Figure 4.24 (a)** represents the monitoring of frequency and dissipation in function on time during baicalein adsorption at a concentration of  $5.10^{-5}$  M in ultrapure water, with a flux of  $25 \mu\text{L} \cdot \text{min}^{-1}$ . As the dissipation is lower than one, we can consider that the hydroxyapatite layer is rigid, and we can use the Sauerbrey's relation (**Equation 4.1**) to obtain the adsorbed weight ( $\Delta w$ , ng) from the frequency variation ( $\Delta F$ , Hz):

$$\Delta F = -N \frac{\Delta w}{C_f}, \text{ with } N \text{ the harmonic order and } C_f = 17.7 \text{ ng} \cdot \text{Hz}^{-1} \cdot \text{cm}^{-2} \text{ (constant)}$$

#### Equation 4.1 Sauerbrey's relation

During this experiment, after air and water stabilization, we started an adsorption step for 2 hours (1<sup>st</sup> injection). A release phase, corresponding to the passage of ultrapure water, followed the adsorption step and lasted for 75 minutes (1<sup>st</sup> release). Another adsorption step was conducted for 260 min (2<sup>nd</sup> adsorption), before a second release step (2<sup>nd</sup> release) for 66 minutes. **Figure 4.24 (b)** represents the adsorbed weight quantity in function on time, obtained with the Sauerbrey's relation. During the 1<sup>st</sup> adsorption step, 136 ng of baicalein were adsorbed, corresponding to 0.5 nmol. After the 1<sup>st</sup> release step, 70 ng were released, corresponding to a remaining quantity of baicalein of 66 ng (0.28 nmol). 44 % of adsorbed baicalein were released in 75 min. It is interesting to note that after the 1<sup>st</sup> release it was still possible to adsorb baicalein, because 89 ng were adsorbed on top of the 66 ng remaining. The total amount adsorbed after the 2<sup>nd</sup> adsorption step is 155 ng, corresponding to 0.57 nmol. During the 2<sup>nd</sup> release step, 47 % of the total adsorbed baicalein were released. At the end of the experiment, 101 ng of baicalein are adsorbed on the hydroxyapatite functionalized quartz, corresponding to 0.37 nmol.



**Figure 4.24** Baicalein adsorption monitoring by QCM on a hydroxyapatite functionalized quartz (a), and adsorbed weight obtained from adsorption monitoring (b)

In a second step, we have successfully synthesized hydroxyapatite on titanium quartz in SBF. However, results of adsorption studies are not concluding, because the coating seems to be degraded by the flux during the experiment. Nevertheless, this method is worth considering and further experiments need to be performed.

The incorporation of BAM in the hydroxyapatite coating therefore appears effective by both methods, although the precise amount of immobilized BAM could not be achieved. In the next part we will investigate the effect of these coatings as antioxidant and antibacterial agents, as well as promoter of osseointegration.

## 4.4 Biological activity of hydroxyapatite-baicalein coatings

### 4.4.1 Introduction

In this part, the biological activity of hydroxyapatite with BAM will be investigated. We decided to focus only on the incorporation of baicalein since it is the molecule with the highest antibacterial activity, as evidenced in [Chapter 2](#), and as a matter of comparison with hydroxyapatite nanoparticles incorporating baicalein studied in [Chapter 3](#). Antioxidant and antibacterial activities of coatings were studied. Preliminary results on the osseointegration properties of the coating with adsorbed baicalein are presented in the last section.

We intended to quantify baicalein release from hydroxyapatite coatings with HPLC as an analytical method using an equipment available at LRS. However, it appeared that the diode array detection device was not sensitive enough to detect baicalein at relevant concentrations. To date, no suitable device was available, so that these studies are for now pending. Studies with UV-Vis spectroscopy were also attempted, but because of the modification of UV-Vis spectrum of baicalein in function of time due to its oxidation, it was not possible to analyze the results.

### 4.4.2 Antioxidant activity

Antioxidant activity of HAp coatings with baicalein (incorporated during synthesis or adsorbed) was tested with the DPPH radical scavenging testing, derived from Blois<sup>22,23</sup> (see [3.4.2](#) for more details). Each sample was immersed in 2 mL of solution corresponding to a 1:1 (v/v) mixture of TRIS buffer at pH 7.4 and DPPH solution in ethanol (100  $\mu$ M). Samples were let to react 20 min in the dark before recovering of the solution, whose absorption was measured at 517 nm. Antioxidant activity is indicated by the DPPH bleaching percentage, compared to a control consisting of the 1:1 mixture of TRIS and DPPH. Antioxidant activity of hydroxyapatite coating with baicalein incorporated during synthesis (HAp-BE) and adsorbed baicalein (HAp + adsorbed BE) are gathered in **Table 4.5**.

Sample	DPPH bleaching percentage %
HAp	0
HAp-BE	1.4
HAp + adsorbed BE	2.0

**Table 4.5** Antioxidant activity of hydroxyapatite coating (HAp), with baicalein incorporated during synthesis (HAp-BE), and with adsorbed baicalein (HAp + adsorbed BE)

The radical scavenging activity of coatings are very low, 1.4 % for the coating with baicalein incorporated during synthesis (HAp-BE), and 2.0 % for hydroxyapatite with adsorbed baicalein (HAp + adsorbed BE). The absence of activity is not surprising when baicalein is incorporated during the synthesis, as we know from the molecular study that baicalein oxidized at neutral pH. The molecule is likely oxidized in the SBF solution, and incorporated in hydroxyapatite as the oxidized form. After oxidation, the molecule is no longer active against radicals. The low activity for coatings with adsorbed baicalein is probably due to their low amount.

Overall, hydroxyapatite coatings incorporating baicalein, whatever the incorporation method, do not have any significant antioxidant activity.

### 4.4.3 Antibacterial activity

#### 4.4.3.1 Antibacterial assays

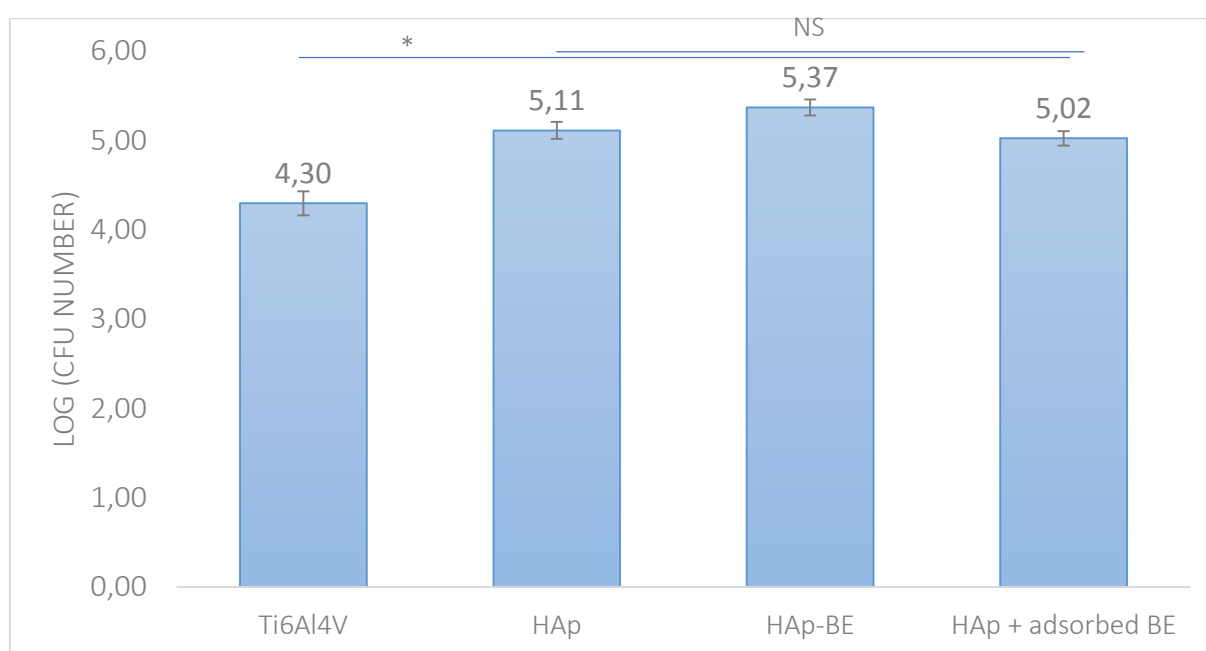
The antibacterial activity of hydroxyapatite coatings with incorporated baicalein were studied with *S. epidermidis* CIP 105.777. Compared to the study with HAp nanoparticles, we decided to change the bacterial strain, because *S. epidermidis* CIP 68.21 cannot form biofilm. Firstly, we determined the MIC of baicalein against *S. epidermidis* CIP 105.777 in Mueller-Hilton culture broth. As for *S. epidermidis* CIP 68.21, MIC of baicalein against *S. epidermidis* CIP 105.777 is 34  $\mu\text{g.mL}^{-1}$ , corresponding to a concentration of 0.126  $\text{mmol.L}^{-1}$ .

The antibacterial activity of the coated plated was investigated with a live/dead assay. Samples were incubated with bacterial suspension of *S. epidermidis* in PBS at a concentration of  $3.10^5$  CFU/mL, for 2 h and 24 h, at 37 °C. After incubation, surfaces were carefully washed to remove non-adherent bacteria, labelled with fluorophores from the live/dead assay kit (LIVE/DEAD BacLight bacterial viability kit, ThermoFisher Scientific), and surfaces were observed under a fluorescence microscope, with  $\lambda_{\text{ex}} = 485$  nm and  $\lambda_{\text{em}} = 530$  nm (green) and  $\lambda_{\text{em}} = 630$  nm (red). Living bacteria are supposed to appear in green, and dead bacteria in red. However, we mainly observed the intrinsic fluorescence of BE, and



the analysis of images was not possible to determine the number of living bacteria. We decided to abandon this technique and to use bacteria counting for the next experiments.

The bacterial adhesion on hydroxyapatite coatings (HAp-BE) and (HAp + adsorbed baicalein) was investigated, and compared with pure HAp and Ti substrates as controls. Samples were incubated with 2 mL of a *S. epidermidis* suspensions at  $9.7 \cdot 10^5$  CFU/mL in PBS. After 3 h incubation at 37 °C, plates were rinsed carefully and adhered bacteria were removed from the surface following this protocol: samples were immersed in 2 mL of PBS, and the surfaces were with a spatula scratched before 5 minutes of sonication and another scratch. The PBS solutions were then diluted to perform plate counting. Experiments were performed in triplicated and results are presented in **Figure 4.25**.

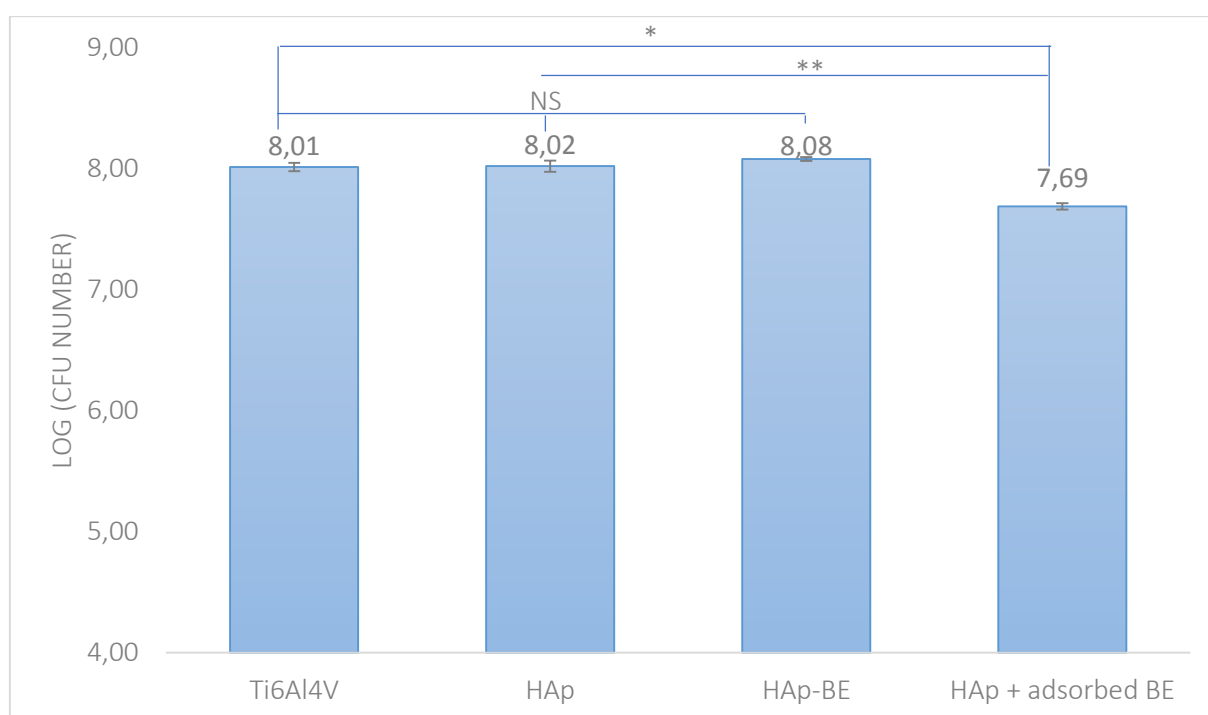


**Figure 4.25** Antiadhesion effect of hydroxyapatite coatings incorporating baicalein on *S. epidermidis* (NS: non significant, \*:  $p \leq 0.05$ )

The number of bacteria after 3 hours of incubation is the same, within the experimental error in absence of presence of baicalein. The adhesion on hydroxyapatite coating is slightly higher than on bare Ti surfaces. The presence of hydroxyapatite may enhance bacterial adhesion, as its surface is rougher than polished bare Ti. From this assay, we can conclude that hydroxyapatite coatings do not have any positive effect on the adhesion of *S. epidermidis* CIP 105.777 and that the presence of baicalein does not influence bacterial adhesion.

The growth ability of adhered bacteria was also assessed. The beginning of the experiment was as stated above (3 h of incubation at 37 °C in 2 mL of *S. epidermidis* suspension in PBS at  $9.7 \cdot 10^5$  CFU/mL), samples were carefully rinsed to remove any poorly adhered bacteria, before being

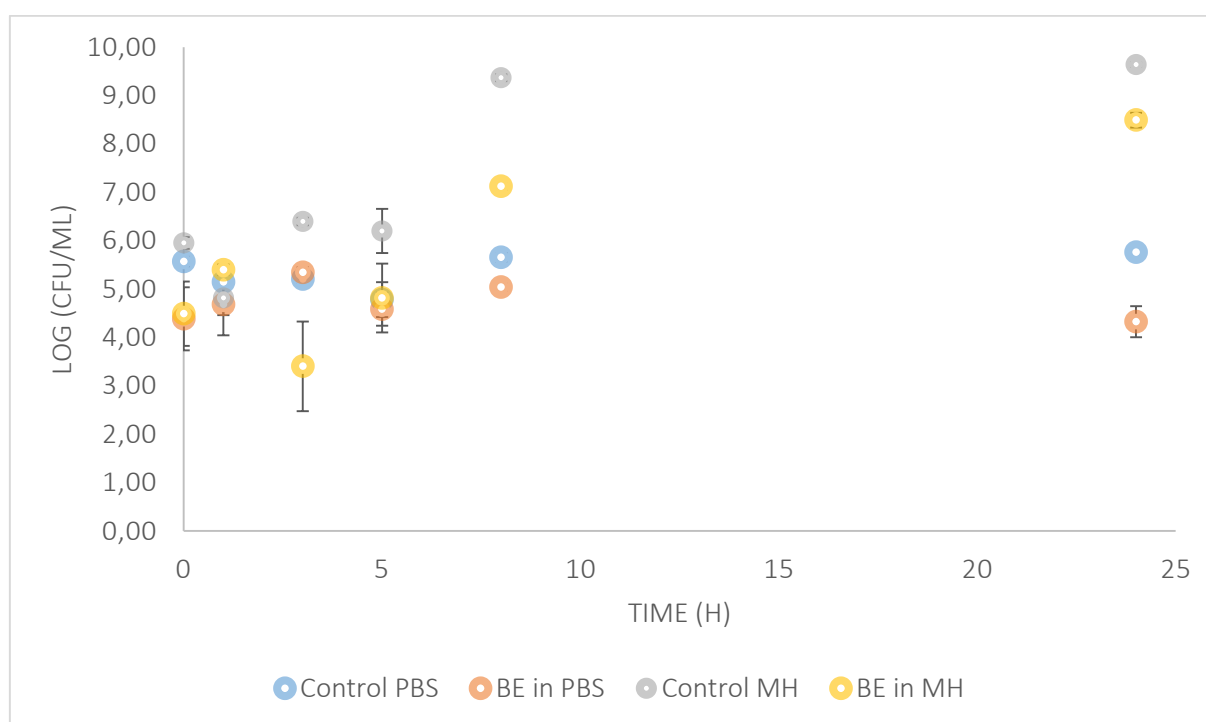
incubated in culture broth (MH) for 24 hours at 37 °C. After incubation, samples were processed as presented before to recover the bacteria present on the surface and plate counting. Results expressed as the log of the number of proliferated CFU are presented in **Figure 4.26**. First, bacteria proliferated on the four different plates, as the number of bacteria grows from *ca.* 5 log to *ca.* 8 log for each surface. The number of proliferated bacteria is the same for HAp and HAp-BE coatings. A slight effect on the proliferation on (HAp + adsorbed BE) is significantly visible ( $p$  value = 0.004 compared to HAp), but with less than a log variation. We can conclude that the coating (HAp + adsorbed BE) can slightly prevent the proliferation of adhered *S. epidermidis* after 24 hours in rich medium. In contrast the HAp-BE coating with baicalein incorporated during the synthesis, does not show any anti-proliferation effect.



**Figure 4.26** Effect of hydroxyapatite coatings incorporating baicalein on *S. epidermidis* proliferation in rich medium after 3 h of initial adhesion (NS: non significant, \*:  $p \leq 0.05$ , \*\*:  $p \leq 0.01$ )

From these two first assays, we can conclude that hydroxyapatite coatings incorporating baicalein do not have a very significant antibacterial effect. Whereas we could expect a reduction on initial adhesion, we showed that the presence of hydroxyapatite in fact enhances the bacterial adhesion compared to bare Ti. The HAp coating with incorporation of baicalein during synthesis did not have any effect on bacteria proliferation, but a reduction of the number of bacteria was visible on the coating with adsorbed baicalein. These results suggested that baicalein is not active in three hours, but can reduce the bacteria growth on a longer timescale. On this basis, we hypothesized that the kinetics of baicalein activity was slow, comprised between 3 and 24 hours.

To confirm this hypothesis, we decided to study growth of *S. epidermidis* CIP 105.777 in presence of BE in solution at a concentration  $C = 2 \times \text{MIC}$ , in rich medium (MH), and poor medium (PBS), for 24 hours, and to compare with bacterial growth in both culture media without BE. Results are presented in **Figure 4.27**. In PBS without baicalein, the density of bacteria in solution remained stable, as bacteria cannot grow in a poor medium. In presence of baicalein, the bacteria concentration was the same than the control until 5 hours, but started to decrease between 10 and 24 hours. After 24 hours, the bacteria concentration in presence of baicalein was lower by one order of magnitude compared to the control. In culture broth (MH) without baicalein, the bacteria concentration increased from 3 hours to 10 hours and remained stable at 9 log. In presence of baicalein, it remained stable during 5 hours, when it started to increase, but to a lower extent than in the control. From these results, we can assume that the baicalein is an antibacterial molecule with a slow kinetics of action. In PBS, the effect is visible after 24 hours, while in MH the presence of baicalein only delayed the bacteria growth. The activity of baicalein in MH is visible after 8 hours.



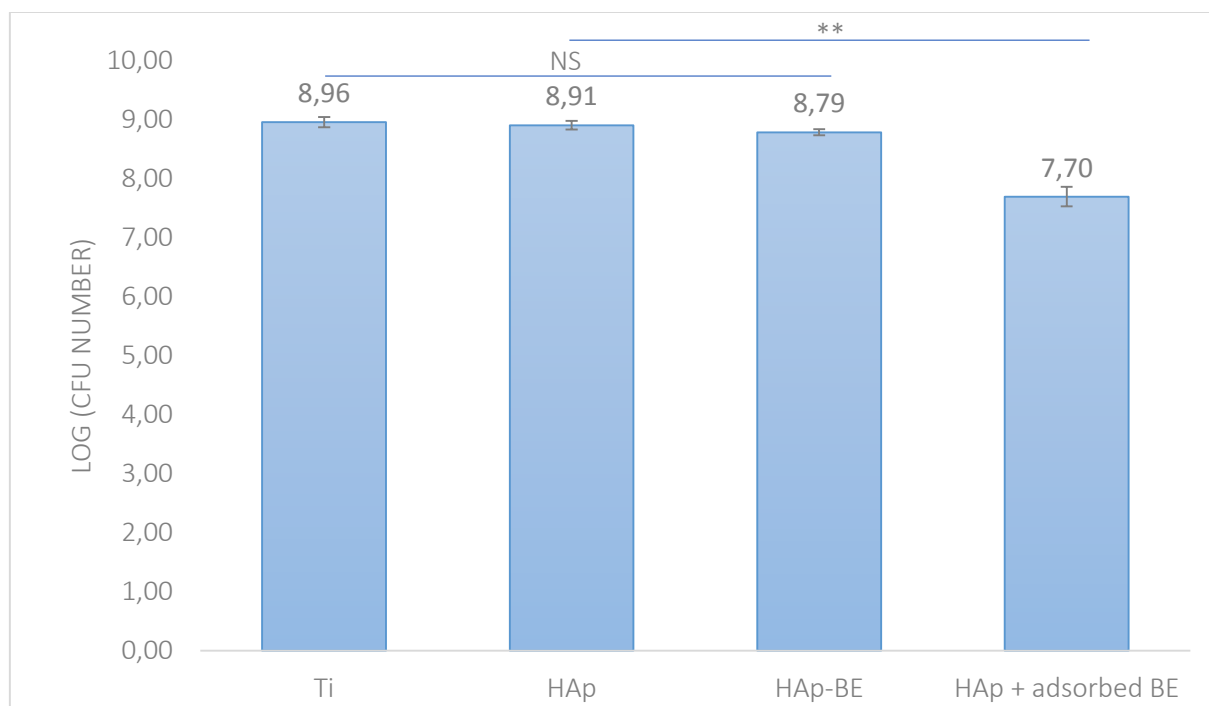
**Figure 4.27** Antibacterial activity kinetics of baicalein against *S. epidermidis* CIP 105.777 in rich and poor medium, at a concentration twice the MIC

Keeping in mind the slow kinetic of baicalein, another antibacterial assay was performed with the HAp coatings against *S. epidermidis* CIP 105.777, to assess the bacterial growth in rich medium in 16 hours. Samples were immersed in 2 mL of bacteria suspension diluted in MH from an overnight preculture to a concentration of  $5 \cdot 10^4$  CFU/mL. After 16 hours, samples were rinsed and adhered bacteria were recovered as presented before, for plate counting. Results expressed as the log of the



number of CFU grew on the surfaces are presented in **Figure 4.28**. First of all, bacteria growth was similar on the controls (Ti and HAp) and HAp-BE, with approximatively 9 log of CFU. The incorporation of baicalein during synthesis does not allow the formation of an antibacterial coating. Two possibilities may explain this result: baicalein lost its activity with immobilization, or the release is too low to reach the MIC in solution. We know from the molecular study in [Chapter 2](#) that baicalein is oxidized in physiological conditions. However, we showed that the oxidized form of the molecule is active. The oxidation of the molecule during the synthesis does not explain the loss of activity with encapsulation.

Unlike what happened with HAp-BE, the bacterial growth is reduced by one order of magnitude on the (HAp + adsorbed BE) surface, compared to HAp coating (p value = 0.008). Thus the adsorption of baicalein on hydroxyapatite coating leads to the formation of an antibacterial coating. The presence of baicalein on the HAp surface is more efficient than the incorporation of the molecule inside the coating, probably because there is no loss of activity during adsorption.



**Figure 4.28** *S. epidermidis* growth inhibition in rich medium by HAp coatings incorporating baicalein (NS: non significant, \*\*:  $p \leq 0.01$ )

To sum up, we observed an inhibition of bacterial growth by the coatings (HAp + adsorbed BE) by one order of magnitude compared to the controls. Unfortunately, the coating HAp-BE did not exhibit any antibacterial activity. We can conclude that adsorption of baicalein is the most efficient method to incorporate baicalein in HAp coating in order to add an antibacterial property.

#### 4.4.3.2 Conclusions

We highlighted the antibacterial activity of hydroxyapatite coating with adsorbed baicalein. However, its activity is lower than the activity of other calcium phosphate coatings incorporating antibiotics from the literature. Hydroxyapatite coatings with adsorbed antibiotics such as tobramycin or cephalotin are efficient against *S. aureus* in 16 h<sup>18</sup>. Tobramycin was also adsorbed on phosphate calcium coating on fixation pin, with a sustained antibacterial activity for 7 days, despite an initial burst release in 15 min<sup>17</sup>. However, the comparison of antibacterial activity is not obvious, because the method of testing is different from the one we used. Authors used an adaptation of disc diffusion method by placing the plate directly on a seeded agar plate. Yet, the major difference between these coatings and ours is the antibacterial activity of the antibiotics alone. Synthetic antibiotics are at least 100 times more active (*i.e.* have MIC two orders of magnitude smaller) than natural antibacterial molecules on susceptible strains. This issue is all the more problematic here as the concentration of the solution that can be used for baicalein adsorption is limited by the poor solubility of BE in water ( $1.10^{-4}$  mol.L<sup>-1</sup>).

#### 4.4.4 Preliminary testing of the cytotoxicity of hybrid coatings

Cytotoxicity studies were performed on Human Osteoblasts, cultured in cell culture medium consisting of DMEM supplemented with glucose, antibiotics, serum and dexametasol. Cells were cultured for three weeks before the experiments. For our studies, samples were seeded with 50 000 cells. We tested the toxicity of our materials towards the osteoblasts at 24 hours, and the proliferation of cells on the plates at 7 days. After 24 hours of cellular culture at 37 °C in an incubator with 5 % of CO<sub>2</sub> in the atmosphere, cellular viability was tested with the AlamarBlue assay, and cells morphology was observed under a fluorescence microscope after labelling with DAPI (4', 6-diamidino-2-phenylindole) and phalloidin. Plates that underwent the AlamarBlue test were then re-incubated with culture medium to investigate the proliferation at 7 days of adhered cells. The viability and morphology of cells on titanium alloy, HAp coatings and HAp coatings with adsorbed baicalein were compared with cells cultured on plastic cell culture plates. Experiments were performed on 6 different samples for each condition (Ti6Al4V, HAp coating, HAp coating + adsorbed baicalein and plastic control plates).

AlamarBlue assay is based on the reduction of rezaruzin by living cells in resarufin. Rezaruzin is blue, with a maximum of absorption at 600 nm while resarufin is pink and absorbs the most at 570 nm. Absorbance values at 570 and 600 nm are used to calculate the percentage of viability of cells on our samples, thanks to **Equation 4.2**:

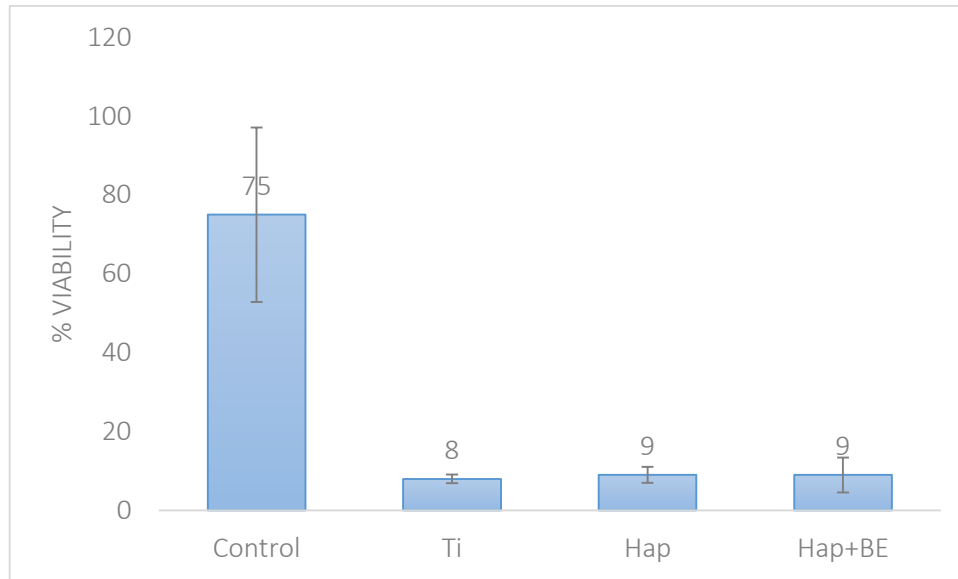
$$\% \text{ viability} = \frac{(\epsilon_{\text{ox},600}) \times A_{570} - (\epsilon_{\text{ox},600}) \times A_{600}}{(\epsilon_{\text{red},570}) \times A_{570} - (\epsilon_{\text{red},570}) \times A_{570}}$$

- $\epsilon_{\text{ox},600}$  = molar extinction coefficient of rezaruzin at 600 nm = 117.216 L.mol<sup>-1</sup>.cm<sup>-1</sup>
- $\epsilon_{\text{ox},570}$  = molar extinction coefficient of rezaruzin at 570 nm = 14.652 L.mol<sup>-1</sup>.cm<sup>-1</sup>
- $\epsilon_{\text{red},600}$  = molar extinction coefficient of resarufin at 600 nm = 80.586 L.mol<sup>-1</sup>.cm<sup>-1</sup>
- $\epsilon_{\text{red},570}$  = molar extinction coefficient of resarufin at 570 nm = 117.216 L.mol<sup>-1</sup>.cm<sup>-1</sup>
- $A_{570}^{\circ}$  = absorbance of control (AlamarBlue solution) at 570 nm
- $A_{600}^{\circ}$  = absorbance of control (AlamarBlue solution) at 600 nm
- $A_{570}$  = absorbance of sample at 570 nm
- $A_{600}$  = absorbance of samples at 600 nm

**Equation 4.2** Percentage difference compared to control of reduction of rezaruzin in resarufin, corresponding to the percentage of viability

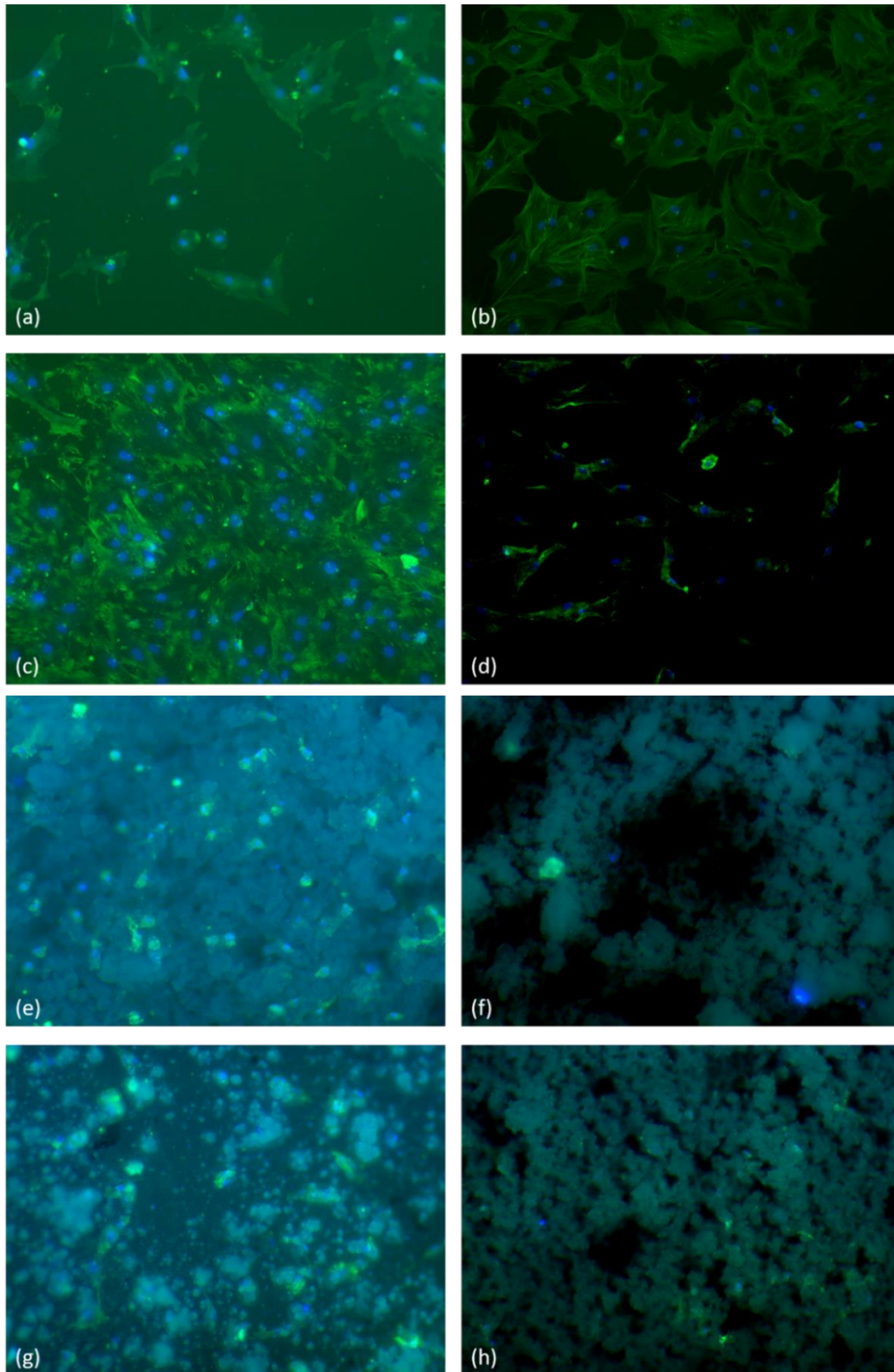
The preliminary results at 24 hours tend to show that viability of cells on HAp coatings with or without baicalein is lower than on titanium surfaces and plastic control. This is confirmed by the visualization with fluorescence microscope **Figure 4.30 (a), (c), (e) and (g)**. On plastic control, cells are well spread. On titanium, the number of cell is higher than on the plastic control plate, with the totality of the surface covered by spread osteoblasts. On the contrary, it is more difficult to find cells on sample with hydroxyapatite, and even worst with hydroxyapatite with adsorbed baicalein. However, cells on these materials are well spread.

After 7 days, we observed a large mortality of cells cultured Ti, HAp coating and HAp coatings with baicalein. On the fluorescence microscope images, we can see that on plastic control plates, cells are abundant, at achieved the confluence (**Figure 4.30 (b)**). On the contrary, on Ti, whereas they were many after 1 day, only a few number are visualized after 7 days (**Figure 4.30 (d)**). We could not find any living cells on HAp coatings and HAp coatings with baicalein (**Figure 4.30 (f) and (h)**). AlamarBlue results showed less than 10 % of viability for cells cultured on the plates, as seen on **Figure 4.29**.



**Figure 4.29** Percentage of viability of human osteoblasts cultured on titanium alloy, hydroxyapatite coating and hydroxyapatite with adsorbed baicalein, compared with plastic culture plate as control

These results are only preliminary, and experiments issues could explain the cell mortality. Indeed, the manipulation of samples at 24 hours to perform the AlamarBlue test may have cause a mortality. This would be consistent with the large experimental error observed for the control, with percentage of viability going from 50 to 100 %. Further experiments will be undertaken, taking more experimental precautions.



**Figure 4.30** Fluorescence microscope images of human osteoblasts cultured on plastic culture plate (a), (b), titanium alloy (c), (d), hydroxyapatite coatings (e), (f), and hydroxyapatite coatings with adsorbed baicalein (g), (h), after 24 hours (a), (c), (e), (g) and 7 days (b), (d), (f) and (h).

Magnification x10, blue: DAPI, green: phalloidin

## 4.5 Conclusions

We investigated the deposition of hydroxyapatite on titanium alloy, and the incorporation of biologically active molecules (BAM) in the coating. The deposition was biomimetic in a 1.5-fold concentrated simulated body fluid, taking place at physiological pH and temperature. The deposition protocol was optimized, both for the substrate pretreatment and the composition of the deposition solution. We found that an alkali pretreatment was suitable to allow hydroxyapatite deposition, without the requirement of an annealing step. For the composition of SBF, we decided to keep the Kokubo's solution with low carbonate content, but concentrated 1.5 fold (1.5-SBF), as the synthesized layer was more homogeneous. In these conditions, after 14 days of deposition with renewal of the solution every 48 h, a 12  $\mu\text{m}$  thick carbonated and substituted hydroxyapatite coating was obtained. The deposition of biomimetic hydroxyapatite was thus successfully achieved.

Two methods were tested for the incorporation of BAM : 1) co-solubilisation of BAM in the SBF, 2) adsorption of BAM on pre-formed HAp. The presence of BAM in the SBF did not prevent the hydroxyapatite crystallization, but coatings presented a morphology different from pure hydroxyapatite. In the case of rosmarinic acid, the coating did not cover the entire surface of the substrate. XRD and vibrational spectroscopies evidenced the deposition of hydroxyapatite as the only calcium phosphate phase. The effect of BAM incorporation was visible on XPS, with lowering of Ca/P ratio. In case of the post-synthesis adsorption, plates after hydroxyapatite deposition were immersed in an aqueous solution of BAM. Adsorption induced a reshaping of the hydroxyapatite surface. Unfortunately, we were not able to quantify the amount of BAM in the coating, either after incorporation during synthesis or adsorption.

The biological activity of coatings was assayed with baicalein, as it is the molecule with the best antibacterial activity. Coatings with baicalein incorporated by the two methods did not possess any antioxidant activity. It can be related to a weak quantity incorporated (which should be checked by finding an appropriate technique to characterize the incorporation), and for the molecule incorporated during synthesis to the oxidation of the molecule in SBF. The antibacterial activity of both coatings was investigated against *S. epidermidis* CIP 105.777. For both coatings, no effect on bacterial adhesion and growth was observed after 6 hours of incubation, but their proliferation was partly inhibited by the coating (HAp + adsorbed baicalein) after 24 hours. The latter coating inhibited the bacterial growth in 16 h in rich medium. Coatings with baicalein incorporated during synthesis did not exhibit any antibacterial activity. Preliminary studies on human osteoblasts were inconclusive. A high cell mortality was observed at 7 days. Further experiments need to be done to better characterize the osseointegration ability of hydroxyapatite coatings in the presence of adsorbed baicalein.

## 4.6 Summary

In the next paragraphs, we will try to sum up the conclusions about the behavior of the four biologically active molecules from the three previous chapters of the manuscript, i.e. the molecular study (Chapter 2), the formation of hybrid hydroxyapatite – biologically active molecules nanoparticles (Chapter 3), and the development of hybrid biomimetic hydroxyapatite – baicalein coatings on Ti6Al4V alloy (Chapter 4).

### Chlorogenic acid

Chlorogenic acid is an ester formed by a caffeic acid and a quinic acid moiety. We characterized its weak antibacterial activity (MIC = 4 mg/mL against *S. epidermidis* CIP 68.21), but significant antioxidant properties. The molecule is stable at acidic and neutral pH. We first demonstrated that the complexation of CA with calcium is pH-dependent. At acidic pH, monomolecular  $[CA-H+Ca]^{2+}$  and bimolecular  $[2CA+Ca]^{2+}$  complexes are formed, with the monomolecular complex more stable than the biomolecular complex. At neutral pH, only the  $[CA-H+Ca]^{2+}$  complex is detected. NMR studies suggested that the preferential complexation site would be the catechol ring rather than the carboxylate. The complexation does not modify the antioxidant activity of CA. The ability of CA to form a complex in solution with calcium is not correlated with an affinity for hydroxyapatite surface. Indeed, CA is one of the molecule with the lowest affinity for the surface of HAp nanoparticles in our study. Regarding the incorporation of the molecule during synthesis of HAp nanoparticles, it was found that CA is poorly incorporated. At the lowest CA:Ca ratio (0.0075), the presence of RA decreases the yield of the reaction. HAp particles with CA are smaller than pure HAp particles, but the crystallite size is equal. At the highest CA:Ca ratio (0.075), besides HAp, a small fraction of  $CaCO_3$  is observed by XRD. HAp synthesis is hindered, that may be explained by an affinity of CA for calcite that is not fully dissolved. Among the studied molecules, CA belongs to the one with the lowest effect on HAp synthesis, either under the form of nanoparticles or coatings. Despite a difference in the morphology of the coating, the presence of CA in the deposition solution does not prevent the HAp synthesis. Overall, despite a strong complexation between calcium and chlorogenic acid in solution, CA does not show a specific affinity for the hydroxyapatite surface.

### Rosmarinic acid

Rosmarinic acid is an ester formed by a caffeic acid and a 3, 4-dihydroxyphenyllactic acid moiety. Its antibacterial activity is higher than the one of chlorogenic acid (MIC = 1.0 mg/mL against *S. epidermidis* CIP 68.21), and it possesses a significant antioxidant activity. As CA, the molecule is stable at acidic and neutral pH. Its affinity for calcium in solution is very similar to the one of CA. At acidic pH, monomolecular  $[RA-H+Ca]^{2+}$  and bimolecular  $[RA+Ca]^{2+}$  complexes are formed. The deprotonated



monomolecular complex has a stability similar to  $[CA-H+Ca]^+$ , but the bimolecular complex is unstable. The monomolecular complex is the only detected one at neutral pH. NMR studies did not allow the discrimination between sites of complexation. On the contrary of CA, the complexation has a small effect on the antioxidant activity of rosmarinic acid. We can assumed that if the catechol is the function responsible for the antioxidant activity, the loss of antioxidant property may be due to the complexation of calcium at the catechol site. From antioxidant assays, we can assume a higher probability of complexation on the catechol site rather than on the carboxylate. Despite a significant complexation between RA and calcium, RA does not have a significant affinity for the HAp surface. The molecule is not significantly adsorbed on HAp particles. While incorporated during the synthesis, RA has a strong effect on the HAp synthesis, but only a low amount is incorporated ( $50 \text{ mg.g}^{-1}$ ). Besides a lowering of the synthesis yield at low RA:Ca ratio, particles are smaller than pure HAp ( $14 \pm 2 \text{ nm}$  in length compared to  $30 \pm 7 \text{ nm}$ ), but with a similar crystallite size. At high ratio, RA totally prevents the HAp synthesis. It is connected with the inhibition of the dissolution of calcite (formed at the beginning of HAp synthesis). The presence of RA in SBF also affects the deposition of HAp on Ti, despite a mechanism of HAp crystallization different from the homogenous precipitation. The deposited layer is thinner than pure HAp coating. Overall, RA has a strong effect on the hydroxyapatite synthesis, either under the form of nanoparticles or coatings, despite a low affinity for HAp surface, as hypothesized from XPS analysis. The inhibition of the synthesis is not related to the complexation between RA and calcium, even if it is significant at neutral pH. RA is not a molecule of choice for the development of hybrid coating, due to its low affinity for HAp surface and its low antibacterial activity.

#### Baicalin

Baicalin is a flavonoid, with interesting antioxidant and antibacterial activity (MIC = 1.2 mg/mL against *S. epidermidis* CIP 68.21). At acidic pH, monomolecular  $[BA-H+Ca]^+$  and bimolecular  $[2BA+Ca]^{2+}$  complexes with calcium are formed, the monomolecular complex being more stable than the bimolecular one. At neutral pH, we evidenced the oxidation of the molecule that we assumed to occur before the complexation with calcium. Consequently, at physiological pH, if any, only complexes involving the oxidized form of baicalin are likely to form. We suggested that the site of complexation is the carboxylate, by comparison with baicalein. As far as interactions of BA with hydroxyapatite are concerned, the molecule has an affinity for the HAp surface. It is adsorbed with higher quantity than RA and CA on HAp nanoparticles. While incorporated during synthesis, BA does not have a significant effect on the HAp crystallization. We can only notice a lower yield and smaller particles. Same comment can be done for the incorporation on BA in the 1.5-SBF solution for the deposition of HAp. The morphology of the coating is different from pure HAp, but BA does not inhibit HAp synthesis. Overall, BA has a significant affinity for both calcium ion in solution and hydroxyapatite surface. The



molecule does not prevent HAp synthesis if incorporated during synthesis of either nanoparticles or coatings.

#### Baicalein

Baicalein is the aglycone of baicalin, with interesting antioxidant activity and high antibacterial activity (MIC = 34  $\mu\text{g/mL}$  against *S. epidermidis* CIP 68.21). The molecule is highly unstable at physiological pH, as we described the oxidation of the molecule at neutral pH at short-term and at acidic pH at long-term. The oxidation of the molecule hampers complexation with calcium, at both acidic and neutral pH. However, BE was found to be the molecule with the highest affinity for hydroxyapatite surface, as it is the molecule adsorbed in the highest amount on HAp nanoparticles. Despite interesting antibacterial activity of BE in solution, HAp nanoparticles with adsorbed baicalein do not have a significant antibacterial activity, but they exhibit an antioxidant activity over 5 days. Among the four tested molecules, BE is the one with the highest amount incorporated while adding during HAp nanoparticles synthesis. Furthermore, it slightly prevents the HAp crystallization, with lower yield, smaller particles size. At high BE:Ca ratio (0.075), it inhibits the dissolution of calcite, but not in the same rate than RA. Due to BE oxidation and degradation in alkaline medium, HAp nanoparticles with BE incorporated during synthesis do not exhibit any antibacterial effect. The molecule may also be incorporated in HAp coatings on Ti substrate. If added in the SBF solution, BE is incorporated in the coating, in interaction with the calcium. Its presence modifies the morphology of HAp coating, but not in the same extent than RA. Baicalein adsorption on HAp coating remodels the surface. HAp coatings with adsorbed BE have some antibacterial activity while HAp with baicalein incorporated during synthesis are inactive. In both cases coatings do not have any antioxidant effect.

Looking back at the chemical structure of the four molecules, we have already pointed out that the higher affinity of BA/BE compared to CA/RA for the HAp surface can be attributed to the presence of a pyrogallol ring in the former compared to a catechol ring for the latter. This assumption is strengthened by the fact that in BE this pyrogallol ring is unsubstituted while it bears a sugar ring in BA, such a difference accounting for the highest affinity of the former for the HAp surface compared to the latter. Such a difference between catechol and pyrogallol was attributed to the fact that the presence of three close aromatic hydroxyl groups allows for cooperative interactions strengthening adsorption to the surface. On the opposite, the catechol group seems more favorable than the pyrogallol one for interaction with calcium ions. Again, as RA bears two catechol groups while CA has only one, it would explain while the former has a more marked inhibitory effect than the latter. the oxidation of the pyrogallol group of BA/BE should be consider to explain the lower complexation affinity of those molecules with calcium ions compared to RA/CA.

To summarize the results, we can conclude that among the four tested BAM, baicalein is the most relevant molecule to develop an antibacterial coating with hydroxyapatite. The molecule has the best antibacterial activity among the four molecules tested, and interacts the most with hydroxyapatite surface. Baicalin may also be considered of interest because it has a non-negligible affinity for hydroxyapatite surface, but its antibacterial activity is 10 times lower than the one of BE. Both molecules have a slight inhibition effect on the hydroxyapatite synthesis while added in the solution medium, but HAp is still the major phase synthesized. Rosmarinic and chlorogenic acids do not have any affinity for hydroxyapatite surface. Furthermore, rosmarinic acid is a strong inhibitor of hydroxyapatite crystallization, probably by preventing the dissolution of calcite formed in the first steps of HAp synthesis because of their high affinity for calcium. The weak antibacterial activity of RA and CA, in addition of their poor affinity for hydroxyapatite, do not make these molecules choice alternatives to develop antibacterial coatings with hydroxyapatite.

## References

- 1 T. Kokubo, *Acta Mater.*, 1998, **46**, 2519–2527.
- 2 D. K. Pattanayak, S. Yamaguchi, T. Matsushita, T. Nakamura and T. Kokubo, *J. R. Soc. Interface*, 2012, **9**, 2145–2155.
- 3 A. Cüneyt Tas, *Biomaterials*, 2000, **21**, 1429–1438.
- 4 U. Brohede, J. Forsgren, S. Roos, A. Mihranyan, H. Engqvist and M. Strømme, *J. Mater. Sci. Mater. Med.*, 2009, **20**, 1859–1867.
- 5 A. Oyane, K. Onuma, A. Ito, H.-M. Kim, T. Kokubo and T. Nakamura, *J. Biomed. Mater. Res. A*, 2003, **64A**, 339–348.
- 6 S. Jalota, S. B. Bhaduri and A. C. Tas, *J. Mater. Sci. Mater. Med.*, 2006, **17**, 697–707.
- 7 E. I. Dorozhkina and S. V. Dorozhkin, *Colloids Surf. Physicochem. Eng. Asp.*, 2002, **210**, 41–48.
- 8 I. A. Karampas and C. G. Kontoyannis, *Vib. Spectrosc.*, 2013, **64**, 126–133.
- 9 G. Penel, C. Delfosse, M. Descamps and G. Leroy, *Bone*, 2005, **36**, 893–901.
- 10 A. Awonusi, M. D. Morris and M. M. J. Tecklenburg, *Calcif. Tissue Int.*, 2007, **81**, 46–52.
- 11 R. Verma, J. Gangwar and A. K. Srivastava, *RSC Adv.*, 2017, **7**, 44199–44224.
- 12 T. Kokubo and H. Takadama, *Biomaterials*, 2006, **27**, 2907–2915.
- 13 S. V. Dorozhkin, *Mater. Sci. Eng. C*, 2015, **55**, 272–326.
- 14 R. Legros, N. Balmain and G. Bonel, *Calcif. Tissue Int.*, 1987, **41**, 137–144.
- 15 W. J. Landis and J. R. Martin, *J. Vac. Sci. Technol. Vac. Surf. Films*, 1984, **2**, 1108–1111.
- 16 J. Forsgren, U. Brohede, M. Strømme and H. Engqvist, *Biotechnol. Lett.*, 2011, **33**, 1265–1268.
- 17 J. H. Sørensen, M. Lilja, T. C. Sørensen, M. Åstrand, P. Procter, S. Fuchs, M. Strømme and H. Steckel, *J. Biomed. Mater. Res. B Appl. Biomater.*, 2014, **102**, 1381–1392.
- 18 M. Stigter, J. Bezemer, K. de Groot and P. Layrolle, *J. Controlled Release*, 2004, **99**, 127–137.
- 19 M. Lilja, J. H. Sørensen, U. Brohede, M. Åstrand, P. Procter, J. Arnoldi, H. Steckel and M. Strømme, *J. Mater. Sci. Mater. Med.*, 2013, **24**, 2265–2274.
- 20 S. Tang, B. Tian, Q.-F. Ke, Z.-A. Zhu and Y.-P. Guo, *RSC Adv*, 2014, **4**, 41500–41509.

- 21 S. E. Bae, J. Choi, Y. K. Joung, K. Park and D. K. Han, *J. Controlled Release*, 2012, **160**, 676–684.
- 22 M. S. Blois, *Nature*, 1958, **181**, 1199–1200.
- 23 M. I. Alvarez Echazú, C. E. Olivetti, C. Anesini, C. J. Perez, G. S. Alvarez and M. F. Desimone, *Mater. Sci. Eng. C*, 2017, **81**, 588–596.





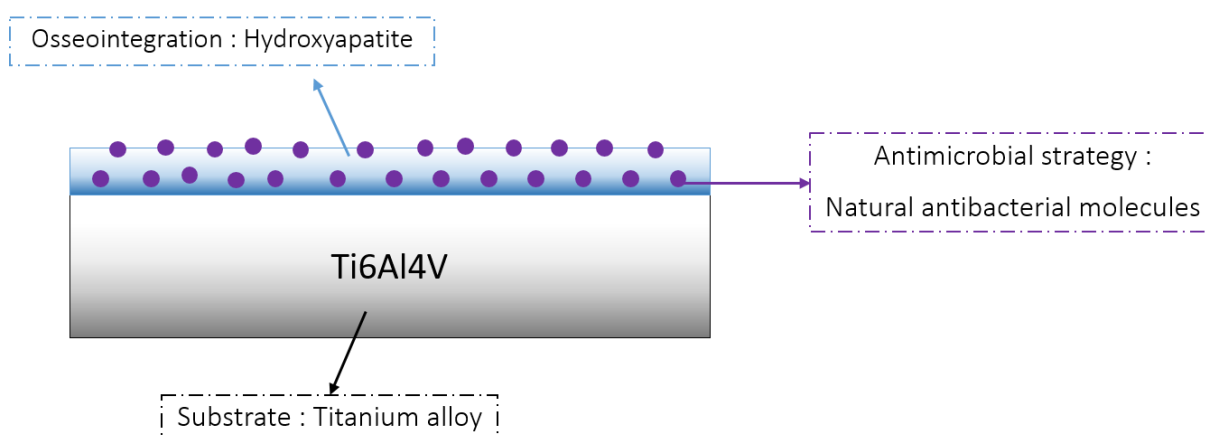
# General conclusions and perspectives





## General conclusions and perspectives

The goal of my PhD work was the development of a hybrid coating consisting of biomimetic hydroxyapatite and natural antibacterial molecules, with the goal to add antibacterial properties and enhance the osseointegration of titanium implant (see **Figure 5.1**). This work falls within the fight against periprosthetic joint infections that are one of the concerns for hip arthroplasty. The other issue it aims at addressing is the lack of interaction between implant and bone that can be improved by the presence of a layer of hydroxyapatite on the implant surface.



**Figure 5.1** Research strategy of this PhD work

We focused on four biologically active molecules (BAMs) extracted from natural products, divided in two classes: polyphenols for rosmarinic and chlorogenic acids and flavonoids for baicalin and baicalein. One of the main objectives was to understand the interaction between those molecules and hydroxyapatite, in order to choose the best candidate for the development of the antibacterial coating. First, we characterized the biological activities of the four molecules, and we investigated their interaction in solution with calcium. Secondly, we attempted to incorporate the biologically active molecules within hydroxyapatite nanoparticles. Finally, we elaborated the hybrid coating with hydroxyapatite and biologically active molecules on titanium alloy. At each step, biological activity of synthesized materials was tested.

By characterization of the DPPH radical scavenging activity, we showed that rosmarinic acid is the molecule with the best antioxidant activity. We measured the minimum inhibitory concentration of the four molecules against Gram-negative and Gram-positive bacteria. Baicalein is the molecule with the best antibacterial activity against *S. aureus*, *S. epidermidis*, and *L. ivanovii* (Gram-positive strains), but none of the molecule was active against *P. aeruginosa* (Gram-negative strain).

Complexation of rosmarinic acid and chlorogenic acid with calcium was studied with spectroscopic and spectrometric methods. Electrospray ionization mass spectrometry was useful to determine the presence of complexes and their stoichiometry. The complexation was found highly pH-dependent. We used NMR spectroscopy to determine the site of complexation, but we were not able to discriminate between the carboxylate and the catechol functions. The complexation does not have a high impact on the antioxidant properties of both molecules. As for baicalin and baicalein, we carefully characterized their stability in aqueous solution at different pH by UV-Vis spectroscopy and ESI-MS. The kinetics of degradation of both molecules is faster when pH rises, and it is related to an oxidation. The oxidation does not affect the antimicrobial activity of baicalin and baicalein, but, as expected, decreases their antioxidant ability. While complexes with calcium are detected for both molecules at pH 5, at pH 7.8 the oxidation overwhelmed the complexation.

Biologically active molecules were incorporated on/within hydroxyapatite nanoparticles by two methods, by adsorption or during the synthesis of hydroxyapatite. Baicalein is the molecule adsorbed with the highest amount on hydroxyapatite, as it was characterized by thermogravimetric analysis and solid-state NMR. Hydroxyapatite synthesis by precipitation in aqueous medium was partially or totally inhibited by the presence of BAMs if incorporated during synthesis. Crystallite size is not modified by the presence of organics, but particle size is decreased. At high concentration in presence of rosmarinic acid, only calcite is recovered at the end of the synthesis. Altogether, we assume that BAMs prevent the dissolution of calcite, which is a transitory phase in HAp synthesis. Finally, considering the degradation of BAM at pH 12 during the synthesis, and the fact that baicalein is the molecule with the best adsorption rate on hydroxyapatite nanoparticle, we decided to study the biological properties of nanoparticles with adsorbed baicalein. 40 % of the total adsorbed amount of baicalein was released from hydroxyapatite nanoparticles, as measured by HPLC. We showed a sustained antioxidant activity of particles with adsorbed baicalein over 5 days, with an initial DPPH radical scavenging of 80 %. However, particles did not exhibit any antibacterial activity against *S. epidermidis* CIP 68.21.

Finally, we deposited hydroxyapatite on titanium alloy by a biomimetic process at physiological pH and temperature in the Simulated Body Fluid (SBF). Parameters of deposition (composition of soaking solution, pretreatment of the substrate) were optimized before the incorporation of BAMs. Without BAMs, we synthesized a calcium-deficient and substituted hydroxyapatite layer, with 12  $\mu\text{m}$  of thickness. The presence of BAMs in SBF partially inhibits the deposition of hydroxyapatite, especially in presence of rosmarinic and chlorogenic acid. Layer is thinner, and the Ca/P ratio is decreased. Interaction between BAM and calcium in the HAp coating was evidenced by XPS. BAMs were also incorporated in hydroxyapatite coating by post-synthesis adsorption, inducing a remodeling of the

surface. Unfortunately, we did not find a pertinent technique of characterization to measure the incorporated quantity of BAMs in the coatings. We studied the antibacterial and antioxidant activities of coatings with baicalein, incorporated during synthesis or after adsorption. Coatings synthesized by both methods did not exhibit any antioxidant activity. On the contrary, we were able to evidence some antibacterial effect of the coating hydroxyapatite with adsorbed baicalein on *S. epidermidis* CIP 105.777.

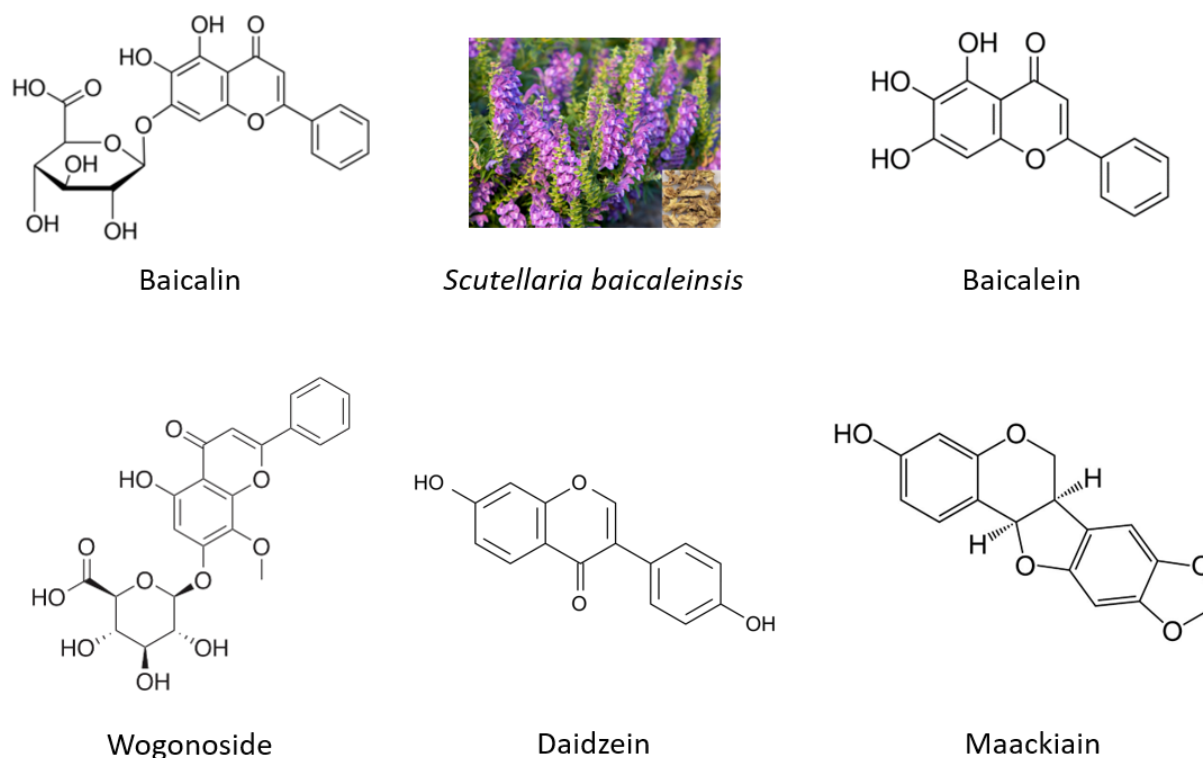
A first issue we met during our project is that the behavior of the four molecules is highly pH-dependent. Therefore, it is very difficult to compare the three parts of this work, because adsorption, nanoparticles synthesis and biomimetic synthesis do not occur at the same pH. Despite a molecular study conducted at pH 5 and pH 7.8, it is not easy to correlate the results of calcium complexation with what we observed during incorporation of BAMs in hydroxyapatite, whatever the method.

The second limitation of our work is the weak antibacterial activity observed for the hydroxyapatite coatings, which is absent for hydroxyapatite nanoparticles. Nevertheless, whereas it was not expected at the beginning of this work, hydroxyapatite nanoparticles with adsorbed baicalein possess sustained antioxidant activity. It could be interesting to try with other BAMs tested in this study, in particular rosmarinic acid as it is the molecule with the best antioxidant activity.

The weak antibacterial activity of hydroxyapatite coatings and nanoparticles with baicalein is explained by the fact that the molecule is not incorporated in a sufficient quantity, and by its weak intrinsic antibacterial activity. The novelty of this PhD work was the use of natural antibacterial molecules, to take advantage to their biological activity and to avoid any phenomenon of antibioresistance because they have never been used in the field. However, those molecules have antibacterial activity far lower than the one of traditional antibiotics (for example, the MIC of ciprofloxacin is 0.5 µg/mL against *S. aureus* ATCC 6538 while it is 34 µg/mL for baicalein). We used rosmarinic acid, chlorogenic acid, baicalin and baicalein because they bear carboxylic acid and/or catechol functions that we assumed to have affinity for hydroxyapatite. However, some of these molecules are not stable at physiological pH, and their poor solubility in water prevents their incorporation in high quantity in hydroxyapatite.

If we think of other natural biologically active molecules, flavonoids are reported in the literature<sup>1-4</sup> to oxidize at different kinetics rate at physiological pH. Any new study with other natural molecule should start with the determination of the stability of the molecule at different pHs. Moreover, in traditional medicine, plant extracts containing several antibacterial molecules acting synergistically are used, and not single components. Hydroxyapatite coatings or nanoparticles incorporating several antibacterial molecules from the same plant could be a solution to improve the

antibacterial activity of the material. For example, in *Scutellaria baicalensis*, baicalin and baicalein are in presence of wogonoside, daidzein and maackiain (see **Figure 5.2**). The immobilization of one or several molecules in addition to baicalein could help to improve the antibacterial activity of the material. Moreover, it has been shown that in presence of other flavonoids, stability of baicalein is improved<sup>5</sup>.



**Figure 5.2** Molecules found in *Scutellaria baicalensis* extracts

In terms of materials, we had expected that the *in situ* approach led to hybrid “supra” particles where the active molecules would have been buried within hydroxyapatite nanoparticles, which could have limited their release rate. This is clearly not the case here, at least for the nanoparticles. If we focus on the adsorption strategy, then a parameter of major importance will be the porosity of the particles/coatings. While mesoporous hydroxyapatite nanoparticles are not easy to obtain, one can think of porous bioglass particles as interesting alternatives. Considering the coating, a better control of the deposition process may allow to tune the interparticle porosity.





## Experimental section

### Materials

Chlorogenic acid (CA) and rosmarinic acid (RA) was purchased from Carbosynth Limited (Compton, Berkshire, UK). Baicalein (BE) and baicalin (BA) were purchased from TCI Europe (Zwijndrecht, Belgium).

Calcium chloride dihydrate was obtained from Jessen Chemica. Sodium chloride, potassium chloride were purchased from Carlo Erba. Sodium Hydrogencarbonate and TRIS were obtained from Sigma. Potassium phosphate monobasic, magnesium chloride hexahydrate and sodium sulfate are obtained from Prolabo. Phosphate buffer 0.1 M was prepared by mixing potassium phosphate monobasic and potassium phosphate dibasic at pH 7.2.

10 mm\*10 mm square Ti6Al4V titanium alloy plates with 1 mm width were obtained from GoodFellow Cambridge Limited (Huntingdon, UK). Before use, they were polished by #500, #800 and #1200 silicon carbide (SiC) disk, washed successively in acetone, ethanol and distilled water under ultrasound for 15 minutes, following by a hydroxylation in sodium hydroxide (Sigma) 5 M at 60 °C for 24 hours.

Solvent were purchased from VWR. Water use was typically deionized water or ultrapure water when mentioned (MilliQ water, 18.2 MΩcm at 25 °C, Millipore).

### Characterization techniques

#### Spectroscopic and spectrometric studies in solution

UV-Visible spectroscopy was performed on a Libra Biochrom S60 spectrometer, between 250 and 600 nm, with stepsize 0.5 nm, bandwidth 2 nm and slow scanspeed.

Electrospray ionization mass spectrometry (ESI-MS) studies were conducted on a LTQ orbitrap mass spectrometer, with a capillary voltage of 20 V and tube lens voltage of 70 V, in positive ion mode. Resonant excitation was carried out using collision-induced dissociation (CID), normalized collision energies (NCE) were between 5 and 30 %. All data analysis was performed using Thermo Xcalibur™ software. Samples were introduced at the rate of 20 μL.min<sup>-1</sup> with a 500 μL syringe. These experiments were performed with the help of Cedric Przybylski at the *Institut Parisien de Chimie Moléculaire*.

NMR liquid spectroscopy was performed in the NMR platform of the *Institut Parisien de Chimie Moléculaire*. <sup>1</sup>H and <sup>13</sup>C spectra were recorded on a Bruker 300 MHz spectrometer equipped with a BBFO probe. Number of scan was 32 for <sup>1</sup>H and 3072 for <sup>13</sup>C.

## Characterizations of hydroxyapatite nanoparticles

### *XRD*

X-ray diffractogram were recorded on a D8 diffractometer (Bruker), equipped with a source CuK $\alpha$  (1.54 Å) and a Bragg-Brentano  $\Theta - \Theta$  geometry, between 7 ° and 80 ° with a variable slit V12. For powder analysis, step was 0.03 ° and scanspeed 1 s/point. For coating analysis, step was 0.05 ° and scanspeed 0.1 s/point, and the record was repeated 5 times to decrease the signal over noise ratio.

### *TGA*

Thermogravimetric analysis was performed with a SDT Q600 apparatus from TA Instruments, between 25 °C and 700 °C, with a ramp of 10 °C/min, under air. Sample weights were typically comprised between 10 and 20 mg.

### *Specific surface area*

Surface specific area was measured with a physisorption apparatus (Belsorpmax), by measuring the adsorbed quantity of N<sub>2</sub> in function of pressure, at T = 77 K. Before measurement, vacuum degree was 3.202.10<sup>-6</sup> Pa. Sample weight was 0.9340 g.

### *Solid state NMR*

Solid state NMR studies were performed on Avance III 300 Bruker spectrometer. In the case of Cross-Polarization (CP MAS) and HPDec MAS experiments, High Power Decoupling was applied during acquisition (spinal 64,  $\nu^1\text{H}$ =50 kHz).

<sup>1</sup>H MAS NMR spectra were obtained at 300.29 MHz (at 7.04 T) using a 4 mm diameter Bruker probe (MAS frequency, 12 kHz; 90° pulse, recycle delay, 1 s; number of scans NS, 4).

{<sup>1</sup>H}-<sup>13</sup>C CP MAS NMR experiments were performed at 75.51 MHz (at 7.04 T) with a 4 mm diameter Bruker probe (MAS frequency, 12 kHz) using 90° pulse, recycle delay of 1 s, a contact time of 2 ms. NS was 47752.

{<sup>1</sup>H}-<sup>31</sup>P HPDec MAS NMR spectra were recorded using a 4 mm Bruker probe (MAS frequency, 12 kHz) at 202.49 MHz (at 11.7 T) using 30° pulse, recycle delay of 60 s and NS, 64.

{<sup>1</sup>H}-<sup>31</sup>P CP-MAS NMR experiments were carried out with a 4 mm diameter triple resonance Bruker probe (MAS frequency, 12 kHz) at a frequency of 121.56 MHz (at 7.04 T) using 90° pulse, recycle delay of 2 s, a contact time of 1 ms or 10 ms and NS, 128. A 2D HETeronuclear CORrelation {<sup>1</sup>H}-<sup>31</sup>P HETCOR-CP experiment was performed for HAp + adsorbed BE sample with a 1 s recycle delay, 10 ms contact time, 180 slices and NS, 256.



During 1D-processing, a line broadening (LB) of 10 Hz was applied for  $^1\text{H}$  MAS spectra, 50 Hz for  $\{^1\text{H}\}$ - $^{13}\text{C}$  CP MAS spectra, 30 Hz for  $\{^1\text{H}\}$ - $^{31}\text{P}$  HPDec MAS and CP MAS spectra. For the 2D  $\{^1\text{H}\}$ - $^{31}\text{P}$  HETCOR-CP experiment, LB was 50Hz in direct dimension ( $^{31}\text{P}$ ) and 50Hz in indirect dimension ( $^1\text{H}$ ).

### *Transmission electronic microscopy*

Samples were observed with Tecnai spirit G2 microscope with a Gatan Orius camera.

## Characterizations of hydroxyapatite coatings

### *Vibrational spectroscopies*

Raman spectra were collected with a Kaiser Optical system, Raman Analyzer RXN1 microprobe equipped with a laser diode at 785 nm ( $P = 10$  mW, accumulation time: 10s, 30 scans per spectrum), and a Leica microscope with x50 long working distance lens.

ATR-IR spectra were recorded on a Nicolet spectrometer (256 scans/spectrum), with a MCT detector.

### *Scanning electron microscopy*

Morphology of coatings was observed by scanning electron microscopy on a Hitachi S-3400N microscope (acceleration voltage 10 kV, probe current 70). Samples are covered with carbon before imaging. Energy dispersive X-ray spectroscopy was performed thanks to an Oxford instrument –X max. Images of HAp coatings tilted with an angle of  $45^\circ$  were recorded on a SEM-FEG Hitachi SU-70 with an acceleration voltage at 1 kV.

### *XPS*

XP spectra were collected on an Omicron Argus X-ray photoelectron spectrometer, using a monochromated Al  $K\alpha$  ( $h\nu = 1486.6$  eV) radiation source having a 300 W electron beam power. The emission of photoelectrons from the sample was analyzed at a takeoff angle of  $45^\circ$  under ultra high vacuum conditions ( $1.10^{-8}$  Pa). XP spectra were collected at pass energy of 20 eV for C1s, O1s, Ti2p, Ca2p, P2p, and Mg2s core XPS levels. After data collection, the binding energies were calibrated with respect to the binding energy of the C1s peak at 284.7 eV. The peak areas were determined after subtraction of a linear background. The atomic ratio calculations were performed after normalization using Scofield factors. Spectrum processing was carried out using the Casa XPS software package.

### *Photoluminescence*

Fluorescence spectra of coatings were obtained with a Fluorolog 3 apparatus from HORIBA Jobin Yvon. Excitation was set at  $\lambda_{\text{ext}} = 300$  nm with 5 nm of bandpass and emission spectrum was recorded between 320 and 650 nm with 1 nm of bandpas. Increment was set at 1.0 nm and integration time at

0.5 s. The surface was tilted from the incident beam (source Xenon, 450 W), and spectrum was collected with an angle of 22 °.

#### *QCM*

QCM apparatus is a QCM-E4 from Q-Sense® (Göteborg, Sweden). Solutions are injected with a peristaltic pump at 25  $\mu\text{L}\cdot\text{min}^{-1}$ . Temperature was set and regulated at 20 °C. Commercial quartz were provided by LOT-Quantum design





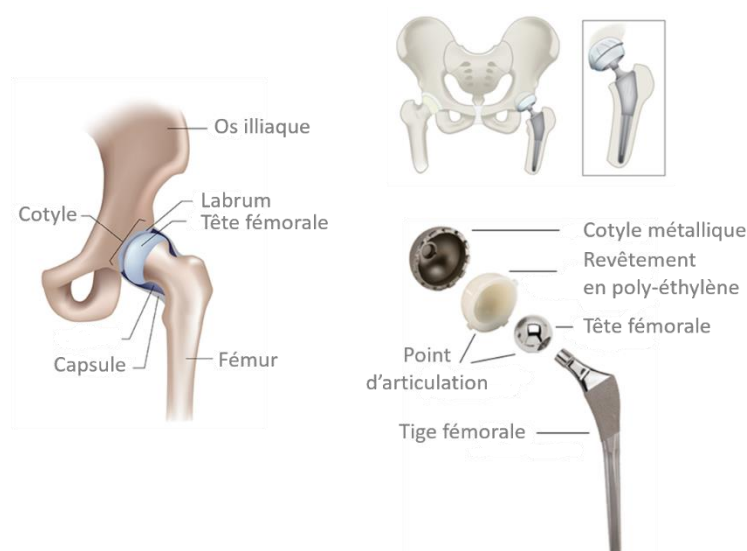
## Résumé de la thèse en français

Développement d'un revêtement hybride aux propriétés antibactériennes associant hydroxyapatite biomimétique et antibiotiques naturels

### Introduction

Le corps humain est constitué de 206 os connectés par plus de 290 articulations. La hanche est un exemple d'articulation qui relie la cuisse au bassin, grâce à la tête fémorale et la cavité cotyloïde (aussi appelée *acetabulum*) qui est formée à la jonction de trois os du bassin (l'ilium, le pubis et l'ischium). Le rôle de l'articulation de la hanche est de supporter le poids du corps, lors de la marche ou en position statique. Cependant, avec l'âge, une douleur au niveau de la hanche, causée par le développement d'arthrose, est commune. L'arthrose est une maladie caractérisée par la disparition du cartilage favorisant le glissement de la tête fémorale dans la cavité cotyloïde. Pour réduire la douleur et retrouver la fonction de l'articulation dans le but d'améliorer la qualité de vie des patients, l'articulation défectueuse est remplacée par un implant pendant une arthroplastie totale de hanche. C'est l'une des chirurgies orthopédiques les plus communes, avec plus de 100 000 personnes opérés chaque année en France<sup>1</sup>.

Depuis toujours les Hommes ont essayé de remplacer des parties défectueuses du corps humain par des implants en matériaux naturels ou synthétiques. Pour la prothèse de hanche les plus anciens essais enregistrés datent de 1891 en Allemagne, avec utilisation de l'ivoire (matériau naturel, composant des dents et des défenses d'éléphants) pour remplacer la tête fémorale<sup>2</sup>. Les implants utilisés de nos jours sont proches de ceux développés dans les années 1960 par Sir John Charnley. Ces implants sont constitués de trois parties, une tête fémorale métallique, une cavité cotyloïde en polyéthylène et un ciment en acrylique. Le ciment permet d'améliorer la fixation de la prothèse, en agissant comme une colle. Aujourd'hui, trois types de prothèses sont disponibles, métal-sur-polyéthylène, métal-sur-métal, et céramique-sur-céramique, chacun avec des avantages et des inconvénients. Des méthodes n'utilisant pas de ciment sont également développées, car celui-ci peut être dégradé pendant la marche, ce qui cause une réponse inflammatoire et peut entraîner le retrait de l'implant.

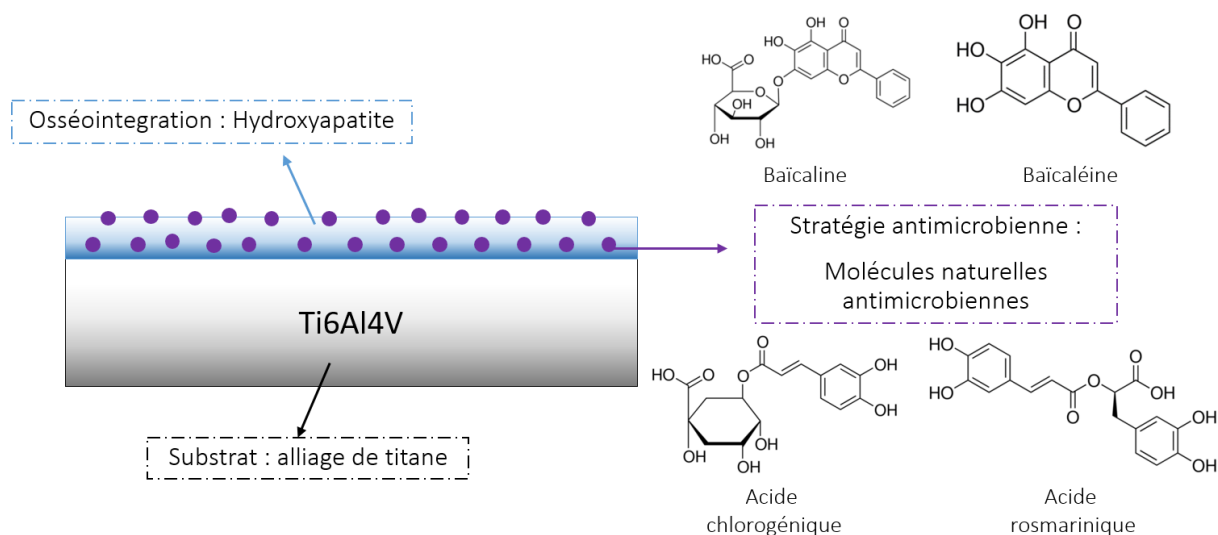


**Figure 1.** Anatomie de la hanche, position de l'implant à la place de l'articulation et description d'un implant classique

Pour les prothèses sans ciment, deux problèmes majeurs causent le retrait de l'implant avec un taux de chirurgie de reprise de 10 %, le descellement aseptique et le développement d'infections<sup>3,4</sup>. Premièrement, le descellement aseptique est causé par la faible interaction existant entre l'implant et l'os. En effet, les implants métalliques, principalement en titane et ses alliages, sont biocompatibles, c'est-à-dire qu'ils n'entraînent pas une réponse inflammatoire. Cependant, ils n'ont pas de propriétés d'ostéoconduction, c'est-à-dire qu'ils ne favorisent pas la croissance osseuse à leur surface. Une modification de la surface de l'implant par des méthodes physiques (polissage, traitements plasma, lithographie) ou chimiques (traitements acides ou basiques, dépôt d'un revêtement) sont disponibles pour améliorer l'ostéointégration. On peut noter par exemple l'utilisation de l'hydroxyapatite, le minéral constituant les os et les dents des mammifères, en tant que revêtement permettant une meilleure interaction entre l'os et l'implant. La seconde cause de reprise des implants est le développement d'infections, en dépit des traitements préventifs par prophylaxie d'antibiotiques et des techniques opératoires stériles. Une technique prometteuse pour éviter le développement d'infection est d'utiliser l'implant comme support de l'activité antimicrobienne, ce qui permet d'atteindre de plus forts dosages au niveau de la zone affectée, tout en réduisant la durée du traitement et les effets secondaires<sup>5</sup>. Différents agents antibactériens peuvent être envisagés, inorganiques (métaux ou ions, comme l'argent ou le cuivre), ou bio-organiques (antibiotiques, peptides antimicrobiens).

Dans ce contexte, cette thèse vise à développer un revêtement de surface ostéoconducteur et antimicrobien pour les implants métalliques, en associant l'hydroxyapatite et des molécules antibactériennes. Nous avons décidé d'utiliser une méthode de synthèse permettant d'obtenir une

hydroxyapatite biomimétique sur des substrats en alliage de titane Ti6Al4V, dans le but d'atteindre la meilleure interaction possible entre l'os et l'implant. Comme le phénomène d'antibiorésistance est l'un des défis majeurs de santé publique du 21<sup>ème</sup> siècle, nous nous sommes intéressés à des molécules naturelles, extraites de plantes, connues pour leurs propriétés antibactériennes mais jamais utilisés dans ce contexte. Quatre molécules ont été choisies, la baïcaline, la baïcaléine, l'acide rosmarinique et l'acide chlorogénique. Ces molécules sont des polyphénols et des flavonoïdes, possédant une ou plusieurs fonctions catéchol, ainsi qu'un groupement acide carboxylique pour 3 d'entre elles. Ces fonctions chimiques sont susceptibles d'interagir avec l'hydroxyapatite. Le principal objectif de ce travail était donc d'incorporer ces molécules dans ou sur l'hydroxyapatite. Pour ce faire, nous nous sommes intéressés à l'interaction entre ces quatre molécules et l'hydroxyapatite à différents niveaux, en solution, avec des nanoparticules, et enfin avec un revêtement de surface sur alliage de titane.



**Figure 2.** Stratégie développée dans cette thèse

## 1. Etude moléculaire

Nous avons dans un premier temps étudié l'interaction entre les quatre molécules naturelles actives biologiquement (MABs) avec l'ion calcium en solution à différents pHs.

Les acides chlorogéniques et rosmariniques sont deux polyphénols avec des structures très proches, partageant la même partie d'acide caféique. La baïcaline et la baïcaléine sont également similaires, puisque la baïcaléine est l'aglycone de la baïcaline. L'activité antibactérienne de ces quatre molécules a été caractérisée par mesure de la concentration minimum d'inhibition (CMI) sur quatre souches bactériennes, trois à Gram positif, *Staphylococcus aureus* ATCC 6538, *Staphylococcus epidermidis* CIP 68.21, *Listeria ivanovii* Li4(pvS2) et une souche à Gram négatif, *Pseudomonas aeruginosa* ATCC 27853. Aucune CMI n'a pu être déterminée contre *P. aeruginosa*, pour les quatre molécules. Contre les trois

souches à Gram positif, la baïcaléine est la molécule avec la plus faible CMI, signifiant que c'est la molécule la plus active, avec une CMI de 34 µg/mL contre *S. aureus* et *S. epidermidis*, et 17 µg/mL contre *L. ivanovii*. Par la suite, l'activité antioxydante des MABs a été caractérisée par mesure du taux de piégeage des radicaux libres du DPPH. L'acide rosmarinique est la molécule avec la meilleure activité antioxydante, avec un taux de 29 %.

L'interaction des quatre molécules avec le calcium a été étudiée à pH 5 et pH 7.8 par spectroscopie UV-Visible et spectrométrie de masse avec ionisation électrospray, afin de déterminer la stoechiométrie des complexes. Pour l'acide chlorogénique et l'acide rosmarinique, la complexation est très dépendante du pH. A pH 5, de nombreux complexes sont formés, soit monomoléculaires ( $[MAB-H+Ca]^+$ ), soit polymoléculaires ( $[2MAB+Ca]^{2+}$ ,  $[3MAB+Ca]^{2+}$ ). Les complexes monomoléculaires formés par des molécules déprotonées sont plus stables que les complexes biomoléculaires. A pH 7.8, seuls les complexes  $[MAB-H+Ca]^+$  sont formés. Nous avons tenté de déterminer le site de complexation du calcium par spectroscopie de résonance magnétique nucléaire (RMN). Pour l'acide rosmarinique, trois sites de complexation sont possibles, le carboxylate, et les deux fonctions catéchol, la fonction avec le pKa le plus bas étant plus probable que l'autre. Pour l'acide chlorogénique, trois sites sont également possibles, le carboxylate, le catéchol, et le site composé d'un hydroxyle du cycle polyol et du carboxylate. Cependant, il n'a pas été possible de discriminer entre le catéchol ou le carboxylate par RMN. L'effet de la complexation avec le calcium sur l'activité antioxydante des deux molécules a été étudiée, mais seulement une légère baisse de l'activité est observée pour l'acide rosmarinique.

Pour la baïcaline et la baïcaléine, nous nous sommes d'abord intéressés à leur dégradation à pH physiologique, qui avait déjà été mentionnée dans la littérature. Nous avons mis en lumière l'oxydation des deux molécules, avec des cinétiques de dégradation différentes selon le pH. La baïcaléine s'oxyde à pH 5, alors que la baïcaline ne s'oxyde pas avant pH 7.2. L'oxydation dépend également du tampon utilisé. Connaissant l'oxydation de la baïcaléine, nous pouvons supposer que c'est la forme oxydée de la molécule qui est active. La complexation avec le calcium a été étudiée à pH 5 et pH 7.8, tout en sachant que les deux molécules sont oxydées à pH 7.8. A pH 5, des complexes sont formés pour les deux molécules, mais à pH 7.8 l'oxydation est en compétition avec la complexation. La baïcaléine oxydée ne peut pas complexer le calcium, alors que seule une petite fraction de la baïcaline forme un complexe. Le reste de la molécule est observée sous forme oxydée ou dégradée après oxydation en baïcaléine oxydée. L'impact de la complexation sur les propriétés antioxydantes et antibactériennes des deux molécules a été vérifié. Il n'y a pas d'effet significatif sur leurs activités biologiques.



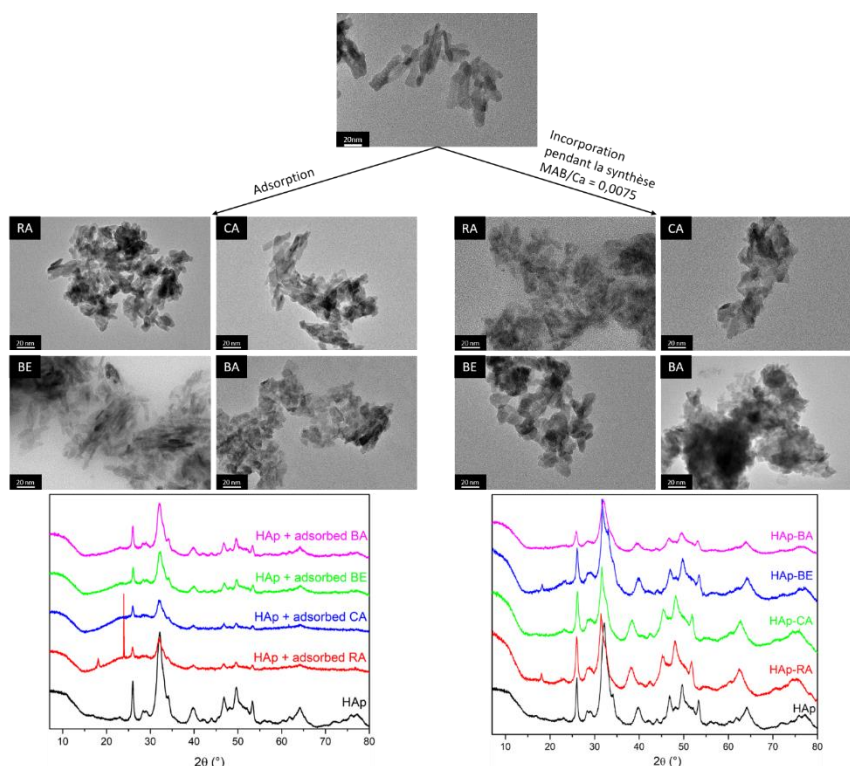
	Complexation		Oxydation	
	pH 5	pH 7,8	pH 5	pH 7,8
Acide rosmarinique	✓	✓	X	X
Acide chlorogénique	✓	✓	X	X
Baïcaline	✓	✓	X	✓
Baïcaléine	✓	X	✓	✓

**Table 1.** Récapitulatif du comportement des quatre molécules actives biologiquement en fonction du pH et de la présence de calcium.

## 2. Formation de nanoparticules hybrides

Les quatre MABs ont par la suite été incorporées dans des nanoparticules d'hydroxyapatite par deux méthodes. D'un côté elles ont été incorporées concomitamment à la synthèse des nanoparticules, directement dans le milieu réactionnel, et de l'autre côté elles ont été adsorbées après la synthèse sur des nanoparticules préformées. L'adsorption de molécules biologiquement actives sur l'hydroxyapatite a déjà été rapportée dans la littérature, pour la délivrance d'agents antibactériens ou ostéogéniques. L'adsorption des quatre molécules ne modifie pas significativement la structure des nanoparticules, comme cela a été montré par microscopie électronique à transmission. La molécule incorporée en plus grande quantité, mesurée par analyse thermogravimétrique, est la baïcaléine. Ceci peut être expliquée par la présence de la fonction pyrogallol sur la baïcaléine, qui a été montré comme étant adsorbée plus vite et avec une interaction plus forte sur l'hydroxyapatite, comparée aux fonctions acide carboxylique et catéchol. Dans le cas de l'incorporation des quatre MABs pendant la synthèse des nanoparticules, deux concentrations de MABs ont été testées, avec des ratios MAB:Ca = 0.075 et 0.0075. La présence des molécules organiques inhibe partiellement ou totalement la synthèse des nanoparticules. A bas ratio, l'hydroxyapatite est bien synthétisée, mais avec un plus faible rendement et une taille des cristallites plus petite qu'en absence de MAB. A plus grand ratio, dans le cas de l'acide rosmarinique ce n'est pas de l'hydroxyapatite mais le carbonate de calcium calcite qui est synthétisé. Cette phase est également trouvée dans les particules synthétisées en présence de baïcaléine et d'acide chlorogénique. La calcite est un intermédiaire lors de la synthèse de l'hydroxyapatite selon notre méthode. Il se forme après dissolution de l'hydroxyde de calcium. Les molécules organiques peuvent s'adsorber à la surface de la calcite, ce qui pourrait limiter voire inhiber sa dissolution et donc la formation de l'hydroxyapatite. Par ailleurs, nous avons souligné la dégradation des MABs à pH basique, qui est le pH employé lors de la synthèse des nanoparticules. En conclusion, la voie de synthèse par incorporation concomitante à la synthèse des nanoparticules n'est pas la plus adaptée pour obtenir des nanoparticules hybrides. C'est la raison pour laquelle nous avons décidé de

tester uniquement l'activité biologique des nanoparticules obtenues après adsorption de molécule active. Notre choix s'est porté sur les particules après adsorption de baicaléine, car c'est la molécule adsorbée en plus grande quantité, et qui présente la meilleure activité antibactérienne. La libération *in vitro* de la molécule dans un tampon phosphate salin (PBS) a été étudié par chromatographie liquide haute performance (HPLC). Il suit un profil typique avec une forte quantité libérée initialement, suivie d'une phase de libération plus lente. La quantité libérée en 5 jours correspond à 40 % de la quantité totale incorporée, ce qui signifie 25 mg de baicaléine libérée pour 1 g de nanoparticules. Après adsorption sur l'hydroxyapatite, la baicaléine reste active. En effet, les nanoparticules montrent une activité antioxydante prolongée sur plusieurs jours. Nous suggérons que c'est la molécule adsorbée qui est responsable de l'activité antioxydante, plutôt que la molécule relarguée dans la solution. En effet, comme la baicaléine est oxydée à pH physiologique, elle perd son activité de piégeage des radicaux libres. Concernant l'activité antibactérienne, notre système n'a pas montré d'activité significative contre *S. epidermidis*. Nos nanoparticules hybrides sont moins efficaces que d'autres systèmes de relargage d'antibiotiques trouvés dans la littérature, mais ceci peut s'expliquer par l'utilisation de molécules naturelles, qui possèdent des CMI bien plus faibles que les antibiotiques classiques utilisés comme la tétracycline ou la vancomycine.



**Figure 3.** Incorporation des molécules actives biologiquement dans/sur des nanoparticules d'hydroxyapatite par incorporation dans la solution de dépôt ou par adsorption. Images de microscopie électronique à transmission et comparaison des diffractogramme des rayons X.

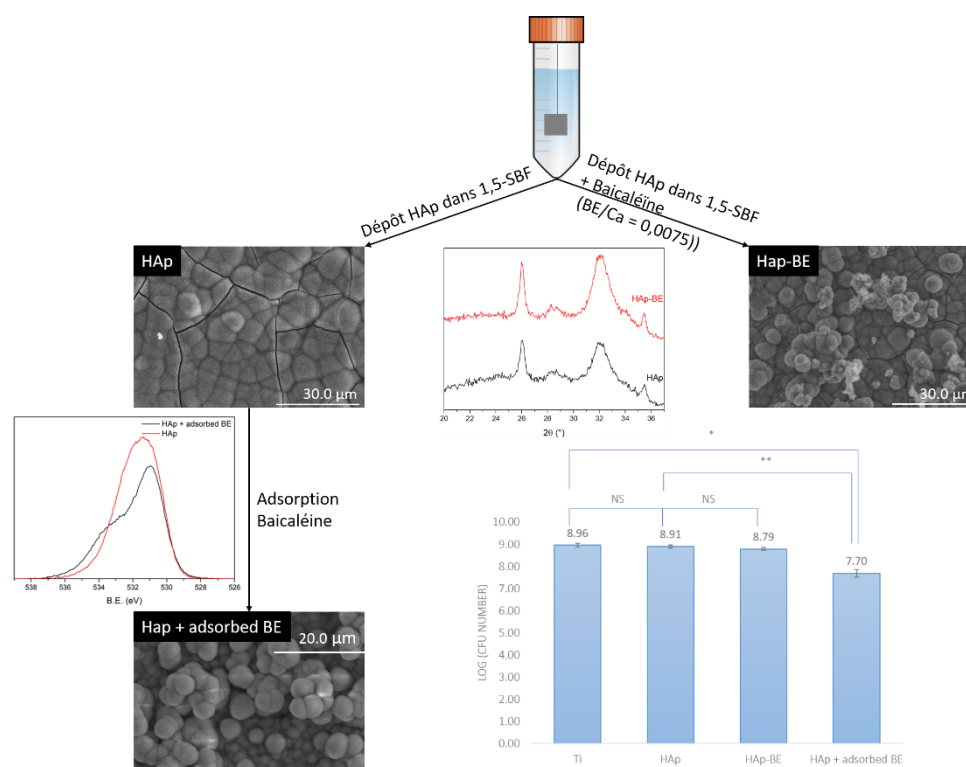
### 3. Formation de revêtements hybrides sur alliage de titane Ti6Al4V

La troisième partie de cette étude est consacrée à l'incorporation des molécules actives biologiquement (MABs) dans des revêtements d'hydroxyapatite déposés sur un alliage de titane Ti6Al4V. L'hydroxyapatite a été synthétisée à partir d'une solution supersaturée appelée fluide corporel simulé (en anglais Simulated Body Fluid, SBF) dont la composition est directement dérivée de la solution rapportée dans la littérature par Kokubo et al<sup>6</sup>. Ces auteurs ont montré que l'hydroxyapatite obtenue selon cette méthode est appropriée pour la croissance des cellules osseuses (ostéoblastes). La composition ionique du SBF est proche de celle du plasma sanguin, en terme de composition et de concentration. La présence d'ions comme  $\text{Na}^+$  ou  $\text{Mg}^{2+}$ , ainsi que des carbonates  $\text{CO}_3^{2-}$ , mène à des substitutions dans l'hydroxyapatite formée qui est aussi déficiente en calcium. Cette méthode de dépôt d'hydroxyapatite est très utilisée dans la littérature, mais avec des paramètres variables, comme la durée du dépôt, la concentration et la composition de la solution, ainsi que le traitement de la surface de titane avant dépôt. Nous nous sommes donc intéressés dans un premier temps à une étape d'optimisation des paramètres de dépôt, en termes de traitement de surface et de composition de la solution supersaturée. Nous avons conclu qu'un prétraitement basique dans une solution de NaOH 5 M pendant 24 h à 60 °C était suffisant pour obtenir une surface favorisant le dépôt d'hydroxyapatite. Concernant la composition de la solution de dépôt, nous avons choisi de concentrer 1,5 fois la solution par rapport au SBF de Kokubo, dans le but d'accélérer la synthèse du matériau. Une plus grande proportion en carbonate a été testée, mais la solution était plus instable et le dépôt final obtenu moins homogène, donc la concentration originale en carbonate a été gardée. Le dépôt d'hydroxyapatite a duré 14 jours, à 37 °C et pH physiologique, avec un renouvellement de la solution supersaturée par une solution fraîchement préparée tous les deux jours. Avec ces paramètres nous avons obtenu une couche d'hydroxyapatite d'une épaisseur d'environ 12  $\mu\text{m}$ . Par spectroscopie Raman et spectroscopie de photoélectron X (XPS) nous avons montré que le matériau est substitué avec des ions  $\text{Na}^+$ ,  $\text{Mg}^{2+}$ , et carbonaté. Cette méthode est donc efficace pour synthétiser de l'hydroxyapatite biomimétique.

Par la suite, les MABs ont été incorporées dans le revêtement par deux méthodes : 1) solubilisation des MABs directement dans le SBF pour ajout concomitant au dépôt d'hydroxyapatite, et 2) adsorption des MABs sur un dépôt d'hydroxyapatite pré-synthétisé. Lors du dépôt en une étape, un rapport MAB:Ca = 0.0075 a été utilisé. La présence des molécules organiques n'inhibe pas la formation de l'hydroxyapatite, mais le dépôt obtenu est plus fragile que celui synthétisé sans MAB, et ne recouvre pas toute la surface du substrat en titane dans le cas de l'acide rosmarinique. La spectroscopie Raman et l'analyse XPS suggèrent que l'hydroxyapatite est la seule phase obtenue. La présence des MABs dans le revêtement a été montrée par XPS, mais la quantification de la quantité incorporée n'a pas pu être réalisée par manque de méthodes adaptées. La seconde méthode utilisée, l'adsorption des molécules

sur un revêtement d'hydroxyapatite préformé, n'a concerné que la baicaline et la baicaléine. Après dépôt dans le SBF, les plaques d'alliage de titane recouvertes d'hydroxyapatite ont été immergées dans une solution aqueuse de baicaline ou baicaléine concentrée à 0.1 mM, pendant 24 heures à température ambiante. La présence des MABs à la surface du revêtement a été montrée par XPS et fluorescence. Cependant, comme dans le cas de l'incorporation pendant la synthèse, il n'a pas été possible de quantifier la quantité incorporée. Nous avons par ailleurs constaté que l'adsorption de ces MABs induit un remodelage de la surface du revêtement.

Pour terminer, nous avons testé les actions antioxydante et antibactérienne des revêtements hydroxyapatite-baicaléine, synthétisés soit par adsorption soit par incorporation concomitante à la synthèse. Les revêtements n'ont pas d'activité antioxydante, quelle que soit leur méthode de synthèse, probablement parce que la quantité de baicaléine incorporée est trop faible. L'activité antibactérienne des revêtements a été testée sur *Staphylococcus epidermidis* CIP 105.777. Les revêtements avec incorporation de la baicaléine pendant la synthèse de l'hydroxyapatite n'ont aucune activité antibactérienne, alors que les revêtements avec adsorption de baicaléine inhibent la croissance bactérienne en 16 h en milieu riche.



**Figure 4.** Incorporation de la baicaléine dans/sur des revêtements d'hydroxyapatite sur des alliages de titane par incorporation dans la solution de dépôt ou par adsorption. Images de microscopie électronique à balayage, diffractogramme des rayons X et spectroscopie de photoélectron X de l'oxygène O 1s. Comparaison de l'effet antibactérien sur *Staphylococcus epidermidis* CIP 105.777.

## Conclusion

En conclusion, durant cette étude nous avons développé un revêtement hybride constitué d'hydroxyapatite biomimétique et de molécules naturelles. La faible activité antibactérienne mesurée est expliquée par deux raisons, la faible quantité de molécule incorporée et la faible activité antibactérienne intrinsèque de la molécule. L'originalité de ce travail est l'utilisation de molécules naturelles, pour profiter de leur activité biologique tout en évitant tout phénomène de résistance parce qu'elles n'ont jamais été utilisées dans ce domaine. Cependant, ces molécules ont des activités antibactériennes beaucoup plus faibles que les antibiotiques traditionnels. De plus, nous avons été limités par leur faible solubilité en phase aqueuse et leur instabilité en conditions physiologiques. Ces différences, peu discutées dans la littérature, sont à prendre en considération pour leur utilisation dans des applications biomédicales. Pour les pallier, nous suggérons d'utiliser des mélanges de molécules naturelles afin de profiter de leur synergie d'action, telle qu'exploitée par les organismes vivants dont elles sont extraites.

## References

- 1 Haute autorité de Santé. Prothèses de hanche. Phase contradictoire suite à la révision d'une catégorie de dispositifs médicaux. Saint Denis La Plaine : HAS ; 2014.
- 2 S. R. Knight, R. Aujla and S. P. Biswas, *Orthop Rev*, 2011, **3**, 72–74.
- 3 S. Kurtz, F. Mowat, K. Ong, N. Chan, E. Lau and M. Halpern, *The Journal of Bone and Joint Surgery*, 2011, **87-A**, 1487–1497.
- 4 B. Zhang, D. Myers, G. Wallace, M. Brandt and P. Choong, *International Journal of Molecular Sciences*, 2014, **15**, 11878–11921.
- 5 R. Dorati, A. DeTrizio, T. Modena, B. Conti, F. Benazzo, G. Gastaldi and I. Genta, *Pharmaceuticals*, 2017, **10**, 96.
- 6 T. Kokubo, *Acta Materialia*, 1998, **46**, 2519–2527.





## Abstract

This thesis aims to develop a hybrid coating based on biomimetic hydroxyapatite and natural antibacterial molecules, with the goal to add antibacterial properties and enhance the osseointegration of titanium (Ti6Al4V) implants. Four natural biologically active molecules (BAMs) were tested, rosmarinic acid, chlorogenic acid, baicalin and baicalein. To understand the interaction between those molecules and hydroxyapatite, we present here three complementary studies: in solution with calcium ion, with hydroxyapatite nanoparticles and with biomimetic hydroxyapatite coatings on titanium alloy. The complexation between BAMs and calcium ion in solution is highly pH-dependent. When incorporated within hydroxyapatite nanoparticles or coatings during synthesis, BAMs inhibit the formation of the mineral phase. On the contrary, they can be efficiently adsorbed on pre-synthesized particles. Finally, we present the biological properties of hydroxyapatite nanoparticles and coatings with adsorbed baicalein. Hybrid nanoparticles are potent antioxidant agents, but they do not exhibit any antibacterial activity, whereas hybrid coatings have a significant effect on the bacterial growth of *Staphylococcus epidermidis* CIP 105.777. This work originality stands on the use of natural antibacterial molecules, but we highlight the difficulty to handle them, due to their poor solubility and stability in physiological pH, which should be considered for further use in biomedical applications.

**Key-words:** hydroxyapatite, biomimetic coating, natural molecules, antibacterial, antioxidant, titanium implant

## Résumé

Cette thèse porte sur l'élaboration de revêtements de surface hybrides composés d'hydroxyapatite biomimétique et de molécules antibactériennes naturelles, dans le but d'ajouter des propriétés antibactériennes et d'améliorer l'osseointégration d'implants en titane (Ti6Al4V). Quatre molécules naturelles biologiquement actives (MABs) ont été étudiées, l'acide rosmarinique, l'acide chlorogénique, la baicaline et la baicaléine. Pour comprendre l'interaction entre ces molécules et l'hydroxyapatite, nous présentons ici trois études complémentaires : en solution avec l'ion calcium, avec des nanoparticules d'hydroxyapatite et avec un revêtement de surface d'hydroxyapatite biomimétique sur alliage de titane. En solution, le pH influence la complexation entre les MABs et le calcium. Les MABs inhibent formation de l'hydroxyapatite lorsqu'elles sont incorporées pendant sa synthèse, sous forme de nanoparticules ou de revêtements. Elles peuvent cependant être efficacement adsorbées à la surface de particules ou de revêtements pré-synthétisés. Enfin, nous présentons les propriétés biologiques des nanoparticules et de revêtements hybrides avec de la baicaléine adsorbée. Les nanoparticules hybrides sont de potentiels agents antioxydants, mais n'ont pas d'activité antibactérienne. Les revêtements de surface hybrides sont quant à eux efficaces pour limiter la croissance bactérienne de *Staphylococcus epidermidis* CIP 105.777. L'originalité de ce travail repose sur l'utilisation de molécules antibactériennes naturelles, mais nous soulignons ici la difficulté de les utiliser, de par leur faible solubilité et stabilité à pH physiologique, ce qui devra être considéré lors de leur future utilisation dans des applications biomédicales.

**Mots-clés :** hydroxyapatite, revêtement de surface biomimétique, molécules naturelles, antibactérien, antioxidant, implant en titane